CONTENTS

Page

INTENTIONALLY LEFT BLANK

TABLES

Page

INTENTIONALLY LEFT BLANK

FIGURES

Page

FIGURES (Continued)

Page

FIGURES (Continued)

Page

FIGURES (Continued)

FIGURES (Continued)

Page

INTENTIONALLY LEFT BLANK

2.3.8 Radionuclide Transport in Unsaturated Zone

[NUREG-1804, Section 2.2.1.3.7.3: AC 1, AC 2, AC 3(1), (2), (4), (5), AC 4, AC 5]

The information presented in this section addresses the requirements of proposed 10 CFR 63.114(a)(1) through (a)(5), (a)(7), and (b) for conducting a performance assessment in the area of radionuclide transport in the unsaturated zone. The requirement of proposed 10 CFR 63.114(a)(6) is not referenced below because degradation, deterioration, and alteration processes are addressed in Sections 2.2, 2.3.4 to 2.3.7, and 2.3.11. This section also provides information that addresses specific acceptance criteria in Section 2.2.1.3.7 of NUREG-1804.

With regard to radionuclide transport in the unsaturated zone, this section presents:

- Data from the site and surrounding region, uncertainties and variabilities in parameter values, and alternative conceptual models used in the analyses
- Specific features, events, and processes (FEPs) included in the analyses, with the technical bases for inclusion
- Technical bases for models used in the performance assessment.

The categories of information provided in this section, as well as the corresponding proposed 10 CFR Part 63 regulatory requirements and NUREG-1804 acceptance criteria, are presented in the table below. With regard to Acceptance Criteria 1(6) and 3(5) in Section 2.2.1.3.7.3 of NUREG-1804, no formal peer reviews or expert elicitations were used directly to support development of the current unsaturated zone radionuclide transport models discussed in this Section 2.3.8. In addition, this section does not discuss the approach used for data qualification. However, scientific analyses, model development, and data qualification activities were conducted in accordance with project procedures that comply with Quality Assurance Program requirements. The project procedures governing data qualification are consistent with NUREG-1298 (Altman et al. 1988) in keeping with Acceptance Criterion 1(6). Acceptance Criterion 3(3) is not referenced below because criticality events are excluded from the total system performance assessment (TSPA), as is discussed in Section 2.2.1.4.1.

SAR Section	Information Category	Proposed 10 CFR Part 63 Reference	NUREG-1804 Reference
2.3.8	Radionuclide Transport in Unsaturated Zone	63.114(a)(1) 63.114(a)(2) 63.114(a)(3) 63.114(a)(4) 63.114(a)(5) 63.114(a)(7) 63.114(b) 63.342(c)	Section 2.2.1.3.7.3: Acceptance Criterion 1 Acceptance Criterion 2 Acceptance Criterion 3(1) Acceptance Criterion 3(2) Acceptance Criterion 3(4) Acceptance Criterion 3(5) Acceptance Criterion 4 Acceptance Criterion 5
2.3.8.1	Summary and Overview	Not applicable	Not applicable

SAR Section	Information Category	Proposed 10 CFR Part 63 Reference	NUREG-1804 Reference
2.3.8.2	Conceptual Description of Unsaturated Zone Transport Processes	63.114(a)(1) 63.114(a)(2) 63.114(a)(5)	Section 2.2.1.3.7.3: Acceptance Criterion 1(1) Acceptance Criterion 1(2) Acceptance Criterion 1(3) Acceptance Criterion 1(4) Acceptance Criterion 1(5) Acceptance Criterion 2(1) Acceptance Criterion 2(3) Acceptance Criterion 3(4) Acceptance Criterion 4 Acceptance Criterion 5(1)
2.3.8.3	Data and Data Uncertainty	63.114(a)(1) 63.114(a)(2) 63.114(a)(3) 63.114(b)	Section 2.2.1.3.7.3: Acceptance Criterion 2 Acceptance Criterion 3(4)
2.3.8.4	Model Development	63.114(a)(1) 63.114(a)(2) 63.114(a)(3) 63.114(a)(4) 63.114(a)(5) 63.114(a)(7) 63.114(b) 63.342(c)	Section 2.2.1.3.7.3: Acceptance Criterion 1(1) Acceptance Criterion 1(2) Acceptance Criterion 1(4) Acceptance Criterion 4
2.3.8.5	Model Abstraction	63.114(a)(1) 63.114(a)(2) 63.114(a)(3) 63.114(a)(7) 63.114(b) 63.342(c)	Section 2.2.1.3.7.3: Acceptance Criterion 1(3) Acceptance Criterion 3(1) Acceptance Criterion 3(2) Acceptance Criterion 3(4) Acceptance Criterion 5
2.3.8.6	Conclusions	Not applicable	Not applicable

2.3.8.1 Summary and Overview

As described in Section 2.1.2.3, the unsaturated zone below the repository is a component of the Lower Natural Barrier, which, for many radionuclides, including most strongly sorbing species, prevents or substantially reduces the rate of movement of radionuclides from the repository to the accessible environment. The flow of water in the unsaturated zone is described in Section 2.3.2. As discussed in Section 2.3.8, the unsaturated zone radionuclide transport process and abstraction models simulate the features and processes that contribute to the capability of the unsaturated zone component of the Lower Natural Barrier to reduce the movement of radionuclides. The transport or advection of radionuclides away from the repository depends on the rate and pathways of flow within the unsaturated zone, the retardation of radionuclides, and the rate of transport by colloids. Several basic processes contribute to the ability of the Lower Natural Barrier to prevent or reduce the movement of radionuclides, including recharge, diffusion of radionuclides from water flowing in fractures into the pores of the rock matrix, sorption of radionuclides onto rock or mineral surfaces, and colloid-facilitated transport.

The processes and characteristics that have been determined to be important to the capability of the unsaturated zone component of the Lower Natural Barrier (Section 2.1.2.3 and Table 2.1-4) include:

- **Fractures**—Fractures below the repository conduct the majority of the percolation flux through the unsaturated zone, although: (1) the low-matrix-permeability zeolitic rocks of the CHn cause increased lateral diversion toward the faults; and (2) the vitric CHn is dominated by matrix flow. The rate of flow and the extent of transport in fractures are influenced by characteristics such as orientation, aperture, asperity, spacing, fracture length, connectivity, and the nature of any linings or infills. Further discussion on the impact of fractures on radionuclide migration in the unsaturated zone is presented in Section 2.3.8.2.2.1.

- **Faults**—Faults of various sizes have been noted in the Yucca Mountain region, and specifically in the repository area. A significant fraction of percolation flux below the repository occurs through faults (SNL 2007a, Section 6.2.2). Faults provide fast flow and radionuclide transport pathways through the unsaturated zone, particularly below the northern region of the repository where the low matrix permeability of the underlying zeolitic CHn unit promotes lateral flow and transport towards and down faults (SNL 2008a, Section 6.6).

- **Climate Change**—Future climate change causes several responses in the unsaturated zone beneath the repository, including changes in percolation flux and attendant radionuclide transport, water table rise, and recharge to the saturated zone. Precipitation and net infiltration into the unsaturated zone tends to increase with future climate change causing an increase in fracture flux and, hence, a reduction in the effectiveness of matrix diffusion, and an increase in recharge during the first 10,000 years after repository closure. After 10,000 years, the rate of percolation at the repository horizon is specified by proposed 10 CFR 63.342(c).

- **Climate Modification Increases Recharge**—The ability of the unsaturated zone to prevent or substantially reduce the rate of movement of radionuclides depends on the flux of water through the unsaturated zone and the distribution of that flux within the fractured rock mass. This flux is directly dependent on the surficial recharge and infiltration that, in turn, is affected by climatic conditions. Climate and infiltration are modeled for the present-day climate and for the monsoon and glacial-transition climates that are expected to occur after the present-day climate but within 10,000 years. For the post-10,000-year period, the water flux boundary condition applied at the ground surface is adjusted to conform to proposed 10 CFR 63.342(c), which stipulates a log-uniform probability distribution for average deep percolation flux to the repository footprint ranging from 13 to 64 mm/yr (Section 2.3.2.4.1.2.4.2). The effects associated with future climate change are included in the TSPA models and described in Sections 2.3.2.5 and 2.3.8.5.3.

- **Stratigraphy**—Stratigraphy and associated hydrologic properties have significant effects on unsaturated zone flow and transport processes due to the contribution of faults in conducting flow below the repository and due to the different flow characteristics of the TSw and zeolitic and vitric CHn and CFu units. In particular, the low matrix permeability

of the zeolitic CHn unit beneath the northern half of the repository block promotes fracture flow and/or lateral diversion towards faults. In contrast, the unaltered, vitric CHn unit beneath the southern region of the repository block has a relatively high matrix porosity and permeability, and matrix flow dominates. As a consequence, radionuclides released from the northern region of the repository tend to have much shorter travel times to the saturated zone than those released in the southern region because transport is primarily downward through fast flowing fractures and faults as opposed to much slower matrix flow. Discussion of the impact of these hydrogeologic characteristics on radionuclide migration through the unsaturated zone is presented in Section 2.3.8.4.5.1.

- **Rock Properties of Host Rock and Other Units—**Percolation of water in the unsaturated zone below the repository is significantly affected by the hydrogeologic properties of the rock units above and below the repository. Where fracture-matrix properties change abruptly, such as at the contact between welded tuffs and low permeability units with sparse fractures, perched water zones may form, leading to lateral diversion of flow. Conversely, the presence of the PTn unit, characterized by porous flow in the matrix, attenuates and dampens the temporally and spatially variable pulses of flow moving through fractures in the welded Tiva Canyon tuff so that the percolation of water in the unsaturated zone above and below the repository is a quasi-steady state.

- **Unsaturated Groundwater Flow in the Geosphere—**Unsaturated groundwater flow below the repository defines the redistribution of percolation flux in the unsaturated zone as a function of time, and is the primary mechanism for radionuclide transport below the repository. Although the flow rate in the unsaturated zone influences the amount of fracture flow, the fracture characteristics are also significant in determining the rate of radionuclide movement in the unsaturated zone (BSC 2004a, Section 6.1).

- **Perched Water Develops—**The strongly altered northern part of the CHn unit is composed of zeolites and clays with low permeability and poorly developed, sparsely connected fractures. Because of low permeability, perched water may form at the contacts with CHn zeolitic (CHnz) tuffs below the northern half of the repository block, and a large portion of the percolating flux may be diverted laterally to the east towards the faults, which act as main pathways for fast flow and transport in the unsaturated zone. The effects of existing perched-water zones below the repository and potential changes in these perched-water zones caused by climate changes are included in the mountain-scale unsaturated zone flow model presented in UZ Flow Models and Submodels (SNL 2007a). Radionuclide transport process and abstraction models for the unsaturated zone incorporate the effects of perched water through the direct use of the flow model developed in UZ Flow Models and Submodels (SNL 2007a).

- **Fracture Flow in the Unsaturated Zone—**The rate of movement of water and radionuclides in the unsaturated zone depends on the flux of water through the fractured rock mass. This flux is distributed between faults, fractures, and the matrix of the host rock and other units in the unsaturated zone. The rate of movement of radionuclides is dependent on the degree of fracture flow, which, in turn, is dependent on the magnitude of the total flux. The bulk of the unsaturated zone flux is in fractures that have a higher transport velocity (and, thus, result in less delay of radionuclide movement). The effects

of fracture flow are included in the TSPA models presented in Sections 2.3.2.2, 2.3.8.2, and 2.4.1.

- **Matrix Imbibition in the Unsaturated Zone**—Water and (dissolved and colloidal) radionuclides may be imbibed into the matrix between the flowing fractures. Matrix imbibition affects the distribution of flow between fractures and the matrix in the fractured unsaturated zone. Matrix imbibition is dominant in the Calico Hills nonwelded vitric rock. The imbibition process results in a transition of water from fracture flow to percolation of water through the rock matrix, which substantially slows radionuclide transport (Section 2.3.8.4.5.1).

- **Advection and Dispersion in the Unsaturated Zone**—Flow in the fractured rock system below the repository is dominated by fracture flow in units for which the permeability of the rock matrix is too low to enable percolating water to pass through it. In this case, radionuclide transport is primarily advection dominated, and the influence of dispersion may be important. However, when compared to the spreading of radionuclides due to matrix diffusion effects, the impact on transport times of longitudinal dispersion is expected to be small (Section 2.3.8.2.2.1).

- **Matrix Diffusion in the Unsaturated Zone**—Matrix diffusion is the diffusion of dissolved radionuclides from the fractures into the matrix of the rock. Because advective transport is significantly slower in the matrix than in the fractures, matrix diffusion can be a very efficient retarding mechanism, especially for moderately to strongly sorbing radionuclides, due to the increase in rock surface accessible to sorption. Matrix diffusion is incorporated in the unsaturated zone radionuclide transport abstraction model described in Section 2.3.8.5.2. However, matrix diffusion of colloidally transported radionuclides has been conservatively excluded from this model.

- **Sorption in the Unsaturated Zone**—Radionuclides released from the repository have varying retardation characteristics. Several radionuclides (^{90}Sr, ^{137}Cs, ^{239}Pu, ^{240}Pu, ^{241}Am, and ^{243}Am) that are the dominant contributors to the total inventory are significantly retarded in the unsaturated zone when there has been significant fracture-matrix exchange by diffusion or advection. The sorption of these radionuclides that diffuse or advect into the matrix, in combination with radioactive decay, prevents the movement or significantly reduces the rate of movement of these radionuclides from the repository to the accessible environment. Sorption is included in the unsaturated zone radionuclide transport models presented in Section 2.3.8.5.2.

In addition, the following processes and characteristics are considered in order to provide a complete treatment of the unsaturated zone component of the Lower Natural Barrier, even though they have been determined to not contribute to barrier capability to the extent required to be considered as important to barrier capability:

- **Water Table Rise Affects Unsaturated Zone**—The change in water table elevation with climate change reduces the flow path lengths in the unsaturated zone between the repository and the water table. For all future, wetter climates, the water table is assumed

to rise relative to the present-day elevation, leading to a shorter unsaturated zone transport distance from the repository to the water table (SNL 2008a, Section 6.4.8).

- **Colloidal Transport in the Unsaturated Zone**—Several radionuclides may be transported colloidally in the unsaturated zone (Section 2.3.8.5.2). These include ^{238}Pu ^{239}Pu, ^{240}Pu, ^{242}Pu, ^{241}Am, and ^{243}Am. Both reversible and irreversible colloidal transport are considered. Retardation of a large fraction of the colloidally transported radionuclides is sufficient to reduce the rate of movement of these radionuclides from the repository to the compliance boundary. A small fraction, about 0.168%, of the colloids is transported unretarded in the unsaturated zone.

Data from laboratory testing, samples from the surface, boreholes, and underground, and testing in alcoves and niches in the Exploratory Studies Facility (ESF), the Enhanced Characterization of the Repository Block (ECRB) Cross-Drift, and the Busted Butte test facility were used to develop the unsaturated zone radionuclide transport models. Aspects of these tests and analyses related to unsaturated zone flow are described in Section 2.3.2.3. Data and testing related to transport include the characterization and distribution of fractures, field and laboratory measurements of transport properties (dispersivity; matrix porosity, rock density, sorption coefficient, and diffusion coefficient; fracture residual saturation, active fracture model γ, fracture porosity, spacing, and aperture; and colloid concentration, sorption coefficient, and retardation factor), characterization of the fluid and rock geochemical environment, radionuclide solubility, and geochemical and isotopic data relevant to the movement of water in the past. These data and test results, with associated uncertainties (Section 2.3.8.3), have been used to develop a conceptual understanding of unsaturated zone transport. The conceptual and numerical process models of unsaturated zone transport, and associated model uncertainties, are described in Section 2.3.8.4. An unsaturated zone radionuclide transport abstraction model (Section 2.3.8.5) was developed to incorporate transport in the TSPA (Section 2.4).

Figure 2.3.8-1 displays the information flow supporting development of the unsaturated zone radionuclide transport process model, the unsaturated zone radionuclide transport abstraction model, and the TSPA. Inputs to the unsaturated zone radionuclide transport process model include the model grid, calibrated properties and flow fields from the site-scale unsaturated zone flow model, and parameter distributions for transport properties (sorption, matrix diffusion, colloidal transport). The unsaturated zone radionuclide transport process model accounts for all major transport processes (Section 2.3.8.4.3), including advection, matrix diffusion, hydrodynamic dispersion, linear equilibrium sorption, radioactive decay and tracking of daughter products, colloid filtration, and colloid-assisted solute transport. To initiate transport calculations, radionuclides are released from the base of the invert of the Engineered Barrier System (EBS) as dissolved species or associated with colloids.

In the unsaturated zone, the welded units are structurally more competent, fracture more readily, and consequently have a higher fracture density and better developed fracture network (faults, joints, random fractures) than the nonwelded units. Open fractures create a secondary porosity that results in a higher net permeability in the welded units than in the nonwelded units, and the open fractures create avenues of preferential flow and fast transport pathways in comparison to matrix flow. To construct a numerical model consistent with this conceptual description, a dual-permeability numerical flow model was selected to realistically incorporate the processes likely to affect

transport. Fracture networks are modeled as a highly permeable continuum with low porosity, while the matrix is modeled as a much less permeable continuum with higher porosity. In this context, fracture porosity is the total volume of voids designated as fractures divided by the total volume, rather than an interstitial porosity within the individual fractures themselves. Fluid exchange between the fracture and matrix continua is simulated using an active fracture model, and the fracture–matrix interaction includes diffusive exchange of radionuclides. Advective transport of solutes in fractures is included, whereas retardation due to sorption in fractures is conservatively not included, except in fault zones, where the medium is treated as a fracture continuum with low effective porosity, and sorption on the rock surfaces. Colloid transport accounts for the fast transport of some radionuclides in fractures. Uncertainties in data have been incorporated into model parameters (Section 2.3.8.4.5) by using distributions commensurate with the available data or conservative bounding values. Uncertainty in models has been assessed through sensitivity analyses and alternative models.

The results of the unsaturated zone transport model have been analyzed and compared to viable alternative conceptual models, and by comparison to field test results and measurements at several scales, up to and including mountain scale. Results were also compared to geologic and geochemical evidence and to natural analogues. Breakthrough curves generated by the unsaturated zone radionuclide transport model (Section 2.3.8.5.4) indicate that the rate of radionuclide transport is highly dependent on the characteristics of individual radionuclides; the form in which the radionuclide is released (dissolved or colloidal); the hydrogeologic conditions in the flow paths, which in turn is a function of release location; and the uncertainties associated with transport parameters. The performance of the unsaturated zone component of the Lower Natural Barrier is very effective at reducing the movement of strongly sorbing radionuclides (e.g., ^{242}Pu) away from the repository in the unsaturated zone, whereas it is less effective for nonsorbing and weakly sorbing species (e.g., ^{99}Tc, ^{129}I, and ^{237}Np). According to model simulations, in regions where the mobile radionuclides travel through fast fracture flow paths (approximately the northern half of the repository block), mean transport times through the unsaturated zone component of the Lower Natural Barrier are predicted to be in the range of 1 to 100 years. For regions with an intervening layer of high-matrix-permeability rock (approximately the southern half of the repository block), mean transport times for unretarded species range from hundreds to a few thousand years. Species that undergo strong sorption are delayed for much longer times, in many cases either greater than 10,000 years, or long enough to allow radioactive decay to reduce significantly their mass flux at the water table (Section 2.3.8.5.5.1). Therefore, the effectiveness of the unsaturated zone component of the Lower Natural Barrier is a function of the specific radionuclide (through the sorption coefficient and half life) and the release location. The evaluation of barrier capability is presented in Section 2.1.

Role of the Unsaturated Zone Radionuclide Transport Abstraction Model in TSPA—The TSPA model integrates the essential components of the conceptual and process models to simulate repository behavior. Figure 2.3.8-2 provides a schematic representation of the role of the unsaturated zone radionuclide transport abstraction model within the TSPA model. As shown on Figures 2.3.8-1 and 2.3.8-2, an abstracted version of the unsaturated zone radionuclide transport process model was developed for use in the TSPA (Sections 2.3.8.5 and 2.4.1). The unsaturated zone radionuclide transport abstraction model calculates the movement of radionuclides in either dissolved or colloidal form released from the EBS transport model (Figure 2.3.8-2 and Section 2.3.7.12.3) into the unsaturated fractured geologic media and downward to the water table

using a particle-tracking technique. The abstraction model relies on the same technical basis as the unsaturated zone radionuclide transport process model, in that the abstraction model incorporates the unsaturated zone flow fields and the same basic transport processes used in the process model and is also based on a dual-permeability formulation, accounting for fracture flow and fracture–matrix interactions on radionuclide transport. The model also includes future changes in water table elevations, which shorten the path length for unsaturated zone transport and are implemented as an instantaneous jump to a higher water table elevation at the first change to a future, wetter climate condition (Section 2.3.8.5.3). In the TSPA, multiple realizations are conducted to capture the uncertainty in transport parameters, unsaturated zone flow fields, and the radionuclide source term.

The integration of the unsaturated zone radionuclide transport abstraction model with other TSPA components is described in Section 2.4.1. The unsaturated zone radionuclide transport abstraction model provides as output the radionuclide mass release rate to the saturated zone flow and transport model described in Section 2.3.9.

Summary of FEPs Evaluated in Models and Analyses of Radionuclide Transport in the Unsaturated Zone—The complete set of FEPs, both included and excluded, is provided in Section 2.2. The technical basis or approach used to implement each FEP included in this section is summarized in Table 2.3.8-1. FEPs related to the unsaturated zone below the repository that are excluded from TSPA are listed in Table 2.2-5. Table 2.3.8-1 lists FEPs that are directly implemented in the models in this section, as well as FEPs related to models that provide inputs, such as fracture and fault characteristics along flow paths, stratigraphy and rock properties, climate change and its impacts, and flow and transport processes. A number of these FEPs are also included in models for climate and infiltration, unsaturated zone flow, seepage into drifts, and in-drift radionuclide transport.

2.3.8.2 Conceptual Description of Unsaturated Zone Transport Processes

[NUREG-1804, Section 2.2.1.3.7.3: AC 1(1) to (5), AC 2(1), (3), AC 3(4), AC 4, AC 5(1)]

Unsaturated zone flow and radionuclide transport are interdependent processes. The conceptual models for these processes are based on ideas originally presented by Montazer and Wilson (1984, pp. 36 to 49). Understanding of and increased confidence in these processes have been developed through the evaluation of collected data and the results of modeling studies. For the aspects of unsaturated zone flow (Section 2.3.2) that are important to radionuclide transport, the conceptual model addresses infiltration and flow partitioning in fractured rock, as well as perched water and faults. For radionuclide transport, the conceptual model addresses advection, fracture–matrix interaction, sorption, and colloid-facilitated transport (BSC 2004a, Section 6.2). Figure 2.3.8-3 illustrates the processes affecting the transport of radionuclides from the repository horizon.

In the unsaturated zone, infiltration of precipitation and subsequent percolation to the water table involve dominantly vertical flow (Figure 2.3.2-3), so the area of principal interest is the immediate vicinity of Yucca Mountain, referred to as the site area (Figure 2.3.8-4). Analysis of hydrogeologic data has led to the definition of five major hydrogeologic units below the surficial alluvium in the site area: the Tiva Canyon welded (TCw), Paintbrush nonwelded (PTn), Topopah Spring welded (TSw), Calico Hills nonwelded (CHn), and Crater Flat undifferentiated (CFu) units (Table 2.3.2-2) (BSC 2004b, Table 6-5). Under the southern half of the repository, the CHn hydrogeologic unit is

predominantly vitric, as shown schematically in Figure 2.3.2-3. Under the northern portion of the repository, the CHn occurs as a zeolitic layer (Figure 2.3.2-3).

Figure 2.3.2-3 depicts the relationship between these hydrogeologic units and the processes that control water movement in the unsaturated zone: net infiltration, evaporation, percolation to the repository horizon, fracture–matrix interaction, accumulation of perched water, lateral flow, and deep percolation to the water table. These processes form the framework for radionuclide transport in the unsaturated zone (SNL 2007b, Section 6.1).

Radionuclide transport through the unsaturated zone is significantly affected by water flow. The conceptual model for water flow through the unsaturated zone, developed from extensive field measurements and modeling studies, is shown schematically in Figure 2.3.2-3. This model demonstrates the geologic effects on the flow of water through the unsaturated zone (SNL 2007b, Section 6.1.5.1).

The repository lies within the TSw hydrogeologic unit (SNL 2007b, Section 6.1.1). Flow in this unit is predominantly in the fractures, and radionuclide transport time in the unsaturated zone will be determined largely by the relative dominance of fracture versus matrix flow, the characteristics of the radionuclide, and the mineralogy of the unit (SNL 2007b, Section 6.1.1).

The other main hydrogeologic units below the repository host rock are the CHn and CFu units. The CFu consists of the Prow Pass, Bullfrog, and Tram tuffs (see Section 2.3.9 for additional discussion of these units where they are below the water table). Both the CHn and the CFu have vitric and zeolitic components that differ in their degree of hydrothermal alteration and subsequent hydrologic properties.

The major vitric layers in the CHn are in the southern half of the area below the repository. These vitric layers in the CHn have relatively high matrix porosity and permeability, and, therefore, a large fraction of the flow occurs through the matrix. The zeolitic rocks have low matrix permeability and some fracture permeability. Perched water may develop in zones of low fracture permeability. Consequently, a relatively small amount of water flows through the zeolitic units, with most of the water flowing laterally in perched-water bodies and then vertically down faults or connected fractures (SNL 2007b, Section 6.1.1).

In addition to advection through the fractures and matrix, other processes involved in unsaturated zone transport are matrix diffusion, dispersion, sorption, colloid-facilitated transport, and radioactive decay. Figure 2.3.8-3 illustrates these processes (SNL 2007b, Section 6.1.2).

Matrix diffusion involves the exchange of radionuclides between fractures and matrix by molecular diffusion. Diffusion is generally a slow transport process as compared with advective transport between the repository and the water table. For transport initiated in fractures, diffusion retards radionuclides by transferring them to the rock matrix, where advective transport is slow (Section 2.3.8.2.2.1).

Hydrodynamic dispersion combines mechanical dispersion, caused by localized velocity variations, with molecular diffusion, and is proportional to the concentration gradient. The dispersion of the radionuclides can occur both along and transverse to the average flow direction.

Hydrodynamic dispersion leads to the smoothing of sharp concentration fronts and reduces the breakthrough time at the water table.

Sorption describes a combination of chemical and physical interactions between the dissolved radionuclides and the solid phases (i.e., either the immobile rock matrix or colloids). In unsaturated zone radionuclide transport studies, sorption includes processes such as surface adsorption, mineral precipitation, ion exchange, and surface complexation. Sorption reduces the rate of advance of the concentration front of a dissolved or suspended radionuclide by removing a portion of the dissolved species from the mobile liquid phase and transferring it to the immobile solid phase (Section 2.3.8.2.2.2).

Colloids are minute particles (generally between 0.001 and 10 µm in diameter) that become suspended and are transportable in a moving liquid. In some conditions, the generation and mobilization of colloids are important to radionuclide transport characterization because they provide a transport mechanism to sorbing radionuclides that may otherwise not be present. Colloids provide sorbing radionuclides a mechanism of becoming partitioned into a mobile solid phase (the colloid) that moves with the water, as compared to sorbing onto an immobile solid phase (the rock) (Section 2.3.8.2.2.3).

Radionuclides considered in the postclosure models were selected on the basis of a screening process described in Section 2.3.7.4.1.2. Both solute and colloidal forms of radionuclides are considered. Because of radioactive decay, the transport of both the parent and daughter products were accounted for (Figure 2.3.8-3f). Daughter products with long half-lives are especially important for performance assessment. Because the transport behavior of daughter products may differ significantly from that of parent radionuclides, the migration of all the important members of the decay chain were considered (SNL 2007b, Section 6.1.2.8).

Transport processes are affected by temperature. The introduced waste will release heat to the environment, resulting in an increase in temperature until the waste heat is dissipated. Therefore, the effects of temperature on these processes are also evaluated to determine their significance (Section 2.3.8.2.3).

2.3.8.2.1 Relationship of Radionuclide Transport to Other Components of the Repository System

The unsaturated zone is a feature of the natural barrier above and below the repository (i.e., the Upper Natural Barrier and Lower Natural Barrier). Precipitation and near-surface processes determine the net infiltration of water into the unsaturated zone, as described in Section 2.3.1. Matrix and fracture flow above the repository and seepage into drifts determine the amount of water entering the drifts, as described in Sections 2.3.2 and 2.3.3. Any radionuclides potentially released from the EBS enter the unsaturated zone in the TSw hydrogeologic unit at the base of the inverts, as described in Section 2.3.7. Radionuclides ultimately decay in the unsaturated zone or leave the unsaturated zone by entering the saturated zone (Section 2.3.9). Details of the processes involved in radionuclide transport in the unsaturated zone are discussed in Section 2.3.8.2.2.

2.3.8.2.2 Conceptual Description of Unsaturated Zone Radionuclide Transport Processes

This section provides a conceptual description of processes important to unsaturated zone radionuclide transport, beginning with the impact of advection, matrix diffusion, and dispersion. Advection in fractures is expected to be the dominant transport mechanism in welded units, and diffusion of radioactive solutes and colloids into the rock matrix is an important retardation mechanism under certain conditions. Dispersion has limited impact on transport of radionuclides in the unsaturated zone, but is included in the transport model despite its low sensitivity. The role of sorption in removing a portion of the dissolved species from the liquid phase and transferring it to the solid phase is also described. Finally, the impacts of colloid transport are discussed. Transport of both parent and daughter radioactive species are accounted for in the models developed in Section 2.3.8.4.3.

2.3.8.2.2.1 Advection, Matrix Diffusion, and Dispersion

The movement of water through the unsaturated zone can transport radionuclides from the repository horizon to the water table. Where fracturing is more prevalent, such as in the welded units (e.g., the TSw), advection in the fractures (or fracture flow) (SNL 2007b, Section 6.1.2.1) is expected to be the dominant transport mechanism for the following reasons:

- High fracture permeability (compared to matrix permeability)
- Limited fracture pore volumes
- Limited fracture–matrix contact areas (i.e., only the wetted walls of flowing fractures)
- Short contact times between the radionuclide-carrying liquid phase and the rock matrix.

Thus, for the reasons outlined above, the first radionuclide arrivals at the water table would be the result of fracture-dominated advective transport (SNL 2007b, Section 6.1.2.1). While advective flow is predominantly downward in response to gravity, some lateral advection is also expected at the boundaries of hydrogeologic units that have sharp contrasts in hydraulic properties. Flow diversion may also occur in the perched-water bodies of the unsaturated zone. The occurrence of perched water suggests that certain layers of the lower TSw (e.g., the basal vitrophyre) and the upper zeolitic CHn serve as barriers to vertical flow. Laterally diverted flow ultimately finds a pathway to the water table through other more permeable zones, such as faults or connected fractures. Figure 2.3.8-5 illustrates one such flow path, where a fault-dominated flow path is associated with a perched-water zone (BSC 2004a, Section 6.1).

In other hydrogeologic units, such as the vitric CHn, matrix flow dominates because of similar permeability of fractures and the matrix (Figure 2.3.2-3). This circumstance, combined with high matrix pore volume, results in much slower transport velocities, increased contact areas between water and rock, and longer radionuclide–matrix contact times (SNL 2007b, Section 6.1.1).

Radionuclide transport is affected by interaction between fractures and the matrix. This interaction involves both advective and diffusive processes. The level of interaction is dependent on the wetted fracture–matrix interface area (SNL 2008a, Appendix C, Section C5). The wetted interface area is a function of the geometric fracture–matrix interface area and the distribution of fracture flow, which determines the fraction of the total geometric area available for interaction (SNL 2008a,

Appendix C, Section C5). The distribution of fracture flow is affected by the heterogeneity of the fracture network and by flow instability. These factors result in preferential flow through a subset of the total fracture population and the development of fingering flow, resulting in a reduction in the wetted fracture–matrix interface area (SNL 2007a, Section 6.1.2). There is some evidence that the available wetted fracture–matrix interface area per unit bulk volume increases with the length scale, leading to enhanced matrix diffusion at larger length scales (BSC 2006a, Section 6.4); however, the mechanisms for this process are not well understood. Therefore, scale-dependent matrix diffusion has not been included in the unsaturated zone transport model. Because the formulation chosen results in less diffusion in the simulations, the approach yields shorter travel times for situations in which diffusion from fractures to slow-moving fluid in the rock matrix occurs, and thus is conservative.

Where fractures and the matrix interact, the diffusion of radioactive solutes and colloids into the rock matrix is an important retardation mechanism (SNL 2007b, Sections 6.1.2.4 and 6.1.5.2). Diffusive transfer of radionuclides between the fractures and the rock matrix (Figure 2.3.8-3c) is an important and demonstrable mechanism for nonsorbing solutes, such as ^{99}Tc (BSC 2004c, Section 6.12). The process of matrix diffusion involves the exchange of radionuclides between the fractures and matrix by molecular diffusion. Matrix diffusion removes some radionuclides from the flowing fractures at the leading edge of a radionuclide contaminant plume, thus slowing radionuclide transport through the fractures. Transport through the rock matrix is relatively slow and sorption or filtration is much more likely to occur because of greater contact areas and longer contact times between water and rock. Diffusive flux of a given species within the matrix is a function of its molecular properties (e.g., electric charge, size, and diffusion coefficient), its concentration gradient, and other properties such as temperature, the matrix pore structure, and water saturation of the pore space (SNL 2007b, Section 6.1.2.4).

In general, matrix diffusion is less significant for colloids than for solutes because the large size of the colloids reduces the colloid diffusion coefficient, reduces the number of colloids entering the matrix because of pore size exclusion, and may enhance advection by guiding the colloids to the center of the fracture pores where velocities are higher than the average water velocity (Ibaraki and Sudicky 1995, p. 2948).

Transport of radionuclides in the unsaturated zone is impacted by dispersion, but the extent of the effect is expected to be minimal compared to the spreading caused by matrix diffusion. When dispersion is used to model solute spreading in porous media, it is introduced to capture variability in the flow velocity existing at smaller scales than are modeled in the numerical grid. Large-scale spreading caused by features explicitly present in the flow simulation is captured directly and is not considered to be dispersion in the sense being used here. Because the purpose of this model is to predict transport time distributions of radionuclides to the water table, longitudinal dispersion is potentially important to capture a dispersed solute front arriving at the water table. By contrast, transverse dispersion will tend to allow mass to migrate short distances in the horizontal direction. Simple approximate methods show that the amount of lateral spreading is small compared to the width of the repository or even the width of a gridblock in the unsaturated zone model. For example, as a rule of thumb, assume that a transverse dispersivity of one tenth the longitudinal

dispersivity of 10 m, a value of 1 m, is representative. The characteristic distance of spreading of a dispersing plume resulting from a point source is given by the following:

$$\sqrt{2D_t t} = \sqrt{2\alpha_t v(L/v)} = \sqrt{2\alpha_t L} \qquad \text{(Eq. 2.3.8-1)}$$

where D_t is the transverse dispersion coefficient; α_t is the transverse dispersivity; and t is the characteristic time equal to the velocity, v, divided by the length, L (Freeze and Cherry 1979, p. 395). For a radionuclide point source traveling vertically to the water table ($L \approx 350$ m, based on a repository elevation of approximately 1080 to 1090 m above sea level to the present-day water table level of approximately 730 to 740 m, values which are representative of the water table under the repository footprint), the transverse spreading of the plume at the water table is approximately 26 m. The velocity field encountered by a plume spreading of this small horizontal distance is not expected to be significantly different than if no transverse dispersion is assumed. On this basis, lateral transverse dispersion is insignificant and is not incorporated in the TSPA models of unsaturated zone transport (SNL 2008a, Section 5).

Furthermore, longitudinal dispersion is not expected to play a significant role in radionuclide transport in the unsaturated zone when compared to other processes, particularly matrix diffusion (SNL 2008a, Section 4.1.6 of Addendum 1). Dispersion effects within the fracture or matrix continuum alone are small compared to the impact of matrix diffusion coupled with the disparity in travel times between advective transport in the fractures and matrix, which are explicitly modeled. Because the impact of longitudinal dispersion on travel times is minimal, the process is included, but a fixed value of the dispersivity parameter is used (Section 2.3.8.5.2.2), informed by field studies conducted at Yucca Mountain and elsewhere.

2.3.8.2.2.2 Sorption

Sorption describes a combination of chemical and physical interactions between dissolved radionuclides and the solid phases. Sorption removes a portion of the dissolved species from the mobile liquid phase and transfers it to the solid phase. The solid phase includes the immobile rock matrix, immobile colloids, and mobile colloids (Figure 2.3.8-3e). Sorption onto the matrix or immobile colloids results in retardation of radionuclide transport in the unsaturated zone (Section 2.3.8.2). However, sorption onto mobile colloids can enhance radionuclide transport (SNL 2007b, Section 6.1.3.3).

The primary controls on sorption behavior of radionuclides in the unsaturated zone flow system include the characteristics of mineral surfaces in the rock units through which water flows from the repository to the saturated zone (SNL 2007b, Appendix A, Section A1). These controls also include the chemistry of pore waters and perched waters in the unsaturated zone along flow paths, the sorption behavior of each radionuclide, and radionuclide concentrations in the groundwater (SNL 2007b, Appendix A, Section A1).

The sorption behavior of radionuclides is described by the sorption coefficient K_d, which quantifies the partitioning of radionuclides between the solid and aqueous phases under an equilibrium approach where the sorbed concentration is proportional to the dissolved concentration. The

sorption of radionuclides is not sensitive to the isotope number; only the atomic number influences sorption behavior. Radionuclides having the same atomic number are all considered the same radioelement regardless of isotope number. Because different isotopes of a given radioelement behave the same in sorption reactions, sorption coefficients were developed for each element for use in TSPA. The K_d of a radioelement in porous media is a lumped parameter that accounts for the effects of mineralogy, groundwater aqueous chemistry (including redox conditions), and heterogeneity at scales smaller than are considered in numerical models. Sorption reactions for the radioelements of interest include ion-exchange reactions and surface complexation reactions. Ion-exchange reactions involve the exchange of a radioelement with ionic constituents on exchange sites in minerals such as zeolites and clays. These exchange reactions are important for radioelements that occur as simple ions, such as cesium, strontium, and radium. Surface complexation reactions involve the adsorption of radioelements onto oxide surfaces. The radioelements that sorb dominantly by surface complexation reactions include americium, neptunium, uranium, plutonium, protactinium, and thorium (SNL 2007b, Section 6.1.3.1).

Sorption studies indicate that the equilibrium approach is applicable to most radionuclides of interest to performance assessment when sorption is limited to the matrix and matrix transport velocities are low (Rundberg 1987, Section VI). The kinetics of sorption reactions for some radionuclides, particularly for isotopes of plutonium and radium, have been found to be slow enough that the magnitude of equilibrium K_ds may not be appropriate. This is because the radionuclides may not have time to achieve equilibrium with specific minerals during transport (SNL 2007b, Appendix A, Sections A8.4.1 and A8.6.1). In these cases, the upper bounds on the K_d distributions have been reduced relative to the available data to account for the effects of sorption kinetics (SNL 2007b Appendix A, Sections A8.4 and A8.6). Additional discussions concerning sorption are provided in Section 2.3.9.

2.3.8.2.2.3 Colloid Transport

Colloids are potentially important to unsaturated zone transport because they may reduce the interaction with the rock matrix and allow for greater mass flux than could transport as aqueous species alone. Because of their size, the larger colloids can only move through the centers of pores and fractures where velocities are larger than the average water velocity. This leads to greater transport velocities for larger colloids. In addition, the larger colloids cannot penetrate into the matrix from the fractures because of size exclusion. Thus, the colloid mass in the fractures is not reduced through colloidal diffusion, and, therefore, practically all of it moves exclusively through the fractures (Figure 2.3.8-3c). Colloid diffusion into the rock matrix is limited, but colloid deposition onto rock surfaces as water flows through pores in the rock matrix is an important process for radionuclide retardation (SNL 2007b, Section 6.1.3.3).

There are two types of radionuclide-bearing colloids: (1) those formed from hydrolysis of dissolved radionuclides (true colloids) and (2) colloidal particles of other materials with attached radionuclides (pseudocolloids) (SNL 2007c, Section 6.3.1). True colloids of radioelements, such as plutonium, are not expected to form in the repository because of the abundance of other sorbing materials. Instead, plutonium is seen either as inclusions in waste form corrosion products or is sorbed onto the two main mineral pseudocolloids expected in the repository: clay and iron minerals (Section 2.3.7.11).

Pseudocolloids in the repository can come from several sources, including natural groundwater, the disturbed rock and invert, and corroding man-made materials. From these sources, clays and iron mineral colloids are expected to be most important. For the glass waste form, waste is seen as radionuclide inclusions in clay corrosion product colloids. Thus, there are expected to be three main sources of pseudocolloids in the repository: glass waste form and clay and iron mineral pseudocolloids (SNL 2007c, Section 6.3.1). Section 2.3.7.11 provides further discussion of colloidal radionuclides, and Section 2.3.8.5.2.5 describes how colloid-facilitated transport is treated in the unsaturated zone radionuclide transport process model.

Effects of radioactive decay and the generation of decay products on colloid transport are complex and not well understood. For ^{243}Am irreversibly attached to colloids, it is assumed that its decay product ^{239}Pu remains attached to colloids in the unsaturated zone transport calculation (SNL 2008a, Section 6.5.14, Table 6-25 in Addendum 1). For other radionuclides irreversibly attached to colloids, TSPA adds their decay products to the aqueous phase in the transport calculation (SNL 2008a, Section 6.5.14, Table 6-25, in Addendum 1). These decay products are all uranium and neptunium isotopes, which are not expected to be present in colloidal form in the repository environment (SNL 2007c, Section 6.6.8).

The extent to which radionuclides transport through the unsaturated zone on colloids depends on the nature of the interactions of the colloids with the surrounding rock. Colloids deposit onto rock surfaces (Figure 2.3.8-3b) in two steps: (1) transport of colloids to rock surfaces by molecular diffusion, interception, or gravitational sedimentation (i.e., colloid–rock collision) and (2) attachment of colloids to rock surfaces (SNL 2007b, Section 6.1.3.3.3). The fraction of collisions between colloids and rock surfaces resulting in attachment is called the attachment efficiency and is strongly influenced by interparticle forces between colloids and rock surfaces, such as van der Waals and electric double-layer interactions, steric stabilization, and hydrodynamic forces (Kretzschmar, Robarge et al. 1995, p. 435). It has been demonstrated (Kretzschmar, Barmettler et al. 1997, p. 1129) that colloid deposition generally follows a first-order kinetic rate law, and the corresponding collision efficiencies were experimentally determined. Attachment reduces radionuclide transport because, once attached, colloid detachment (known as declogging) is generally slow in the absence of significant changes in ionic strength, and attachment can appear to be irreversible (Kretzschmar, Barmettler et al. 1997).

Colloid straining, or filtration (Figure 2.3.8-3c), can also affect the distribution and transport of colloids. Straining mechanisms can be classified according to the relative size of the colloid as conventional straining, where the colloid is larger than the pore throat, and film straining, where the colloid is larger than the thickness of the adsorbed water film coating the grains of the rock (Wan and Tokunaga 1997, p. 2413). It has also been found that filtration has a strong dependence on the colloid size under unsaturated conditions (McGraw and Kaplan 1997, p. 5.2). Colloid removal from fracture flow increased exponentially with colloid size, and the decrease in colloid mobility at low volumetric water contents was attributed to resistance due to friction (i.e., as the colloids were dragged along the sand-sized particles). When the water saturation of the pore space is lower than a critical saturation value, colloids can only move in the thin film of water that lines the grain boundaries. Colloid retardation increased as the ratio of the water-film thickness to the colloid diameter decreased (Wan and Tokunaga 1997, pp. 2413 and 2419).

2.3.8.2.3 Temperature Effects on Transport Properties

The transport parameters and processes that can be affected by a temperature increase in the unsaturated zone include the diffusion coefficient D_0 of the dissolved or colloidal species (Robin et al. 1987, pp. 1105 to 1106), the sorption parameters of the dissolved species, and the filtration parameters of the suspended colloids (SNL 2007b, Section 6.1.2.9).

Ambient temperature at the repository horizon at Yucca Mountain is about 24°C, but substantial temperature increases are expected after waste emplacement in the repository (SNL 2007b, Section 6.1.2.9). Increased temperature will affect hydrologic conditions and potentially alter minerals near waste emplacement drifts, affecting radionuclide transport. Temperature enhances diffusion by increasing the kinetic energy of the ions. This effect is quantified by an increase in the D_0 of radionuclides. Based on a relationship given by Robin et al. (1987, pp. 1105 to 1106), a difference in temperature from 20°C (at the top of the unsaturated zone domain) to 30°C (at the water table) due to the natural geothermal gradient leads to an increase of D_0 of about 30%. Somewhat higher differences might be expected due to repository heat effects, but if most of the thermal perturbation has dissipated at the time of radionuclide release, then the impact of repository heat and increased temperature on the diffusion coefficient should be small. Furthermore, when compared to the level of uncertainty in the diffusion coefficient under ambient conditions, an impact of 30% can be considered to be small. Therefore, the TSPA model conservatively addresses the impact of repository heat on diffusion by assuming that diffusion coefficients under ambient conditions apply throughout the simulation period (SNL 2007b, Section 6.1.2.9).

When modeling solute radionuclide transport in the unsaturated zone, the temperature dependence on sorption for all radioelements considered except strontium, uranium(VI), and neptunium is negligible (SNL 2007b, Appendix I, Section I1.5). The critical parameter defining the temperature dependence of K_d is the enthalpy of sorption ΔH_r, which is relatively small in magnitude for all radioelements considered except strontium, uranium(VI), and neptunium (SNL 2007b, Appendix I, Section I1.4.4). The mean value of ΔH_r is positive for all species considered, leading to increased sorption with temperature. Sorption measurements were conducted at low (ambient) temperatures. Sensitivity studies for the effects of K_d on radionuclide transport have shown that changes in K_d in the Calico Hills Formation have low impact on transport rates (SNL 2007b, Sections 6.9.1.5 and 6.10.1.4). Therefore, the simplifying approximation that sorption is independent of temperature is conservative (SNL 2007b, Appendix I, Section I1.5).

Changes in the sorptive properties of the host rocks and zeolites may result from changes in the thermal, hydrologic, and geochemical conditions prevailing during the thermal perturbation caused by waste emplacement. In the Calico Hills Formation, the dominant zeolitic zone underlying the repository horizon, alteration of zeolites due to repository heat is unlikely as long as temperatures remain below 90°C to 100°C (Section 2.3.2.5.1.6.2). The temperature is expected to rise to about 70°C, and about 15% (volume) of the clinoptilolite is predicted to alter to more stable secondary feldspars and stellerite (BSC 2005a, Sections 6.4.3.3.3 and 6.4.3.3.4), even if partial dehydration of the clinoptilolite occurs (Carey and Bish 1996; Carey and Bish 1997). However, the expected temperature excursion would be insufficient to alter coexisting opal-CT to quartz. Opal-CT maintains a high silica activity in the system and curtails alteration of the zeolites to more stable but less sorptive phases (Duffy 1993a; Duffy 1993b).

Changes in sorption as a result of changes in temperature for the same mineral-species reactions are predicted to be small and generally to result in increases in sorption for cationic species (SNL 2007b, Section 6.1.2.9). Therefore, the effects of temperature on sorption are conservatively not included in the TSPA model (SNL 2007b, Section 6.1.2.9).

The impact of temperature effects on unsaturated zone transport were additionally examined via model results assessing the duration of perturbations in pore water chemistry due to thermal effects caused by repository decay heat. A model of the process of seepage in the presence of coupled thermal-hydrologic-chemical effects is presented in *Drift-Scale THC Seepage Model* (SNL 2007d). This model indicates that upon rewetting, pore-water chemistries recover compositions typical of unperturbed conditions in 10,000 to 30,000 years. Thus, the relatively minor, and reversible impact on water chemistry, as a result of decay heat on geochemistry in the unsaturated zone, was reasonably excluded from unsaturated zone transport (Table 2.2-5, FEP 2.2.10.06.0A, Thermal-chemical alteration in the UZ (Solubility, Speciation, Phase Changes, Precipitation/Dissolution)).

In summary, the impact of temperature, both in terms of spatial variability and changes with time due to waste emplacement, have been determined to be small, and thus are not included explicitly in the unsaturated zone transport model calculations. *Features, Events, and Processes for the Total System Performance Assessment: Analyses* (SNL 2008b) presents additional information regarding the exclusion of these processes in the TSPA model, including analyses demonstrating that significant changes in the hydrologic properties of the fractures and matrix as a result of rock alteration are not expected (FEP 2.2.08.03.0B, Geochemical interactions and evolution in the UZ, and FEP 2.2.10.07.0A, Thermal-chemical alteration of the Calico Hills unit).

2.3.8.3 Data and Data Uncertainty

[NUREG-1804, Section 2.2.1.3.7.3: AC 2, AC 3(4)]

In support of studies of the unsaturated zone and subsequent TSPA calculations, many boreholes have been drilled in the immediate vicinity of Yucca Mountain (as shown in Figure 2.3.8-6), including some drilled within the repository area. Boreholes drilled, sampled, tested, and monitored at the site have provided information on the vertical and lateral distribution of hydrogeologic units, hydrologic properties of the rocks, thermal and other geophysical conditions and properties, chemistry of the contained fluids, pneumatic pressure, and water content and potential. Field and in situ data important for developing unsaturated zone flow models are described in Section 2.3.2.3. Additional data have been obtained from test alcoves and niches in tunnels for the ESF and the ECRB Cross-Drift, and at the Busted Butte unsaturated zone test facility. These test locations (with the exception of Busted Butte) are shown in Figure 2.3.8-7. The Busted Butte test facility is located in Area 25 of the Nevada Test Site, approximately 8 km southeast of the repository area.

The major areas of data limitations are associated with testing below the repository units and the inability to directly measure transport properties in fractured, unsaturated tuff under natural conditions. The distance between the repository and the water table is on the order of 350 m. Characteristic transport times predicted by the unsaturated zone radionuclide transport model used in TSPA are on the order of a minimum of 1 year under fracture flow conditions without diffusion or sorption and much higher in regions in which transport through matrix rock occurs. Sorbing tracers would require even longer testing times. The impracticality of conducting direct transport

tests over the entire unsaturated zone constitutes a primary source of uncertainty in the modeling results (Section 2.3.8.3) that are used to develop transport abstractions for TSPA.

2.3.8.3.1 Laboratory Sorption Measurements

This section describes the measurement of sorption coefficients for use in the unsaturated zone transport calculations (SNL 2007b, Section 6.1.3.1). These measurements include laboratory batch sorption experiments using crushed rock samples from Yucca Mountain and water having the characteristics of Yucca Mountain groundwater. Sorption coefficients were measured for all radionuclides potentially important to the TSPA based on a radionuclide inventory screening analysis (Table 2.3.8-2) (SNL 2007e). In addition, confirmatory column tests were performed to compare sorption behavior under dynamic (i.e., flowing) conditions with static conditions used for batch sorption tests. The column tests were conducted on selected radionuclides that were considered important contributors to mean annual dose (including technetium, neptunium, and uranium), based on previous TSPA calculations (SNL 2008c, Table 4-1). Sorption experiments were carried out as a function of time, element concentration, atmospheric composition, water composition, particle size, rock type, and temperature. In some cases, the solids remaining from sorption experiments were contacted with unspiked (no added radionuclides) groundwater in desorption experiments. Together, the sorption and desorption experiments provide information on the equilibration rates of the forward and backward sorption reactions. Because sorption experiments provide a lower bound for K_d relative to desorption experiments, K_d values are primarily set through sorption experiments. Differences in the chemistry of groundwater in the unsaturated zone and groundwater in the saturated zone lead to different sorption coefficient distributions for most radionuclides in the unsaturated zone and in the saturated zone (SNL 2007b, Appendix B).

Data were collected on the three dominant rock types in the unsaturated zone along potential flow paths from the repository to the saturated zone: devitrified tuff, zeolitic tuff, and vitric tuff (BSC 2004b, Section 6). The correlation between these sorption rock types to the unsaturated zone model layers is presented in *Particle Tracking Model and Abstraction of Transport Processes* (SNL 2008a, Table 6-6). Sorption coefficient distributions for devitrified tuff are based on data obtained from samples that are composed primarily of silica phases and feldspar with trace amounts of mica, hematite, calcite, tridymite, kaolinite, and hornblende, as well as minor amounts (less than 25%) of smectite or zeolite (or both). Sorption coefficient distributions for zeolitic tuff are taken exclusively from samples that contain more than 50% zeolite, with the balance made up of clay, silica phases, alkali feldspar, glass, or a combination of these. Zeolitic tuffs have significantly higher surface areas than other tuffs (Triay et al. 1996, p. 62). For vitric tuffs, sorption coefficient distributions are based on samples that contain more than 50% glass, with the remainder composed predominantly of feldspar, silica phases, zeolites, and clay (Triay et al. 1996; SNL 2007b, Appendix A, Section A2).

Sorption coefficients are often a function of the concentrations of the radionuclides present in solution. In most cases, experiments were carried out over a range of concentrations. Experiments carried out at concentrations over the solubility limit were not included in the derivation of sorption coefficient distributions. Because experiments were carried out at concentrations up to the solubility limit for most elements, the experimental results and the probability distributions derived from them include a dependence on concentration. The only elements for which the experimental concentrations did not approach the solubility limit were cesium and selenium, which have very

high solubilities in Yucca Mountain waters. Adjustments to the expected cesium and selenium sorption ranges were made based on the expected maximum concentrations so that sorption would not be overestimated (SNL 2007b, Appendix A, Section A8.2). The K_d distributions for cesium, a strongly sorbing radioelement, were significantly reduced from the experimental values to account for potential high concentrations of cesium. Selenium is weakly sorbing. An analysis of potential selenium concentrations in the unsaturated zone indicated that concentrations above the levels used for the sorption experiments could only occur in the TSw (i.e., close to waste emplacement drifts). Therefore, for selenium the concentration effect was accounted for by using a K_d of zero in the TSw and the experimentally derived values elsewhere.

There are two distinct water types in the unsaturated zone: perched water and pore water. Perched waters generally contain lower concentrations of major ions than do pore waters, due to less time for rock-water interaction. To evaluate the impact of water chemistry on the sorption behavior of the radionuclides of interest, laboratory experiments were conducted using two natural water compositions that bound the range of compositions expected in the unsaturated zone. These fluids are intended to be representative of the natural fluids encountered in the unsaturated zone, including containing representative quantities of complexing agents such as humic and fulvic acids. In this manner, FEP 2.2.08.06.0B, Complexation in the UZ, is included in the TSPA model through the use of natural fluids in the measurements that led to the sorption coefficient uncertainty distributions. With respect to microbial activity and its potential to affect sorption in the unsaturated zone, this potential impact has been determined to be of low consequence (see Table 2.2-5, excluded FEP 2.2.09.01.0B, Microbial activity in the UZ). This conclusion is based on several lines of reasoning: (1) the expected low concentrations of the complexing agents; (2) the fact that the inorganic groundwater colloid load is expected to overshadow the microbial load; and (3) the fact that the K_d distributions were obtained from experiments that used representative fluids from the site, such that any impact of microbial activity on the water chemistry should already be reflected in the measurements. Samples representative of these two water types were collected from wells at the Yucca Mountain site: UE-25 J-13 and UE-25 p#1 (BSC 2004d, Figure 3-7). Well UE-25 J-13 is on the east side of Fortymile Wash, near where H Road enters Fortymile Wash. Well UE-25 p#1 is about 2 km north and 2.5 km west of UE-25 J-13, or about 1 km east of the South Portal pad. The intent of this approach was to examine the potential dependence of water chemistry on sorption, rather than to represent the exact geochemical conditions in the fracture, perched, or pore water. Surrogates for these water compositions were synthesized when the supply of natural waters ran out. The sorption coefficient data obtained with the natural and surrogate waters were used to derive sorption coefficient distributions for use in unsaturated zone radionuclide transport calculations (SNL 2007b, Appendix A, Section A.4). These sorption coefficients will not be impacted significantly by potential geochemical changes caused by contact of fluid with engineered materials such as cement because of the very limited use of such materials in areas near waste emplacement drifts Table 2.2-5; (SNL 2008b, excluded FEP 2.2.08.03.0B, Geochemical interactions and evolution in the UZ). The relatively small amount of cementitious material, and its horizontal distance from the waste packages, minimizes the degree to which an alkaline plume from cement dissolution will intersect with a plume of released radionuclides.

Sorption data were obtained as a function of time, element concentration, atmospheric composition, water composition, particle size, rock type, and temperature. Here we present the data and interpretation of one such data set, the sorption of neptunium on devitrified tuff. For a complete analysis of data associated with sorption of neptunium, see *Radionuclide Transport Models Under*

Ambient Conditions (SNL 2007b, Appendix A). For this example, the data and interpretation are described here, and the process for using this information to establish the uncertainty distribution for neptunium K_d on devitrified tuff is outlined in Section 2.3.8.5.2.3. An example of the laboratory results is given in Figure 2.3.8-8, which shows that the different specific data sets were taken under a limited range of pH conditions. To better evaluate the functional dependence of the sorption coefficient on pH, surface complexation models were developed for key radionuclides. Key radionuclides are identified as those important for dose in TSPA (SNL 2007b, Appendix A, Section A3; SNL 2007e, Table 7-1). The equilibrium surface complexation model used in this analysis is based on the code PHREEQC V2.3. Figure 2.3.8-8 also includes an example of experimental and modeling results. The modeling results show that experiments conducted before 1990, designated in the figure as the "old" sorption and desorption data, bracket the theoretical model for sorption in UE-25 J-13 water. The old data were from longer-duration tests that are expected to be closer to equilibrium than the "new" (post-1990) data, thus showing sorption kinetics effects. Thus, the scatter in the new data is likely the result of kinetics effects, along with difficulties in accurately measuring sorption coefficients at low values of K_d. The placement of the J-13 surface complexation model curve, lying in between the old sorption and desorption points, suggests that the curve reflects the equilibrium values of neptunium K_d on devitrified tuff better than the experimental data (SNL 2007b, Appendix A, Section A8.3.1). Based on this analysis and geochemical modeling, this K_d appears to be only a weak function of pH, except at pH values less than 7.

The resulting sorption coefficient probability distributions for radionuclides in the unsaturated zone are provided in Table 2.3.8-2 (SNL 2007b, Appendix A). The example of neptunium sorption onto devitrified tuff is used to illustrate the process for establishing uncertainty distributions for K_d in Section 2.3.8.5.2.3.

Laboratory Sorption Data Uncertainty—The potential major sources of uncertainty for sorption data are the use of crushed tuff, kinetics, concentration of radionuclides, and competitive effects among different radionuclides. The crushing of the tuff does not impact sorption because of the high surface area of the intact rock (SNL 2007b, Section 6.1.3.1). Although sorption kinetics are a source of uncertainty in batch and column sorption experiments, the sorption coefficients obtained in these experiments have a conservative bias. That is, the sorption coefficients obtained in these experiments are generally smaller than sorption coefficients that would apply during transport in the natural environment because kinetic effects limit the effectiveness of sorption processes in short-duration laboratory tests. Batch sorption experiments have been performed up to the solubility limit for most of the key radionuclides. Thus, the impact of the concentration of radionuclides has been incorporated into the distribution for the sorption coefficients. For cesium, experiments were conducted to high concentrations but not to its solubility limit, which is extremely high. For selenium, experiments were conducted at both low and high concentrations, but sorption evaluations were limited to low concentration experiments. Selenium sorption is not evaluated within the repository host rock where higher concentrations are expected because concentrations are conservatively taken to be high enough in this rock unit for sorption coefficient to be zero (SNL 2007b, Section A2.5[a]). Experiments investigating a mixture of all the potential radionuclides could not be performed due to experimental limitations associated with safety concerns that would result from high radiation doses. However, chromatographic effects (separation of radionuclides resulting from velocity differences due to differences in K_d) (SNL

2007b, Section 6.2.3.4) will limit the influence of competitive effects at the front of any releases from the repository.

2.3.8.3.2 Laboratory Matrix Diffusion Measurements

Laboratory measurements of matrix diffusion coefficients support the matrix diffusion model developed for use in the unsaturated zone radionuclide transport calculations (SNL 2007b, Section 6.2). This section describes the measurements and the synthesis of these data, whereas the validity of using laboratory-scale diffusion measurements in field-scale models is examined in the context of the interpretation of field tests in Section 2.3.8.4.4. The matrix diffusion coefficient is given by the product of the tortuosity coefficient times the free-water diffusion coefficient. The free-water diffusion coefficient describes diffusion in water without any other materials present. The tortuosity coefficient quantifies the reduction in diffusion rates resulting from the tortuous diffusion pathways through the rock (SNL 2007b, Section 6.1.2.4). The tortuosity is correlated with the porosity and permeability of the rock matrix (SNL 2008a, Section 6.5.5.1 in Addendum 1). Diffusion cell (an apparatus consisting of two fluid reservoirs separated by a rock wafer) tests were conducted to determine matrix diffusion coefficients of tritium, bromide, and iodide (Reimus, Callahan et al. 2007). Tritium, bromide, and iodide are standard nonreactive tracers used for transport tests. The studies used volcanic tuffs from the Yucca Mountain region and consisted of devitrified, welded tuffs and zeolitic, nonwelded tuffs. In addition, diffusion cell tests were conducted using tritium to investigate diffusion through pure matrix material and matrix with a mineral-coated fracture on one of its surfaces. Confirmatory diffusion cell tests were conducted using ^{14}C and ^{99}Tc, which are radionuclides present in the radionuclide inventory for Yucca Mountain. Additional confirmatory tests were conducted for tritium, ^{14}C, and ^{99}Tc in dynamic transport tests through fractures to investigate the effects of dynamic (i.e., flowing) conditions on diffusion results (Reimus, Ware et al. 2002, Section 3.2).

The permeabilities and porosities of the rocks tested span a similar range of values as found for the rock matrix of the unsaturated zone between the repository and the water table, excluding the Calico Hills nonwelded vitric unit. This vitric unit has much larger matrix permeabilities than rock tested for matrix diffusion; however, the unsaturated zone radionuclide transport process model has only low sensitivity to matrix diffusion in the vitric unit because fracture-matrix exchange is dominated by advective transport due to the higher matrix permeability (SNL 2007a).

The radionuclide concentration gradients were imposed across the thickness of the rock wafers to initiate diffusive transport in the diffusion cell tests. The solution concentration at the outlet was collected and measured. This time-varying concentration was matched using a diffusion transport model through adjustment of the matrix diffusion coefficient (Reimus, Callahan et al. 2007).

The dynamic transport tests were conducted at several different flow rates in each fractured rock sample as a way of varying the residence time of the radionuclides in the fractures. Five of the seven fractured rock samples were taken from the same intervals as rocks that were used in diffusion cell tests. This one-to-one correspondence allowed a direct comparison of the diffusive mass transfer rates observed in the fractures and in the diffusion cells (Reimus, Ware et al. 2002, Section 3).

Data for determining the matrix diffusion coefficient were obtained as a function of porosity and permeability. The matrix diffusion coefficient, porosity, and permeability are all related to the

water-filled pore geometry. Stepwise statistical F-tests, used to evaluate the importance of the parameter, verified that both matrix porosity and log permeability make significant contributions to the regression equation at the 95% confidence level. The analysis also showed that the permeability was a better predictor variable than porosity for the matrix diffusion coefficient (Reimus, Callahan et al. 2007). Regarding the effects of mineral coatings on fractures, there appeared to be little or no diffusion resistance offered by mineralized fracture surfaces in diffusion cell tests in which rock wafers with and without fracture surfaces were compared (Reimus, Callahan et al. 2007).

In general, the relative attenuation of ^{14}C and tritium in the fracture experiments was consistent with the diffusion rates measured in the diffusion cell experiments (i.e., the radionuclide that diffused faster in the diffusion cells tended to be more attenuated by matrix diffusion in the fracture experiments) (Reimus, Ware et al. 2002, Section 4.0). The dynamic tests showed greater attenuation of ^{99}Tc than did the diffusion cell tests, which may have resulted from slight sorption of this isotope (Reimus, Ware et al. 2002, Section 3.2).

Laboratory Matrix Diffusion Data Uncertainty—To obtain insights into experimental errors, reproducibility, and uncertainty of diffusive properties resulting from heterogeneities in the rocks, 10 of the laboratory matrix diffusion experiments were repeated using the same rock wafers, and several experiments were replicated using different rock wafers from the same borehole and interval. The test results show that the uncertainty in the matrix diffusion coefficient is within a factor of two (Reimus, Callahan et al. 2007, Section 4). The uncertainty in the predicted values for tortuosity using the correlation between tortuosity and porosity and permeability were also evaluated. The residuals between the experimentally observed tortuosity (the observed matrix diffusion coefficient divided by the free-water diffusion coefficient) and the predicted values for tortuosity from the correlation were found to be log-normally distributed (SNL 2008a, Appendix A, Section A.4 in Addendum 1).

2.3.8.3.3 Field Test Observations

This section presents a summary of field experiments designed to investigate radionuclide transport in the unsaturated zone and build confidence in the unsaturated zone radionuclide transport process model. These tests include the Busted Butte test series, the Alcove 8–Niche 3 test, and the Alcove 1 test. The tests involve lengths ranging from a few meters to a maximum of 30 m, over time periods up to two years. The test results establish the basic conceptual framework of transport and form the basis for extension to large-scale transport. The test data are used to build confidence in the unsaturated zone radionuclide transport process model through comparisons with and corroboration of model results presented in Section 2.3.8.4.4. In the descriptions that follow, a combination of lithostratigraphic, hydrogeologic, and unsaturated zone flow and transport model nomenclatures are used, depending on the context of the discussion. For a listing of the correlations between these different classification schemes, see Table 2.3.2-2.

2.3.8.3.3.1 Busted Butte Test Series

The Busted Butte unsaturated zone transport tests were a series of experiments conducted at Busted Butte near Yucca Mountain to investigate flow and transport issues in the unsaturated zone flow and transport models for Yucca Mountain (BSC 2004c, Section 6.13).

The Busted Butte test facility is located in Area 25 of the Nevada Test Site, approximately 8 km southeast of the repository area (Figure 2.3.8-4). The site was selected because of the presence of a readily accessible exposure of the Topopah Spring Tuff (Tpt) and the Calico Hills Formation (Tac) and the qualitative similarity of these units to those beneath the repository horizon (Figure 2.3.8-9). The Busted Butte data is used for model validation. The test facility consists of an underground excavation along a hydrogeologic contact between the TSw unit and the CHn unit (Figure 2.3.8-9). This contact comprises the nonwelded portion of the basal vitrophyre of the Topopah Spring Tuff. The study of the TSw–CHn interface is important because of the significant role that the vitric layers of the CHn unit play in retardation of radionuclide transport (SNL 2007b, Section 7.2.4.1).

The test proceeded in two phases of differing designs, purposes, and experimental scales, among other factors. Phase 1, including test Phases 1A and 1B, was designed as a scoping study to assist in design and analysis of Phase 2, including Phases 2A, 2B, and 2C, and as a short-term experiment aimed at providing initial transport data on a fracture near an interface. Phase 2 incorporated a larger region than Phase 1, with a broader, more complex scope for tracer injection, monitoring, and collection (SNL 2007b, Section 7.2.4.1).

2.3.8.3.3.1.1 Phase 1A Test

The Phase 1A test, located in the CHn hydrogeologic unit spanning the lowermost Tpt (Tptpv1) to the uppermost Tac nonwelded unit, was a noninstrumented test consisting of four horizontal single-point injection boreholes. A schematic of the borehole layout in the Phase 1A test is shown in Figure 2.3.8-10. Continuous tracer injection started on April 2, 1998, with a duration of 286 days. Injection rates varied from 1 mL/hr (boreholes 2 and 4) to 10 mL/hr (boreholes 1 and 3) (Figure 2.3.8-10). The field test was completed through excavation by mini-mineback and auger sampling in March and April 1999 (BSC 2004c, Section 6.13.2.1).

All Phase 1 horizontal boreholes were 2 m long and 10 cm in diameter. The injected species included a mixture of conservative or nonsorbing tracers (bromide, fluorescein, and fluorinated benzoic acids), a reactive or sorbing tracer (lithium) as analogues for nonsorbing and sorbing radionuclides, and an analogue for a colloidal tracer (fluorescent polystyrene microspheres) (SNL 2007b, Section 7.2.4.1). Of all the tracers injected during the field experiment, only the transport of the nonsorbing bromide and fluorescein tracers can be studied, because the response of the other tracers was too weak to be reliable (SNL 2007b, Section 7.2.4.1.2).

Only data from injection into horizontal borehole 3 (located in the Tptpv1 lithostratigraphic layer, which is part of the CHn hydrogeologic unit) were considered. Horizontal borehole 3 is about 20 cm above the Tptpv1–Tac interface. The injection tests into boreholes 1 (located in the Tptpv1 unit, but further removed from the interface), 2, and 4 (located in the Tpbt1 unit) were not analyzed because of the lower quality of the data (SNL 2007b, Section 7.2.4.1). Horizontal boreholes 2 and 4 were injected at rates about an order of magnitude smaller than in boreholes 1 and 3 (BSC 2004c, Section 6.13.2.1). The resulting smaller plumes in boreholes 2 and 4 provided data that were less reliable for analysis. Borehole 3 had the greater average injection rate with less variability in the injection rate over the test period as compared to borehole 1 (SNL 2007b, Section 7.2.4.1). Therefore, it exhibited a stronger signal.

The field test was completed through excavation by mineback and auger sampling. During mineback, as successive vertical slices were removed, digital photographs were taken under visible and ultraviolet light to record the distribution of moisture and fluorescein. In addition, rock samples were collected by augering, and the exposed plane was surveyed. The auger samples were analyzed for tracer concentration (BSC 2004c, Section 6.13.2.1).

The fluorescein plume in the vicinity of borehole 3 at various locations along the y-axis (i.e., originating at the rock face and going into the rock) is shown in Figure 2.3.8-11. The plume cross sections show a relatively uniform distribution of fluorescein around the injection borehole, although some borehole shielding effects (i.e., tracer blocked or delayed from moving in the direction of the borehole) can be seen. At all of the mineback faces, the corresponding plume cross sections are more oval than round. The Phase 1A test shows that lithologic contacts clearly influence flow and tracer transport. Figure 2.3.8-11 shows the distinct geologic layering, denoted by the limited penetration and higher fluorescein concentrations in the less permeable lower layer (BSC 2004c, Section 6.13.2.1).

2.3.8.3.3.1.2 Phase 1B Tests

Phase 1B was designed to acquire data on fracture–matrix interactions in the TSw, and its results were used to calibrate fracture properties for the Phase 2 analysis. This test involved the injection of the tracers discussed in the Phase 1A test (plus pyridone) and collection of pore-water and tracer samples in the lower section of the Topopah Spring Tuff (Tptpv2). In the Phase 1B field test, the tracers were injected into two horizontal boreholes (borehole 5 at a rate of 10 mL/hr and borehole 7 at a rate of 1 mL/hr) in the lower portion of the Topopah Spring Tuff basal vitrophyre (Tptpv2 in lithostratigraphic units and tsw39 in the unsaturated zone layers of the hydrogeologic units) (Table 2.3.2-2), which is a relatively low-permeability fractured rock. Samples were obtained in collection boreholes 6 and 8 (Figure 2.3.8-12) (BSC 2004c, Section 6.13.2.2). The tracer solutions were injected at a depth of 1.30 m, measured from the rock face into the horizontal injection boreholes. Water samples from horizontal boreholes were collected and analyzed regularly during the injection period (Tseng and Bussod 2001).

Five solute tracers were injected in horizontal borehole 5 at a rate of 10 mL/hr, and their concentrations were observed in horizontal collection borehole 6 (which lies directly below borehole 5). These concentration changes with time are known as breakthrough curves. No tracer breakthrough was discernible in horizontal collection borehole 8 (which is below injection borehole 7), where tracers were injected at a rate of 1 mL/hr. The breakthrough concentrations of bromide and 2,6-difluorobenzoic acid (DFBA) in borehole 6 are shown in Figures 2.3.8-13 and 2.3.8-14, respectively (BSC 2004c, Section 6.13.2.2).

Maximum concentrations were observed at a horizontal depth of approximately 1.3 cm into the rock face, which is directly underneath the injection port in horizontal borehole 5. However, the value of the maximum concentration and amount of mass recovery vary greatly. Bromide and 2,6-DFBA (both nonsorbing anionic tracers) exhibit similar and reasonable breakthrough patterns and approximately equal maximum relative concentrations. The low concentrations and late breakthrough for lithium indicate that lithium transport was significantly retarded by sorption (BSC 2004c, Section 6.13.2.2).

2.3.8.3.3.1.3 Phase 2 Tests

Phase 2 tests were designed to incorporate large volumes of rock and involved a 7-m-high, 10-m-wide, and 10-m-deep block that was determined to represent all of the rock units of Phase 1 Figure 2.3.8-12. The larger domain of the Phase 2 tests provided information on the effects of heterogeneity and upscaling on radionuclide transport (BSC 2004c, Section 6.13.3.6). The injection points for this phase were distributed in two horizontal, parallel planes arranged to test the hydrologic properties of the lower Topopah Spring welded tuff (Tptpv2) and the hydrologic Calico Hills Formation (lithostratigraphic units Tptpv1 and Tac) (BSC 2004c, Section 6.13.3.1).

Six upper injection boreholes (boreholes 18 to 23), of which four were used for injection, and four lower boreholes (boreholes 24 to 27) were drilled into the block, as shown in Figure 2.3.8-12. The other two boreholes (boreholes 19 and 22) were used for ground-penetrating radar measurement (BSC 2004c, Section 6.13.4.1.3). The upper injection plane consisted of 37 injection points distributed along the axes of the injection boreholes and was located in the fractured Tptpv2 unit. As in Phase 1B, this unit represents the base of the TSw basal vitrophyre and is characterized by subvertical fractured surfaces that form columnar joints. The natural fracture pattern present in this unit served as the conduit for tracer migration into the CHn. The lower horizontal injection plane was located in the Tac and included 40 injection points distributed in the four horizontal and parallel injection boreholes. These boreholes were located to incorporate the lower part of the block, in the event that the fluid injected into the top injection boreholes did not penetrate the entire block during the testing program. Phase 2 also included 15 collection boreholes drilled in a lower horizontal plane parallel to the other two planes, in a direction perpendicular to that of the injection boreholes (Figure 2.3.8-12). These boreholes contained collection pads evenly distributed on membranes to collect samples (BSC 2004c, Section 6.13.3.1).

Phase 2 included three subphases—2A, 2B, and 2C—that tested a range of injection rates. Phase 2A involved injection (at a rate of 1 mL/hr per injection point) into a single instrumented borehole (borehole 23) in the upper injection plane. This borehole is located entirely within the Tptpv2 unit, which consists of fractured, moderately welded tuffs from the basal vitrophyre. In Phase 2B, four instrumented injection boreholes (boreholes 24 to 27) in the lower injection plane were used, and the injection rate was much higher than in Phase 2A (10 mL/hr per injection point). In this case, the injection plane was restricted to the Calico Hills Formation (Tac). Thus, the Phase 2B test was designed to incorporate the lower section of the test block, while the upper section of the block was incorporated during the Phase 2A and 2C tests. Phase 2C involved injection into three upper boreholes (boreholes 18, 20, and 21) at much higher rates than in Phases 2A and 2B (50 mL/hr per injection point). As in Phase 2A, the injection system was located on a horizontal plane in the Tptpv2 unit (BSC 2004c, Section 6.13.1.7).

The tracers used in the Phase 2 tests included all the tracers used in Phase 1. Additionally, three other fluorinated benzoic acids, a mixture of sorbing solute species that served as analogues for radionuclides that may be transported in the repository system (Ni^{2+}, Co^{2+}, Mn^{2+}, Sm^{3+}, Ce^{3+}, and rhodamine WT), and a nonsorbing anionic tracer (I^{-}) were used (BSC 2004c, Section 6.13.3.1). Pad analyses confirmed breakthrough of the nonsorbing tracers in 14 of the 15 collection boreholes. Of the sorbing tracers, breakthrough was confirmed only for lithium, the sorbing tracer having the lowest sorption coefficient, in 10 of the 15 collection boreholes (BSC 2004c, Section 6.13.3.4). Boreholes where bromide or lithium did not appear indicate the effects of heterogeneity, larger

distances from the injection holes, or both (BSC 2004c, Sections 6.13.3.6 and 6.13.3.7). The spatial distributions of bromide and lithium in sampling borehole 16 at different times are shown in Figures 2.3.8-15 and 2.3.8-16, respectively. As expected, lithium breakthrough was retarded with respect to bromide, consistent with the laboratory sorption measurements for lithium (BSC 2004c, Section 6.13.3).

2.3.8.3.3.1.4 Results of Busted Butte Test Series

The Busted Butte test series was conducted to investigate flow and transport in the unsaturated zone. The purpose of this calibration and verification was to demonstrate that the unsaturated zone radionuclide transport process model could predict transport behavior in the CHn vitric rock. Phase 1A results were used to gain confidence in the unsaturated zone radionuclide transport process model with regard to overall geometry of transport, values for diffusion coefficients, and the impact of rock inhomogeneities on transport (SNL 2007b, Section 7.2.4.1.1). Phase 1B acquired data on fracture–matrix interactions for calibration of fracture properties in the unsaturated zone radionuclide transport process model, and breakthrough curves for tracers were adequately reproduced when the unsaturated zone radionuclide transport process model was calibrated with observed data. Phase 2C allowed calibration of the radionuclide transport process model on a larger scale (SNL 2007b, Section 7.2.4.1.4). Sorbing and nonsorbing tracers were injected, and the predicted tracer distributions were compared with measurements of locations of peak concentration and distributions. Results were generally comparable, and differences could be explained. See Section 2.3.8.4.4 for further discussion of the use of these results to build confidence in the unsaturated zone radionuclide transport process model.

2.3.8.3.3.1.5 Radionuclide Migration Experiments Using Tuff Samples from Busted Butte

Migration experiments under unsaturated conditions have been conducted at the Whiteshell Laboratories (of Atomic Energy of Canada Limited), in Pinawa, Manitoba, on blocks excavated from the Busted Butte test facility. The following discussion is based on an abstracts by Vandergraaf, Drew, Ticknor et al. (2002) and a report by Vandergraaf, Drew, and Ticknor (2002). The migration experiments were conducted with radionuclides to corroborate and compare with field experiments that used nonradioactive chemical analogues for tracers to evaluate flow and transport through nonwelded tuff.

The duration of the migration experiment on a trial block approximately 1 cubic foot in size was 87 days. The trial block was removed from 60 cm below the interface between the Tptpv1 and the Tac formations. After a vertical flow of synthetic Busted Butte pore water as transport solution was set up under unsaturated conditions, a suite of conservative and chemically reactive radionuclide tracers was injected at volumetric flow rates of 20 mL/hr. Na-fluorescein dye, ^{3}H (as tritiated water), ^{22}Na, ^{60}Co, $^{95m+99}Tc$ (as the pertechnetate anion), ^{137}Cs, and ^{237}Np were used as tracers (Vandergraaf, Drew, Ticknor et al. 2002). Results showed that transport of $^{95m+99}Tc$ was slightly faster than that of the transport solution, using tritiated water ($^{3}H_2O$) as a flow indicator. The finding of Tc and dye tracer eluted ahead of triatiated water has been attributed to an anion exclusion effect. Retardation of ^{237}Np was consistent with that predicted from results obtained in supporting static-batch-sorption studies (BSC 2004c, Section 6.13.6). Post-migration analysis of the flow field in the trial block showed that the front of the ^{22}Na had migrated approximately half the distance

through the block and that ^{60}Co and ^{137}Cs had been retained near the inlet. This agrees qualitatively with that predicted from the results from static-batch-sorption studies (BSC 2004c, Section 6.13.6).

The migration experiment on a nominally 1-m^3 block (approximately 1 m by 1 m by 1 m) lasted for more than 700 days, and was initiated in April 2001. The tracer solution was injected continuously at two locations at the top of the block, at a flow rate of 10 mL/h per injection point (20 mL/h with both injections). By June 2002, the normalized concentrations of ^{3}H, ^{99}Tc, and dye tracer in the water collected from the bottom of the block had reached a value of approximately 0.08. The transport behavior of ^{99}Tc is very similar to that of the transport solution (BSC 2004c, Section 6.13.6). None of the other tracers were observed in the effluent from the larger block. This is consistent with the observations from the smaller block.

2.3.8.3.3.2 Alcove 8–Niche 3 Test

The tests at Alcove 8–Niche 3 provide information on seepage and transport over spatial scales on the order of 20 m. This is the relevant scale for relating site-scale processes of seepage and percolation with drift-scale processes of diversion and seepage (BSC 2004e, Figure 6-1). Along these long flow paths, the corresponding advective transport is affected by fracture-matrix interaction, which is shown to be an important retardation mechanism that delays the movement of dissolved solutes through the unsaturated units (BSC 2004c, Section 6.12).

Figure 2.3.8-17 shows the location of the Alcove 8–Niche 3 test site within the ESF main drift and the ECRB Cross-Drift, as well as a three-dimensional representation of the test area. Alcove 8 is located within the upper lithophysal zone of the TSw (Tptpul). This unit has some lithophysal cavities that may intersect fractures. A distinctive feature of the test bed in Alcove 8 is a near-vertical fault that cuts across the floor. The fault is open on the ceiling of the alcove and appears to be closed along the floor. Two tests were conducted. In the first test, water and tracers were introduced along the fault. In a subsequent test, water and tracers were introduced in a 12 square meter plot on fractured rock at the center of Alcove 8 (Figure 2.3.8-18).

2.3.8.3.3.2.1 Alcove 8–Niche 3 Fault Test

In the fault test, water and tracers were released in trenches about 5 cm wide and about 5 cm deep that were excavated along this fault. Niche 3 (also referred to as Niche 3107) is approximately 4 m wide, extends to approximately 14 m from the centerline in the ESF main drift, and is in the Tptpmn, about 20 m below the floor of the alcove. The interface between Tptpul and Tptpmn is about 17 m below the floor of Alcove 8 (BSC 2006a, Section 6.1). The fault in Alcove 8 is visible along the ceiling of Niche 3 (BSC 2004c, Section 6.12.1.2).

Water was introduced along the fault (about 5 m long) (BSC 2004c, Figure 6-150) under ponded conditions (with 2 cm of water head) (BSC 2004c, Section 6.12.1.3.1). The plot consists of four trenches that have different percolation rates of applied water as a result of heterogeneity along the fault. Figure 2.3.8-19 shows the total percolation rate as a function of time. The considerable temporal variability of percolation rate observed during the test was attributed to infill materials within the fault just below the infiltration plot (BSC 2004c, Section 6.12.2.1). After quasi-steady-state seepage was observed in Niche 3, a finite volume of water containing two tracers (bromide and pentafluorobenzoic acid) with different molecular diffusion coefficients was

introduced into the fault. The use of tracers with different diffusion coefficients provides data that can be used to demonstrate the effects of matrix diffusion. Once the tracer-laced water had been released into the fault, more tracer-free water was released. Both tracer-laced and tracer-free releases occurred under the same ponded condition. This release of tracer-free water continued until a few months after breakthrough of the two tracers was observed in the seepage collected in Niche 3 (BSC 2004c, Section 6.12.1.1).

After 209 days of water application, two nonsorbing tracers (bromide and pentafluorobenzoic acid) with different molecular diffusion coefficients and a sorbing tracer (lithium) were introduced into the water at the infiltration plot. Tracer concentrations were measured at the niche in three of the trays capturing seeping water from the fault. Figure 2.3.8-20 shows the evolution over time of bromide concentration and of the daily seepage rates for a 1.5-month period following arrival of the wetting front. The bromide concentration increases from a low initial level of about 3 ppm to the release concentration of 30 ppm about 30 days after the onset of seepage. Given the nonsorbing behavior of bromide, the delayed bromide breakthrough is a good indicator of the importance of matrix diffusion, the absence of which would have resulted in much earlier observations of the 30 ppm concentration (BSC 2004c, Section 6.12).

Figure 2.3.8-21 shows the tracer concentration in the seepage water at two sampling locations in Niche 3 (sampling tray 7 and tray 9+23 in field tests), which were picked for discussion because they are the points where lower and upper seepage fluxes were observed. In tray 7, both bromide and pentafluorobenzoic acid were first detected three weeks after the initial release of the tracers into the fault. The concentration of both tracers gradually increased, though the rise in pentafluorobenzoic acid concentration clearly preceded that of bromide, indicating a lower molecular diffusion coefficient for pentafluorobenzoic acid, consistent with the relative sizes of the two species. After peaking, the concentrations decreased and finally reached a relatively constant level (BSC 2004c, Section 6.12.2.4). Similar patterns were observed in tray 9+23, but the magnitude and times at which peak concentrations occurred were larger and faster, respectively, suggesting the involvement of different fractures with different flow pathways and leading to different rates of advective transport. This notion is further supported by the measured lithium concentrations, which are much higher in tray 9+23 than in tray 7 because the shorter pathway and faster flowing fractures that were intercepted allow less time for matrix diffusion and retardation through sorption. Similar tracer behavior with different diffusion coefficients was observed by Reimus, Adams et al. (1999) in tracer experiments in fractured volcanic tuffs at the C-Wells site. This consistency confirms that similar transport processes (i.e., advection and matrix diffusion) occur in the unsaturated and saturated zone in the fractured tuffs of low matrix permeability.

2.3.8.3.3.2.2 Alcove 8–Niche 3 Large Plot Test

The introduction of water to the large plot began immediately following the termination of the fault test. The 3 m by 4 m large plot infiltration area in Alcove 8 consisted of 12, 1 square meter sections as shown in Figure 2.3.8-18. Water was introduced under ponded conditions with 2 cm of water head. The ponded infiltration test along the 12 subplots continued for 790 days. During this period, there were three distinct stages of liquid release. Stage 1 began with the ponding of the 12 subplots and continued for 216 days. During Stage 2, water was ponded in subplots 2 and 12 for 132 days, while the surface of the remaining 10 subplots was kept free of standing water. For approximately the last three weeks of Stage 2, all subplots were dry. For Stage 3, ponded water was reintroduced

to all subplots. During this phase, in six of the subplots, the water application was briefly terminated, and the surface was scrubbed to remove biofilms that had developed. The effects of drying and resumption of ponded conditions produced changes in percolation rates for subplots 1 and 2, whereas the other subplots resumed percolation at the same rate as observed at the end of the Stage 1 ponded infiltration. Subplots 1 and 2 displayed substantial increases in percolation rate following the scrubbing, but the scrubbing of subplot 1, which occurred after the scrubbing of subplot 2, appeared to result in a reduction in the percolation rate in subplot 2 as percolation rates in subplot 1 increased (BSC 2006a, Section 6.1).

The total flow rate into the large plot is shown in Figure 2.3.8-22. The considerable temporal variability of the percolation rate of applied water observed during the test is attributed to infill materials just below the infiltration plot, as well as to changes in water ponding conditions and removal of biofilms in the different subplots during the test. Furthermore, the percolation rates were generally nonuniform over the 12 subplots, with most of the percolation occurring in subplots 2 and 12 (BSC 2006a, Section 6.1).

The equivalent percolation rates in this test, averaged over the 12 m^2 plot area, are significantly higher than the representative values of the percolation rates specified in the unsaturated zone flow and transport model for TSPA. For example, the mean percolation rate during the relatively steady period from day 500 to day 734 is approximately 1450 mm/yr, compared to a median value of percolation flux in the repository footprint of approximately 97 mm/yr for the 90th percentile monsoon climate, the wettest of the climate scenarios applied in the first 10,000 years of the TSPA model. The need to obtain experimental field results in a reasonable time period resulted in the application of percolation scenarios that were more rapid than expected under natural conditions; this is a potential limitation of field testing in the unsaturated zone that must be considered when interpreting the results. Despite the high percolation rates, the medium is expected to be in a condition of gravity-driven flow under unsaturated conditions (BSC 2006a, Section 6.2.1), a prerequisite for the test to be directly applicable to the unsaturated zone transport model.

The 16 seepage collection areas, shown in Figure 2.3.8-18, are designated U1-T1, U2-T2, etc. The "U" designates collection unit, and there are four collection units (U1 to U4). Each collection unit has five sample collection bottles labeled T1 to T5. Only collection bottles where seepage was collected are shown in Figure 2.3.8-18. The ceiling of Niche 3 is also divided into 12 columns used in the numerical model grid (Section 2.3.8.4.4.4), designated by T1, T2, etc. One zone may cover one or more seepage tray units.

Total seepage collection in Niche 3 is shown in Figure 2.3.8-23. Seepage did not achieve the same level of stability as observed for percolation in Alcove 8. After quasi-steady-state seepage was observed in Niche 3, from approximately 400 days to 559 days, a finite volume of water containing six tracers was introduced over a period of 41 days. Different tracers were applied to three groups of infiltration plots (BSC 2006a, Section 6.1):

- Subplots 1 and 2: 2, 6-difluorobenzoic acid and potassium iodide
- Subplots 3 through 9: 2, 5-difluorobenzoic acid and calcium bromide
- Subplots 10 through 12: 2, 4, 5-trifluorobenzoic acid and potassium fluoride.

Prior to scrubbing of the infiltration subplots, none of the tracers were observed at levels discernable above background or detection limits in the seepage water entering Niche 3. Following the scrubbing, iodide and 2, 6-difluorobenzoic acid from subplots 1 and 2 were observed at relative concentrations less than 1% in seepage water collected in Niche 3 (BSC 2006a, Section 6.1). Therefore, it appears that the scrubbing either resulted in a direct release of tracer trapped in the biofilms or affected the flow fields to mobilize tracer remaining in the test bed between Alcove 8 and Niche 3 (see BSC 2006a, Section 6.2.4 for further discussion).

2.3.8.3.3.3 Alcove 1 Tests

An infiltration and tracer transport test was performed in ESF Alcove 1, analogous to the repository host rock. Transport processes include advective transport and matrix diffusion. Alcove 1 is located (Figure 2.3.8-7) near the North Portal of the ESF in the upper lithophysal zone of the Tiva Canyon Tuff (Tpcpul) unit, corresponding to hydrogeologic unit CUL (Table 2.3.2-2) (Liu, Haukwa et al. 2003, Section 3.3). The alcove is approximately 5.5 m high and 5.8 m wide. In the Alcove 1 tests, water was applied in a plot on the ground surface approximately 30 m directly above the alcove. The size of the infiltration plot was 7.9 m by 10.6 m (Liu, Haukwa et al. 2003, pp. 174-175). Irrigation drip tubing, with 490 drippers uniformly distributed within the infiltration plot, was used to apply the water. The test consisted of two phases. Phase I was performed from March to August 1998, and Phase II was performed from January 1999 to June 2000 (Liu, Haukwa et al. 2003, Section 2). Phase I involved applying water at the ground surface directly over the end of Alcove 1 at rates on the order of 30 mm/day (BSC 2004c, Section 6.12.5.2). These rates were much higher than those expected under natural conditions, to facilitate the collection of data in a reasonable time period. At a late stage of the Phase II test, a conservative (nonsorbing) bromide tracer was introduced into the applied water. The seepage into the alcove and the tracer arrival time were recorded.

During Phase II, water traced with lithium bromide was injected over a period of approximately 100 days. A sustained, increasing trend in the tracer concentration was found approximately one month after the initiation of tracer application. Tracer concentrations increased to approximately one-half of the injected concentration and then decreased after the use of tracer in the applied water was discontinued.

The results from the Alcove 1 test indicate that (1) the continuum approach is valid for modeling flow and transport in unsaturated fractured rock, (2) the use of an active fracture model can capture the major features of fingering flow and transport in fractures, (3) matrix diffusion has a significant effect on the overall transport behavior in unsaturated fractured rocks, and (4) dispersion in fractures may not have a significant effect on the overall transport behavior (Liu, Haukwa et al. 2003).

The findings from the Alcove 1 test are qualitatively similar to the findings from the Alcove 8–Niche 3 fault test in that both fractures and matrix influence transport in the fractured rock, with diffusion from fractures to matrix having a significant effect on transport processes (Liu, Haukwa et al. 2003). See Section 2.3.8.4.4.5 for more quantitative interpretations of matrix diffusion in the Alcove 1 test.

2.3.8.3.4 Colloid Data Sources and Testing

The Busted Butte field tests were conducted, in part, to provide data, confirmatory evidence, and a validation basis for the transport of colloids through the unsaturated zone at Yucca Mountain (BSC 2004c, Section 6.13). The colloids consisted of two sizes of fluorescent polystyrene microspheres of 0.3 and 1.0 μm (BSC 2004c, Section 6.13.1).

The fluorescent polystyrene microspheres were significantly attenuated in the unsaturated media at Busted Butte. The microspheres were typically injected in relatively high-ionic-strength solutions of solute tracers that would have tended to destabilize them and make them more susceptible to attachment to rock surfaces. It should be noted that flow at Busted Butte was matrix dominated, not fracture dominated (SNL 2007b, Section 7.2.4.1.3.2). Therefore, the Busted Butte microsphere experiments probably do not provide a good representation of colloid transport in fractures in the unsaturated zone. No evidence of microsphere breakthrough was observed in either Phase 1B or Phase 2, effectively providing no breakthrough data (BSC 2004c, Sections 6.13.2.2 and 6.13.3.2). Because of this, microspheres were eliminated from the experimental matrix early in Phase 2.

To support colloid retardation estimates in the fracture continuum, field experiments were conducted at the C-Wells complex using a carboxylate-modified polystyrene latex microspheres as analogues for natural colloids (SNL 2007f, Section 6.3). These tests were conducted in fractured volcanic tuffs at the C-Wells (UE-25 c#1, c#2, and c#3), which are located approximately 2 km southeast of the repository footprint. Microsphere tracer experiments were conducted in both the conductive Bullfrog Tuff and less conductive Prow Pass Tuff. Additional laboratory fracture experiments were conducted using silica, montmorillonite, and clinoptilolite colloids in addition to carboxylate-modified latex microspheres. The breakthrough curves from these tests were fitted to obtain estimates of forward and reverse filtration rates. These rates were then used to calculate a retardation factor for colloid transport through saturated fractured rock (BSC 2004f, Section 6.4). The evaluation of test data resulted in considerable retardation of colloids in both the volcanic and alluvial regions of the saturated zone (BSC 2004f, Section 7.1).

Colloid transport data obtained under saturated conditions from the C-Wells and other field and lab tests provide a conservative measure of unsaturated zone colloidal transport (SNL 2007f, Section 6.3). The characterization of colloid transport is believed to be conservative because colloidal transport under saturated conditions would be greater than colloidal transport under unsaturated conditions (SNL 2008a, Section 4.1.9 in Addendum 1).

2.3.8.3.5 Chlorine-36

Measurements of chloride concentrations and $^{36}Cl/Cl$ for salts extracted from water, soil, and rocks have been used to provide information on characteristics of water movement and solute transport through the unsaturated zone at Yucca Mountain (Fabryka-Martin, Wolfsberg et al. 1997, pp. 75 and 77 to 79; Fabryka-Martin, Wolfsberg, Levy et al. 1998, p. 93; Fabryka-Martin, Wolfsberg, Roach et al. 1998, p. 264; Wolfsberg et al. 1998, p. 81). ^{36}Cl is a radioactive isotope of chlorine, with a half-life of 3.01×10^5 yr (Parrington et al. 1996, p. 22) and occurs primarily as the chloride anion. As such, it is relatively inert in the subsurface environment and behaves conservatively. This radionuclide is present in infiltrating waters as a natural tracer produced mainly in the upper atmosphere by the bombardment of argon (Ar) by cosmic radiation (BSC 2004d, Section 5.2.2.5.3).

Global fallout from thermonuclear tests, conducted primarily in the Pacific Proving Grounds, resulted in a ^{36}Cl bomb pulse with maximum meteoric ratios in excess of $200{,}000 \times 10^{-15}$. These extremely high values were diluted by mixing processes in the soil zone and subsurface and are not observable today. For comparison, modern precipitation has $^{36}Cl/Cl$ ratios on the order of 500×10^{-15} (see Figure 2.3.2-29). Nevertheless, high $^{36}Cl/Cl$ ratios (those greater than about $1{,}250 \times 10^{-15}$) indicate some ^{36}Cl-enriched component, and their appearance in an environmental sample signals the presence of at least a small component of anthropogenic ^{36}Cl. Present-day $^{36}Cl/Cl$ ratios in Yucca Mountain surface soils generally range from $1{,}500 \times 10^{-15}$ to $3{,}000 \times 10^{-15}$ (CRWMS M&O 1998, pp 3 to 5). In subsurface water, similar high ratios suggest travel times from the ground surface of 50 years or less (BSC 2004d, Section 5.2.2.5.3). Ratios over $1{,}250 \times 10^{-15}$ suggest bomb-pulse influence and may indicate the presence of some rapid transport pathways (Fabryka-Martin, Wolfsberg et al. 1997, p. 18; BSC 2004d, Section 5.2.2.5.3). These pathways may be either faults, fault zones, open fractures, or a combination of these features, in which rapid downward water flow can occur to depth.

Evidence for fast pathways that persist into the TSw unit is provided by bomb-pulse $^{36}Cl/Cl$ ratios measured at locations in the ESF tunnel and the cross-drift (see the data labeled "Los Alamos National Laboratory data" in Figure 2.3.2-28). More than 250 samples have been analyzed from the ESF tunnel. Of these, more than 40 had ^{36}Cl levels sufficiently elevated as to be interpreted as evidence for the presence of elevated ^{36}Cl (Fabryka-Martin et al. 1996; Fabryka-Martin, Wolfsberg et al. 1997; Fabryka-Martin, Turin et al. 1998). ^{36}Cl measurements from boreholes, corrected for dilution from rock chloride, were found to be consistent with measurements from the ESF. None of the few $^{36}Cl/Cl$ measurements available for samples collected below the current repository horizon were sufficiently high to suggest the presence of bomb-pulse ^{36}Cl (BSC 2004d, Section 5.2.2.5.3). Therefore, small amounts of water following fast transport pathways may be expected between the ground surface and the repository level, primarily through faults.

In the description of unsaturated zone flow, an independent ^{36}Cl validation study is discussed (Section 2.3.2.3.4.3; BSC 2006b). The findings of this validation study were ambiguous; discrepancies in the measurements performed by different groups of researchers at different times remain unresolved. Because the ^{36}Cl bomb-pulse findings in the ESF samples lead to a more conservative result and cannot be ruled out given the current information, the unsaturated zone flow and transport models have been developed to be qualitatively consistent with a fast pathway conceptual model implied by the bomb pulse observations reported in the aforementioned studies by explicitly modeling major faults and flow through the network of connected fractures (Section 2.3.2.2.1.2).

The correlation of the elevated ^{36}Cl measurements found in the Los Alamos National Laboratory study with the surface expression of faulting indicates that the pathway and travel time may involve locally modified PTn unit fracture properties (Fabryka-Martin, Wolfsberg et al. 1997, p. 78; Fabryka-Martin, Flint et al. 1997, pp. 6-22 and 8-18). These data support the hypothesis that faulting or other disturbances are zones of preferential fracturing and larger fracture permeabilities in the PTn, thereby generating a local environment in the PTn unit that supports fracture flow and hence rapid transport of solutes. Once through the PTn unit, flux distributions favor fracture flow in the TSw unit, thereby providing a continuous pathway to the sampled depths (BSC 2004d, Section 5.2.2.5.3).

The pre-2000 ^{36}Cl results conducted by Los Alamos National Laboratory were used to develop a conceptual model for flow through the unsaturated zone at Yucca Mountain (Campbell et al. 2003). As a general rule, fracture flow is prevalent in the welded Tiva Canyon tuffs but transitions to matrix-dominated flow in the Paintbrush tuff nonwelded hydrogeologic unit. In order for bomb-pulse ^{36}Cl to have reached the level of the repository in less than 50 yr, a zone of higher than average infiltration must intersect a region with higher than average fracture permeability, presumably due to faulting. Then, rapid transport through the nonwelded tuff can occur through the preferential fracture pathways, and in these areas bomb-pulse ^{36}Cl has reached the repository level. Away from PTn-cutting faults, the ages of water samples at the ESF appear to be a function of the thickness of the nonwelded tuff between the ground-surface and the ESF (BSC 2004d, Section 5.2.2.5.3). Despite the fact that these fast flow paths are thought to exist, it is likely that the percentage of flow that travels rapidly to depth is low. For example, Section 2.3.2.2.1.2 concludes that fast flow paths are few, carry a small amount of the water (primarily through faults and isolated fractures), and do not significantly affect the overall flow paths in the unsaturated zone. Therefore, the locations at which rapid, episodic flow of water occurs to the depth of the ESF are sparse, and in the remainder of the repository footprint where faults are not present, the PTn dampens episodic pulses of infiltration (Table 2.2-5, excluded FEP 2.2.07.05.0A, Flow in the UZ from episodic infiltration).

Further evidence of fast transport has also been found from the detection of subsurface tritium at the repository horizon (BSC 2004d, Section 5.2.2.5.2). Like ^{36}Cl, tritium is produced at levels of 2 to 25 tritium units in the upper atmosphere, and is the result of cosmic radiation bombardment of nitrogen. Also similar to ^{36}Cl, large amounts of tritium relative to natural levels occurred as a result of global fallout from thermonuclear tests. However, unlike ^{36}Cl, the short half-life of tritium, 12.3 years, means that levels in excess of 1 to 2 tritium units indicates that some water has traveled from the ground surface to the depth of measurement in 50 years or less.

In the North Ramp of the ESF, the only elevated tritium activities were found in samples from the Bow Ridge Fault in Alcove 2 (BSC 2006b, Section 5.3). These samples are from the Tiva Canyon Tuff, above the Paintbrush Group nonwelded units. Samples of the Topopah Spring Tuff from the Drill Hole Wash Fault and from the vicinity of the Ghost Dance Fault contained no tritium activities significantly above the 2 tritium unit threshold, and only one of the samples from the Sundance Fault area did (2.6 tritium units). In the South Ramp of the ESF, over half of the samples contained tritium activities significantly over 2 tritium units, including samples from both above and below the Paintbrush Group nonwelded units. In the ECRB Cross-Drift, several samples of the Topopah Spring Tuff, especially from the upper lithophysal unit, had tritium activities greater than 2 tritium units. However, attempts to reproduce the latter results with adjacent core samples yielded mixed results, an outcome that reflects the difficulty in obtaining homogeneous material for testing and the likelihood that if fast-paths are present, they are heterogeneously distributed over small distances.

High tritium and $^{36}Cl/Cl$ values are typically not correlated, although residual uncertainty exists in the interpretation of the data (BSC 2006b, Section 6.3.3). The tritium results for samples from the Sundance and Drill Hole Wash Faults are consistent with the USGS ^{36}Cl validation study results for the Sundance Fault, and inconsistent with Los Alamos National Laboratory ^{36}Cl results for both fault zones. The tritium data also indicate the presence of fast paths in the Topopah Spring Tuff in the South Ramp of the ESF. Pre-2000 ^{36}Cl data showed no evidence for fast path behavior in the South Ramp; there is no validation study ^{36}Cl data from this area.

2.3.8.4 Model Development

[NUREG-1804, Section 2.2.1.3.7.3: AC 1(1), (2), (4), AC 4]

Development of the unsaturated zone radionuclide transport process model followed a logical progression designed to address uncertainties, build on available data, and include the most significant processes that affect transport. The FEPs included in the model are summarized in Table 2.3.8-1. Radionuclide transport in the unsaturated zone is strongly affected by advection and is closely tied to the unsaturated zone flow models discussed in Section 2.3.2. The unsaturated zone radionuclide transport process model was developed, calibrated, and validated (SNL 2007b). The model is developed on the same model domain used by the site-scale unsaturated zone flow model. This model was used to validate the unsaturated zone radionuclide transport abstraction model (Section 2.3.8.5) which is also based on the same model domain as the flow and transport process models. Because of this common development framework and the validation of both the process and abstraction models, the two models are essentially interchangeable. In the presentation that follows, the unsaturated zone radionuclide transport behavior is illustrated principally with the abstraction model.

The primary model development objectives for the unsaturated zone radionuclide transport process and abstraction models were as follows:

- To integrate the available data for the development of a comprehensive model of radionuclide transport through the unsaturated zone of Yucca Mountain for a range of current and future climate conditions
- To identify the controlling transport processes and phenomena, determine their relative importance, and evaluate the effectiveness of matrix diffusion and sorption as retardation processes, including treatment of uncertainty
- To identify the geologic features and release mechanisms that are important to radionuclide transport
- To assess the migration of important radionuclide solutes and their decay products from the repository toward the water table
- To evaluate the effects of various climatic conditions on radionuclide transport
- To estimate the migration of radioactive colloids from the repository toward the water table
- To evaluate through sensitivity analyses the effect of uncertainty in important parameters on the transport behavior (SNL 2008a, Section 6.8[b]).

2.3.8.4.1 Framework for Unsaturated Zone Transport

The site-scale unsaturated zone flow model uses the dual-continuum approach for flow through both the fractures and matrix (Section 2.3.2). The dual-continuum formulation consists of overlapping interacting fracture and matrix domains so that there are separate fracture and matrix

properties at each location in the domain. This approach includes the effects of fast-flow paths and allows for fracture–matrix coupling because flow is modeled in two interacting continua (fracture and matrix), with each continuum assigned its own spatially variable hydrologic properties, such as permeability and porosity (SNL 2007b, Section 6.1.5.3). In general, the fractures are modeled as part of a highly permeable continuum having low porosity, while the matrix is modeled as a much less permeable continuum having higher porosity than the fracture continuum. Major faults are included explicitly in the unsaturated zone radionuclide transport process and abstraction models. In fault zones, fracture density and permeability are higher than in the rest of the model; this enables faults to act as preferential flow paths in parts of the model. Because the unsaturated zone radionuclide transport process model is consistent with the site-scale unsaturated zone flow model, it includes the same flow-related limitations and uncertainties (Section 2.3.2.4.2) (SNL 2007b, Section 6.8.3.1).

Fracture–matrix interaction is represented using the active fracture model (Liu, Doughty et al. 1998; SNL 2007b, Section 7.6). The active fracture model, developed within the context of the dual-continuum approach, is based on the reasoning that, because of fingering flow, only a portion of fractures in a connected, unsaturated fracture network contribute to liquid water flow, while other fractures are simply bypassed. The portion of the connected fractures that actively conduct water are called active fractures. As such, the active fracture model merges the continuum approach and a flow-focusing concept to model fracture flow. Inactive fractures are filtered out in modeling fracture–matrix interaction and flow in the fracture continuum (SNL 2007a, Section 6.1.2).

The ground surface of Yucca Mountain is taken as the model's top boundary, and the water table is taken as the model's bottom boundary. The bottom boundary (water table) is assigned a fixed water pressure. Spatially varying net surface infiltration is used as the boundary conditions for the top boundary (SNL 2007a, Section 6.1.3).

The approach described above leads to a reasonable representation of the relative importance of those fracture and matrix flow components that are included in the unsaturated zone radionuclide transport process and abstraction models (SNL 2007b; SNL 2007a).

Flow in fractures is typically much faster than flow in the matrix, leading to much shorter radionuclide transport times in fractures than in the matrix. The characteristic flow behavior in each of the major hydrogeologic units shown schematically in Figure 2.3.2-3 is supported by extensive field observations and modeling studies. This conceptual understanding was the basis for the development of the site-scale unsaturated zone flow model (BSC 2004a, Section 6.1).

The repository resides within the TSw unit (SNL 2007b, Section 6.1.1). The spatially and temporally damped fluxes from the PTn flow into the fractures of the TSw, where the flow becomes focused into fewer fractures as it approaches the repository horizon. Section 2.3.2.4.1.2.4.6 describes the distribution of calculated percolation fluxes at the repository level and provides the percentages of flux in fracture–matrix flow versus fault flow. Table 2.3.2-7 provides these results in tabular form. Flow behavior below the repository is especially important for calculating radionuclide transport from the repository horizon to the water table because transport paths follow the pattern of water flow. The main hydrogeologic units below the repository are the TSw, CHn, and CFu units. The CHn and CFu units have vitric and zeolitic zones that differ in their degree of hydrothermal alteration and associated hydrologic properties. The zeolitic rocks have low matrix

permeability and some fracture permeability; consequently, a relatively small amount of water may flow through the zeolitic units, with most of the water flowing laterally in perched water bodies and then vertically down faults to the saturated zone (SNL 2007b, Section 6.1.1).

The perched-water zones, which have been reported in seven boreholes within the lower portion of the TSw unit and the upper portion of the CHn unit, are a prevalent feature of the unsaturated zone below the repository (SNL 2007a, Section 6.2.2.2). As discussed in Section 2.3.2.3.4, geochemical analyses of perched water below the repository horizon yield ^{14}C dates ranging from 3,300 to 11,000 years. These ages can be reconciled with the observations of fast pathways in the ESF by recognizing that the fast pathways are expected to conduct only a small portion of the total flow. The perched-water bodies were found primarily in the northern part of the repository area, where lower-permeability, sparsely fractured zeolitic rock units predominate. The occurrence of perched water suggests that certain layers of the lower TSw (e.g., the basal vitrophyre) and the upper zeolitic CHn serve as barriers to vertical flow. On the other hand, similar to the PTn unit, the vitric units have relatively high matrix porosity and permeability, and matrix flow dominates (Section 2.3.2.2). Test results within the CHn at the Busted Butte underground facility show that water flow and radionuclide transport occur mainly within the matrix of the CHn, implying that fracture flow is limited in this unit (BSC 2004c, Section 6.13).

Major faults may have the potential to significantly affect the unsaturated zone flow processes at Yucca Mountain. Fault properties are variable and generally controlled by deformational processes occurring during displacement, by rock type, and by stratigraphic displacement. A fault is modeled as a localized, fast-flow conduit for water. Fracture–matrix interaction in faults is treated using the same approach as for fractured rock. However, fracture properties in fault zones differ from the fracture properties in the general fractured rock mass. Matrix properties in the faults are the same as in the fractured rock mass. Low-permeability layers or perched water zones at the base of the TSw and in the CHn may laterally divert a considerable amount of flow to major faults, which may focus flow downward to the water table. However, it is also possible that alteration within or along faults in the CHn and CFu reduces their permeability, increasing water transport times from the TSw to the water table. Nevertheless, to be conservative, faults have been treated as localized fast flow paths in the site-scale unsaturated zone flow model (see Section 2.3.2.4.2.1.4 for additional details) (SNL 2007a, Section 6.6).

The site-scale unsaturated zone flow model is used to generate 16 unsaturated zone flow fields based on climate and infiltration evaluations (Section 2.3.2). Because these 16 flow fields span the range of current and expected long-term future climate conditions, they are used directly as the representation of flow in the TSPA. These flow fields are for (1) present-day conditions that persist for 600 years, followed by (2) a warmer and much wetter monsoon climate for 1,400 years, followed by (3) a glacial-transition climate that is cooler and wetter than present-day conditions for 8,000 years, followed by (4) a long-term average condition for the remaining 990,000 years. The different climates identified for the first 10,000 years are used to quantify infiltration and deep percolation rates for these time periods. A specific climate is not specified for the final 990,000 years because proposed 10 CFR 63.342(c) specifies a distribution of deep percolation flux through the repository footprint for this time period ranging from 13 to 64 mm/yr. Using the results for the percolation flux through the repository footprint from the simulations for the first 10,000 years, and the correlation between infiltration and percolation that comes out of those analyses, the infiltration rates are then established for the final 990,000 years in a manner in which

the percolation fluxes prescribed by the proposed regulations can be attained (see Section 2.3.2.3.5.1 for details). For each of these four time periods, there are four uncertainty cases resulting in a total of 16 scenarios (SNL 2007a). The 16 flow fields generated by the site-scale unsaturated zone flow model are used in the TSPA model to simulate transport of radionuclides in the unsaturated zone, as illustrated in the information flow diagram in Figure 2.3.8-1 (SNL 2008a, Section 6.5.1 in Addendum 1).

2.3.8.4.2 Alternative Conceptual and Numerical Models of Unsaturated Zone Radionuclide Transport

Because water flow is the radionuclide transport mechanism in the unsaturated zone and the medium in which flow occurs consists of both fractures and unfractured but porous matrix, the conceptual transport model is based on a concept of fracture–matrix interaction as represented in the dual-permeability model. At the site scale, other conceptual models have been considered and tested. These include single-porosity models, effective continuum models, and dual-porosity models. Single-porosity models could not be supported as realistic for Yucca Mountain because they represent only the rock matrix, under the assumption that water flow is confined to the rock matrix as a result of capillary forces. However, interpretation of data related to the infiltration and percolation rates in the unsaturated zone at Yucca Mountain indicates that the rock matrix is not sufficiently permeable to conduct this flux in many of the hydrogeologic units. Therefore, flow in both fractures and matrix is implied. The effective continuum model allows for flow in both fractures and matrix; however, this model presumes thermodynamic equilibrium between the fractures and rock matrix. The assumption of thermodynamic equilibrium between the fractures and matrix cannot be supported and would be nonconservative with regard to transport behavior. The dual-porosity model allows for nonequilibrium flow and transport behavior between the fractures and rock matrix, as does the dual-permeability model. However, unlike the dual-permeability model, the dual-porosity model assumes that water in the rock matrix flows only in one dimension normal to the fractures, and large-scale flow only occurs in the rock fractures. Measurements on rock from Yucca Mountain show that the rock matrix is permeable (see Table 2.3.2-3) and that gravitational and capillary forces result in flow through the matrix. In some units in the unsaturated zone, such as the vitric portions of the Calico Hills Formation, downward flow and transport are expected to be primarily through the rock matrix as a result of the high permeability of the matrix in these units. Field evidence for the prevalence of matrix-dominated flow in this unit is presented in the description of the results of the Busted Butte tests in Section 2.3.8.4.4. Therefore, the dual-porosity model is not appropriate for Yucca Mountain (Doughty 1999).

Fracture–matrix interaction can be evaluated using three mathematical representations: (1) dual-permeability (dual-k) model, which uses a coarse grid; (2) multiple interactive continua (MINC) models (Pruess and Narasimhan 1985), which use a more refined gridding scheme; and (3) particle-tracking models. In the dual-k model, fracture–matrix interaction is approximated by a single grid in the fractures connected to a single grid in the matrix. Such a representation cannot resolve steep gradients in the matrix, particularly near the fracture–matrix interface, so the dual-k model tends to underestimate fracture–matrix interaction. In the MINC method, the steep gradients at the matrix fracture surface are resolved by subgridding the matrix blocks in an appropriate number of cells. The MINC behavior is expected to result in slower breakthrough curves (as the enhanced fracture–matrix interaction allows for increased diffusion), longer contact times, and more effective sorption (in sorbing media–solute systems). The particle-tracking approach used in

the TSPA model computes transport based on routing particles through the computational grid and represents fracture–matrix interaction using a travel time transfer function methodology (SNL 2008a, Section 6.4.3; BSC 2004a, Figure 6-7). Both a dual-k version and a version that is closer to that of the MINC approach are available in the particle tracking module used in FEHM for the abstraction model.

Figure 2.3.8-24 shows the results of simulations using the three numerical representations. The dual-k model as represented in T2R3D and EOS9nT has been found to be capable of representing transport in fractured rock (Section 2.3.8.4.4). The FEHM-based dual-k particle tracking model yields a very similar result. By contrast, the MINC model and the FEHM discrete fracture model yield later first arrival of mass at the water table. Furthermore, the MINC method is too computationally intensive for practical implementation over the site-scale unsaturated zone domain. Given that the dual-k approach has been subjected to extensive model validation and leads to a more conservative representation of unsaturated zone transport, this approach was selected for use (SNL 2007b, Section 6.19).

The conceptual model of transport in the unsaturated zone and its numerical implementation have undergone a continual process of improvement and enhancement. Transport studies indicate there is a wide range of groundwater or tracer transport times associated with different infiltration rates, radionuclide sorption capacities, and the wetted fracture-matrix interface area. The two most important factors affecting transport times in the unsaturated zone are found to be the percolation flux and sorption effects (SNL 2007b, Section 6.6.5).

2.3.8.4.3 Description of the Unsaturated Zone Radionuclide Transport Process Model

For a large, three-dimensional, mountain-scale domain, the fractured rock is conceptualized as a heterogeneous, dual-permeability system in which the distinct hydraulic and transport behavior of fractures and matrix is described using separate properties (SNL 2007b, Section 6.7). This conceptualization allows the description of the complex unsaturated zone flow field where fracture flow plays a dominant role, as described in Section 2.3.2.

The grid, conditions, and calibrated hydraulic parameters used in the unsaturated zone radionuclide transport simulations are identical to those used for the analysis of flow in the development of the site-scale unsaturated zone flow model (SNL 2007a, Section 6.1). These parameters correspond to the permeability barrier model, also called the conceptual model of perched water, which uses the calibrated perched-water parameters (for fractures and matrix in the northern part of the model domain) and modified property layers (including the tsw38, tsw39, ch1z, and ch2z layers) (Table 2.3.2-2), where the lower basal vitrophyre of the TSw overlies the zeolites of the CHn (SNL 2007a, Section 6.2.2.2). A two-dimensional plan view of the grid with the locations of the repository cells is shown in Figure 2.3.2-10. All three-dimensional transport simulations are based on steady-state flow fields developed for present percolation conditions (SNL 2007a, Section 6.5.2).

In the abstraction model, radionuclides are released from nodes corresponding to the repository location (SNL 2008a, Section 6.5.15 in Addendum 1). These nodes were grouped into bins (zones) that shared common percolation rate ranges, to be compatible with the TSPA model, in which radionuclide releases are computed as a function of the percolation rates at the repository horizon.

Percolation rates at the repository are divided into five bins, chosen based on the cumulative probability of percolation for the 12 flow fields (three different climate periods: Present-day, Monsoon and Glacial transition; each climate period is categorized with 4 infiltration maps: 10%, 30%, 50% and 90%). Figure 2.3.8-25 shows a representation of the repository nodes colored by percolation bin for the glacial transition flow field based on the 10th percentile infiltration case. In the abstraction model, this representation is used for subdividing the repository into bins of similar percolation flux.

The unsaturated zone radionuclide transport process model (SNL 2007b, Section 6) accounts for all major known transport processes, including advection, matrix diffusion, hydrodynamic dispersion, linear equilibrium sorption, radioactive decay and tracking of daughter products, colloid filtration, and colloid-assisted solute transport (SNL 2007b, Section 6.1.2).

Radionuclides would be released at the base of the drift as dissolved species or associated with colloids (Section 2.3.7.12). The form of the mobilized radionuclides (i.e., dissolved or colloids) affects the magnitude of matrix diffusion (which is a function of the molecule and colloid size and electrical properties), sorption and filtration affinity for the unsaturated zone rocks, and pore-size exclusion (i.e., straining, which is for colloids only).

Data for the description of the sorption behavior of radionuclides potentially important to the TSPA are taken from the analysis of laboratory experiments (Section 2.3.8.3.1), while a wide range of possible filtration parameters is used to address the lack of experimental data. The diffusion coefficient, D_0, of solutes was obtained from the literature (Lide 1992, pp. 5-111 and 5-112), while the Stokes-Einstein equation (Bird et al. 1960, p. 514) is used to estimate the colloidal diffusion coefficients.

The following radioactive solutes were included in the unsaturated zone radionuclide transport process model (SNL 2007b, Sections 6.7.4 and 6.13):

- ^{99}Tc: a nonsorbing species
- ^{237}Np, ^{235}U, and ^{233}U: moderately sorbing species
- ^{241}Am, ^{239}Pu, ^{231}Pa, ^{229}Th, ^{226}Ra, ^{90}Sr, and ^{135}Cs: strongly sorbing species.

There are four additional radioisotopes listed in the waste inventory in Table 2.3.7-4: ^{14}C, ^{129}I, ^{227}Ac, and ^{245}Cm. Similar to ^{99}Tc, both ^{14}C and ^{129}I are treated as nonsorbing species (SNL 2008a, Table 8-2 in Addendum 1). Although they were not explicitly considered in the unsaturated zone radionuclide transport process model development, they are represented in the unsaturated zone radionuclide transport abstraction model as nonsorbing. ^{227}Ac is included in TSPA for dose calculations, but not transported through the unsaturated zone or saturated zone models (see Section 2.4.2.3.2.1.10). However, as a result of its short half-life (22 years) and strong sorption characteristics (SNL 2007e, Tables 4-3 and 6-3), it is transported to the accessible environment via its radionuclide precursor, ^{231}Pa, which has a half-life of 32,800 years and is not as strongly sorbing (SNL 2007e, Tables 4-3 and 6-3). ^{245}Cm is included in the radionuclide inventory as a precursor to ^{241}Am. ^{245}Cm is not considered as a radionuclide for transport because it is in the same solubility and sorption class (i.e., medium solubility and high sorption) as ^{241}Am (SNL 2007e, Table 6-3), and the initial inventory of ^{245}Cm is negligible compared with ^{241}Am (SNL 2007g). Therefore, ^{245}Cm is only included as a precursor to ^{241}Am to define the appropriate initial

inventory of ^{241}Am (Section 2.3.7). Similarly, decay chains starting from ^{243}Am, ^{242}Pu, and ^{238}Pu were not included in the unsaturated zone radionuclide transport process model (SNL 2007b, Section 6.7.4) because the process model was not used for dose calculations. However, these decay chains are included in the unsaturated zone radionuclide transport abstraction model (SNL 2008a, Table 6-25 in Addendum 1). Additionally, for the three-dimensional simulations of continuous release, all the important members in the decay chains of ^{241}Am and ^{239}Pu were considered as follows (Pigford et al. 1980):

- ^{241}Am decay chain: $^{241}\text{Am} \rightarrow {}^{237}\text{Np} \rightarrow {}^{233}\text{U} \rightarrow {}^{229}\text{Th}$
- ^{239}Pu decay chain: $^{239}\text{Pu} \rightarrow {}^{235}\text{U} \rightarrow {}^{231}\text{Pa}$.

Only the most important members of the radioactive chain are included in these decay equations, which omit decay products with short half-lives because they have a minor effect on the relative abundance of the decay products. Alpha decay is the decay mode of all the members in the ^{241}Am and ^{239}Pu chains (SNL 2007b, Section 6.7.4).

Waste-form colloids were investigated in the process model (SNL 2007b, Section 6.18) because these colloids result in radionuclide transport times that are shorter than other colloid transport forms or aqueous radionuclide transport. Colloid-facilitated radionuclide transport differs from aqueous radionuclide transport because colloids are larger than aqueous radionuclides and because colloids interact differently with the rock than aqueous radionuclides. Colloids may be excluded from pores that aqueous radionuclides may enter as a result of the larger size of colloids as compared with aqueous species. Colloid size also affects colloid diffusion and advection rates. In the process model, colloid diffusion is treated using the Stokes-Einstein model to account for the effects of colloid size and results in lower diffusion rates for colloids than aqueous radionuclides. Advection is enhanced for larger colloid sizes due to preferential transport of larger colloids in higher-velocity water pathways. The analysis considers four different colloid sizes, 6, 100, 200, and 450 nm, to evaluate the effects of colloid size. Radionuclides attached to colloids are effectively prevented from sorbing onto rock surfaces. In the abstraction model, colloid diffusion is conservatively assumed to be negligible (SNL 2008a, Section 6.4.5). Sorption processes affecting colloid-facilitated radionuclide transport are a function of the interaction of the colloid with the rock surface. Colloid interactions with the rock surface are treated as a linear kinetic process with the colloid attachment rate proportional to the aqueous colloid concentration and detachment rate proportional to the filtered concentration on the rock surfaces. Colloid attachment and detachment processes are investigated for both the matrix and fractures. In the abstraction model, an equilibrium approach to colloidal retardation is taken, using data available from field tests to constrain the uncertain parameters.

2.3.8.4.4 Building Confidence in the Unsaturated Zone Radionuclide Transport Process Model

Building confidence in the unsaturated zone radionuclide transport process model is achieved through corroboration and comparison with data from the field tests at Busted Butte (Section 2.3.8.3.3.1), Alcove 8–Niche 3 (Section 2.3.8.3.3.2), and Alcove 1 (Section 2.3.8.3.3.3). To compare process model predictions with the results of field tests, it was necessary to calibrate the flow-related hydraulic properties to the test-bed flow behavior. Transport parameters were established using data available from other sources, including laboratory tests and external

publications. As discussed in the following sections, the process model qualitatively reproduced and confirmed the observed transport behavior of tracers used as radionuclide analogues.

2.3.8.4.4.1 Busted Butte Phase 1A Test

The purpose of this calibration and verification was to demonstrate that the unsaturated zone radionuclide transport process model could predict transport behavior in the CHn vitric rock. A fluorescein tracer test was used to calibrate the model by establishing the advective transport component, and a bromide tracer test was used to verify transport predictions. The advective component was established by injecting fluorescein into the Ttptv1 unit and observing the subsequent flow and transport in the Tptpv1 and Tac units. The Phase 1A test is described in Section 2.3.8.3.3.1.1. Model predictions were verified by simultaneously injecting bromide into the Ttptv1 and observing the subsequent flow and transport in the Tptpv1 and Tac units. The underlying geologic model was mathematically treated as a homogeneous and anisotropic unfractured rock matrix with the properties of the Tptpv1 and Tac units (Table 2.3.2-2). The results of the fluorescein tracer tests (Figure 2.3.8-11) were compared with the results of the mathematical calculations of transport (Figure 2.3.8-26). A comparison of the two figures shows qualitative agreement between the observations and predictions. As shown in these figures, the model predicted several important features of the observed tracer plume: its ellipsoidal shape, the compression of the lower half of the plume that results from its proximity to the less permeable Tac, uniformity at the scale of observation, and its vertical dimension (SNL 2007b, Section 7.2.4.1.2.3). Note also from the figures that the model results were consistent with the observed absence of stringers and other features indicative of fractures (SNL 2007b, Section 7.2.4.1.2.3). These results provide justification for treatment of the CHn vitric formation as a single continuum porous medium (SNL 2007b, Section 7.2.4.1.2.4).

The unsaturated zone radionuclide transport process model was verified by comparing predictions of bromide concentrations with field data. These predictions were made using the calibrated properties obtained in the fluorescein simulation (Table 2.3.8-3) and the known diffusion coefficient (D_0) of bromide. Figure 2.3.8-27 shows the numerically predicted bromide distribution at a mineback distance of 0.9 m and the field measurements of the bromide concentration, which were obtained from samples taken during the mineback (SNL 2007b, Section 7.2.4.1.2.4).

The unsaturated zone radionuclide transport process model reasonably predicted the observed concentrations in the central part of the plume along the horizontal axis. Toward the outer extent of the plume, the differences between observed and predicted concentrations likely result from inhomogeneities in the rock. These differences are magnified by the steepness of the concentration gradient. The good agreement between observations and numerical predictions supports the applicability of the unsaturated zone radionuclide transport process model to the CHn vitric rock (SNL 2007b, Section 7.2.4.1.2.4).

2.3.8.4.4.2 Busted Butte Phase 1B Test

The purpose of this test was to acquire data on fracture–matrix interactions in the TSw. The results were used to calibrate fracture properties for the Phase 2 analysis. The Busted Butte Phase 1B test is described in Section 2.3.8.3.3.1.2. Of the five tracers injected during Phase 1B, the transport of two nonsorbing tracers having different diffusion coefficients, 2,6-DFBA and bromide, were

analyzed to determine the influence of diffusion on transport. The 2,6-DFBA data were used for calibration, and the bromide data were used for verification. The same model assumptions on model design and the grid used in the simulation of Phase 1A were used in the Busted Butte Phase 1B test (SNL 2007b, Section 7.2.4.1.3).

Figure 2.3.8-28 shows that the breakthrough curve for 2,6-DFBA can be reproduced by calibrating the model with the observed data. The shape of the breakthrough curve is consistent with the visual observation that the system did not exhibit fracture flow behavior during the Phase 1B test, despite the presence of a known fracture intersecting the two boreholes. This consistency supports the validity of the unfractured medium approach used in the simulations (SNL 2007b, Section 7.2.4.1.3.3).

The calibrated parameters that are based on the 2,6-DFBA transport analysis were used to predict bromide transport in Phase 1B of the Busted Butte test (Table 2.3.8-4). A comparison of the measured and numerically predicted breakthrough curves for bromide in Figure 2.3.8-29 shows good quantitative agreement (SNL 2007b, Section 7.2.4.1.3.4).

2.3.8.4.4.3 Busted Butte Phase 2C Test

The purpose of the Busted Butte Phase 2 tests was to calibrate and verify the unsaturated zone radionuclide transport process model on a large scale. The Busted Butte Phase 2 tests are described in Section 2.3.8.3.3.1.3. The calibration and verification is limited to Phase 2C, which yielded the best-quality data. Because of the relatively short spacing between injection boreholes and the long injection period of 695 days, the injection was assumed to be uniform along the three injection boreholes (boreholes 18, 20, and 21 in Figure 2.3.8-12). While this assumption of uniformity introduces a slight inaccuracy, the effect is rather small, is limited to the very early stages of injection (i.e., when flow is spherical rather than quasi-cylindrical at the later stages), and decreases over time. This assumption of uniformity also allowed the system to be modeled using a two-dimensional grid, which results in higher spatial resolution (SNL 2007b, Section 7.2.4.1.4.1).

Based on a review of concentration data for all of the tracers injected, the bromide and lithium tracers were selected for calibration and verification analysis. The use of bromide and lithium offered two advantages, which caused them to be favored: (1) they registered relatively strong and generally consistent signals in borehole 16, and (2) they were injected as a solution of lithium bromide with equal moles of lithium and bromide in the system, which provided an additional mass-balance constraint for verification (SNL 2007b, Section 7.2.4.1.4.1).

The process of calibration was intended to determine the main hydraulic parameters of the medium under consideration. The calibrated hydraulic parameters were then used to validate and enhance confidence in the unsaturated zone radionuclide transport process model using transport parameters available from other independent sources. To accomplish the task, two separate data sets of tracer concentrations were used from each of the three test phases, of which one data set was used for calibration and the other for validation. This is an appropriate approach because the transport behavior of the two tracers used for calibration and validation was completely independent (i.e., there is no sorption-related correlation). If a particular tracer was known (or expected) to have a sorbing affinity for the tested rock, the corresponding data set was used for the calibration effort, which included an estimation of the tracer's transport parameters (i.e., the K_d distribution coefficient

and tortuosity) in addition to the hydraulic parameters. In this case, lithium is sorbing, and bromide is nonsorbing. The nonsorbing tracer was used for validation because it is more demanding as a conservative species, and it has a well-known (and independently determined) K_d (zero) and molecular distribution coefficient (SNL 2007b, Section 7.2.4.1.4.1).

Data collected from the collection boreholes showed that only the observations from borehole 16 provided signals that could be interpreted. The data from borehole 16 are useful because this borehole is closest to the horizontal plane of the three injection wells, and it registered the strongest signals in terms of tracer concentrations. Borehole 16 extends along a horizontal plane that roughly coincides with the Tptpv2–Tptpv1 interface and is about 0.6 m below the plane of the injection boreholes and perpendicular to their main axis (SNL 2007b, Section 7.2.4.1.4.1).

Preliminary simulations indicated that matrix diffusion and lithium sorption data would be needed to describe the transport of bromide and lithium. This observation required that the transport be modeled by a fracture–matrix system, as opposed to a porous medium without fractures or one that considered transport only in fractures. A dual-permeability model was employed with a fine-resolution, two-dimensional grid (SNL 2007b, Section 7.2.4.1.4.2).

For the lithium calibration process, the data for the periods at 337 and 440 days were used. Because of the sorbing behavior of lithium, the data for the periods up to 337 days were marked by very low concentrations, significant variability, and the corresponding uncertainty. For time periods after 440 days, lithium concentrations started decreasing, followed by periods of concentration increases. This is because the pad concentrations were diluted as a result of the hydraulic characteristics of the pad. Therefore, the most accurate data are those collected between the periods of 337 and 440 days. For the bromide verification process, the data for the period between 125 and 183 days were used because bromide does not sorb and, compared to lithium, has a faster breakthrough (SNL 2007b, Section 7.2.4.1.4.2).

Figure 2.3.8-30 shows the measured and the numerically calculated lithium distributions along the collection borehole. These distributions are based on the calibrated parameters shown in Table 2.3.8-5. The locations of the peaks, the peak concentration values, and the concentration distributions are comparable (SNL 2007b, Section 7.2.4.1.4.3).

Figure 2.3.8-31 shows the measured and numerically predicted bromide distribution along the collection borehole. This distribution was obtained using the calibrated properties from the analysis of the lithium data and from the known D_0 and sorption of zero for bromide. The comparison of the predictions and the observed data shows good correlation between the unsaturated zone radionuclide transport process model and the locations and concentrations of the peaks, and the distributions of concentration (SNL 2007b, Section 7.2.4.1.4.4).

Inspection of the simulated bromide distribution in Figure 2.3.8-31 reveals that the numerical simulation accurately predicts the location and magnitude of the concentration peaks but exhibits narrower peaks and indicates a deeper trough compared to the measurements between the second and third peaks. More specifically, the measured concentration of bromide is more uniform along the collection borehole axis than predicted by the numerical simulation, indicating a system that is more dispersive than the advective one described by the simulation. This is expected because small-scale heterogeneities present in all natural systems will enhance dispersion of tracer

concentrations relative to a homogenous system, as in the model. Such effects are not important for models predicting system performance, however, because lateral dispersion has little effect on the radionuclide mass arrival rates at the water table (SNL 2007b, Section 7.2.4.1.4.4).

The differences between the predicted values and measured data are attributed to the effects of the collection pad on transport through the host rock. The properties of the collection pad, characterized by high permeability, porosity, irreducible water saturation, and capillary pressure, differ significantly from those of the host rock. Tracer-carrying fracture flow that first reaches the collection pad arrives at distinct points (i.e., the points where the fractures intercept the borehole) and is quickly redistributed on the initially dry pad. Therefore, the tracer in the pad is more uniform than the one in the overlying rock, and the samples indicate a more diffusive system. Under these conditions, it is expected that the most accurate data will be at early times and at locations roughly under the injection boreholes (i.e., where the effects of the pad are minimized) (SNL 2007b, Section 7.2.4.1.4.4).

2.3.8.4.4.4 Alcove 8–Niche 3 Test

This section discusses results of simulations performed to evaluate the relative importance of matrix diffusion on radionuclide transport in the unsaturated zone (SNL 2007b, Section 7.3). The purpose of modeling the Alcove 8–Niche 3 test was to demonstrate that the unsaturated zone radionuclide transport process model could predict transport behavior. For long flow paths, the advective transport is affected by fracture-matrix interaction, which is shown to be an important retardation mechanism that delays the movement of water and tracers through the unsaturated units (BSC 2004c, Section 6.12). A description of the test bed and test configurations are given in Section 2.3.8.3.3.2.

2.3.8.4.4.4.1 Alcove 8–Niche 3 Fault Test

The calibrated flow field (SNL 2007b, Section 7.3.3.1) from the seepage data of the Alcove 8–Niche 3 test was used in the simulation of tracer transport processes. A three-dimensional numerical grid was constructed for the simulation. The fault was represented as a vertical fracture, and surrounding fractured rock is approximated as a dual-continuum system consisting of overlapped, interacting fracture and matrix continua. A fine grid in the vicinity of the fault provided sufficient resolution for flow and transport fracture-matrix interaction processes such that the MINC gridding method used for the large plot test (see below) was not needed. The results of the transport simulations are compared with the Alcove 8–Niche 3 tracer tests for verification of the matrix diffusion model (SNL 2007b, Section 7.3).

The role of matrix diffusion was examined by conducting transport simulations for tracers (i.e., bromide and pentafluorobenzoic acid) having different molecular diffusion coefficients. Different values were chosen for the fracture-matrix interface area to determine the magnitude of the impact of this parameter on fracture-matrix interaction. Changes in the interface area would not significantly alter the flow field during the period of the tracer test because the flow field is calibrated. Because tracers were introduced into the applied water at about 200 days after the percolation started, the matrix near the fault was almost saturated during the tracer test, and the matrix imbibition was insignificant. High saturation would limit the effects of interface area on the flow field by limiting matrix imbibition, but would not limit the effects of interface area on matrix

diffusion. This supports the modeling approach used. The transport simulations also assumed zero dispersivity because the modeling indicated that the transport results may be insensitive to this parameter (Liu, Haukwa et al. 2003; SNL 2007b, Section 7.3.3.2).

Figure 2.3.8-32 provides a comparison of simulated breakthrough curves at the niche to the observed data. The simulated breakthrough curve for the original fracture-matrix interface area, which was estimated from the fracture data, exhibits a much larger peak concentration value but only slightly earlier arrival times compared to the field data. The simulations were found to match the data more closely when the interface area was increased by a factor of 45; however, the concentration at a given time for the bromide tracer is generally underestimated by the model, while the simulated pentafluorobenzoic acid concentrations are very close to the data (SNL 2007b, Section 7.3.3.3).

The improved fit from the increased interface area is a result of the rough fracture walls, which cause the actual interface areas between fractures (and faults) and the matrix to be larger than the values calculated using flat fracture walls. In addition, the fault zone may include a great number of crushed matrix blocks that have smaller sizes than the fracture spacing in a nonfault zone. These crushed matrix blocks can make a significant contribution to the matrix diffusion within the fault but are not considered in the numerical grid, where the fault is simply treated as a vertical fracture. Finally, the factor of 45 is consistent with the range of values that Neretnieks (2002) reported on transport studies in different media (SNL 2007b, Section 7.3.3.3).

2.3.8.4.4.4.2 Alcove 8–Niche 3 Large Plot Test

The calibrated flow field (BSC 2006a, Section 7.3) from the seepage data of the Alcove 8–Niche 3 test was used in the simulation of tracer transport processes. A three-dimensional numerical grid was constructed for the simulation. Modeling of the Alcove 8–Niche 3 large plot test used a MINC approach. The numerical grid in the Alcove 8–Niche 3 test differs from the grid used for performance assessment calculations because of the difference in time scales for these two analyses. Accurate simulation of the Alcove 8–Niche 3 test requires finer grid discretization near the flowing fractures than does the Mountain-scale unsaturated zone transport model. The transients associated with the Alcove 8–Niche 3 test mean that the simplification of a single-node matrix connection in the dual-permeability grid would not be suitable. The steady-state flow and slower transients in radionuclide concentration associated with repository performance analysis are appropriately modeled using a dual-permeability grid (SNL 2007b, Section 6.1.5.3). Even in the context of repository performance calculations, however, analyses indicate that the dual-permeability gridding scheme is conservative relative to the MINC gridding scheme (Section 2.3.8.4.2) (Liu, Haukwa et al. 2003). The Alcove 8–Niche 3 test was performed under flow conditions that are highly accelerated, as compared with natural flow conditions. This leads to greater fracture-matrix disequilibrium in the associated transport process than are likely to be representative of repository performance conditions, except for the zones of highest percolation. Under these conditions, the more detailed representation of fracture-matrix interaction available in the MINC model is needed to simulate the test results at this scale.

Model predictions for tracer transport indicated that peak breakthrough concentrations would occur between 30 to 90 days after application of the tracer, with peak concentrations generally between about 2 to 20% of the applied concentrations (BSC 2006a, Section 6.2.3). However, as discussed in

Section 2.3.8.3.3.2.2, no tracer concentrations above background or detection limits were observed in Niche 3 until the infiltration subplots were scrubbed 132 days following the tracer application. The observed concentrations following the subplot scrubbing were only significant for iodide and 2, 4 DFBA from subplots 1 and 2, reaching about 5 percent relative concentration. None of the other tracers from subplots 3 through 12 were observed at sufficiently high concentration levels to definitively identify breakthrough.

Seepage into Niche 3 during the period following tracer application can be seen in Figure 2.3.8-23. The general decline in seepage, combined with the more stable percolation rate into Alcove 8 over this time period (Figure 2.3.8-22) suggests that flow between Alcove 8 and Niche 3 was being redirected. Whether or not this re-direction occurred closer to Alcove 8 or Niche 3 remains unresolved. The change in flow patterns may have been a result of either colloid migration and plugging of flow pathways or by the build-up of biofilms on the infiltration subplots. Alternatively, the general expansion of the flow field over time with the wetting of the test bed may have led to the gradual activation of new flow paths resulting in reduced flow to Niche 3.

The observed transport behavior was found to be consistent with the existing model if the diffusion coefficient is scaled by the factor of 45 as found in fault test (Section 2.3.8.4.4.4.1). In this case, the enhanced diffusion leads to simulated tracer concentrations that are below background and/or detection limit levels. Furthermore, the simulated peak concentrations occur at roughly day 600 of the test, or approximately 40 days after tracer application (BSC 2006a, Figures 6.3-3 through 6.3-5), which is beyond the observation period following tracer application in Niche 3.

2.3.8.4.4.4.3 Implications of Alcove 8–Niche 3 Tests

The Alcove 8–Niche 3 testing program provided valuable information relevant to the establishment of the appropriate conceptual model for radionuclide transport through the unsaturated zone, and the development of parameter uncertainty ranges. The fault test was used to confirm that the processes of fracture transport and matrix diffusion apply to the unsaturated zone. This conclusion, obtained by observing the breakthrough curves of two tracers with different diffusion coefficients, parallels that reached in the interpretation of tracer tests in the saturated zone at the C-Wells complex (Section 2.3.9.3.2.1). Despite the fact that the driving forces for water flow are different in the two cases (gravity-driven flow in the unsaturated zone, versus low-gradient horizontal flow in the saturated zone), the two testing programs achieved a similar conceptual model result for transport, which lends credibility to both results.

Regarding the transport parameters related to diffusion that were obtained in the Alcove 8–Niche 3 tests, it was found to be necessary to apply an increase in the value of the effective fracture-matrix interface area by a factor of 45 in order to explain the data from the fault test. Similarly, the large plot test required an increase to explain the observations, although the results are less definitive. The fact that this increase is needed must be viewed with respect to the understanding that several parameters applied to a fracture transport and matrix diffusion model are uncertain and variable. Among these are geometric parameters such as the fracture aperture and spacing, and physicochemical parameters such as the tortuosity coefficient for diffusion. In the abstraction model, geometric parameters and the diffusion coefficient are uncertain parameters, with values that, when applied in combination, result in uncertain behavior with respect to matrix diffusion (Section 2.3.8.5.2.4). Viewed in this light, the factor of 45 obtained in this field test interpretation can be thought of as one

value on the high end of the resulting distribution of effective matrix diffusion parameterizations from the stochastic realizations in the TSPA model.

The fact that the field observations and interpretation yielded more diffusion than was expected based on the estimated parameters is an indication that the TSPA analyses are conservative with respect to matrix diffusion in the unsaturated zone because increased matrix diffusion results in longer travel times to the water table for radionuclides travelling through fractures (Section 2.3.8.5.5.3). Nevertheless, as discussed below, the decision was made not to renormalize the matrix diffusion model to obtain greater fracture-matrix interactions, on the basis of Alcove 1 and Alcove 8–Niche 3 the field results obtained to date.

Ambiguities in the test results that preclude using the enhancement factor parameter directly in the TSPA compliance model include:

- Representativeness: the test locations and the specifics of the fracture systems tested at Alcove 8–Niche 3 and Alcove 1 may not be fully representative of conditions across the entire repository region.

- Difference in model grid resolution: direct transfer of parameters from one set of spatial and temporal scales and computational grid resolution to another is a source of uncertainty.

- High flux of the field tests: due to the high percolation rates employed in the tests, a larger number of fractures, including more fractures with small apertures, may be flowing than under natural conditions, leading to a greater level of matrix diffusion.

- Conceptual uncertainty: the reasons for the apparent increase in matrix diffusion with scale is the subject of active research, so the conceptual basis for assuming a scale dependence is not well developed.

In summary, the analyses support the conclusion that the TSPA model captures the effect of unsaturated zone matrix diffusion in a conservative way, but the level of confidence in the scale dependence of matrix diffusion is insufficient to incorporate the field results leading to a matrix diffusion enhancement factor directly into the TSPA.

2.3.8.4.4.5 Modeling of the Alcove 1 Test Results

This section discusses results of simulations performed to evaluate the relative importance of matrix diffusion on radionuclide transport in the unsaturated zone. The purpose of this calibration and verification was to demonstrate that the unsaturated zone radionuclide transport process model could predict transport behavior in a fractured, welded tuff analogous to tuffs comprising the repository host rock (Section 2.3.8.3.3.3). For long flow paths, advective transport is affected by fracture–matrix interaction, which is shown to be an important retardation mechanism that delays the movement of water and tracers through the unsaturated units (Liu, Haukwa et al. 2003).

Modeling of the Alcove 1 test results used a MINC approach because this methodology is better suited than the DKM for describing the transient flow and transport phenomena observed in the

Alcove 1 test. The MINC methodology also better represents the extent of fracture–matrix interaction than does the dual-k model approach (Section 2.3.8.4.2). This is a result of the matrix being further subdivided into several continua (Liu, Haukwa et al. 2003, Section 3.1). The Alcove 1 test was performed under flow conditions that are highly accelerated compared with natural flow conditions. This leads to much greater fracture–matrix disequilibrium in the associated transport process. The more detailed representation of fracture–matrix interaction available in the MINC model is needed to simulate the test results at this scale and for the accelerated test conditions.

The active fracture model (Liu, Doughty et al. 1998, pp. 2633 to 2646) was employed to describe flow and transport within fractures and between fractures and the matrix. Three matrix continua were used for developing the numerical grid (Liu, Haukwa et al. 2003, Section 3.1).

The hydraulic properties for fractures and the matrix are assumed to be homogeneously distributed within the model domain, as a result of data limitations. The fracture spacing was calculated using fracture-frequency data obtained from mapping studies in the ESF. The initial estimate for these properties is in Table 2.3.8-6 (Liu, Haukwa et al. 2003, Section 3.3).

The test consisted of two phases. Phase I was performed from March to August 1998 and Phase II was performed from January to June 1999 (Liu, Haukwa et al. 2003, Section 2). The seepage rate data for Phase I of the test were used to develop calibrated hydrologic properties, as shown in Table 2.3.8-7. The test data and model calibration predictions based on the Phase I portion of the test are shown in Figure 2.3.8-33 (Liu, Haukwa et al. 2003). Although the model reproduces the arrival times of three major peaks in the seepage rate observed in the Phase I seepage test, there are substantial differences between the simulated and observed seepage rate values at these peaks. While it is possible that the homogeneity assumption and the continuum approach underestimate the variability of seepage rates, another and possibly more important explanation is the simplicity of the model in representing the site conditions during the Phase I test (Liu, Haukwa et al. 2003, Section 4.2). The model is limited to isothermal conditions and single-phase unsaturated flow; however, the Phase I test was conducted from March to August 1998, and ambient air temperatures were relatively high in the later period of the test, which may have caused considerable vapor transport and evaporation (Liu, Haukwa et al. 2003, Section 4.2).

The Phase II test data, shown in Figure 2.3.8-33, were collected from January to May 1999. Despite the potential for evaporation in this period, test conditions were assumed to approximate isothermal, single-phase flow for the sake of simplicity (Liu, Haukwa et al. 2003, Section 4.2).

Figure 2.3.8-33 shows a comparison of the predicted seepage rates with the data for Phase II of the test. Properties calibrated against Phase I test data were used for the prediction. The comparison is fairly reasonable considering that a relatively limited match was obtained for the Phase I test using the inverse modeling. For the Phase II test, simulated seepage occurs earlier than the observed test data, and the simulated seepage rates are generally higher than the test data in the 350-to-380-day period (Figure 2.3.8-33). After 380 days, the model prediction improves, corresponding to the period when the system is very wet and actual matrix saturation values approximate the modeled results. More importantly, the percolation and seepage processes can be reasonably represented by the model. Therefore, a continuum approach is shown to be valid for capturing the complex flow processes in an unsaturated, fractured, porous medium, as shown in Figure 2.3.8-33 (Liu, Haukwa et al. 2003, Section 1). Since pore velocities in the matrix are generally small, the mechanical

dispersion is negligible. The calibrated hydrologic properties based on both Phase I and II seepage data (Table 2.3.8-8) were used in the simulation, which was developed by a second inversion based on data from both the Phase I and II seepage rate data (Liu, Haukwa et al. 2003, Section 4.1 and Table 1).

Figure 2.3.8-34 shows tracer transport simulation results obtained with T2R3D (Version 1.4) for two fracture-matrix interface areas, indicating that the breakthrough is very sensitive to the interface area. The tortuosity value is similar to the 0.70 matrix tortuosity suggested by Francis (1997, p. 5). Figure 2.3.8-35 shows breakthrough curves for selected combinations of dispersivity ranging from 0 to 30 m and tortuosity ranging from 0.5 to 0.75. The breakthrough curves are not sensitive to the fracture dispersivity value (Liu, Haukwa et al. 2003). Comparing results for the two tortuosity values, Figure 2.3.8-35 shows that the simulation is more closely matched with the tracer concentration data for a tortuosity value of 0.75. Nevertheless, considerable differences exist between the simulated and the observed tracer concentrations. An important finding from the simulations is that the tracer transport is sensitive to the matrix molecular diffusion coefficient and tortuosity, suggesting that matrix diffusion is an important mechanism for unsaturated zone transport. An improved match between the model and the data was obtained using a larger fracture–matrix interface area, which results in greater fracture–matrix interaction through diffusive transport. These results suggest that the existing formulation and parameterization methods lead to conservative predictions of transport (Figure 2.3.8-34). However, the increase in diffusion with scale observed here and in the Alcove 8–Niche 3 fault test were deemed to be not sufficiently well understood to warrant including this process directly in the TSPA model. In addition, the simulation result does not appear to be very sensitive to the fracture dispersivity, a reflection of the fact that the overall distribution of transport times is dominated by fracture–matrix interaction. Fracture–matrix velocity variations are the largest variations in the system. Dispersion caused by fracture–matrix interaction is explicitly represented in the model for fracture–matrix interaction, not in the dispersion coefficient. Therefore, the dispersion due to velocity variations that are strictly limited to the fracture continuum is insignificant (Liu, Haukwa et al. 2003, Section 4.3).

2.3.8.4.4.6 Other Data and Natural Analogues Used for Model Confidence

Additional confidence in the unsaturated zone radionuclide transport process model is provided by (1) analyzing field measurements of ^{14}C ages in gas samples, pore-water chloride concentrations in the ESF, strontium isotope data, and calcite deposition in fractures (SNL 2007a, Sections 6.5, 7.5, 7.6, and 7.7); and (2) evaluating similarities and differences between Yucca Mountain and a natural analogue (BSC 2004g, Section 10).

The ^{14}C ages in gas samples and pore-water chloride concentrations in the ESF are compared with outputs from the unsaturated zone radionuclide transport process model (SNL 2007a, Sections 6.5.1.1 and 7.5). Evaluation of ^{14}C ages and the validation modeling performed in *UZ Flow Models and Submodels* (SNL 2007a, Section 7.5) supports the conceptualization of flow focusing in fractures and fracture–matrix interaction. The chloride evaluation provides insight into flow mechanisms. Discussion of model comparisons with these data is given in Section 2.3.2.2.2. The calcite and strontium data are compared with outputs from the unsaturated zone radionuclide transport process model. These data support the conceptualization of fracture–matrix-interactions, as well as fractures as the main transport pathways in the repository host rock. The strontium data

also confirmed the model treatment of ion exchange for strontium and calcium in zeolitic rock (SNL 2007a, Section 7.6).

The term "natural analogue" here refers to a natural system in which processes similar to those expected to occur in a nuclear waste repository and surrounding area are thought to have occurred over long time periods (decades or longer), and large spatial scales (up to tens of kilometers) (BSC 2004g, Section 1.2). Natural analogues can provide descriptive information about the occurrence of relevant processes beyond the limitations of laboratory or field-scale experiments. Analogue studies thus comprise a unique aspect of building confidence in conceptual models and the process models developed from them (BSC 2004g, Section 1.3). To support unsaturated zone radionuclide transport models, analogues were analyzed to provide information on processes that may affect the natural system features of the repository. The Peña Blanca analogue site provides indications that actinide mobility was minimal due to the geochemical system (BSC 2004g, Section 10.4).

At Nopal I (Peña Blanca, Mexico), uranium and its daughter products have been transported relatively small distances over roughly the past 300,000 years, almost solely along fractures. The Nopal I uranium deposit represents an environment that closely approximates the unsaturated zone at Yucca Mountain because both environments are climatologically similar, are part of the Basin and Range Province that is composed of rhyolitic tuffs, have a thick unsaturated zone (greater than 100 m), and are oxidizing environments. The alteration of uraninite to secondary uranium minerals at Nopal I provides insights into the alteration of exposed uranium fuel rods emplaced in the repository because of the similar environments. At Nopal I, uranium and its daughter products have been sorbed or precipitated onto fracture-coating iron-oxides and calcites (BSC 2004g, Section 10.1). Results from Nopal I indicate low actinide mobility in unsaturated siliceous tuffs under semiarid oxidizing conditions. Data for $^{230}Th/^{238}U$ ages indicate that the primary transport of uranium away from the Nopal I deposit along fractures occurred more than 300,000 years ago. The $^{226}Ra/^{230}Th$ activity ratios indicate redistribution of radium within the last 5,000 years as a result of secondary fluid events. Therefore, the data demonstrate stability over approximately 100,000-year time scales for ^{235}U, ^{238}U, thorium, and protactinium in fracture-filling materials (BSC 2004g, Sections 10.1).

Studies at Nopal I emphasize the dominant role of fracture transport, and in this respect they support the conceptual model and implementation of the radionuclide flow and transport models for Yucca Mountain. The relative importance of matrix diffusion or other matrix transport processes at Nopal I remains ambiguous. Pearcy et al. (1995, pp. 702 to 703) emphasized the dominant role of fractures in transporting and sequestering uranium. However, they also found that bulk-rock samples from within 0.5 m beyond the area of visible uranium mineralization showed significant ^{234}U enrichment, indicating that these rocks have been open with respect to uranium-transport processes within about the last million years. In contrast, samples from within the deposit are close to secular equilibrium, indicating limited fractional mass transport (i.e., transport of uranium in any form that is out of secular equilibrium). Evidence of matrix diffusion within the deposit may be overshadowed by bulk uranium concentrations in the range of 5,282 ppm to 33,000 ppm that reside mostly in fractures (Pearcy et al. 1995, Figure 7). Uranium contents of samples from about 1 to 11 m outside the deposit range from 15 to 820 ppm (Goodell 1981, pp. 283 to 284). Given that almost all Topopah Spring Tuff samples analyzed for uranium have values less than about 5 ppm (BSC 2004c, Section 6.14.3.2, Table 6-45), the background uranium values at Nopal I may represent products of

matrix transport and retardation. Therefore, the natural-analogue data are not incompatible with the use of a dual-permeability radionuclide flow and transport model that incorporates matrix retardation processes in the unsaturated zone.

2.3.8.4.5 Impacts of Uncertainties and Variabilities

The uncertainties related to the modeling of radionuclide transport through the unsaturated zone are described in the following sections. In these sections, a combination of process and abstraction model results are presented, since for the purposes of this description of unsaturated zone transport behavior, the two models are interchangeable.

Estimates of net infiltration in the region immediately surrounding Yucca Mountain (Section 2.3.2 and SNL 2008d) were used to generate the unsaturated zone flow fields presented in Section 2.3.2. This updated flow model forms the basis of the unsaturated zone flow component used in TSPA. Many of the simulation results presented in this section and Section 2.3.8.5 use these flow fields. However, some simulation results presented herein for the purpose of illustrating parameter sensitivities were generated using an older version of the unsaturated zone flow model that used a set of infiltration maps (BSC 2004h, Sections 6.11.1 and 6.11.3) that have since been updated. These model results are acceptable for this purpose because the conclusions reached are still valid despite the differences in infiltration maps, and because the specific results are used for illustrative purposes, rather than as direct input to TSPA. For each instance in which the older flow fields are used, the basis for the statement that the results can be used for illustrative purposes despite the use of an older version of the flow model is also provided.

2.3.8.4.5.1 Variability in Flow Paths and Transport Times

To examine the statistics of the simulated travel time and exit location (defined as the coordinate location at which mass reaches the water table), the abstraction model is used, with conservative particles released at the repository horizon. For this purpose, a dissolved species without decay or matrix diffusion was chosen to examine fluid flow properties of the unsaturated zone. Particles are released at each individual node, and then the statistics of transport time from the repository to the water table and of exit locations are computed based on all particles released at the node. Organizing the simulations in this way, information on the spatial variability across the repository is examined, thereby allowing for an exploration of the dependence of transport time statistics on the release location. For each of the flow fields, 560 model runs were performed in which 10,000 particles were released at each repository node. Simulations for glacial-transition climate conditions are examined, using a raised water table with a minimum elevation of 850 m to represent the higher water table under future, wetter climate conditions.

Figure 2.3.8-36 illustrates statistics of the transport time for the glacial-transition, 10th percentile infiltration scenario. This mean travel time map shows a dramatic spatial variability in which releases in the northern repository region yield much shorter travel times than releases in the southern region. This result is due to the presence of an unaltered, vitric Calico Hills unit beneath the repository in the southern region. In contrast, the northern release yields fracture flow from the repository horizon to the water table, with Calico Hills units altered to low-matrix-permeability rocks in which fracture flow and/or lateral diversion occurs. Figure 2.3.8-36 also shows contour maps of the minimum travel time (first arrival) among the 10,000 particles across the repository

horizon, as well as a contour map for the maximum travel time. Like the mean transport times, the minimum transport time in the southern region is larger than that in the northern region. However, the maximum transport time in the southern region is smaller than that in the northern region. In other words, the spread of transport times is greater for the northern release locations. This result is due to the different transport mechanisms at work in the two regions. For an area dominated by fracture flow, slow matrix transport spreads the arrival times over a greater range than for a system in which only matrix flow and transport occurs (SNL 2008a, Section 6.6.2.1 in Addendum 1).

The particle tracking approach allows the mean position and spreading of these particles at the water table (irrespective of the arrival times of the particles) to be determined. In this analysis, the mean displacement, from the repository release point to the location at the water table, is computed in each of the horizontal directions. Thus, the mean displacement is an indication of the trajectory of the particle pathways from different repository release locations to the water table. Figure 2.3.8-37 shows the mean locations at the water table for releases across the repository for the glacial-transition, 10th percentile infiltration scenario. Each point in the figures represents a release location of 10,000 particles from a given computational grid cell in the repository region and is colored by the percolation bin classification in the left and middle figures and by travel time in the right figure. The percolation bin represents the water flux at the repository horizon, with Bin 1 representing the lowest flux values and Bin 5 representing the highest flux values. For the northern release locations, the trends are for lateral diversion to yield arrivals that coincide with several fault zones, including the Drillhole Wash Fault and Pagany Wash Fault (for the locations of these faults, see Figure 2.3.2-9). These results are consistent with a model of vertical transport to the perching horizons beneath the repository, followed by lateral diversion to fault zones, and vertical transport down the faults. In contrast, the paths followed by particles originating from southern release locations are essentially vertical. The plot in which the locations are colored based on travel time (the right plot) shows that the particles with shortest mean travel time (less than 10 years) reach the water table in the fault zones. These pathways represent releases over a broad region (not just releases into the fault itself) that are diverted laterally in the perching horizon and eventually reach the fault zones. As a result of lateral diversion, the shortest mean travel times (< 10 years) are coincidentally associated with the repository area with the lowest percolation flux (Bin 1, < 1 mm/yr) because of its location relative to the Drillhole Wash fault zone. Other analyses indicate that the spatial variability of travel time and the mean displacements in both the x and y directions are very similar for different flow scenarios, implying that the infiltration scenarios result in different rates of migration but similar flow directions (SNL 2008a, Section 6.6.2.1 in Addendum 1).

2.3.8.4.5.2 Uncertainties in Matrix Diffusion and Fracture–Matrix Interaction

Uncertainties in the diffusive flux are reflected in the values and spatial distribution of the effective diffusion coefficient and fracture–matrix interface area. The effective diffusion coefficient is a composite quantity involving the molecular diffusion coefficient D_0, medium tortuosity, and water saturation. The diffusive flux is proportional to the product of the effective diffusion coefficient and the fracture–matrix interface area. Transport tests at Alcove 8–Niche 3 and Alcove 1 suggest that the combined product of the effective diffusion and fracture–matrix interface area increases with the scale at which the transport is observed (BSC 2006a, Section 6.4.1). The range of variability in the effective diffusion coefficient and in the diffusive flux can be represented by the range of variability of D_0. To understand how the diffusive flux component of the fracture–matrix interaction affects the

transport of nonsorbing radionuclides, sensitivity analyses were conducted on the diffusion coefficient for ^{99}Tc, colloid size, and the active fracture γ parameter. A wide range of D_0 values (i.e., spanning factor of 20) was investigated for ^{99}Tc (Figure 2.3.8-38). The use of the mean present-day flow field from a previous version of the infiltration model (BSC 2004h, Section 6.11.1) is acceptable for examining the sensitivity to diffusion coefficient because of the similarity of the mean infiltration over the repository footprint (4.7 mm/yr) to the mean percolation flux through the repository of the most likely present-day flow field used in TSPA (3.93 mm/yr; SNL 2008a, Table 6-26 in Addendum 1). Conclusions on the role of diffusion are not expected to change with differences in the flow field of this magnitude. As expected, D_0 has a significant impact on breakthrough predictions examined in this figure for a uniform release of mass across the entire repository. Arrival times vary directly as a function of D_0 values (SNL 2007b, Section 6.8.3.2). Uncertainties related to the effective D_0 are included in TSPA through sampling of a wide range of matrix diffusion coefficients, which accounts for the uncertainties in diffusive flux (Section 2.3.8.5.2.4). Additional sensitivity analyses examining uncertainties in diffusion coefficient, alone and in combination with other uncertainties, are examined using the unsaturated zone transport abstraction model in Section 2.3.8.5.5.1.

With respect to colloid behavior, analyses have been performed to determine the significance of colloid diffusion on transport. The use of the mean present-day flow field from a previous version of the infiltration model (BSC 2004h, Section 6.11.1) is acceptable for examining the sensitivity of transport of colloids to diffusion because of the similarity of the mean infiltration over the repository footprint (4.7 mm/yr) to the mean percolation flux through the repository of the most likely present-day flow field used in TSPA (3.93 mm/yr) (SNL 2008a, Table 6-26 in Addendum 1). Conclusions on the impact of colloid diffusion are not expected to change with differences in the flow field of this magnitude. The colloid diffusion coefficient is smaller because of the colloid's larger size and because size-exclusion effects at the interfaces of different geologic units further limit entry through diffusion into the matrix, especially for larger colloids (SNL 2007b, Section 6.1.4). Therefore, diffusion is less significant for colloid transport than for solute transport. However, matrix diffusion effects become increasingly important for decreasing colloid size (Figure 2.3.8-39) due to the inverse relationship between colloid size and diffusion coefficient. Nevertheless, in the abstraction model used in TSPA, the effect of colloid matrix diffusion is not included due to the lack of detailed knowledge of the size and diffusion coefficient characteristics of the colloid population. This approach conservatively results in the increased rate of migration of colloids (SNL 2007b, Section 8.3.2.3).

The interaction between fractures and the rock matrix is described using the active fracture matrix conceptualization (Liu, Doughty et al. 1998, pp. 2638 to 2641), in which only a portion of fracture networks are active (i.e., hydraulically conductive) under unsaturated conditions. The active portion is defined as a function of water saturation S to the power of the active fracture parameter γ (which is less than or equal to 1 and greater than or equal to 0) (Liu, Doughty et al. 1998, pp. 2638 to 2641). When γ equals 0 or S equals 1 (i.e., corresponding to a saturated condition), all fractures are active, while a γ value of 1 indicates that the smallest portion of fractures are active for a given saturation (Liu, Doughty et al. 1998).

The impact of uncertainties in γ on three-dimensional site-scale flow and transport through the unsaturated zone was investigated with sensitivity studies (BSC 2004i], Section 6.8). The studies indicated that transport is more sensitive than flow to uncertainty in the value of γ. In comparison,

flow exhibits relative insensitivity to γ. Additionally, the effect is more pronounced when the first portion of the breakthrough curve arrives at the water table because diffusive fluxes become progressively smaller as the concentrations in the matrix and fractures approach equilibrium. The sensitivity of transport to γ is demonstrated in Figure 2.3.8-40, which shows a substantial retardation in the arrival of a nonsorbing radionuclide at the water table (for a uniform release of mass across the entire repository) when γ is reduced from its upper limit value of approximately 0.6 to 0.2.

The use of the mean glacial-transition flow field from a previous version of the infiltration model (BSC 2004h, Section 6.11.3) is acceptable for examining the sensitivity of transport to the value of γ because of the similarity of the mean infiltration rate over the repository footprint (19.8 mm/yr) to the mean percolation flux through the repository for the two most likely glacial-transition flow fields used in the TSPA (glacial-transition, 10th and 30th percentile infiltration maps: 8.97 and 24.02 mm/yr, respectively) (SNL 2008a, Table 6-26 in Addendum 1). Conclusions on the impact of γ on transport are not expected to change with differences in the flow field of this magnitude. In this sensitivity analysis, which involved radionuclide release directly into the repository fractures, the time for 50% fractional mass breakthrough increased by more than one order of magnitude for this range of the γ parameter. Because the flow conditions are relatively insensitive to γ (BSC 2004i, Section 6.8), but the transport behavior is influenced by γ, uncertainty in flow due to uncertainty in active fracture parameter is not explicitly considered in TSPA. Instead, the abstraction model considers uncertainty of the γ parameter with respect to transport by assigning an uncertain value (ranging from 0.2 to 0.6; see SNL 2008a (Section 6.5.6 in Addendum 1) and Section 2.3.8.5.2.4) to all units below the repository while applying the same calibrated flow field to each simulation.

2.3.8.4.5.3 Uncertainties in Sorption

Uncertainties in sorption are reflected in the distribution of the sorption coefficient K_d. To address this uncertainty, the sensitivity of radionuclide transport through the unsaturated zone is studied for K_d values that cover the range between zero (no sorption) to maximum reported values (SNL 2007b, Section 8.3.2.4, Table 6-3). ^{237}Np was studied because of its importance to dose. The breakthrough of ^{237}Np at the water table for a uniform release of mass across the entire repository is shown in Figure 2.3.8-41 for a range of K_d values. The use of the mean present-day flow field from a previous version of the infiltration model (BSC 2004h, Section 6.11.1) is acceptable for examining the sensitivity to sorption coefficient because of the similarity of the mean infiltration over the repository footprint (4.7 mm/yr) to the mean percolation flux through the repository of the most likely present-day flow field used in the TSPA (3.93 mm/yr) (Figure 2.3.8-38) (SNL 2008, Table 6-26 in Addendum 1). Conclusions on the role of sorption are not expected to change with differences in the flow field of this magnitude. The results in Figure 2.3.8-41 indicate that K_d has a significant impact on breakthrough, with earlier arrival times predicted for lower values of K_d (SNL 2007b, Section 8.3.2.4). The uncertainty represented in this example is addressed in the abstraction model used in TSPA through sampling of probability distributions for K_d for all sorbing radionuclides considered. The uncertainty is captured using a methodology for developing the K_d probability distributions (SNL 2007b, Appendix A, Section A1; and Section 2.3.8.5.2.3).

2.3.8.4.5.4 Uncertainties in Colloid Filtration

The kinetic filtration of colloids through clogging and unclogging could affect colloid transport. Because basic knowledge of the parameters that control the kinetic filtration of colloids (i.e., clogging and declogging coefficients) in unsaturated matrix and fractures is limited, the effects of colloid filtration are uncertain. Although analyses indicate that transport is insensitive to the filtration parameters in the matrix, the significance of this observation may be limited given the difficulty of larger colloids in penetrating the matrix. Colloid filtration is treated conservatively as physical straining at fracture–matrix interfaces resulting in size exclusion and preferential transport of colloids within the fracture domain. The size exclusion process is only invoked for colloids with radionuclides irreversibly sorbed. Therefore, the effect of this uncertainty is conservatively bounded in the TSPA by limiting colloid filtration in the matrix to the physical process of size exclusion (SNL 2007b, Section 6.2.4; SNL 2008a, Section 4.1.8 in Addendum 1).

2.3.8.4.5.5 Impacts of Climate Variabilities and Uncertainties

Climatic changes affect the amount of infiltration and can shift transport rates dramatically. Higher infiltration is invariably associated with faster transport of radionuclides to the water table (SNL 2007b, Section 8.3.2.2). The uncertainty associated with climate change is addressed by estimating transport under the entire range of climatic scenarios, which also includes an associated change in water table elevation for all future climates (Section 2.3.9.2.4.1). The different climates identified for the first 10,000 years are used to quantify percolation for these time periods. A specific climate is not specified for the final 990,000 years because proposed revisions to 10 CFR Part 63 specify a distribution of percolation flux through the repository footprint for this time period. The close relationship between the applied water flux boundary condition at the ground surface and the resulting percolation flux is then used to establish a range of infiltration flux for this time period (Section 2.3.2.3.5.1). In addition to variability due to climate change, uncertainty in infiltration rate is propagated through the unsaturated zone transport model through the selection of four discrete infiltration scenarios that cover the uncertainty range (the 10th, 30th, 50th, and 90th infiltration scenarios; see Section 2.3.2.4.1.2.4.2).

Figure 2.3.8-42 presents the travel times to the water table (plotted as mean $\log_{10}$-based travel time) for releases from the repository, categorized by percolation bin assignment. These percolation bin assignments are those presented in Figure 2.3.8-37a. The plotted travel times are the averages of all travel times associated with repository release nodes within a given percolation bin, for the four infiltration scenarios for the present-day (upper figure), monsoon (middle figure), and glacial-transition (bottom figure) climate states. The expected trend of longer travel times for the 10th percentile case, compared to the 30th, 50th, and 90th percentile cases, are clearly reflected in these simulations. However, note that a smaller bin number, which corresponds to a smaller percolation rate at the repository horizon, often results in smaller travel times, despite the lower water flux at that location. In fact, for several of these flow fields, including all of the present-day flow fields, there is a positive correlation between percolation rate at the repository and travel time (i.e., travel times from percolation bin 5 result in longer travel times despite the higher percolation

rates at the repository horizon). The results indicate that factors other than the local percolation flux, principally the hydrogeologic conditions beneath the repository, actually drive the results; the location of the release point (north versus south) with respect to the underlying hydrogeologic strata and faults is the controlling factor in determining the travel time to the water table (SNL 2008a, Section 6.6.2.1 in Addendum 1). The presence of a layer of vitric Calico Hills Formation beneath the release location leads to matrix-dominated flow and longer transport times to the water table than for releases in which the pathway does not include this rock type (SNL 2008a, Section 8.2.2 in Addendum 1). Therefore, while percolation bin may have an important impact on radionuclide releases predicted in other parts of the TSPA model, such as the radionuclide release rate from the engineered barrier system, it is relatively unimportant as a factor controlling the travel times through the unsaturated zone (SNL 2008a, Section 6.6.2.1 in Addendum 1).

2.3.8.5 Model Abstraction

[NUREG-1804, Section 2.2.1.3.7.3: AC 1(3), AC 3(1), (2), (4), AC 5]

The TSPA utilizes a Monte Carlo methodology that requires a large number of realizations to represent the total system uncertainty. Accordingly, the unsaturated zone radionuclide transport abstraction model was developed to allow calculations of radionuclide transport as part of the TSPA model.

The main purpose for utilizing an abstraction model for unsaturated zone transport in the TSPA is to gain computational efficiency. The particle tracking approach used for the unsaturated zone transport abstraction model represents many processes in a way that are equivalent to those in the unsaturated zone transport process model. Global dispersion and fracture-matrix interaction are two exceptions for which the abstraction and process models are not the same in that the abstraction model simulates only longitudinal dispersion rather than the full dispersion tensor. For dispersion, the unsaturated zone transport abstraction model approach tends to be more accurate for non-dispersive systems due to the use of particle tracking to solve the transport equation, whereas the unsaturated zone transport process model tends to be more accurate for dispersive systems. Advective and diffusive fracture-matrix exchange, in principle, are coupled processes as represented in the unsaturated zone transport process model. These processes are approximated as decoupled in the unsaturated zone transport abstraction model. However, model comparisons presented in *Particle Tracking Model and Abstraction of Transport Processes* (SNL 2008a) and Section 2.3.8.5.6.2 have shown that both approaches provide results that are sufficiently similar that the unsaturated zone transport abstraction model can be considered adequate for its intended use.

Consistent with the site-scale unsaturated zone radionuclide transport process model, the unsaturated zone radionuclide transport abstraction model is based on a dual-permeability formulation to address the importance of fracture flow and fracture–matrix interactions on radionuclide transport. The dual-permeability formulation consists of overlapping, interacting fracture and matrix domains so that there are separate fracture and matrix properties at each location in the domain (SNL 2008a, Section 6.4).

The influence of spatial variability is included in the unsaturated zone radionuclide transport abstraction model through a three-dimensional model that incorporates the appropriate geometry and geology (SNL 2007b, Section 6.1.1). Within a hydrogeologic unit, properties are assumed to be constant (not spatially variable within a unit), with appropriate representative values selected. The

unsaturated zone radionuclide transport abstraction model couples and calculates fracture and matrix transport using the finite element heat and mass transfer (FEHM) code.

The unsaturated zone radionuclide transport abstraction model computes the movement of radionuclides released from the EBS into the unsaturated fractured geologic media and downward to the water table using the residence-time transfer-function particle-tracking technique implemented in the FEHM code as a dynamically linked module (SNL 2008a, Section 6.4.1) in the TSPA. The abstraction model operates within the same modeling domain as the three-dimensional, site-scale, unsaturated zone flow and transport process models (Figure 2.3.2-9). The TOUGH2 software code is used to generate the flow fields that are used by the abstraction model in the TSPA computations (SNL 2008a, Section 6.5.1).

Radionuclides that enter the unsaturated zone from the EBS are carried by water traveling through the fractured media downward to the water table. At the water table, the radionuclides are collected in four regions directly beneath the repository (Section 2.3.9). For TSPA computations, any radionuclide that reaches the water table is transferred from the unsaturated zone transport system to the saturated zone system (SNL 2008a, Section 6.5.16).

In the TSPA simulations, the transport calculations are carried out using multiple realizations to capture the uncertainty in the transport parameterization, the unsaturated zone flow fields, and the radionuclide source term. Advection, dispersion, sorption, and fracture–matrix interaction (including matrix diffusion, colloid-facilitated transport, radioactive decay and ingrowth, climate change, and water table rise) are represented in the abstraction model (SNL 2008a, Section 6.2). Section 2.4.1 summarizes the TSPA implementation and points out the effect of dispersion for transport through the matrix, as compared to fractures.

2.3.8.5.1 Particle-Tracking Methodology

The abstraction model uses a cell-based particle-tracking technique in which particles move from cell to cell in the three-dimensional site-scale grid. Particle movement from cell to cell is computed probabilistically based on transfer functions. The transfer functions are defined using dual-permeability numerical solutions of the transport equations (SNL 2008a, Section 6.4.3 and Appendix C) and represent probability distributions of the residence time (i.e., the amount of time that a particle resides in a cell). The probability that a particle will move to a given neighboring cell is proportional to the water flow rate to that cell (SNL 2008a, Section 6.4.1).

The abstraction model is comprised of a network of fracture cells representing the fracture continuum and a network of matrix cells representing the matrix continuum, with each fracture cell connected to a corresponding matrix cell. The following transport phenomena are simulated (SNL 2008a, Section 6.2, Table 6-1):

- Advection through fracture and matrix continua, including between these continua
- Dispersion of both aqueous and colloidal species
- Sorption of dissolved radionuclides to the matrix continuum, and within the fault zones
- Molecular diffusion between the fractures and matrix
- Colloid-facilitated transport
- Radioactive decay and ingrowth.

Uncertainty is included in the unsaturated zone radionuclide transport process and abstraction models by developing parameter distributions for a number of input parameters (SNL 2008a, Section 6.5). Values of these parameters for each TSPA model realization are sampled from these distributions. Thus, each realization of the total system has a unique set of input parameters (SNL 2008a, Section 8.1, Table 8-2 in Addendum 1).

Some of the uncertainty in the abstraction model results from uncertainties incorporated from other contributing models. For example, there is uncertainty in infiltration and unsaturated zone flow from the site-scale unsaturated zone flow model, in the number of breached waste packages from the waste package degradation model, in numerous EBS model parameters and processes, and in the radionuclide source term received from the EBS transport model (SNL 2008a, Section 8.2.2).

Some parameters such as fracture residual water saturation, fraction of colloids travelling unretarded, and decay half-lives, are treated as certain in the TSPA (i.e., parameters that have single values rather than uncertainty distributions). Single values are used when model results are insensitive to changes in the parameter within the range of the parameter uncertainty (SNL 2008a, Section 4.1 in Addendum 1).

Radionuclide transport in the unsaturated zone is assumed not to be influenced by repository waste heat effects in the TSPA because these effects are determined to be of short duration (i.e., on the order of 1,000 years at or above the boiling point of water) (Section 2.3.3.3.3.1), and the dryout zone would likely impede radionuclide transport (SNL 2008a, Section 5). Thus, the beneficial effect of waste heat on radionuclide transport in the unsaturated zone is conservatively not included in the TSPA.

Climate change is treated by imparting an instantaneous change from one steady-state flow field to another, with a corresponding change in the minimum water table elevation representing the bottom of the unsaturated zone radionuclide transport abstraction model (SNL 2008a, Section 5). The changes occur at transitions from the present-day climate to monsoon climate, from the monsoon climate to glacial-transition climate, and from the glacial-transition climate to the post-10,000-year period (Section 2.3.2.3.5.1). Analyses conducted with the site-scale unsaturated zone flow model (Section 2.3.2) have shown that short-term transients in flow associated with individual storm events or other short-term weather variations do not effectively penetrate the PTn hydrogeologic unit that overlies the repository (SNL 2007a, Section 6.9). Therefore, the assumption of steady-state flow based on long-term average behavior is appropriate for analyses of transport processes between the repository and the water table in the TSPA.

2.3.8.5.2 Transport Mechanisms and Associated Inputs Required for Model Abstraction

Parameter inputs associated with the various transport mechanisms are discussed in this section, including advection, dispersion, sorption, matrix diffusion, colloid-facilitated transport, and radioactive decay.

2.3.8.5.2.1 Advection

The modeling of advection in the TSPA incorporates the important aspects of the underlying process models, including variability due to changes in climate and uncertainty. This is done through directly incorporating the unsaturated zone flow fields from the site-scale unsaturated zone flow model (Section 2.3.2). In this manner, FEP 2.2.07.04.0A, Focusing of unsaturated flow (fingers, weeps), 2.2.07.07.0A, Perched water develops, 2.2.07.08.0A, Fracture flow in the UZ, and 2.2.07.09.0A, Matrix imbibition in the UZ, are included in the TSPA model. To convert water flux to radionuclide transport velocity, the water content (saturation multiplied by porosity) is required. Fracture and matrix porosities and saturations are obtained directly from the flow model. Porosities are constant within a layer based on average values but vary from layer to layer (SNL 2008a, Section 4.1). Saturations vary spatially across the model domain and temporally due to climate change and the corresponding shift to a new flow field, and are determined from the flow simulations.

2.3.8.5.2.2 Dispersion

The modeling of dispersion in the TSPA is based on fixed values for longitudinal dispersivity, with transverse dispersion assumed to be negligible. The large-scale lateral transport of radionuclides is included explicitly in the flow fields. Additional transverse spreading caused by the small-scale heterogeneities in the rock is negligible compared with these large-scale effects. Therefore, transverse dispersivity is not included in the unsaturated zone radionuclide transport abstraction model (Section 2.3.8.2.2.1).

The value set for longitudinal dispersivity is based on data in the saturated zone, informed by relevant information from unsaturated zone tracer tests and modeling. Use of the available data from the saturated zone is appropriate for the following reasons:

- The fundamental processes that give rise to longitudinal dispersion (variations in velocity leading to solute spreading) are comparable in the saturated and unsaturated zones.

- Neuman (1990) showed that field dispersivity is most sensitive to the scale of the measurement. Field tracer tests in the saturated zone at the C-Wells complex at Yucca Mountain are relevant because they were conducted on the appropriate scale (100-m). The estimated field dispersivity from these tests had a range of approximately 3 to 63 m (SNL 2007f, Table 6.3-3).

With respect to tracer tests under unsaturated conditions, none of the field tests conducted either at the Busted Butte or Alcove 8–Niche 3 site provided definitive information on either the longitudinal or transverse dispersion. For example, the Busted Butte Phase 2C data were shown to be consistent with a longitudinal dispersivity of 0.1 m; transverse dispersivity was set to zero for these simulations. Results of these simulations indicated that these low values of the longitudinal and transverse dispersivities are consistent with the data but that further analysis to refine the dispersivity estimates was unwarranted due to the uncertainties associated with the sample collection system and its effect on the measured breakthrough curves (SNL 2008a, Section 4.1.6 in Addendum 1). The transport distance for this tracer analysis was approximately 0.6 m, making this test a relatively small scale test compared to the entire transport distance through the unsaturated

zone. Analyses of tracer responses from the Alcove 8–Niche 3 fault test (characteristic transport distance on the order of 20 m) indicated that assuming dispersivity values significantly larger than zero made it more difficult to match the breakthrough curve data for the two tracers injected. In this case, matrix diffusion is the predominant mechanism affecting the transport, and hydrodynamic dispersion is taken to exert a relatively minor influence on the results. Given the lack of definitive information to constrain the longitudinal dispersivity based on unsaturated zone tests, the disparity in scale between field tests and the unsaturated zone transport system, and the finding that diffusion is more important than dispersion in controlling tracer breakthrough, the approach taken was to rely on longitudinal dispersivity estimates from the saturated zone to set the dispersivity in the unsaturated zone transport model (SNL 2008a, Section 6.5.2).

In TSPA, the fracture longitudinal dispersivity is set at 10 m. This dispersivity is toward the lower end of the value from C-Wells field studies described above. Because the impact of dispersion is believed to be small, the value chosen is fixed at 10 m rather than developing an uncertainty distribution or a scale-dependence (SNL 2008a, Section 4.1.6 in Addendum 1). In this manner, FEP 2.2.07.15.0B, Advection and dispersion in the UZ, is included in the TSPA model.

2.3.8.5.2.3 Sorption

The modeling of sorption in the TSPA is based on the linear sorption model, which is characterized by the same lumped parameter for the sorption coefficient, K_d (Table 2.3.8-2), that is used in the unsaturated zone radionuclide transport process models (Section 2.3.8.3). This section summarizes the manner in which FEP 2.2.08.09.0B, Sorption in the UZ, is included in the TSPA model. All aqueous radionuclides that travel in fractures are conservatively assumed not to be adsorbed to the fracture walls (SNL 2007b, Appendix A, Section A6), except within zones designated as fault zones. The fracture continuum in these zones are treated as an effective continuum with low porosity to accentuate fracture transport without matrix diffusion. However, sorption is also considered within these zones. For radionuclides that travel in the matrix, the partitioning of radionuclides between the solute and the matrix is described by the sorption coefficient for each radionuclide. The matrix sorption coefficients that have been developed for different rock types (zeolitic, devitrified, and vitric) (Section 2.3.8.3.1) are listed in Table 2.3.8-2 with their statistical distributions. These distributions are sampled to represent the uncertainty in sorption in the TSPA. The influence of expected variations in water chemistry, radionuclide concentrations, and variations in rock surface properties within each of the major rock types was incorporated into the probability distributions. Effective K_d values, obtained from batch experiments involving high-concentration solutions, will tend to conservatively underestimate the field K_d values if the expected field concentrations are low, and nonlinear sorption prevails (SNL 2007b, Section 6.1.2.3).

The K_d distributions were derived from available project data combined with external data that indicate the functional dependencies of sorption on several independent variables. Many site-specific K_d measurements have been made using Yucca Mountain rocks and representative groundwater. Project experimental data bound the function for some but not all variables because of practical limitations on the number of experiments that could be conducted. Data from the literature (e.g., Allard 1982; Allard and Beall 1979; Allard, Beall et al. 1980; Allard, Olofsson et al. 1983) provided further insights into how other variables affect sorption behavior. PHREEQC model results were used to assess how water chemistry and surface area affect sorption behavior. Chemical insights regarding the kinds of reactions involved were also used. These insights included potential

impacts from variations in water compositions (e.g., Eh) that are outside those addressed in the experimental program, variations in surface areas, and variations in mineralogical composition. In the case of mineralogical composition, an attempt was made to emphasize those experiments that used samples closest to the mean composition of the hydrologic units as defined in the process and abstraction models. All of this information was considered in the derivation of the final distribution for each radioelement on each rock type. To bound uncertainties in project and literature data and their application for this purpose, the results were conservatively biased (SNL 2008c, Appendix A).

An example of the process of establishing the uncertainty distribution of K_d from the available data and geochemical modeling is now presented for neptunium sorption on devitrified tuff, the data for which was presented in Section 2.3.8.3.1 and Figure 2.3.8-8. The geochemical modeling results and data showed a small impact of variations in pH on K_d (SNL 2007b, Appendix A, Section A8.3.1), so in this case the data are used to establish the uncertainty distribution without explicit consideration of the uncertainty in pH. In this manner, the potential impact of groundwater chemistry on sorption of neptunium is included in the TSPA model (FEP 2.2.08.01.0B, Chemical characteristics of groundwater in the UZ). The neptunium sorption-coefficient probability distribution selected for devitrified tuff in the unsaturated zone is a cumulative distribution, starting with a value of 0.0 mL/g at 0.0, increasing to a value of 0.5 mL/g at 0.5 (the median value), and to a value of 6.0 mL/g at 1.0 (Table 2.3.8-2). The low end of the chosen range (0.0 mL/g) is selected based on the minimum value obtained in short-term experiments (up to 21 days). The upper end of the distribution was chosen as a minimum upper limit for a neptunium concentration near the solubility limit, with emphasis on results from experiments with p#1 water at pH near 7.0. It is acknowledged that a higher limit could have been selected for the upper end of the distribution, based on the available data and modeling results reflected in Figure 2.3.8-8. However, as discussed in *Radionuclide Transport Models Under Ambient Conditions* (SNL 2007b, Section A6), not all the empirical data were equally weighted in selecting the probability distribution, as the influence of expected variations in water chemistry, radionuclide concentrations, and variations in rock surface properties within each major rock type were incorporated in making the selection. The decision to truncate the data on the upper end of the empirical cumulative distribution is intentionally conservative in order to ensure that sorption in this unit is not overestimated, and to avoid risk dilution. Finally, the median value of 0.5 mL/g was selected so that the lowest 50% of the empirical cumulative distribution of the data displayed in Figure 2.3.8-8 is accurately represented by the straight line from 0 to 50%. This example illustrates the approach for establishing the uncertainty distributions for the K_d for one radioelement on one particular rock type; a complete analysis for all radioelements and rock types is presented in *Radionuclide Transport Models Under Ambient Conditions* (SNL 2007b, Appendix A).

Retardation factors developed from the sorption coefficient also depend on matrix porosity (SNL 2008a, Section 6.5.3 in Addendum 1) and bulk rock density (SNL 2008a, Section 6.5.3 in Addendum 1), as described in *Particle Tracking Model and Abstraction of Transport Processes* (SNL 2008a, Section 6.4.1). These two parameters are fixed, based on values developed in the site-scale unsaturated zone flow model (SNL 2008a, Tables 6-5 and 6-6 in Addendum 1).

2.3.8.5.2.4 Matrix Diffusion

The modeling of matrix diffusion in the TSPA accounts for diffusive transport of radionuclides between the fracture and matrix continua. The description in this section outlines the approach taken

to include matrix diffusion in the TSPA model (FEP 2.2.08.08.0B, Matrix diffusion in the UZ). This process requires the construction of an effective matrix diffusion coefficient. The effective matrix diffusion coefficient is the product of the tortuosity coefficient, which describes the tortuous nature of the pore networks, and the free-water diffusion coefficient (SNL 2008a, Section 6.5.5 in Addendum 1). In addition, diffusive flux between fractures and matrix is a function of the fracture aperture and the effective distance between the flowing fractures. For these parameters, the active fracture model described in Section 2.3.8.4.1 is adapted for transport to account for the fact that not all fractures flow. All parameters associated with matrix diffusion are described in this section (SNL 2008a, Section 6.5.5, Appendix A in Addendum 1).

In the unsaturated zone radionuclide transport abstraction model, correlations between the tortuosity coefficient, water content, and effective matrix permeability were developed from experimental data (SNL 2008a, Section 6.5.5.1 in Addendum 1). Free-water diffusion coefficients were developed for each radionuclide from information about radionuclide aqueous speciation. Free-water diffusion coefficients for ionic species were taken from tabulated values or developed from analogue species that have the same ionic charge and similar molecular size. In so doing, the chemical characteristics of the water are considered (FEP 2.2.08.01.0B, Chemical characteristics of the groundwater in the UZ). The effects of differences in molecular size were accounted for when an analogue species was used to develop the free-water diffusion coefficient. For uncharged species, the free-water diffusion coefficients were developed from an application of the Stokes-Einstein equation (SNL 2008a, Appendix A, Section A.3 in Addendum 1). The resulting range of effective matrix diffusion coefficients includes the uncertainty in the mechanisms associated with diffusion through tortuous pore spaces (Section 2.3.8.3.2). In the TSPA simulations, unsaturated matrix diffusion coefficients are based on the correlation between tortuosity, porosity, and saturated permeability developed for the saturated zone. Data collected under saturated conditions can be used for this purpose by adapting the corresponding relationship for the unsaturated zone. In the equation from Reimus, Callahan et al. (2007, Equation 2), porosity could be replaced with water content, and permeability could be replaced with effective permeability because diffusion is controlled by the geometry of the water-filled pore space (SNL 2008a, Section 6.5.5.2 in Addendum 1).

The uncertainty in the matrix diffusion coefficient was assigned based on the uncertainty in the correlation between tortuosity, porosity, and permeability. Other uncertainties (e.g., in water content and effective permeability) were specifically not included to account for the uncertainty reduction resulting from scale-up. This scale-up occurs because the matrix diffusion measurements are conducted on laboratory samples that are much smaller than the volume of a numerical grid element to which they are applied in the model (SNL 2008a, Section 6.5.5.4 and Appendix A, Section A.4 in Addendum 1).

The fracture porosity and fracture frequency are sampled independently to address the uncertainty of fracture properties (SNL 2008a, Section 6.5.7). The basis for this sampling approach is that there is only a weak correlation between fracture porosity and frequency (SNL 2008a, Figure 6-13). Aperture is then computed from the ratio of the fracture porosity and the fracture frequency. Among the geologic rock layers in the unsaturated zone, only those below the repository that could affect the transport of radionuclides downward toward the water table are required. Rock layers below the repository are grouped together based on similarity in the fracture porosity and fracture frequency characteristics. For groups with multiple units having different parameter values, an arithmetic

average value is used for the group. There is only one standard deviation for fracture porosity, so the other groups are assigned a fracture porosity standard deviation such that the ratio of the standard deviation to the mean is constant for all the groups. Group 9 (tswf3) has its own standard deviation for fracture frequency, which is used. For the other groups, the standard deviation is set equal to 0.831 times the mean (SNL 2008a, Section 6.5.7). This factor is based on the relationship between fracture frequency and the standard deviation of fracture frequency found for model units above the repository (SNL 2008a, Figure 6-12). Using this approach, the mean and standard deviation for each parameter in each group were computed (SNL 2008a, Table 6-15).

Because porosity must lie within the finite range of 0 to 1, a beta distribution with these bounds is suitable for studying the influence of fracture porosity uncertainty on radionuclide transport (SNL 2008a, Section 6.5.7, Table 6-15). Given that fracture frequency can theoretically span values from 0 to infinity, the lognormal distribution is suitable (SNL 2008a, Section 6.5.7, Table 6-15). These distribution types were used to synthesize relevant site data to obtain the uncertainty distributions for these parameters.

In TSPA, the fracture residual saturation (SNL 2008a, Section 6.5.6) is obtained from the process model for site-scale unsaturated zone flow (Section 2.3.2).

For the fracture spacing and active fracture model, γ parameter values are used to calculate the flowing fracture spacing based on the active fracture model (Liu, Doughty et al. 1998). The active fracture parameter is sampled from a range to incorporate uncertainty into the model. Process flow model results (BSC 2004i, Section 6.8.1) have demonstrated that the active fracture model parameters have very little influence on the relevant flow model parameters for transport, namely the fluid saturations and flow rates in the fracture and matrix continua. Therefore, it is an appropriate approximation to simply apply active fracture model parameter changes to the unsaturated zone radionuclide transport model using flow model results obtained from the base case flow simulation.

A single, uncertain value of γ is used for rock units below the repository. It has been shown in sensitivity analyses (SNL 2008a Sections 6.6.4 and 7.2.3.3) that assigning independent values for all units does not impact the breakthrough at the water table and that a single value for all units provides a result very similar to that of a more detailed, layer-by-layer specification. This result is due to the fact that the γ parameters for the TSw units are the ones that influence the breakthrough curves rather than the values in other units below the water table.

Previous analyses indicate that a value of γ less than or equal to 0.4 in the TSw provides an acceptable fit to the ^{14}C ages measured in wells USW UZ-1 and USW SD-12 (BSC 2004a, Section 7.4.1). This range reflects the degree to which this parameter can be varied in a series of one-dimensional simulations and still result in mountain-scale model simulations that match the observed data. Those simulations showed that for values of γ greater than 0.4 the simulated ^{14}C concentration deviates from the data. To examine multidimensional effects, a similar set of three-dimensional model simulations showed that parameter values of 0.4 and 0.6 provide equally good matches to the data for depths at or below the repository horizon (BSC 2004i, Section 7.5). More recent simulation results confirm the conclusions of previous analyses by showing that for values of γ equal to those used to develop the calibrated flow fields (0.4 in the TSw units), measured ^{14}C values in these two wells are bracketed by simulations with local or spatially averaged percolation rates from the 10th and 30th percentile, present-day infiltration models (SNL 2007a,

Section 7.5). Finally, a separate analysis of mineral coating data showed that the model is consistent with γ values in this range (BSC 2004a, Section 7.4.2).

Potential limitations in using ^{14}C to set the γ parameter are as follows (SNL 2007a, Section 7.5):

- Possible inadequacy of the use of gas ^{14}C as an approximation of the liquid ^{14}C age, which is the value the model uses for comparison
- Uncertainty in infiltration rate at the wells used for the simulations
- Model structural errors such as inappropriate use of one-dimensional models or inexact flow patterns in the three-dimensional simulations.

Given the potential limitations of these data and methods, it would be inappropriate to assume that the γ parameter is tightly constrained by the ^{14}C simulations. A reasonable upper bound, given these limitations, is 0.6, which is the highest value demonstrated in past analyses to be consistent with the ^{14}C simulations (BSC 2004i, Section 7.5). To constrain the lower bound, note first that the one-dimensional ^{14}C simulations do not rule out values as low as zero. However, zero would imply that every fracture in the system flows, and that no preferential flow through the network exists. This extreme is not credible, given the body of evidence in favor of preferential flow under unsaturated conditions through a relatively small subset of the total number of fractures (Liu, Doughty et al. 1998). In addition, constraining the lower bound to restrict values as low as 0 prevents potential risk dilution by narrowing the uncertainty range of this parameter. As 0.4 appears to provide a good match to the ^{14}C data, and 0.6 is the upper bound, a range that extends down to 0.2 provides an overall range that is equally distributed above and below the nominal value of 0.4. With no additional information available to define this parameter uncertainty distribution, the parameter will be sampled from a uniform distribution from 0.2 to 0.6. This range is consistent with the available data and maintains the model within a range in which preferential flow through a subset of fractures will occur for all realizations.

2.3.8.5.2.5 Colloid-Facilitated Transport

This section summarizes the method by which colloidal transport is included in the TSPA model (FEP 2.2.08.10.0B, Colloidal transport in the UZ). The modeling of colloid transport in the TSPA includes two colloid types (both are pseudocolloids: see Section 2.3.8.2.2.3) that have been determined to be important: glass waste-form colloids, in which radionuclides are permanently attached, and groundwater colloids, to which radionuclides reversibly sorb (SNL 2008a, Section 6.4.5). Colloid matrix diffusion is conservatively not treated because of the low diffusivities for most colloids. The linear equilibrium sorption model is used to describe radionuclide sorption onto colloids. Waste form colloids are assumed to undergo reversible filtration in fractures (SNL 2008a, Sections 6.4.5 in Revision 2 and 4.1.9 in Addendum 1). This is included in FEHM simulations through the use of the colloid retardation factor R_c, which is evaluated based on field experiments at the C-Wells complex using microspheres as analogues for colloids. Field experiments have shown that a small percentage of colloids transport through the groundwater system essentially without retardation (BSC 2004f, Section 6.6). The fractions of unretarded colloids have been developed based on field data (BSC 2004f, Section 6.6). In developing these fractions, it is postulated that the fraction of colloids escaping retardation due to physical and

chemical processes is a function of the residence time of the colloid: progressively fewer colloids migrate unretarded with time (SNL 2008a, Section 6.5.13). The difficulty with simulating transport for the unretarded colloids is that the transport times are not known beforehand. Therefore, for TSPA calculations, a fraction of colloids is chosen conservatively for a 100-year transport time in the unsaturated zone. The fraction of colloids transported with no retardation corresponding to a 100-year transport time is set at 1.68×10^{-3} based on field experiments and modeling (Section 2.3.9) (SNL 2008a, Table 6-23).

2.3.8.5.2.6 Radioactive Decay

The unsaturated zone radionuclide transport abstraction model includes the effects of radioactive decay either to stable isotopes or to other radioactive isotopes. For species that have decay chains, the code uses an integral approximation to the exact summation for ingrowth products (radionuclides that originate as decay products of other radionuclides) and tracks the locations and numbers of each type of radionuclide. The accuracy of the integral approach depends on the number of particles and their release history. In general, the use of a greater number of particles increases the accuracy. With respect to release, for the same number of particles, a simulation with a constant release rate will exhibit less error than a time-varying release, such as a shorter pulse. If the release rate changes with time, the release period is divided into segments so that within each segment the release rate can be treated as a constant. Simulation results from the unsaturated zone radionuclide transport abstraction model with decay and ingrowth were verified against results from semianalytical solutions for a four-species chain decay-ingrowth model (SNL 2008a, Section 6.4.4; LANL 2003). Decay chains included in TSPA for unsaturated zone transport are the same as those described in Section 2.3.9.3.4.2.1. In this manner, FEP 3.1.01.01.0A, Radionuclide decay and ingrowth, is included in the unsaturated zone radionuclide transport model for TSPA.

2.3.8.5.3 Radionuclide Transport under Future Climatic Conditions

A higher water table is expected in the Yucca Mountain region for future wetter climatic conditions (SNL 2008a, Section 6.4.8). A rise in the water table could impact radionuclide transport in the unsaturated zone by shortening the transport distance between the repository and the water table, thereby shortening travel time to the saturated zone. Estimates of the magnitude of the rise in the water table beneath the repository at Yucca Mountain under future climate conditions are available from several independent lines of evidence (Section 2.3.9). Section 2.3.9.2 presents a discussion of several water table rise estimates. A maximum water table rise of 120 m was determined based on these studies for the site-scale unsaturated zone flow model, which corresponds to a water table located roughly 190 to 260 meters below the repository horizon, depending on the local repository elevation. In this manner, FEP 1.3.07.02.0B, Water table rise affects UZ, is included in the TSPA model.

The TSPA approximates unsaturated zone flow under future climates as a series of steady states and uses pregenerated flow fields to represent corresponding climates. In this manner, FEP 1.3.01.00.0A, Climate change, and 1.4.01.01.0A, Climate modification increases recharge, are included in the TSPA model. Section 2.3.2 discusses the development of unsaturated zone flow fields for future climates. Because the water table is not flat, a nominal elevation for the present-day water table must be selected, and the future water table must then be based on that selection. For the typical water table elevation under present-day conditions beneath the repository of 730 m

(SNL 2008a, Section 6.4.8), a rise of 120 m results in an elevation of 850 m. In comparison to the impact analysis of a future water table rise on saturated zone transport processes (Section 2.3.9), the selection of a minimum elevation of 850 m for processing the unsaturated zone flow fields for the future climate cases is consistent with available site data and with saturated zone studies. The minimum elevation of 850 m is used for all future climate flow fields. This treatment is conservative because a reasonable maximum elevation results in a minimum unsaturated zone flow-path length. The flow fields processed to incorporate the higher water table for the future, wetter climates are described in Section 2.3.2.

2.3.8.5.4 Comparison of Transport of Radionuclide Species

This section presents breakthrough curves for different radionuclides from the specified release location to the water table for parameters selected for the representative case, which consists of a model run assuming the median values for all uncertain parameters. A set of breakthrough curves was developed (SNL 2008a, Section 6.6[b]) using the unsaturated zone radionuclide transport abstraction model to compare behaviors of the radionuclide species that are modeled in the TSPA. The species in the unsaturated zone radionuclide transport abstraction model consist of all species listed for all scenarios involving the groundwater pathway for the 10^2 year to 10^4 year model listed in Table 2.3.7-2 of Section 2.3.7.4, as well as additional radionuclides that must be tracked through the unsaturated and saturated zones for the 10^4 year to 10^6 year time period. The representative results presented here, along with simulations in which the impact of key parameter uncertainties are determined, illustrate the behavior of the unsaturated zone as a barrier to radionuclide migration for the purposes of understanding the role of the unsaturated zone in the overall repository system. However, none of the results from these runs will be used directly by TSPA. In TSPA, the abstraction model is used directly with combinations of parameters sampled from their uncertainty distributions to study the uncertainty of parameters and flow fields on radionuclide transport through the unsaturated zone and its impacts on system performance. The parameters for the representative case (Table 2.3.8-9) are selected as the median values within the uncertainty distribution.

In the figures of this section and others in which the term “normalized” is used, the simulation consists of a pulse input of particles, with the breakthrough curve plot representing the cumulative number of particles reaching the water table, normalized by the total number of particles injected. Therefore, if all particles released from the repository reach the water table, the breakthrough curve value will reach unity. Under the conditions of steady state flow, this integral plot represents the mass flux (normalized by the input mass flux) that would have been obtained if a constant mass flux had been input, even though the actual input was a pulse.

In TSPA, radionuclides released from the near field environment will migrate from individual point sources, the location of which is determined randomly based on the EBS radionuclide release model. If multiple waste packages fail, then the releases will occur from several point sources. However, as long as only a few waste packages fail in a given realization, then the unsaturated zone model behavior will depend on the local conditions from a few point sources. Therefore, it is important to examine the behavior under such conditions. Given the results reflected in Section 2.3.8.4.5.1, particularly Figure 2.3.8-36, the repository behavior can be characterized, to first order, by examining breakthrough curves from two locations: one in the northern region, and one in the southern region. This simplification, for the purposes of demonstrating unsaturated zone behavior, captures the primary dependence of the model in terms of hydrogeologic variability in that

one region with predominantly fracture transport (the northern release location) and one region with an interval with matrix-dominated transport (the southern release location) are selected. The locations of the two release locations are plotted in the mean travel time plot of Figure 2.3.8-36; the pink dot represents the northern release location, and the black dot represents the southern release location. Thus, the northern release point is a useful surrogate for all release points in the blue and green portions of the mean transport time plot, and the southern release point represents release locations in the yellow, orange, and red portions of the plot.

Figure 2.3.8-43 shows the normalized cumulative breakthrough curves for all species modeled as simple decay radionuclides (^{14}C, ^{135}Cs, ^{137}Cs, ^{129}I, ^{90}Sr, ^{99}Tc, ^{231}Pa, ^{229}Th, ^{232}Th, ^{232}U, ^{226}Ra, ^{36}Cl, ^{79}Se, and ^{126}Sn). The upper figure presents breakthrough curves for the northern release location, while the lower figure shows the breakthrough curves for the southern release location. These and other results for this representative case are for the glacial transition, 10th percentile infiltration scenario, selected for illustrative purposes in this section because it is the flow scenario that received the largest weight in the TSPA model after calibration using temperature and chloride observations (Section 2.3.2.4.1.2.4.5). This flow field and others used in the TSPA model are presented in Section 2.3.2. Due to pervasive fracture transport along the entire flow path, arrival times for all species are much shorter for particles released from the northern location compared to those released from the southern location. The first arrival at the water table from the northern location is within a year, versus about 400 years from the southern location. Because of the longer travel time through the matrix units, cumulative arrivals at the water table are negligible for radionuclides released from the southern location, for either relatively short-lived or strongly sorbing radionuclides, including ^{137}Cs, ^{90}Sr, ^{231}Pa, ^{229}Th, ^{232}Th, ^{232}U, ^{226}Ra, and ^{126}Sn. However, significant proportions of all 14 of these radioactive species reach the water table for releases from the northern location. This result illustrates the model's prediction that the unsaturated zone serves as a significant barrier to radionuclide migration for sorbed species released in the southern region, whereas for the northern region, the unsaturated zone provides a limited barrier to radionuclide migration even for sorbing species (for parameter values selected for this representative case). A more complete examination of the uncertainties of key parameters and their influence on the unsaturated zone as a barrier to radionuclide migration is presented in Section 2.3.8.5.5.1. Finally, the breakthrough curves for nonsorbing radionuclides with long half lives (^{129}I, ^{99}Tc, and ^{36}Cl), reach normalized breakthrough values close to unity for both release locations. The unsaturated zone provides limited barrier capability for these species, a result that also depends on the release location in the repository (SNL 2008a, Section 6.6.2.2 in Addendum 1).

Radionuclides that participate in decay chains are simulated by modeling the entire decay chain in the TSPA model. The four decay chain species that are treated in the unsaturated and saturated zone transport models are the Actinium, Neptunium, Thorium, and Uranium series; these series are presented in Section 2.3.9.3.4.2.1 and Figure 2.4-21. Important radionuclides contained in these series include the various species of the radioelements americium, plutonium, neptunium, uranium, thorium, and radium. To illustrate the model behavior of the aqueous forms of these species, simulations of the species in the decay chain are presented in which either the first or an intermediate species is input at the source (the northern or southern release point) and the behavior of the species and its daughters are plotted. Figure 2.3.8-44 shows the behavior of the Neptunium series, with ^{241}Am input as the source in Figure 2.3.8-44a, and ^{237}Np input as the source in Figure 2.3.8-44b. The parent ^{241}Am (half life of 432.7 years) is effectively retarded for the southern release point, but a small fraction reaches the water table due to fracture transport for the northern release point.

Consequently, most of the ^{241}Am releases reach the water table as ^{237}Np. The behavior of ^{237}Np in the figure is similar to that of the non- to weakly-sorbing species presented earlier. The northern release point leads to very rapid transport to the water table, whereas the southern release point exhibits significant travel times due to matrix flow and, for the case of ^{237}Np, weak sorption. The long half-life of ^{237}Np (2.14×10^6 years) leads to the eventual breakthrough of this species at the water table, and consequently the breakthroughs of the daughter species are very low.

A similar analysis for the Thorium series is presented in Figure 2.3.8-45a, with mass input at the repository as ^{240}Pu. The moderately strong sorption of ^{240}Pu and half-life of 6,560 years leads to almost complete decay of this species for the southern release location, whereas significant breakthrough at the water table is predicted for the northern release point. The first daughter in this chain, ^{236}U, has a long half life (2.342×10^7 years) and transport properties similar to those of ^{237}Np, and therefore, like ^{237}Np, ^{236}U breaks through at the water table in significant quantities. This point with respect to uranium is amplified in Figure 2.3.8-45b, a simulation of the Uranium series, with releases at the repository as ^{238}U rather than the precursor species ^{242}Pu. Note the similarity of the behavior of ^{238}U (and, by inference, of other long-lived uranium radionuclides) to that of ^{237}Np.

The Actinium series is presented in Figure 2.3.8-46, with releases as ^{243}Am shown in Figure 2.3.8-46a, and releases as ^{239}Pu shown in Figure 2.3.8-46b. The northern release location leads to significant arrivals at the water table as ^{243}Am, with lower amounts arriving as ^{239}Pu and ^{235}U. The southern release point leads to large enough travel times for essentially complete decay of both ^{243}Am and ^{239}Pu to occur, so the arrivals at the water table are as ^{235}U. A similar result with respect to release location is observed when the releases are as ^{239}Pu (Figure 2.3.8-46b).

The final decay series, the Uranium series, has two potential parent radionuclides, ^{242}Pu and ^{238}Pu, with the chains meeting at ^{234}U and decaying to ^{230}Th and ^{226}Ra thereafter. Figure 2.3.8-47a shows the results for the Uranium series for the ^{242}Pu starting point, and Figure 2.3.8-47b shows the results for the ^{238}Pu starting point. As for other cases of plutonium releases, the northern release point leads to significant arrivals of ^{242}Pu and ^{238}Pu at the water table, with the decayed fractions of these species arriving as ^{238}U (for the ^{242}Pu parent) or ^{234}U (for the ^{238}Pu parent). Because of the long half life of ^{242}Pu (3.75×10^5 years), a small fraction of ^{242}Pu reaches the water table from the southern release location (Figure 2.3.8-47a), with most of the remaining mass arriving as ^{238}U. The short half life of ^{238}Pu (87.7 years) leads to arrivals at the water table from the southern release point being dominated by ^{234}U (Figure 2.3.8-47b). The behavior of releases as ^{238}U were shown previously in Figure 2.3.8-45b, and transport of the daughter species ^{234}U closely mirrors that of ^{238}U.

Comparisons of breakthrough curves for 12 colloidal species (the irreversible colloid or Ic species, and the irreversible fast colloid or If species of ^{243}Am, ^{239}Pu, ^{241}Am, ^{240}Pu, ^{242}Pu, and ^{238}Pu) released from both the locations are illustrated in Figure 2.3.8-48. In this illustrative example, each species is modeled as a simple decaying species, with no daughter products tracked. The simulation results show that, as expected, radionuclides that are irreversibly attached to “fast” colloids (If species, representing 0.168% of the released colloidal species), which are not affected by matrix diffusion and retardation, have the shortest breakthrough times. At the northern location, within about 10 years after release, over 90% of the irreversible fast colloids travel through the unsaturated zone. Radionuclides that are irreversibly attached to “slow” colloids (Ic species), which undergo retardation due to colloid attachment/detachment processes, move more slowly than their corresponding fast colloid counterparts. The transport time of the irreversible slow colloids depends

on the colloid retardation factor, a parameter that is explored more fully in Section 2.3.8.5.5.1. Compared to the fast colloids released at the northern location, the first arrival times for the southern release location are about one order of magnitude larger, due to the thickness of the interval of unfractured rock governed by slower matrix transport. The cumulative breakthroughs for most of these irreversible fast colloids are close to unity except for Ic ^{238}Pu and Ic ^{241}Am, which are subject to radioactive decay under these conditions. In summary, most of the Ic and If colloidal species have very limited reduction due to decay in the unsaturated zone from the northern release location, whereas a somewhat larger proportion of the radionuclides decay in the unsaturated zone before reaching the water table for the southern release location.

In TSPA, radionuclides can enter the unsaturated zone transport model in either the fracture or matrix domain, depending on the nature of the hydrodynamic and transport conditions in the EBS. The results presented so far were based on the assumption that radionuclides are released at fracture nodes. Figure 2.3.8-49 compares the normalized breakthrough curves for fracture versus matrix release for ^{99}Tc released at the northern (upper figure) or southern (lower figure) release locations. For the northern release location, nearly 50% of mass released into the fracture reaches the water table within about 20 years, compared to about 5,000 years for 50% arrival for the matrix releases. For the southern release location, the breakthrough curves are very similar regardless of whether the releases are in the fracture or the matrix. When radionuclide mass is released into the matrix of the TSw at the repository horizon, local matrix percolation rates are so low that for radionuclides to escape the unsaturated zone, they must first diffuse to a nearby flowing fracture. Thus, the additional transport time is due to the slow rate of the diffusion process transporting radionuclides to the fracture. For the northern release location, the increase in travel time is pronounced for the matrix releases because the time required for back-diffusion into the fractures in the TSw is much longer than the subsequent fracture transport to the water table. In contrast, for the southern release location, the back-diffusion time is relatively short compared to the subsequent transport time through the matrix in the Calico Hills, resulting in similar breakthrough curves for the fracture and matrix releases. Overall, this process will be governed by the diffusion coefficient, spacing between flowing fractures, and, for sorbing species, sorption coefficient.

2.3.8.5.5 Sensitivity Analyses of the Unsaturated Zone Radionuclide Transport Abstraction Model

This section presents a series of sensitivity analyses examining the impact of key uncertainties in flow and transport properties on the transport of radionuclides from the repository to the water table. The unsaturated zone transport abstraction model is used for this purpose; therefore, the results reflect the uncertainty at the subsystem level of the unsaturated zone behavior as represented in the TSPA model.

In addition to transport parameter sensitivity, sensitivity analyses of hydrologic properties that were calibrated during flow field development were examined by individually varying the parameters for $\pm 1\sigma$ from their calibrated value. Representative radionuclides, including ^{99}Tc (nonsorbing), ^{237}Np (weakly sorbing), ^{240}Pu or ^{242}Pu (two strongly sorbing species differing only in their half lives), and

a colloidal radionuclide represented by ^{240}PuIc (irreversible colloid), were analyzed. In cases related to fracture–matrix interaction (i.e., matrix diffusion) (Section 2.3.8.5.5.3), colloidal radionuclides were not included because they were modeled as nondiffusive species in the unsaturated zone radionuclide transport abstraction model (SNL 2008a, Section 6.4.5).

2.3.8.5.5.1 Uncertainty in Transport Parameters and Models

The degree to which the unsaturated zone acts to limit the migration of radionuclides must be assessed with a full accounting of the uncertainties of key transport parameters and processes. Because the actual role of the unsaturated zone in the repository system as a whole must be assessed within the total-system model, simulations involving only the unsaturated zone submodel must be synthesized using a "figure of merit" that serves as a proxy for unsaturated zone performance. Two metrics of unsaturated zone performance are used in the analyses of this section. The first is the mean travel time of a radionuclide from the repository to the water table. While this travel time will be a function of the individual radionuclides through their transport parameters, it also serves as a measure of unsaturated zone travel times for other radionuclides with similar transport characteristics. The second metric, which takes into consideration the extent of radioactive decay, is defined by the following:

$$C/C_0 = \int_0^\infty f(t)e^{-kt}dt \qquad \text{(Eq. 2.3.8-2)}$$

where $f(t)$ is the travel time distribution to the water table for a radionuclide in the absence of decay, and k is the radioactive decay rate constant, which is related to the half life by the relationship $t_{1/2} = \ln(2)/k$. Physically, C/C_0 is the fraction of the releases of a radionuclide from the repository that reaches the water table before decaying and as such provides a radionuclide-specific measure of unsaturated zone performance in limiting radionuclide migration. It is especially suitable to assess the unsaturated zone performance with respect to the long term, peak dose regulatory criterion because it integrates over all travel times not just those in the first 10,000 years. In contrast, the mean travel time is a metric that can be compared to the regulatory time period of 10,000 years to assess whether the unsaturated zone alone will retard a radionuclide during that period.

The travel-time distribution depends on a number of factors, including sorption coefficient K_d, matrix diffusion coefficient D_m, and infiltration scenario. In this section, simulations covering the uncertainty ranges of these key parameters have been conducted for several selected species, including conservative species ^{99}Tc and ^{14}C, weakly sorbing species ^{237}Np, and strongly sorbing species ^{240}Pu. To ensure that simulations span the entire range of uncertainty for each parameter of interest, a common method was developed that accommodates an arbitrary uncertainty distribution. In this study, parameter values are sampled from the cumulative distribution functions (CDF) for that parameter, in equal intervals of 0.1 on the CDF axis. The exception to this approach is for the low and high ends of the CDF, which can be asymptotic at the 0 and 1 ends of the distribution, such as for the case of a normal distribution. Instead, the low and high ends are defined by values close to 0 and 1, namely minus and plus three standard deviations from the mean for a normal distribution (i.e., 0.00135 and 0.99865). For each of the species examined in these calculations, 11 values of D_m

were chosen in such a way that the values of their corresponding CDF of log(D_m) are 0.00135, 0.1, 0.2, 0.3, 0.4, 0.5, 0.6, 0.7, 0.8, 0.9, and 0.99865. Similarly, 11 values of sorption coefficient K_d selected to cover the uncertainty range. For studies in which the interrelationship between these parameters was examined, an 11 × 11 matrix of parameter combinations was used.

Figure 2.3.8-50 shows the mean log travel time (in years) of ^{99}Tc as a function of diffusion coefficient D_m for particles released at northern and southern locations, for each of the four flow fields developed in Section 2.3.2 to represent uncertainty in percolation flux for the glacial-transition climate condition. Consistent with results presented in Figure 2.3.8-42 that did not include diffusion, the mean travel time decreases significantly with the infiltration rate for both release locations. There is roughly an order of magnitude uncertainty in travel times over the range of infiltration rates in the model. With respect to diffusion coefficient, the mean travel time increases with the matrix diffusion coefficient for the northern release node, while for the southern node, the travel time is virtually independent of D_m. For the southern release location, matrix diffusion does have an impact in the fracture-dominated TSw, but the effect is masked by the longer travel times within the matrix-dominated Calico Hills units. Under matrix-dominated flow and transport conditions, the travel times are a function of the flow velocity in the matrix, and fractures play no role in providing a short-circuit pathway. Therefore, diffusion is irrelevant under these conditions. For this reason, the travel times are longer from the southern release location, and are virtually independent of diffusion coefficient.

For sorbing species, both diffusion coefficient and sorption coefficient have an influence on the travel time to the water table. In the analyses that follow, each simulation consists of a separate pair of D_m and K_d values from the 11 × 11 matrix of simulations, the mean travel time is computed, and the results are displayed in contour plots of travel time, with CDFs of K_d and D_m as the axes. Figures 2.3.8-51 and 2.3.8-52 show the mean travel times for the weakly sorbing species ^{237}Np released at the northern (Figure 2.3.8-51) and southern (Figure 2.3.8-52) nodes under four different flow fields (glacial transition, 10th, 30th, 50th, and 90th percentile infiltration rates). These comparisons reveal the following results:

- For the northern release location, mean travel times range from very short (approximately one year) for the highest infiltration scenario to greater than 100 years (but still short compared to the long half life of ^{237}Np).
- The travel times from the northern release location are a function of both K_d and D_m.
- The releases from the southern location are much longer than those in the north, and the travel times depend, to first order, on the K_d but are virtually insensitive to D_m.

The interplay between diffusion and sorption for transport through units with fracture-dominated flow is reflected in these results. Greater diffusion leads to both diffusion and sorption related delays in the transport time. This leads to larger travel times for larger values of either K_d or D_m, as well as for the discrete fracture model case, which leads to an enhancement in the contact of radionuclides with the matrix rock. However, for the southern release, all of these effects are masked by the significant travel time delays associated with slow matrix transport and sorption in the Calico Hills unit.

An analogous set of comparisons for the mean travel time for the strongly sorbing ^{240}Pu (reversibly sorbed species) are illustrated in Figures 2.3.8-53 and 2.3.8-54. Similar overall trends are observed for this strongly sorbing species as were discussed for ^{237}Np, but the travel time disparity between the northern and southern release locations is more striking. A matrix-dominated transport layer in the flow path has an extremely beneficial impact on travel time when combined with strong sorption.

The analyses presented earlier used the mean travel time as a metric. For the decay fraction C/C_0, the distribution of travel times to the water table are all considered to determine the fraction of the released radionuclide that travels through the unsaturated zone without undergoing radioactive decay. Thus, as opposed to the metric of mean travel time, which is the same for any radionuclide with similar transport properties, the decay fraction takes into account the half-life of the radionuclide when determining the effectiveness of the unsaturated zone. The results of these analyses for non-sorbing and weakly sorbing species are summarized as follows (SNL 2008a, Section 6.8.2.2 in Addendum 1):

- Due to the long half life and relatively short travel times for ^{99}Tc, this species essentially all reaches the water table without decay, yielding C/C_0 values close to unity for either the northern or southern release locations.

- A similar result is obtained for ^{237}Np due to its long half life. Despite differences due to the selection of different parameters and infiltration scenarios, more than 90% of ^{237}Np will eventually reach the water table under any of the scenarios selected (SNL 2008a, Section 6.8.2.2[b]). Although sorption delays the breakthrough curves to some extent, the delay is insufficiently long to allow significant decay to occur.

- For the nonsorbing species ^{14}C, the general patterns are similar to those of ^{99}Tc, but the shorter half life results in more substantial reduction in arrivals due to radioactive decay, especially for the 10th percentile flow case.

For more strongly sorbing radionuclides, results for aqueous ^{240}Pu are presented as an example in Figures 2.3.8-55 and 2.3.8-56. From the plots for the southern release location (Figure 2.3.8-56), it is apparent that the unsaturated zone in the southern region significantly reduces the movement of ^{240}Pu, as only less than about 1% of ^{240}Pu will reach the water table even under the most unfavorable combination of parameter values. This is due to the long travel time in this region (matrix transport and strong sorption) and relatively short half life (6.56×10^3 years) of ^{240}Pu. In contrast, the contour maps of C/C_0 for the northern release location (Figure 2.3.8-55) show greater than 80% of ^{240}Pu is predicted to reach the water table, unless the D_m is very high.

The final set of analyses examines the influence of uncertainty in the value of the colloid retardation factor R_{coll} for the irreversible Ic species of ^{240}Pu. Figure 2.3.8-57 shows the results of the decay fraction as a function of R_{coll} for the four glacial-transition flow fields. For the northern release location, travel times are larger for either lower fluid flow rates or larger values of R_{coll}, but the predicted transport times are low enough that the impact of transport time on the decay fraction is minimal for this radionuclide. The southern release location, with its interval of matrix-dominated transport, has generally larger travel times, and a smaller impact of fracture retardation of colloids, since this effect "competes with" the matrix transport time for importance. For either release

location, the decay fraction is close to unity for this species of ^{240}Pu except for the highest values of R_{coll} in the uncertainty distribution. For other Ic species with shorter half lives such as ^{238}Pu and ^{241}Am, a larger effect of R_{coll} uncertainty on the decay fraction would be expected.

2.3.8.5.5.2 Sensitivity to Hydrologic Properties

The unsaturated zone radionuclide transport abstraction model uses hydrologic properties calibrated with the site-scale unsaturated zone flow model. Uncertainty in the hydrologic properties was evaluated through a sensitivity analysis of the unsaturated zone radionuclide transport abstraction model for two key parameters: absolute permeability of both the matrix and fracture continua, and van Genuchten parameter α for both fracture and matrix continua (SNL 2008a, Section 6.6.3).

The pore size distribution index, *m*, was not investigated. Matrix *m*, which is essentially a pore-size distribution index, is well constrained in the desaturation data from core measurements and not expected to be scale dependent. There are no systematic studies in the literature to suggest that the pore-size distribution index depends on scale. As a result of the gravity-dominated water-flow process in fractures, percolation flux for fractures is similar to the unsaturated conductivity that is proportional to both absolute permeability and relative permeability determined by *m* for fractures. In this case, effects of absolute permeability and fracture *m* on percolation flux and its spatial distribution are not independent, but highly correlated. Therefore, it is adequate to employ one of the two parameters for purposes of the sensitivity study (BSC 2005b, Section 6).

Results presented in *Particle Tracking Model and Abstraction of Transport Processes* (SNL 2008a, Section 6.6.3) show that radionuclide transport time is more sensitive to matrix permeability than to the van Genuchten parameter α and fracture permeability. Increasing the matrix permeabilities results in longer transport times to the water table (representative breakthrough curve results for ^{242}Pu are shown in Figure 2.3.8-58), due to an increased relative flow fraction in the matrix. The use of the mean glacial-transition flow field from a previous version of the infiltration model (BSC 2004h, Section 6.11.3) is acceptable for examining the sensitivity of transport to changes in hydrologic properties because of the similarity of the mean infiltration rate over the repository footprint (19.8 mm/yr) to the mean percolation flux through the repository for the two most likely glacial-transition flow fields used in TSPA (Glacial-transition, 10th and 30th percentile infiltration maps: 8.97 and 24.02 mm/yr, respectively; SNL 2008a, Table 6-26 in Addendum 1). Flow conditions and their sensitivity to changes in hydrologic parameters are not expected to change with differences in the flow field of this magnitude. Decreasing the matrix permeabilities by one standard deviation from the calibrated values has a very small impact on the breakthrough curves because the flow fractions are unchanged by this parameter variation (SNL 2008a, Section 6.6.3). This results from the fact that, at very high fracture flow fractions, reducing the matrix permeability has very little effect because virtually all of the water is already flowing in the fractures. Conversely, in regions such as the CHn where flow is matrix-dominated, changing the matrix permeability affects the matrix saturation slightly but not the flow regime.

In comparison, the sensitivity of unsaturated zone transport to changes in values of the van Genuchten α parameter in both the fracture and matrix continuum is very small, as indicated by the subtle differences between the breakthrough curves for the various flow fields (SNL 2008a, Section 6.6.3, Figures 6-25 through 6-28). The breakthrough curves presented in *Particle Tracking*

Model and Abstraction of Transport Processes (SNL 2008a, Section 6.6.3) also show moderate sensitivity to changes in the value of fracture permeability (SNL 2008a, Section 6.6.3, Figures 6-29 and 6-30).

In summary, due to the low sensitivity of the model results to changes in the hydrologic parameters, as demonstrated in the analyses just presented, these uncertainties are not propagated to TSPA. In contrast, uncertainty in percolation flux is propagated due to its direct impact on transport times.

2.3.8.5.5.3 Sensitivity to Fracture–Matrix Interaction Parameters

The unsaturated zone radionuclide transport abstraction model includes two parameters that are associated with fracture–matrix interaction (i.e., matrix diffusion): the active fracture model γ parameter and the effective fracture aperture *b* (SNL 2008a, Section 6.6.4). A sensitivity analysis was performed for each parameter.

The γ parameter is associated with the effective size of the matrix block in the active fracture model. Reducing the value of γ reduces the effective size of the matrix block and therefore increases the strength of the fracture–matrix flux term. In the sensitivity analysis, the γ value of the TSw unit was varied within 0.2 to 0.6, the uncertainty range set for the TSPA model, established through comparison of the site-scale unsaturated zone flow model with the ^{14}C data (BSC 2004a, Sections 7.4.1 and 7.4.2). The γ value in other units was set to the base-case value in all but the TSw unit, because it was found that breakthrough curves were not sensitive to changing γ in other units (SNL 2008a, Section 6.6.4, Figure 6-36 and Section 7.2.3.3, Figure 7-13). Breakthrough curve results for ^{99}Tc presented previously in Section 2.3.8.4.5.2 show that lower values of γ in the TSw unit result in longer transport times and later breakthroughs, although breakthrough curves converge after approximately 6,000 years, showing less sensitivity to γ at later times (Figure 2.3.8-40).

In the unsaturated zone radionuclide transport abstraction model, the effective fracture aperture *b* is inversely proportional to the interface area between fractures and matrix available for matrix diffusion, and the area may increase with the scale of observation (SNL 2008a, Section 6.6.4). Based on results of field tracer tests, Liu, Bodvarsson et al. (2004, Figure 2) present a correlation showing the effective matrix diffusion coefficient increases with observation scale, with a typical 10- to 100-fold increase in effective diffusion coefficient for the gridblock size utilized in the unsaturated zone radionuclide transport abstraction model. Sensitivity of breakthrough curves to 10- to 100-fold increases in effective surface area for diffusion is shown in Figure 2.3.8-59. The use of the mean glacial-transition flow field from a previous version of the infiltration model (BSC 2004h, Section 6.11.3) is acceptable for examining the sensitivity of transport to changes in the surface area available for diffusion because of the similarity of the mean infiltration rate over the repository footprint (19.8 mm/yr) to the mean percolation flux through the repository for the two most likely glacial-transition flow fields used in TSPA (Glacial-transition, 10th and 30th percentile infiltration maps: 8.97 and 24.02 mm/yr, respectively; SNL 2008a, Table 6-26 in Addendum 1). The sensitivity of transport to changes in surface area are not expected to change with differences in the flow field of this magnitude. For the nonsorbing radionuclide ^{99}Tc, first arrival times are later and larger, whereas the breakthrough curves cross over at later times. This behavior is expected for transport in a fracture with diffusion into a matrix of finite dimension. For the more strongly sorbing radionuclide ^{242}Pu, much longer first arrival times are also observed with increasing surface area.

In this case, radioactive decay and very long transport times result in a reduction in late-time arrivals with increasing surface area (SNL 2008a, Section 6.6.4, Figure 6-37). This analysis suggests that as more confidence is built in the basis for the scale dependence of diffusion, the predicted performance of the unsaturated zone component of the Lower Natural Barrier would be expected to improve substantially for some radionuclides by increasing the travel times and level of radioactive decay. Nevertheless, as discussed in Section 2.3.8.4.4.4.3, the potential enhancement to matrix diffusion at larger scales is conservatively not included in TSPA.

2.3.8.5.6 Building Confidence in the Unsaturated Zone Radionuclide Transport Abstraction Model

Confidence in the unsaturated zone radionuclide transport abstraction model is developed principally through a comparison of results of the abstraction model to process model results. In addition, simulations assuming an alternative conceptual model for fracture matrix interactions provide support for the choice of the model used in TSPA, as well as illuminating the implications of that choice on the performance of the unsaturated zone in limiting radionuclide migration.

2.3.8.5.6.1 Sensitivity to Numerical Approach for Treating Fracture–Matrix Interaction

Model uncertainty was evaluated in the development of the unsaturated zone radionuclide transport process model (SNL 2007b, Section 6.19.1; see also Sections 2.3.8.4.2 and 2.3.8.4.5). Additional confidence in the model abstraction is provided by comparing the dual-permeability representation of the fracture–matrix system of the unsaturated zone, as used in the model abstraction, to an alternative representation known as the discrete fracture model (SNL 2008a, Section 7.2.3.2). The discrete fracture model alternative conceptual model produces behavior similar to that of the MINC formulation when transfer functions developed with a discrete fracture model are used (SNL 2008a, Section 6.7). The MINC model and the discrete fracture model capture sharp gradients in concentration in the matrix near each fracture, thereby resulting in later breakthrough times because the fracture–matrix interaction allows for increased diffusion. This approach also enhances radionuclide retardation due to sorption (SNL 2008a, Section 6.7). The approach used to capture sharp gradients in the matrix embodied in either the MINC or discrete fracture models is deemed to be reasonable because it is based on sound physical principles. For this reason, the MINC approach itself has been used to interpret some of the tracer test results.

For ^{99}Tc, a nonsorbing radionuclide, Figure 2.3.8-60 shows first arrival times are later with the discrete fracture model than the dual-permeability model, although breakthrough curves for both the dual-permeability and the discrete fracture models converge at later times. This figure also shows that the conceptual uncertainty between the dual-permeability model versus the alternative discrete fracture model is more significant than parameter uncertainty related to the γ parameter, which is varied from 0.2 to 0.6 in the sensitivity cases shown. The differences among the breakthrough curves are more pronounced with sorbing radionuclides, as illustrated in Figure 2.3.8-61 for ^{242}Pu. The use of the mean glacial-transition flow field from a previous version of the infiltration model (BSC 2004h, Section 6.11.3) is acceptable for examining the sensitivity of transport to changes in the conceptual model for matrix diffusion because of the similarity of the mean infiltration rate over the repository footprint (19.8 mm/yr) to the mean percolation flux through the repository for the two most likely glacial-transition flow fields used in TSPA

(Glacial-transition, 10th and 30th percentile infiltration maps: 8.97 and 24.02 mm/yr, respectively; SNL 2008a, Table 6-26 in Addendum 1). The sensitivity of transport to changes in the matrix diffusion conceptual model are not expected to change with differences in the flow field of this magnitude. The differences, as indicated by the separation in time between breakthrough curves for the dual-permeability and discrete fracture model, increase with increasing sorption coefficient. The discrete fracture model results in much longer transport times to the water table for sorbing radionuclides (SNL 2008a, Section 6.7).

This result is reinforced in Figure 2.3.8-62, plots of decay fraction of ^{240}Pu for the northern release location for the discrete fracture model. These results are to be compared to those of the dual-k model in Figure 2.3.8-55. For example, for the discrete fracture model under glacial transition, 10th percentile flow field, the unsaturated zone is predicted to significantly limit the migration of this radionuclide if both K_d and D_m are large, while at the same conditions with the dual-k model, greater than 80% of ^{240}Pu is predicted to reach the water table, unless the D_m is very high (SNL 2008a, Section 6.8.2.2[b]). This result shows that under certain conditions (fracture-dominated transport) and for certain species (strongly sorbing species with half lives up to thousands of years, rather than millions of years), the predicted performance of the unsaturated zone barrier depends strongly on the choice of conceptual model for diffusion (SNL 2008a, Section 6.8.2.2[b]; SNL 2007b, Section 7). Because the dual-k model has been validated in the process model validation activities, and has been shown to provide a more conservative result with respect to first arrival times at the water table (SNL 2007b, Section 7), it has been selected for use in the TSPA model (SNL 2008a, Section 7.3).

2.3.8.5.6.2 Comparison with the Unsaturated Zone Radionuclide Transport Process Model

Confidence in the unsaturated zone radionuclide transport abstraction model is developed by comparing it to the three-dimensional unsaturated zone radionuclide transport process model (Section 2.3.8.4). In these comparisons, the nonsorbing radionuclide ^{99}Tc was selected because it is representative of all nonsorbing radionuclides in the TSPA model. For all model comparisons, breakthrough at the present-day water table is simulated for a release function consisting of a pulse of radionuclide introduced uniformly across the repository horizon (SNL 2008a, Section 7.2.3.1).

In this benchmarking exercise, the three present-day flow fields from a previous version of the infiltration model (BSC 2004h, Section 6.11.1) are used for the comparison. This approach is acceptable for the purposes of benchmarking the abstraction model against the process model. The main differences between the flow fields presented in Section 2.3.2 and those used for these benchmarking runs are the mean infiltration rate and the spatial variability of the local percolation rate (SNL 2008a, Section 7.2.3). Despite these differences, the mean infiltration rates from the older flow fields span a considerable portion of the range of repository percolation rates of the new flow fields as is demonstrated by comparing the range of mean infiltration rates under present-day climate conditions of 0.4 to 11.6 mm/yr from *Simulation of Net Infiltration for Present-Day and Potential Future Climates* (BSC 2004h, Table 6-10) to the range of median percolation rates of 3.93 to 35.27 mm/yr from *Particle Tracking Model and Abstraction of Transport Processes* (SNL 2008a, Table 6-26 in Addendum 1). Furthermore, the basic flow and transport processes simulated in the model used in TSPA are the same as those used in previous versions of the model. Thus, the TSPA model, though different in detail, is fundamentally similar to the model on which this comparison

is based. Therefore, the use of older process model results (based on an older flow field developed with a previous version of the infiltration model) for the purposes of benchmarking the abstraction model is justified. The exact results of these model runs are not used in TSPA except for confidence building of the validity of the abstraction model via this benchmarking exercise.

Figure 2.3.8-63 shows the cumulative transport time distributions through the unsaturated zone for the two models. For the lowest infiltration scenario, the early arrival of a small fraction of the released mass and the steepening breakthrough curve after 10,000 years are observed in both models (SNL 2008a, Section 7.2.3.1). The plateau in normalized breakthrough values between 0.4 and 0.5 at long times is due to radioactive decay of ^{99}Tc for the conditions of this comparison test. For the mean infiltration flow field, the agreement of the process and abstraction models is also excellent at all transport times. For the upper infiltration scenario, the unsaturated zone radionuclide transport abstraction model predicts a somewhat earlier arrival for the fastest-moving solute, indicating a difference in the way the two models handle diffusion in rapid fracture flow. Nevertheless, the unsaturated zone radionuclide transport abstraction model bounds the early portion of the breakthrough curve for this case (SNL 2008a, Section 7.2.3.1). The comparison indicates that the main features of the unsaturated zone radionuclide transport process model are included in the unsaturated zone radionuclide transport abstraction model.

Additional unsaturated zone radionuclide transport abstraction model validation simulations, including comparisons to discrete fracture models and comparisons to the process model on a two-dimensional cross-sectional grid, show comparable consistency between the unsaturated zone radionuclide transport abstraction model and alternative numerical models (SNL 2008a, Sections 7.2.1 and 7.2.2).

2.3.8.6 Conclusions

The transport of radionuclides away from the repository in the unsaturated zone component of the Lower Natural Barrier depends on the rate and pathways of flow within the unsaturated zone, the solubility of radionuclides, and the rate of transport by colloids. Several processes contribute to the ability of the unsaturated zone component of the Lower Natural Barrier to reduce the movement of radionuclides, including the diffusion of radionuclides from water flowing in fractures into the pores of the rock matrix, sorption of radionuclides onto rock or mineral surfaces, hydrodynamic dispersion or spreading, colloid filtration, and radioactive decay.

The processes and characteristics that have been determined to be important to the capability of the unsaturated zone component of the Lower Natural Barrier (Section 2.1.2.3) include:

- **Fractures**—Fractures below the repository conduct the majority of the percolation flux through the unsaturated zone, although: (1) the low-matrix-permeability zeolitic rocks of the CHn cause increased lateral diversion toward the faults; and (2) the vitric CHn is dominated by matrix flow. The extent to which fractures control unsaturated zone radionuclide transport varies spatially, and depends on the local hydrogeologic characteristics of the rock.

- **Faults**—Faults provide fast flow and radionuclide transport pathways through the unsaturated zone, particularly below the northern region of the repository where the low

matrix permeability of the underlying zeolitic CHn unit promotes lateral flow and transport towards and down faults.

- **Climate Change**—Future climate change causes several responses in the unsaturated zone beneath the repository, including changes in percolation flux and attendant radionuclide transport, water table rise, and recharge to the saturated zone. Precipitation and net infiltration into the unsaturated zone tends to increase with future climate change causing an increase in fracture flux and, hence, a reduction in the effectiveness of matrix diffusion.

- **Climate Modification Increases Recharge**—The ability of the unsaturated zone to prevent or substantially reduce the rate of movement of radionuclides is dependent on the flux of water through the unsaturated zone and the distribution of that flux within the fractured rock mass. An increase in recharge associated with the monsoon and glacial-transition climate states can significantly reduce the capability of the unsaturated zone feature to reduce the rate of radionuclide movement.

- **Stratigraphy**—Stratigraphy and associated hydrologic properties have significant effects on radionuclide migration through the unsaturated zone due to the contribution of faults in conducting flow below the repository and due to the different flow characteristics of the TSw and zeolitic and vitric CHn and CFu units. In particular, the low matrix permeability of the zeolitic CHn unit beneath the northern half of the repository block promotes fracture flow and/or lateral diversion towards faults. In contrast, the unaltered, vitric CHn unit beneath the southern region of the repository block has a relatively high matrix porosity and permeability, and matrix flow dominates.

- **Rock Properties of Host Rock and Other Units**—Percolation of water in the unsaturated zone below the repository is significantly affected by the hydrogeologic properties of the rock units above and below the repository. In addition, radionuclide transport is affected by the sorptive and diffusive properties of the host rock and underlying units.

- **Unsaturated Groundwater Flow in the Geosphere**—Unsaturated groundwater flow below the repository defines the redistribution of percolation flux in the unsaturated zone as a function of time, and is the primary mechanism for radionuclide transport below the repository. The fracture characteristics are also significant in determining the rate of radionuclide movement in the unsaturated zone.

- **Perched Water Develops**—The strongly altered northern part of the CHn unit is composed of zeolites and clays with low permeability and poorly developed, sparsely connected fractures. Because of low permeability, perched water may form at the contacts with CHn zeolitic (CHnz) tuffs below the northern half of the repository block, and a large portion of the percolating flux may be diverted laterally to the east towards the faults, which act as main pathways for fast flow and transport in the unsaturated zone.

- **Fracture Flow in the Unsaturated Zone**—The rate of movement of radionuclides in the unsaturated zone is dependent on the flux of water through the fractured rock mass. This

flux is distributed between faults, fractures, and the matrix of the host rock and other units in the unsaturated zone.

- **Matrix Imbibition in the UZ**—Water and radionuclides may be imbibed into the matrix between the flowing fractures. Matrix imbibition affects the distribution of flow between fractures and the matrix in the fractured unsaturated zone. Matrix imbibition is dominant in the Calico Hills nonwelded vitric rock. The imbibition process results in a transition of water from fracture flow to percolation of water through the rock matrix, which substantially slows radionuclide transport.

- **Advection and Dispersion in the Unsaturated Zone**—Flow in the fractured rock system below the repository is dominated by fracture flow in units for which the permeability of the rock matrix is too low to enable percolating water to pass through it. In this case, radionuclide transport is primarily advection dominated, and the influence of dispersion may be important. However, when compared to the spreading of radionuclides due to matrix diffusion effects, the impact on transport times of longitudinal dispersion is expected to be small.

- **Matrix Diffusion in the Unsaturated Zone**—Matrix diffusion results in the diffusion of dissolved radionuclides from the fractures into the matrix of the rock. Because the advective transport is significantly slower in the matrix, matrix diffusion can be an efficient retarding mechanism for nonsorbing radionuclides and can facilitate contact with sorbing matrix minerals to further retard moderately to strongly sorbing radionuclides.

- **Sorption in the Unsaturated Zone**—Radionuclides released from the repository have varying retardation characteristics. Several radionuclides (^{90}Sr, ^{137}Cs, ^{239}Pu, ^{240}Pu, ^{241}Am, and ^{243}Am) that are the dominant contributors to the total inventory are significantly retarded in the unsaturated zone when there has been significant matrix diffusion or matrix dominated flow in the vitric Calico Hills.

The results of the unsaturated zone radionuclide transport process and abstraction models (Section 2.3.8.4) indicate that the rate of radionuclide transport is highly dependent on the characteristics of individual radionuclides, the form in which the radionuclide is released (dissolved or colloidal), and the uncertainties associated with transport parameters. The unsaturated portion of the Lower Natural Barrier is very effective at reducing the movement of strongly sorbing radioelements (e.g., cesium, strontium, americium, and plutonium) through the unsaturated zone, particularly for releases below which an interval of vitric Calico Hills exists. Transport through the rock matrix in that unit, which is present beneath release points in the southern repository region, leads to very long travel times compared to release locations in the northern repository region. The unsaturated zone is less effective for nonsorbing species (e.g., ^{99}Tc and ^{129}I) that travel through fast fracture flow paths, and are not significantly retarded.

Uncertainties Associated with Lower Natural Barrier Capability—The performance of the unsaturated zone component of the Lower Natural Barrier is subject to uncertainty that is a function of the applicability of the conceptual and numerical models used to describe flow and transport. Additional uncertainty results from the degree of knowledge of the flow and transport characteristics of the Yucca Mountain site. Uncertainties related to the site-scale unsaturated zone

flow model are summarized in Section 2.3.2. To accommodate both variability and uncertainty, many of the input parameters to the unsaturated zone radionuclide transport process and abstraction models have been defined as probabilistic distributions, including sorption coefficients, matrix diffusion coefficients, fracture–matrix interaction parameters, colloid sorption coefficients and colloid concentrations, and colloid retardation factors for unsaturated zone transport. This approach allows a range of uncertainty commensurate with the available information to be directly incorporated into the unsaturated zone radionuclide transport process and abstraction models and the TSPA. Data uncertainties associated with analyses of the unsaturated zone component of the Lower Natural Barrier are described in Sections 2.3.8.3 and 2.3.2.3. The model uncertainties associated with the analysis of the unsaturated zone component of the Lower Natural Barrier are described in Sections 2.3.8.4 and 2.3.2.4.

Model uncertainty has been assessed by comparison with results from alternative conceptual models (Section 2.3.8.4.2). In addition, the unsaturated zone radionuclide transport model accounts for uncertainties associated with several processes that affect transport, including potential fracture flow in the vitric CHn unit, diversion of groundwater flow away from the zeolitic CHn unit, and fracture–matrix interaction along flow paths in fracture systems within the TSw unit.

The variability and uncertainty in barrier capability is reflected in the broad range of transport times and radionuclide breakthrough curves resulting from the unsaturated zone radionuclide transport models. Sensitivity studies indicate that uncertainty in the performance of the Lower Natural Barrier is significant with respect to TSPA (Section 2.3.8.4.5). For example, uncertainty in the effectiveness of matrix diffusion and sorption can have a substantial effect on transport times for many radionuclides. In addition, climatic changes affecting infiltration can shift transport rates by about an order of magnitude, and uncertainties at a given climatic condition are similar in magnitude. Higher infiltration is invariably associated with faster transport of radionuclides to the water table.

Conservatisms in Models Used to Assess the Capability of the Unsaturated Zone Portion of the Lower Natural Barrier—Several conservative assumptions have been incorporated in models of unsaturated zone radionuclide transport. The consequence of these assumptions is faster and greater transport of radionuclides through the unsaturated zone at Yucca Mountain than would have been predicted had geologic observations and geochemical and experimental data relevant to flow and transport been interpreted with a less conservative model. For example, median (50%) breakthrough curves for some aqueous radionuclides (Section 2.3.8.5.4) occur in less than 100 years, even though isotopic analyses of water in the unsaturated zone (perched water and pore water in the nonwelded units) indicate apparent ages of thousands of years (Section 2.3.2.3.4). The explanation for this discrepancy is that the apparent age obtained from an isotopic measurement likely derives from a mixture of unknown quantities of fluids of different isotopic compositions and hence ages. The resulting age measurement is therefore a mixed age reflecting the mixing of old and young fluids, resulting in an apparent age in the thousands of years. Thus, models developed for use in unsaturated zone transport analyses conservatively err on the side of honoring the presence of short travel times, perhaps at the expense of under-predicting the performance of the unsaturated zone.

Comparison of radionuclide breakthrough curves produced by the dual-permeability modeling approach used in the unsaturated zone radionuclide transport abstraction model (Figures 2.3.8-60

to 2.3.8-61) to those produced by the discrete fracture model demonstrates the dual-permeability approach is conservative. The alternative approach produces later breakthrough times because it includes increased fracture–matrix interaction, which results in increased diffusion and longer contact times leading to stronger sorption. Conditions along some portions of the unsaturated zone flow paths are likely to lead to increased fracture–matrix interaction. Therefore, use of the dual-permeability modeling approach provides conservative estimates of transport times through the unsaturated zone.

There are also several specific conservative assumptions contained in the unsaturated zone radionuclide transport model. Climate change is implemented by an instantaneous change from one steady-state flow field to another, with a corresponding instantaneous rise in the water table to a minimum value of 850 m. This approach is conservative because when the climate change occurs, the time it takes for radionuclides to reach the saturated zone is immediately shortened, despite evidence from isotopic and geochemical studies that changes in the unsaturated zone flow regime at depth occur over thousands of years (Section 2.3.2.3.4). The amount of rise in the water table is also conservative (Section 2.3.9.2.4).

Sorption of radionuclides on fracture surfaces is not considered in the unsaturated zone radionuclide transport model despite the moderately to strongly sorbing characteristics of many radionuclides and the presence of sorbing minerals in fractures. The exception to this statement is for radionuclide transport within zones designated as fault zones, which nevertheless have short transport times due to the low effective fracture porosity assigned to accentuate rapid fracture transport. The conservatism of assuming no sorption on fractures throughout most of the domain eliminates retardation of radionuclides in fractures and yields smaller radionuclide transport times. The treatment of colloid transport in the unsaturated zone radionuclide transport model is also conservative, in that the model includes an unretarded colloid fraction that is based on a 100-year transport time which, for a combined unsaturated zone and saturated zone flow path, will typically be short compared to the actual modeled transport time (SNL 2008a, Section 6.5.13). The use of a shorter time results in a conservatively high unretarded colloid fraction, thereby increasing the radionuclide mass that reaches the saturated zone rapidly via colloids.

Summary of Consistency between TSPA Model Abstractions and Process Models—The unsaturated zone radionuclide transport process model, abstraction model, and the TSPA model all use consistent definitions of the Yucca Mountain site and system and flow within the unsaturated zone (Section 2.4.2.3.1). The model grid, calibrated properties, and flow fields (percolation fluxes) developed for the site-scale unsaturated zone flow model are also used by the unsaturated zone radionuclide transport process and abstraction models, as well as the thermal-hydrologic-chemical environment model and the seepage model in TSPA (Figure 2.3.8-2). The effects of future climate changes are also propagated consistently through the flow, thermal-hydrologic-chemical environment, and transport abstraction models.

One difference between the unsaturated zone flow and transport models implemented in the TSPA is that, in the unsaturated zone radionuclide abstraction model, fracture frequency, matrix water content, effective permeability and fracture porosity are sampled from a probabilistic distribution for every realization for different rock units. In calculating the flow fields in the site-scale unsaturated zone flow model, these properties were held constant at conservative fixed values. This is appropriate because the uncertainty in flow fields was derived primarily from variation in

infiltration rather than from variation in rock properties. In the transport models, rock properties significantly affect the movement of radionuclides. Therefore, probabilistic distributions were used to more realistically propagate uncertainty in transport.

Summary of Key Output Parameters to TSPA—The unsaturated zone radionuclide transport abstraction model, called the unsaturated zone transport submodel in the TSPA, calculates the movement of radionuclides released from the EBS into the unsaturated zone and downward to the water table. Breakthrough curves for 27 aqueous and 12 colloidal species are calculated for present-day, monsoon, and glacial-transition climates states. Representative transport results in the form of an example plot of normalized cumulative breakthrough curves are presented in Section 2.3.8.5.4. Section 2.3.8.5.5 shows the results of sensitivity studies that were used to establish the parameters most important to unsaturated zone radionuclide transport. The radionuclide mass flux reaching the water table depends on release rates and locations, and is simulated in the TSPA. At the water table, radionuclides are captured at the base of the model in four regions directly beneath the repository. The TSPA transfers any radionuclide that reaches the water table from the unsaturated zone transport system to the saturated zone transport system.

2.3.8.7 General References

Allard, B. 1982. *Sorption of Actinides in Granitic Rock.* SKB TR-82-21. Stockholm, Sweden: Svensk Kärnbränsleförsörjning A.B. TIC: 205892.

Allard, B. and Beall, G.W. 1979. "Sorption of Americium on Geologic Media." *Journal of Environmental Science and Health*, *A14* (6), 507–518. New York, New York: Marcel Dekker. TIC: 224102.

Allard, B.; Beall, G.W.; and Krajewski, T. 1980. "The Sorption of Actinides in Igneous Rocks." *Nuclear Technology*, *49* (3), 474–480. La Grange Park, Illinois: American Nuclear Society. TIC: 245772.

Allard, B.; Olofsson, U.; Torstenfelt, B.; and Kipatsi, H. 1983. *Sorption Behaviour of Well-Defined Oxidation States.* SKB TR-83-61. Stockholm, Sweden: Svensk Kärnbränsleförsörjning A.B. TIC: 206122.

Altman, W.D.; Donnelly, J.P.; and Kennedy, J.E. 1988. *Qualification of Existing Data for High-Level Nuclear Waste Repositories: Generic Technical Position*. NUREG-1298. Washington, D.C.: U.S. Nuclear Regulatory Commission. TIC: 200652.

Bird, R.B.; Stewart, W.E.; and Lightfoot, E.N. 1960. *Transport Phenomena.* New York, New York: John Wiley & Sons. TIC: 208957.

BSC (Bechtel SAIC Company) 2004a. *Conceptual Model and Numerical Approaches for Unsaturated Zone Flow and Transport.* MDL-NBS-HS-000005 REV 01. Las Vegas, Nevada: Bechtel SAIC Company. ACC: DOC.20040922.0006.

BSC 2004b. *Development of Numerical Grids for UZ Flow and Transport Modeling.* ANL-NBS-HS-000015 REV 02. Las Vegas, Nevada: Bechtel SAIC Company. ACC: DOC.20040901.0001.

BSC 2004c. *In Situ Field Testing of Processes*. ANL-NBS-HS-000005 REV 03. Las Vegas, Nevada: Bechtel SAIC Company. ACC: DOC.20041109.0001.

BSC 2004d. *Yucca Mountain Site Description.* TDR-CRW-GS-000001 REV 02 ICN 01. Two volumes. Las Vegas, Nevada: Bechtel SAIC Company. ACC: DOC.20040504.0008.

BSC 2004e. *Seepage Model for PA Including Drift Collapse.* MDL-NBS-HS-000002 REV 03. Las Vegas, Nevada: Bechtel SAIC Company. ACC: DOC.20040922.0008.

BSC 2004f. *Saturated Zone Colloid Transport*. ANL-NBS-HS-000031 REV 02. Las Vegas, Nevada: Bechtel SAIC Company. ACC: DOC.20041008.0007.

BSC 2004g. *Natural Analogue Synthesis Report*. TDR-NBS-GS-000027 REV 01. Las Vegas, Nevada: Bechtel SAIC Company. ACC: DOC.20040524.0008.

BSC 2004h. *Simulation of Net Infiltration for Present-Day and Potential Future Climates.* MDL-NBS-HS-000023 REV 00. Las Vegas, Nevada: Bechtel SAIC Company. ACC: DOC.20041109.0004.

BSC 2004i. *UZ Flow Models and Submodels.* MDL-NBS-HS-000006 REV 02. Las Vegas, Nevada: Bechtel SAIC Company. ACC: DOC.20041101.0004; DOC.20050629.0003.

BSC 2005a. *Mountain-Scale Coupled Processes (TH/THC/THM) Models*. MDL-NBS-HS-000007 REV 03. Las Vegas, Nevada: Bechtel SAIC Company. ACC: DOC.20050825.0007.

BSC 2005b. *Parameter Sensitivity Analysis for Unsaturated Zone Flow.* ANL-NBS-HS-000049 REV 00. Las Vegas, Nevada: Bechtel SAIC Company. ACC: DOC.20050808.0005.

BSC 2006a. *Analysis of Alcove 8/Niche 3 Flow and Transport Tests.* ANL-NBS-HS-000056 REV 00. Las Vegas, Nevada: Bechtel SAIC Company. ACC: DOC.20060901.0003.

BSC 2006b. *Chlorine-36 Validation Study at Yucca Mountain, Nevada.* TDR-NBS-HS-000017 REV 00. Las Vegas, Nevada: Bechtel SAIC Company. ACC: DOC.20060829.0002.

Campbell, K.; Wolfsberg, A.; Fabryka-Martin, J.; and Sweetkind, D. 2003. "Chlorine-36 Data at Yucca Mountain: Statistical Tests of Conceptual Models for Unsaturated-Zone Flow." *Journal of Contaminant Hydrology, 62–63*, 43–61. New York, New York: Elsevier. TIC: 254205.

Carey, J.W. and Bish, D.L. 1996. "Equilibrium in the Clinoptilolite–H_2O System." *American Mineralogist*, *81*, 952–962. Washington, D.C.: Mineralogical Society of America. TIC: 233145.

Carey, J.W. and Bish, D.L. 1997. "Calorimetric Measurement of the Enthalpy of Hydration of Clinoptilolite." *Clays and Clay Minerals*, *45* (6), 826–833. Long Island City, New York: Pergamon Press. TIC: 235733.

CRWMS M&O (Civilian Radioactive Waste Management System Management and Operating Contractor) 1998. *Evaluation of Flow and Transport Models of Yucca Mountain, Based on Chlorine-36 and Chloride Studies for FY98.* BA0000000-01717-5700-00007 REV 00. Las Vegas, Nevada: Civilian Radioactive Waste Management System Management and Operating Contractor. ACC: MOL.19981208.0119.

Doughty, C. 1999. "Investigation of Conceptual and Numerical Approaches for Evaluating Moisture, Gas, Chemical, and Heat Transport in Fractured Unsaturated Rock." *Journal of Contaminant Hydrology*, *38* (1–3), 69–106. New York, New York: Elsevier. TIC: 244160.

Duffy, C.J. 1993a. *Kinetics of Silica-Phase Transitions*. LA-12564-MS. Los Alamos, New Mexico: Los Alamos National Laboratory. ACC: NNA.19900112.0346.

Duffy, C.J. 1993b. *Preliminary Conceptual Model for Mineral Evolution in Yucca Mountain.* LA-12708-MS. Los Alamos, New Mexico: Los Alamos National Laboratory. ACC: NNA.19900117.0152.

Fabryka-Martin, J.T.; Flint, A.L.; Sweetkind, D.S.; Wolfsberg, A.V.; Levy, S.S.; Roemer, G.J.C.; Roach, J.L.; Wolfsberg, L.E.; and Duff, M.C. 1997. *Evaluation of Flow and Transport Models of Yucca Mountain, Based on Chlorine-36 Studies for FY97.* LA-CST-TIP-97-010. Los Alamos, New Mexico: Los Alamos National Laboratory. ACC: MOL.19980204.0916.

Fabryka-Martin, J.T.; Turin, H.J.; Wolfsberg, A.V.; Brenner, D.L.; Dixon, P.R.; and Musgrave, J.A. 1998. *Summary Report of Chlorine-36 Studies as of August 1996.* LA-13458-MS. Los Alamos, New Mexico: Los Alamos National Laboratory. ACC: MOL.20031119.0395.

Fabryka-Martin, J.; Wolfsberg, A.V.; Dixon, P.R.; Levy, S.; Musgrave, J.; and Turin, H.J. 1996. *Summary Report of Chlorine-36 Studies: Sampling, Analysis and Simulation of Chlorine-36 in the Exploratory Studies Facility.* Milestone 3783M. Los Alamos, New Mexico: Los Alamos National Laboratory. ACC: MOL.19970103.0047.

Fabryka-Martin, J.T.; Wolfsberg, A.V.; Dixon, P.R.; Levy, S.S.; Musgrave, J.A.; and Turin, H.J. 1997. *Summary Report of Chlorine-36 Studies: Sampling, Analysis, and Simulation of Chlorine-36 in the Exploratory Studies Facility.* LA-13352-MS. Los Alamos, New Mexico: Los Alamos National Laboratory. ACC: MOL.19980812.0254.

Fabryka-Martin, J.T.; Wolfsberg, A.V.; Levy, S.S.; Roach, J.L.; Winters, S.T.; Wolfsberg, L.E.; Elmore, D.; and Sharma, P. 1998. "Distribution of Fast Hydrologic Paths in the Unsaturated Zone at Yucca Mountain." *High-Level Radioactive Waste Management, Proceedings of the Eighth International Conference, Las Vegas, Nevada, May 11-14, 1998.* Pages 93–96. La Grange Park, Illinois: American Nuclear Society. TIC: 237082.

Fabryka-Martin, J.T.; Wolfsberg, A.V.; Roach, J.L.; Winters, S.T.; and Wolfsberg, L.E. 1998. "Using Chloride to Trace Water Movement in the Unsaturated Zone at Yucca Mountain." *High-Level Radioactive Waste Management, Proceedings of the Eighth International Conference, Las Vegas, Nevada, May 11-14, 1998.* Pages 264–268. La Grange Park, Illinois: American Nuclear Society. TIC: 237082.

Francis, N.D. 1997. "The Base-Case Thermal Properties for TSPA-VA Modeling." Memorandum from N.D. Francis (SNL) to Distribution, April 16, 1997. ACC: MOL.19980518.0229.

Freeze, R.A. and Cherry, J.A. 1979. *Groundwater.* Englewood Cliffs, New Jersey: Prentice-Hall. TIC: 217571.

Goodell, P.C. 1981. "Geology of the Peña Blanca Uranium Deposits, Chihuahua, Mexico." *Uranium in Volcanic and Volcaniclastic Rocks, Symposium held in El Paso, Texas, February 25-27, 1980.* Goodell, P.C. and Waters, A.C., eds. AAPG Studies in Geology No. 13. Pages 275-291. Tulsa, Oklahoma: American Association of Petroleum Geologists. TIC: 247861.

Ibaraki, M. and Sudicky, E.A. 1995. "Colloid-Facilitated Contaminant Transport in Discretely Fractured Porous Media 1. Numerical Formulation and Sensitivity Analysis." *Water Resources Research*, *31* (12), 2945–2960. Washington, D.C.: American Geophysical Union. TIC: 245719.

Kretzschmar, R.; Barmettler, K.; Grolimund, D.; Yan, Y.; Borkovec, M.; and Sticher, H. 1997. "Experimental Determination of Colloid Deposition Rates and Collision Efficiencies in Natural Porous Media." *Water Resources Research*, *33* (5), 1129–1137. Washington, D.C.: American Geophysical Union. TIC: 246817.

Kretzschmar, R.; Robarge, W.P.; and Amoozegar, A. 1995. "Influence of Natural Organic Matter on Colloid Transport Through Saprolite." *Water Resources Research*, *31* (3), 435–445. Washington, D.C.: American Geophysical Union. TIC: 246819.

LA0112WS831372.003. Busted Butte UZ Transport Test: Phase II Normalized Collection Pad Tracer Concentrations. Submittal date: 12/05/2001.

LA0201WS831372.007. Busted Butte UZ Transport Test: Phase II Normalized Collection Pad Metal Tracer Concentrations. Submittal date: 01/22/2002.

LANL (Los Alamos National Laboratory) 2003. *Validation Test Plan (VTP) for the FEHM Application Version 2.21*. 10086-VTP-2.21-00. Los Alamos, New Mexico: Los Alamos National Laboratory. ACC: MOL.20031031.0264; MOL.20031031.0265.

Lide, D.R., ed. 1992. *CRC Handbook of Chemistry and Physics.* 73rd Edition. Boca Raton, Florida: CRC Press. TIC: 255239.

Liu, H.H.; Bodvarsson, G.S.; and Zhang, G. 2004. "Scale Dependency of the Effective Matrix Diffusion Coefficient." *Vadose Zone Journal, 3* (1), 312–315. Madison, Wisconsin: Soil Science Society of America. TIC: 256150.

Liu, H. H.; Doughty, C.; and Bodvarsson, G.S. 1998. "An Active Fracture Model for Unsaturated Flow and Transport in Fractured Rocks." *Water Resources Research*, *34* (10), 2633–2646. Washington, D.C.: American Geophysical Union. TIC: 243012.

Liu, H. H.; Haukwa, C.B.; Ahlers, C.F.; Bodvarsson, G.S.; Flint, A.L.; and Guertal, W.B. 2003. "Modeling Flow and Transport in Unsaturated Fractured Rock: An Evaluation of the Continuum Approach." *Journal of Contaminant Hydrology*, *62–63*, 173–188. New York, New York: Elsevier. TIC: 254205.

McGraw, M.A. and Kaplan, D.I. 1997. *Colloid Suspension Stability and Transport Through Unsaturated Porous Media*. PNNL-11565. Richland, Washington: Pacific Northwest National Laboratory. TIC: 246723.

Montazer, P. and Wilson, W.E. 1984. *Conceptual Hydrologic Model of Flow in the Unsaturated Zone, Yucca Mountain, Nevada*. Water-Resources Investigations Report 84-4345. Lakewood, Colorado: U.S. Geological Survey. ACC: NNA.19890327.0051.

Neretnieks, I. 2002. "A Stochastic Multi-Channel Model for Solute Transport—Analysis of Tracer Tests in Fractured Rock." *Journal of Contaminant Hydrology*, *55* (3–4), 175–211. New York, New York: Elsevier. TIC: 253977.

Neuman, S.P. 1990. "Universal Scaling of Hydraulic Conductivities and Dispersivities in Geologic Media." *Water Resources Research*, *26* (8), 1749–1758. Washington, D.C.: American Geophysical Union. TIC: 237977.

Parrington, J.R.; Knox, H.D.; Breneman, S.L.; Baum, E.M.; and Feiner, F. 1996. *Nuclides and Isotopes, Chart of the Nuclides.* 15th Edition. San Jose, California: General Electric Company and KAPL, Inc. TIC: 233705.

Pearcy, E.C.; Prikryl, J.D.; and Leslie, B.W. 1995. "Uranium Transport Through Fractured Silicic Tuff and Relative Retention in Areas with Distinct Fracture Characteristics." *Applied Geochemistry, 10,* 685-704. Oxford, United Kingdom: Elsevier. TIC: 246848.

Pigford, T.H.; Chambré, P.L.; Albert, M.; Foglia, M.; Harada, M.; Iwamoto, F.; Kanki, T.; Leung, D.; Masuda, S.; Muraoka, S.; and Ting, D. 1980. *Migration of Radionuclides Through Sorbing Media Analytical Solutions II*. LBL-11616. Two volumes. Berkeley, California: Lawrence Berkeley National Laboratory. TIC: 211541.

Potter, C.J.; Dickerson, R.P.; Sweetkind, D.S.; Drake, R.M., II; Taylor, E.M.; Fridrich, C.J.; San Juan, C.A.; and Day, W.C. 2002. *Geologic Map of the Yucca Mountain Region, Nye County, Nevada.* Geologic Investigations Series I-2755. Denver, Colorado: U.S. Geological Survey. TIC: 253945.

Pruess, K. and Narasimhan, T.N. 1985. "A Practical Method for Modeling Fluid and Heat Flow in Fractured Porous Media." *Society of Petroleum Engineers Journal*, *25* (1), 14–26. Dallas, Texas: Society of Petroleum Engineers. TIC: 221917.

Reimus, P.W.; Adams, A.; Haga, M.J.; Humphrey, A.; Callahan, T.; Anghel, I.; and Counce, D. 1999. *Results and Interpretation of Hydraulic and Tracer Testing in the Prow Pass Tuff at the C-Holes.* Milestone SP32E7M4. Los Alamos, New Mexico: Los Alamos National Laboratory. TIC: 246377.

Reimus, P.W.; Callahan, T.J.; Ware, S.D.; Haga, M.J.; and Counce, D.A. 2007. "Matrix Diffusion Coefficients in Volcanic Rocks at the Nevada Test Site: Influence of Matrix Porosity, Matrix Permeability, and Fracture Coating Minerals." *Journal of Contaminant Hydrology, 93*, 85–95. New York, New York: Elsevier. TIC: 259673.

Reimus, P.W.; Ware, S.D.; Benedict, F.C.; Warren, R.G.; Humphrey, A.; Adams, A.; Wilson, B.; and Gonzales, D. 2002. *Diffusive and Advective Transport of ^{3}H, ^{14}C, and ^{99}Tc in Saturated, Fractured Volcanic Rocks from Pahute Mesa, Nevada.* LA-13891-MS. Los Alamos, New Mexico: Los Alamos National Laboratory. TIC: 253905.

Robin, M.J.L.; Gillham, R.W.; and Oscarson, D.W. 1987. "Diffusion of Strontium and Chloride in Compacted Clay-Based Materials." *Soil Science Society of America Journal*, *51* (5), 1102–1108. Madison, Wisconsin: Soil Science Society of America. TIC: 246867.

Rundberg, R.S. 1987. *Assessment Report on the Kinetics of Radionuclide Adsorption on Yucca Mountain Tuff*. LA-11026-MS. Los Alamos, New Mexico: Los Alamos National Laboratory. ACC: NNA.19930405.0075.

SNL (Sandia National Laboratories) 2007a. *UZ Flow Models and Submodels.* MDL-NBS-HS-000006 REV 03 ADD 01. Las Vegas, Nevada: Sandia National Laboratories. ACC: DOC.20080108.0003.

SNL 2007b. *Radionuclide Transport Models Under Ambient Conditions*. MDL-NBS-HS-000008 REV 02 ADD 01. Las Vegas, Nevada: Sandia National Laboratories. ACC: DOC.20070718.0003.

SNL 2007c. *Waste Form and In-Drift Colloids-Associated Radionuclide Concentrations: Abstraction and Summary.* MDL-EBS-PA-000004 REV 03. Las Vegas, Nevada: Sandia National Laboratories. ACC: DOC.20071018.0019.

SNL 2007d. *Drift-Scale THC Seepage Model.* MDL-NBS-HS-000001 REV 05. Las Vegas, Nevada: Sandia National Laboratories. ACC: DOC.20071010.0004.

SNL 2007e. *Radionuclide Screening*. ANL-WIS-MD-000006 REV 02. Las Vegas, Nevada: Sandia National Laboratories. ACC: DOC.20070326.0003.

SNL 2007f. *Saturated Zone In-Situ Testing.* ANL-NBS-HS-000039 REV 02. Las Vegas, Nevada: Sandia National Laboratories. ACC: DOC.20070608.0004.

SNL 2007g. *Initial Radionuclide Inventories.* ANL-WIS-MD-000020 REV 01 ADD 01. Las Vegas, Nevada: Sandia National Laboratories. ACC: DOC.20070801.0001.

SNL 2008a. *Particle Tracking Model and Abstraction of Transport Processes.* MDL-NBS-HS-000020 REV 02 ADD 02. Las Vegas, Nevada: Sandia National Laboratories. ACC: DOC.2008.0129.0008.

SNL 2008b. *Features, Events, and Processes for the Total System Performance Assessment: Analyses*. ANL-WIS-MD-000027 REV 00. Las Vegas, Nevada: Sandia National Laboratories. ACC: DOC.20080307.0003.

SNL 2008c. *Site-Scale Saturated Zone Transport.* MDL-NBS-HS-000010 REV 03 ADD 01. Las Vegas, Nevada: Sandia National Laboratories. ACC: DOC.20080121.0003.

SNL 2008d. *Simulation of Net Infiltration for Present-Day and Potential Future Climates.* MDL-NBS-HS-000023 REV 01 ADD 01. Las Vegas, Nevada: Sandia National Laboratories. ACC: DOC.20080201.0002.

Triay, I.R.; Cotter, C.R.; Huddleston, M.H.; Leonard, D.E.; Weaver, S.C.; Chipera, S.J.; Bish, D.L.; Meijer, A.; and Canepa, J.A. 1996. *Batch Sorption Results for Neptunium Transport Through Yucca Mountain Tuffs*. LA-12961-MS. Los Alamos, New Mexico: Los Alamos National Laboratory. ACC: MOL.19980924.0050.

Tseng, P.H. and Bussod, G.Y. 2001. "Evaluation of the Filter Paper Technique for In Situ Sampling of Solute Transport in Unsaturated Soils and Tuffs." *Water Resources Research*, *37* (7), 1913–1928. Washington, D.C.: American Geophysical Union. TIC: 255448.

Vandergraaf, T.T.; Drew, D.J.; and Ticknor, K.V. 2002. *Busted Butte Report on Laboratory Radionuclide Migration Experiments in Non-Welded Tuff Under Unsaturated Conditions*. AECL-12170. Pinawa, Manitoba, Canada: Atomic Energy of Canada Limited. ACC: MOL.20030919.0118.

Vandergraaf, T.T.; Drew, D.J.; Ticknor, K.V.; and Seddon, W.A. 2002. "Radionuclide Migration Experiments at a Scale of up to 1 Metre in Tuff Blocks Under Unsaturated Conditions." *Abstracts with Programs—Geological Society of America, 34* (6), 237. Boulder, Colorado: Geological Society of America. TIC: 254868.

Wan, J. and Tokunaga, T.K. 1997. "Film Straining on Colloids in Unsaturated Porous Media: Conceptual Model and Experimental Testing." *Environmental Science & Technology*, *31* (8), 2413–2420. Washington, D.C.: American Chemical Society. TIC: 234804.

Wolfsberg, A.V.; Fabryka-Martin, J.T.; Roemer, G.J.C.; and Robinson, B.A. 1998. "Modeling Flow and Transport Pathways to the Potential Repository Horizon at Yucca Mountain." *High-Level Radioactive Waste Management, Proceedings of the Eighth International Conference, Las Vegas, Nevada, May 11-14, 1998.* Pages 81–84. La Grange Park, Illinois: American Nuclear Society. TIC: 237082.

Table 2.3.8-1. Included Features, Events, and Processes Associated with the Unsaturated Zone Radionuclide Transport Abstraction Model

FEP Number and FEP Name	FEP Description	Summary of Technical Basis/ Approach for FEP Inclusion
1.2.02.01.0A Fractures	Groundwater flow in the Yucca Mountain region and transport of any released radionuclides may take place along fractures. The rate of flow and the extent of transport in fractures are influenced by characteristics such as orientation, aperture, asperity, fracture length, connectivity, and the nature of any linings or infills.	The influence of fractures on radionuclide transport is included through the dual-permeability model for unsaturated zone flow and transport. Fracture aperture, porosity, and frequency are treated directly in the unsaturated zone radionuclide transport abstraction model (Sections 2.3.8.3, 2.3.8.2, 2.3.8.4).
1.2.02.02.0A Faults	Numerous faults of various sizes have been noted in the Yucca Mountain region, and specifically in the repository area. Faults may represent an alteration of the rock permeability and continuity of the rock mass, an alteration or short-circuiting of the flow paths and flow distributions close to the repository, and/or unexpected pathways through the repository.	The influence of faults on radionuclide transport is included through the use of the dual-permeability flow model that directly represent the effects of faults on unsaturated zone flow. Fracture aperture, porosity, and frequency within faults are treated directly in the unsaturated zone radionuclide transport abstraction model (Sections 2.3.8.4.4, 2.3.8.4.1).
1.3.01.00.0A Climate change	Climate change may affect the long-term performance of the repository. This includes the effects of long-term change in global climate (e.g., glacial interglacial cycles) and shorter-term change in regional and local climate. Climate is typically characterized by temporal variations in precipitation and temperature.	The effect of climate change on radionuclide transport in the unsaturated zone is included by using pregenerated flow fields for different climates. Shorter term climate changes are incorporated in the range of uncertainty for all climate states (Sections 2.3.8.4.1, 2.3.8.5, 2.3.8.5.3).
1.3.07.02.0B Water table rise affects UZ	Climate change could produce increased infiltration, leading to a rise in the regional water table, possibly affecting radionuclide release from the repository by altering flow and transport pathways in the unsaturated zone. A regionally higher water table and change in unsaturated zone flow patterns might flood the repository.	The potential for water table rise caused by climate change is included in TSPA calculations using a water table rise model based on paleoclimate data. Water table changes are implemented in the TSPA by allowing the water table to change elevation instantaneously upon change in climate, concurrent with changes in infiltration. Section 2.3.8.5.3 describes the lines of evidence used to bound water table rise in the TSPA. Even these extreme values would not result in a water table that reaches the level of the repository (Section 2.3.8.5.3).
1.4.01.01.0A Climate modification increases recharge	Climate modification causes an increase in recharge in the Yucca Mountain region. Increased recharge might lead to increased flux through the repository, perched water, or water table rise.	The effect of climate changes in the form of increased recharge is included in the unsaturated zone radionuclide transport abstraction model for TSPA through the use of pregenerated flow fields (Section 2.3.8.5.3).

Table 2.3.8-1. Included Features, Events, and Processes Associated with the Unsaturated Zone Radionuclide Transport Abstraction Model (Continued)

FEP Number and FEP Name	FEP Description	Summary of Technical Basis/ Approach for FEP Inclusion
2.1.08.01.0A Water influx at the repository	An increase in the unsaturated water flux at the repository may affect thermal, hydrologic, chemical, and mechanical behavior of the system. Increases in flux could result from climate change, but the cause of the increase is not an essential part of the FEP.	The influence of water influx at the repository on radionuclide transport is included through the use of pregenerated flow fields under different climates in the unsaturated zone radionuclide transport abstraction model (Section 2.3.8.5.3).
2.2.03.01.0A Stratigraphy	Stratigraphic information is necessary information for the performance assessment. This information should include identification of the relevant rock units, soils and alluvium, and their thickness, lateral extents, and relationships to each other. Major discontinuities should be identified.	Stratigraphy is included in the unsaturated zone radionuclide transport abstraction model through the use of pregenerated flow fields (Section 2.3.8.4.1).
2.2.03.02.0A Rock properties of host rock and other units	Physical properties such as porosity and permeability of the relevant rock units, soils, and alluvium are necessary for the performance assessment. Possible heterogeneities in these properties should be considered. Questions concerning events and processes that may cause these physical properties to change over time are considered in other FEPs.	Rock properties of host rock and other units are included and used in the simulations of radionuclide transport through the unsaturated zone. Matrix porosity, rock density, fracture porosity, fracture spacing, and aperture data are incorporated into the transport simulations (Sections 2.3.8.4.1, 2.3.8.5.2).
2.2.07.02.0A Unsaturated groundwater flow in the geosphere	Groundwater flow occurs in unsaturated rocks in most locations above the water table at Yucca Mountain, including at the location of the repository. See related FEPs for discussions of specific issues related to unsaturated flow.	Water flow is the driving force for radionuclide transport through the unsaturated zone. This process is included through the use of pregenerated flow fields for transport (Sections 2.3.8.2.2.1, 2.3.8.4.1, 2.3.8.5.2.1).
2.2.07.04.0A Focusing of unsaturated flow (fingers, weeps)	Unsaturated flow can differentiate into zones of greater and lower saturation (fingers) that may persist as preferential flow paths. Heterogeneities in rock properties, including fractures and faults, may contribute to focusing. Focused flow may become locally saturated.	The effect of focusing unsaturated flow is included through the use of pregenerated flow fields in transport simulations (Sections 2.3.8.4 and 2.3.8.5.2.1).
2.2.07.06.0B Long-term release of radionuclides from the repository	The release of radionuclides from the repository may occur over a long period of time, as a result of the timing and magnitude of the waste packages and drip shield failures, waste form degradation, and radionuclide transport through the invert.	The effects of waste package breaches over a long period of time are included in the source term model for TSPA, which affects the source term of radionuclide mass for the unsaturated zone radionuclide transport abstraction model (Section 2.3.8.5).
2.2.07.07.0A Perched water develops	Zones of perched water may develop above the water table. If these zones occur above the repository, they may affect unsaturated zone flow between the surface and the waste packages. If they develop below the repository, for example, at the base of the Topopah Spring welded unit, they may affect flow pathways and radionuclide transport between the waste packages and the saturated zone.	Perched water is included through the use of pregenerated flow fields for radionuclide transport in the unsaturated zone (Sections 2.3.8.2, 2.3.8.4, 2.3.8.5.2.1).

Table 2.3.8-1. Included Features, Events, and Processes Associated with the Unsaturated Zone Radionuclide Transport Abstraction Model (Continued)

FEP Number and FEP Name	FEP Description	Summary of Technical Basis/ Approach for FEP Inclusion
2.2.07.08.0A Fracture flow in the UZ	Fractures or other analogous channels may act as conduits for fluids to move into the subsurface to interact with the repository and as conduits for fluids to leave the vicinity of the repository and be conducted to the saturated zone. Water may flow through only a portion of the fracture network, including flow through a restricted portion of a given fracture plane.	The effects of fracture flow on radionuclide transport (advection) is included in the unsaturated zone radionuclide transport abstraction model through the use of pregenerated unsaturated flow fields that include the occurrence of perched water (Sections 2.3.8.3, 2.3.8.2, 2.3.8.4.1, 2.3.8.5).
2.2.07.09.0A Matrix imbibition in the UZ	Water flowing in fractures or other channels in the unsaturated zone may be imbibed into the surrounding rock matrix. This may occur during steady flow, episodic flow, or into matrix pores that have been dried out during the thermal period.	Matrix imbibition in the unsaturated zone is included through the use of pregenerated flow fields for radionuclide transport in the unsaturated zone (Sections 2.3.8.2, 2.3.8.5.2.1).
2.2.07.15.0B Advection and dispersion in the UZ	Advection and dispersion processes may affect radionuclide transport in the unsaturated zone.	Dispersion is incorporated in the unsaturated zone radionuclide transport abstraction model through the use of a transfer function based on an analytical solution to the advection–dispersion equation (Section 2.3.8.5.2).
2.2.08.01.0B Chemical characteristics of groundwater in the UZ	Chemistry and other characteristics of groundwater in the unsaturated zone may affect groundwater flow and radionuclide transport of dissolved and colloidal species. Groundwater chemistry and other characteristics, including temperature, pH, Eh, ionic strength, and major ionic concentrations, may vary spatially throughout the system as a result of different rock mineralogy.	The effects of groundwater composition are incorporated into the probability distributions for radionuclide sorption sampled in TSPA (Sections 2.3.8.2.2.2, 2.3.8.5.2.3, 2.3.8.5.2.4).
2.2.08.06.0B Complexation in the UZ	Complexing agents, such as humic and fulvic acids, present in natural groundwaters could affect radionuclide transport in the unsaturated zone.	The effects of complexation are included in the experimental data used to derive radionuclide sorption coefficients under ambient conditions (Sections 2.3.8.2.2.2, 2.3.8.5.2.3).
2.2.08.08.0B Matrix diffusion in the UZ	Matrix diffusion is the process by which radionuclides and other species transported in the unsaturated zone by advective flow in fractures or other pathways move into the matrix of the porous rock by diffusion. This includes osmotic processes in response to chemical gradients. Matrix diffusion can be a very efficient retarding mechanism, especially for strongly sorbed radionuclides, due to the increase in rock surface accessible to sorption.	Transfer functions that are used in the unsaturated zone radionuclide transport abstraction model for TSPA include the mechanism of matrix diffusion (Section 2.3.8.3.1).

Table 2.3.8-1. Included Features, Events, and Processes Associated with the Unsaturated Zone Radionuclide Transport Abstraction Model (Continued)

FEP Number and FEP Name	FEP Description	Summary of Technical Basis/ Approach for FEP Inclusion
2.2.08.09.0B Sorption in the UZ	Sorption of dissolved and colloidal radionuclides in the unsaturated zone can occur on the surfaces of both fractures and matrix in rock or soil along the transport path. Sorption may be reversible or irreversible, and it may occur as a linear or nonlinear process. Sorption kinetics and the availability of sites for sorption should be considered. Sorption is a function of the radioelement type, mineral type, and groundwater composition.	Linear, equilibrium sorption is accounted for in the rock matrix continuum, with the conservative assumption of no sorption in the fractures. Sorption coefficients are implemented in TSPA in terms of probability distributions for the sorption coefficient of each element of interest among the three major rock types (devitrified, zeolitic, and vitric) found in the unsaturated zone. The probability distributions account for uncertainties in water chemistry, mineralogy, potential kinetics effects and sorption mechanisms (Sections 2.3.8.2.2.2, 2.3.8.5.2.3).
2.2.08.10.0B Colloidal transport in the UZ	Radionuclides may be transported in groundwater in the unsaturated zone as colloidal species. Types of colloids include true colloids, pseudocolloids, and microbial colloids.	Colloid-facilitated radionuclide transport included in TSPA treats both radionuclides permanently attached to colloids and radionuclides that partition between colloids, the aqueous phase, and the rock matrix. Diffusion of colloids into the rock matrix is not included, which leads to greater facilitation of radionuclide transport by colloids (Sections 2.3.8.2.2.3, 2.3.8.5.2.5).
3.1.01.01.0A Radioactive decay and ingrowth	Radioactivity is the spontaneous disintegration of an unstable atomic nucleus that results in the emission of subatomic particles. Radioactive species (isotopes) of a given element are known as radionuclides. Radioactive decay of the fuel in the repository changes the radionuclide content in the fuel with time and generates heat. Radionuclide quantities in the system at any time are the result of the radioactive decay and the ingrowth of decay products as a consequence of that decay. Over a 10,000-year performance period, these processes will produce decay products that need to be considered in order to adequately evaluate the release and transport of radionuclides to the accessible environment.	Both simple decay and radionuclide chain-decay are directly included in the unsaturated zone transport methodology used in TSPA (Sections 2.3.8.2, 2.3.8.5.2.6).

Table 2.3.8-2. Sorption Coefficient (K_d) Probability Distributions for Radioisotopes Based on Evaluation of Laboratory Data

Species[a]	Unit	Distribution Type	Distribution Statistics for K_d Value (mL/g)[b, c]
Uranium	Zeolitic	cumulative	(K_d value, probability) (0, 0) (**0.5**, 0.5) (30, 1.0)
	Devitrified	cumulative	(K_d value, probability) (0, 0) (**0.2**, 0.5) (4, 1.0)
	Vitric	cumulative	(K_d value, probability) (0, 0) (**0.2**, 0.5) (3, 1.0)
Neptunium	Zeolitic	cumulative	(K_d value, probability) (0, 0) (**0.5**, 0.5) (6, 1.0)
	Devitrified	cumulative	(K_d value, probability) (0, 0) (**0.5**, 0.5) (6, 1.0)
	Vitric	cumulative	(K_d value, probability) (0, 0) (**1.0**, 0.5) (3, 1.0)
Plutonium	Zeolitic	cumulative	(K_d value, probability) (10, 0) (**100**, 0.5) (200, 1.0)
	Devitrified	cumulative	(K_d value, probability) (10, 0) (**70**, 0.5) (200, 1.0)
	Vitric	cumulative	(K_d value, probability) (10, 0) (**100**, 0.5) (200, 1.0)
Americium	Zeolitic	truncated normal	Range = 1,000 to 10,000 Mean = 5,500 Std Dev = 1,500 (**500**)
	Devitrified	truncated normal	Range = 1,000 to 10,000 Mean = 5,500 Std Dev = 1,500 (**1,000**)
	Vitric	cumulative	(K_d value, probability) (100, 0) (**400**, 0.5) (1,000, 1.0)
Protactinium	Zeolitic	truncated normal	Range = 1,000 to 10,000 Mean = 5,500 Std Dev = 1,500 (**10,000**)
	Devitrified	truncated normal	Range = 1,000 to 10,000 Mean = 5,500 Std Dev = 1,500 (**10,000**)
	Vitric	truncated normal	Range = 1,000 to 10,000 Mean = 5,500 Std Dev = 1,500 (**10,000**)
Cesium	Zeolitic	cumulative	(K_d value, probability) (425, 0) (**5,000**, 0.5) (20,000, 1.0)
	Devitrified	uniform	Range = 1 to 15 (**7.5**)
	Vitric	cumulative	(K_d value, probability) (0, 0) (**2**, 0.5) (100, 1.0)
Strontium	Zeolitic	uniform	Range = 50 to 2,000 (**1,000**)
	Devitrified	uniform	Range = 10 to 70 (**40**)
	Vitric	uniform	Range = 0 to 50 (**25**)
Radium	Zeolitic	uniform	Range = 1,000 to 5,000 (**2,500**)
	Devitrified	uniform	Range = 100 to 1,000 (**500**)
	Vitric	uniform	Range = 50 to 600 (**300**)
Thorium	Zeolitic	uniform	Range = 1,000 to 30,000 (**15,000**)
	Devitrified	uniform	Range = 1,000 to 10,000 (**5,000**)
	Vitric	uniform	Range = 1,000 to 10,000 (**5,000**)

Table 2.3.8-2. Sorption Coefficient (K_d) Probability Distributions for Radioisotopes Based on Evaluation of Laboratory Data (Continued)

Species[a]	Unit	Distribution Type	Distribution Statistics for K_d Value (mL/g)[b, c]
Selenium[d]	Zeolitic	truncated log-normal	Range = 1.0 to 35.0; Mean = 14.3 Std Dev = 7.9
	Devitrified	truncated log-normal	Range = 1.0 to 50.0; Mean = 14.0 Std Dev = 11.2
	Vitric	truncated log-normal	Range = 0.0 to 25.0; Mean = 8.6 Std Dev = 7.9
Tin	Zeolitic	Log-uniform	Range = 100 to 5,000
	Devitrified	Log-uniform	Range = 100 to 100,000
	Vitric	Log-uniform	Range = 100 to 5,000

NOTE: [a]Only sorbing species are listed in this table.
[b]For the cumulative distributions, K_d value and cumulative probability of occurrence are provided in parentheses for three probabilities (0.0, 0.5, and 1.0). For the uniform distributions, the overall range is provided. For the truncated normal and truncated log-normal distributions, the mean, standard deviation, and range are provided.
[c]The number in boldface is the representative K_d value used for the unsaturated zone radionuclide transport process model calculations.
[d]Se K_d is set at zero for rock in the TSw.

Source: SNL 2007b, Table 6-1[a].

Table 2.3.8-3. Calibrated Flow and Transport Parameters from the Analysis of the Busted Butte Phase 1A Field Test

Parameter	Site-Scale Unsaturated Zone Flow Model Layer	
	ch1v	ch2v
Porosity (ϕ)	0.320	0.360
Permeability in the x direction (k_x (m^2))	2.14×10^{-13}	8.20×10^{-13}
Permeability in the y direction (k_y (m^2))	4.14×10^{-13}	2.82×10^{-13}
Permeability in the z direction (k_z (m^2))	6.28×10^{-14}	3.64×10^{-14}
Tortuosity (τ)	0.22	0.12
van Genuchten parameter α (1/m)	0.471	0.741
van Genuchten parameter *n*	1.332	1.200
Residual saturation (S_r)	0.07	0.07
Molecular Diffusion Coefficient (D_0) of fluorescein (m^2/s)	4×10^{-10}	

Source: SNL 2007b, Table 7-9.

Table 2.3.8-4. Calibrated Flow and Transport Parameters from the Analysis of the Busted Butte Phase 1B Field Test

Parameter	Value
Porosity (ϕ)	0.270
Permeability in the x direction (k_x (m^2))	3.06×10^{-17}
Permeability in the y direction (k_y (m^2))	4.06×10^{-17}
Permeability in the z direction (k_z (m^2))	1.53×10^{-17}
Tortuosity (τ)	0.07
Sorption coefficient (K_d) of 2,6-DFBA (m^3/kg)	1.47×10^{-5}

Source: SNL 2007b, Table 7-11.

Table 2.3.8-5. Calibrated Flow and Transport Parameters from the Analysis of the Busted Butte Phase 2C Field Test

Parameter	Site-Scale Unsaturated Zone Flow Model Layer			
	Fracture ch1v	**Matrix ch1v**	**Fracture ch2v**	**Matrix ch2v**
Porosity (ϕ)	1	0.354	1	0.060
Permeability in the x direction (k_x (m^2))	3×10^{-13}	1.3×10^{-13}	1.96×10^{-12}	1.2×10^{-13}
Permeability in the z direction (k_z (m^2))	10^{-13}	8×10^{-14}	7.1×10^{-13}	8×10^{-14}
Tortuosity (τ)	2	0.9	2	0.654
Sorption coefficient (K_d) of lithium (m^3/kg)	—	5.5×10^{-4}	—	9.3×10^{-4}
Sorption coefficient (K_d) of lithium (m^3/kg)[a]	2.5×10^{-6}	—	4.3×10^{-6}	—

NOTE: [a]K_d denotes surface distribution coefficient in fractures.

Source: SNL 2007b, Table 7-14.

Table 2.3.8-6. Initial Estimated Hydraulic Properties for Alcove 1 Infiltration Test

Parameter	Fracture	Matrix
Porosity	0.01	0.164
Permeability[a] (m^2)	2.29×10^{-11}	1.2×10^{-15}
van Genuchten parameter α (Pa^{-1})	2.37×10^{-3}	7.12×10^{-6}
van Genuchten parameter m	0.633	0.346
Residual saturation	0.01	0.06
Fracture spacing (m)	0.377	Not applicable
Active fracture parameter γ	0.15	Not applicable

NOTE: [a]In both the vertical and horizontal directions.

Source: Liu, Haukwa et al. 2003, Table 1.

Table 2.3.8-7. Calibrated Hydrologic Properties for Infiltration Test Model Based on the Phase I Seepage Rate Data

Parameter	Fracture	Matrix
Porosity	0.028	0.164
Vertical Permeability (m^2)	2.90×10^{-11}	3.64×10^{-16}
Horizontal Permeability (m^2)	3.14×10^{-11}	9.35×10^{-16}
van Genuchten parameter α (Pa^{-1})	2.07×10^{-3}	1.84×10^{-5}
Active fracture parameter γ	0.28	Not applicable

NOTE: Parameters that are not shown in this table are the same as those in Table 2.3.8-6. They are fixed in the inversion.

Source: Liu, Haukwa et al. 2003, Table 1.

Table 2.3.8-8. Calibrated Hydrologic Properties Based on the Phase I and Phase II Seepage Rate Data

Parameter	Fracture	Matrix
Porosity	0.03	0.164
Vertical Permeability (m^2)	3.08×10^{-11}	1.01×10^{-15}
Horizontal Permeability (m^2)	2.99×10^{-11}	3.42×10^{-16}
van Genuchten parameter α (Pa^{-1})	2.34×10^{-3}	1.90×10^{-5}
Active fracture parameter γ	0.21	Not applicable

NOTE: Parameters that are not shown in this table are the same as those in Table 2.3.8-6. They are fixed in the inversion.

Source: Liu, Haukwa et al. 2003, Table 1.

Table 2.3.8-9. Selected Parameter Values for Representative-Case Unsaturated Zone Model

Key	Parameter Type	Value
Aperture (m) 2b		
–1	Group 1 Units	7.94×10^{-3}
–2	Group 2 Units	1.43×10^{-2}
–3	Group 3 Units	2.64×10^{-3}
–4	Group 4 Units	4.85×10^{-3}
–5	Group 5 Units	4.00×10^{-3}
–6	Group 6 Units	5.75×10^{-3}
–7	Group 7 Units	4.48×10^{-3}
–8	Group 8 Units	2.64×10^{-3}
–9	Group 9 Units	7.16×10^{-3}
Gamma Parameter, all units		
–10	Gamma Parameter[a]	0.6
D (m^2/s): Mean Values from Table 6.5.5-3 in Addendum 1 of SNL 2008a		
–11	Am in Rock Group 1	6.718×10^{-11}
–12	Am in Rock Group 2	2.554×10^{-11}
–13	Am in Rock Group 3	1.372×10^{-11}
–14	C in Rock Group 1	8.354×10^{-11}
–15	C in Rock Group 2	3.176×10^{-11}
–16	C in Rock Group 3	1.706×10^{-11}
–17	Cl in Rock Group 1	1.437×10^{-10}
–18	Cl in Rock Group 2	5.464×10^{-11}
–19	Cl in Rock Group 3	2.934×10^{-11}
–20	Cs in Rock Group 1	1.458×10^{-10}
–21	Cs in Rock Group 2	5.545×10^{-11}
–22	Cs in Rock Group 3	2.978×10^{-11}
–23	I in Rock Group 1	1.451×10^{-10}
–24	I in Rock Group 2	5.518×10^{-11}
–25	I in Rock Group 3	2.963×10^{-11}

Table 2.3.8-9. Selected Parameter Values for Representative-Case Unsaturated Zone Model (Continued)

Key	Parameter Type	Value
–26	Np in Rock Group 1	4.375×10^{-11}
–27	Np in Rock Group 2	1.663×10^{-11}
–28	Np in Rock Group 3	8.933×10^{-12}
–29	Pa in Rock Group 1	4.276×10^{-11}
–30	Pa in Rock Group 2	1.626×10^{-11}
–31	Pa in Rock Group 3	8.730×10^{-12}
–32	Pu in Rock Group 1	9.203×10^{-11}
–33	Pu in Rock Group 2	3.499×10^{-11}
–34	Pu in Rock Group 3	1.879×10^{-11}
–35	Ra in Rock Group 1	6.294×10^{-11}
–36	Ra in Rock Group 2	2.393×10^{-11}
–37	Ra in Rock Group 3	1.285×10^{-11}
–38	Se in Rock Group 1	7.363×10^{-11}
–39	Se in Rock Group 2	2.799×10^{-11}
–40	Se in Rock Group 3	1.503×10^{-11}
–41	Sn in Rock Group 1	1.097×10^{-10}
–42	Sn in Rock Group 2	4.172×10^{-11}
–43	Sn in Rock Group 3	2.240×10^{-11}
–44	Sr in Rock Group 1	5.600×10^{-11}
–45	Sr in Rock Group 2	2.129×10^{-11}
–46	Sr in Rock Group 3	1.143×10^{-11}
–47	Tc in Rock Group 1	1.380×10^{-10}
–48	Tc in Rock Group 2	5.248×10^{-11}
–49	Tc in Rock Group 3	2.819×10^{-11}
–50	Th in Rock Group 1	4.226×10^{-11}
–51	Th in Rock Group 2	1.607×10^{-11}
–52	Th in Rock Group 3	8.629×10^{-12}
–53	U in Rock Group 1	4.701×10^{-11}
–54	U in Rock Group 2	1.787×10^{-11}

Table 2.3.8-9. Selected Parameter Values for Representative-Case Unsaturated Zone Model (Continued)

Key	Parameter Type	Value
–55	U in Rock Group 3	9.598×10^{-12}
Representative Value Sorption Coefficients (K_d: mL/g) from SNL 2007b.		
–56	Am in Rock Group 1	5,500
–57	Am in Rock Group 2	5,500
–58	Am in Rock Group 3	400
–59	C in Rock Group 1	0
–60	C in Rock Group 2	0
–61	C in Rock Group 3	0
–62	Cl in Rock Group 1	0
–63	Cl in Rock Group 2	0
–64	Cl in Rock Group 3	0
–65	Cs in Rock Group 1	5,000
–66	Cs in Rock Group 2	8
–67	Cs in Rock Group 3	2
–68	I in Rock Group 1	0
–69	I in Rock Group 2	0
–70	I in Rock Group 3	0
–71	Np in Rock Group 1	0.5
–72	Np in Rock Group 2	0.5
–73	Np in Rock Group 3	1
–74	Pa in Rock Group 1	5,500
–75	Pa in Rock Group 2	5,500
–76	Pa in Rock Group 3	5,500
–77	Pu in Rock Group 1	100
–78	Pu in Rock Group 2	70
–79	Pu in Rock Group 3	100
–80	Ra in Rock Group 1	3,000
–81	Ra in Rock Group 2	550
–82	Ra in Rock Group 3	325

Table 2.3.8-9. Selected Parameter Values for Representative-Case Unsaturated Zone Model (Continued)

Key	Parameter Type	Value
–83	Se in Rock Group 1	14.3
–84	Se in Rock Group 2	14.0
–85	Se in Rock Group 3	8.6
–86	Sn in Rock Group 1	707
–87	Sn in Rock Group 2	3,162
–88	Sn in Rock Group 3	707
–89	Sr in Rock Group 1	1,025
–90	Sr in Rock Group 2	40
–91	Sr in Rock Group 3	25
–92	Tc in Rock Group 1	0
–93	Tc in Rock Group 2	0
–94	Tc in Rock Group 3	0
–95	Th in Rock Group 1	15,500
–96	Th in Rock Group 2	5,500
–97	Th in Rock Group 3	5,500
–98	U in Rock Group 1	0.5
–99	U in Rock Group 2	0.2
–100	U in Rock Group 3	0.2
Sorption Distribution Coefficient onto Colloids		
–101	Am[b]	0.075
–102	Cs	6.67×10^{-5}
–103	Pa	0.075
–104	Pu	0.0005714
–105	Sn	0.0316
–106	Th	0.075

Table 2.3.8-9. Selected Parameter Values for Representative-Case Unsaturated Zone Model (Continued)

Key	Parameter Type	Value
–107	Retardation factor[c]	26

NOTE: [a]Median value is 0.4, but calculations presented for the representative case used 0.6
[b]Example calculation for Am on smectite: Median C_{coll} = 0.1 mg/L = 0.1 × 10^{-6} kg/L from SNL 2008a, Table 6-21 in Addendum 1, Median $K_{d,coll}$ = 7.5 × 10^{5} mL/g = 7.5 × 10^{5} L/kg, K_c = 0.1 × 10^{-6} kg/L*7.5 × 10^{5} L/kg = .075
[c]Does not apply to the If (irreversible fast colloids). Value from Table 6-24 of SNL 2008a.
The key values represent a file input location for a distribution of values that are sampled to represent the uncertainty parameters in runs for TSPA. Northern Release Location (top) and Southern Release Location (bottom). These results are for comparison purposes only and are not input to the TSPA. Actual radionuclide mass flux reaching the water table depends on release rates and locations and is simulated in the TSPA. Normalized cumulative breakthrough is the cumulative mass arrival at the water table for the given radionuclide form (aqueous or colloidal) divided by the initial mass of that radionuclide form released at the repository. Source term is pulse input of particles. The cumulative value for any radionuclide will be unity if all particles released from the repository reach the water table.

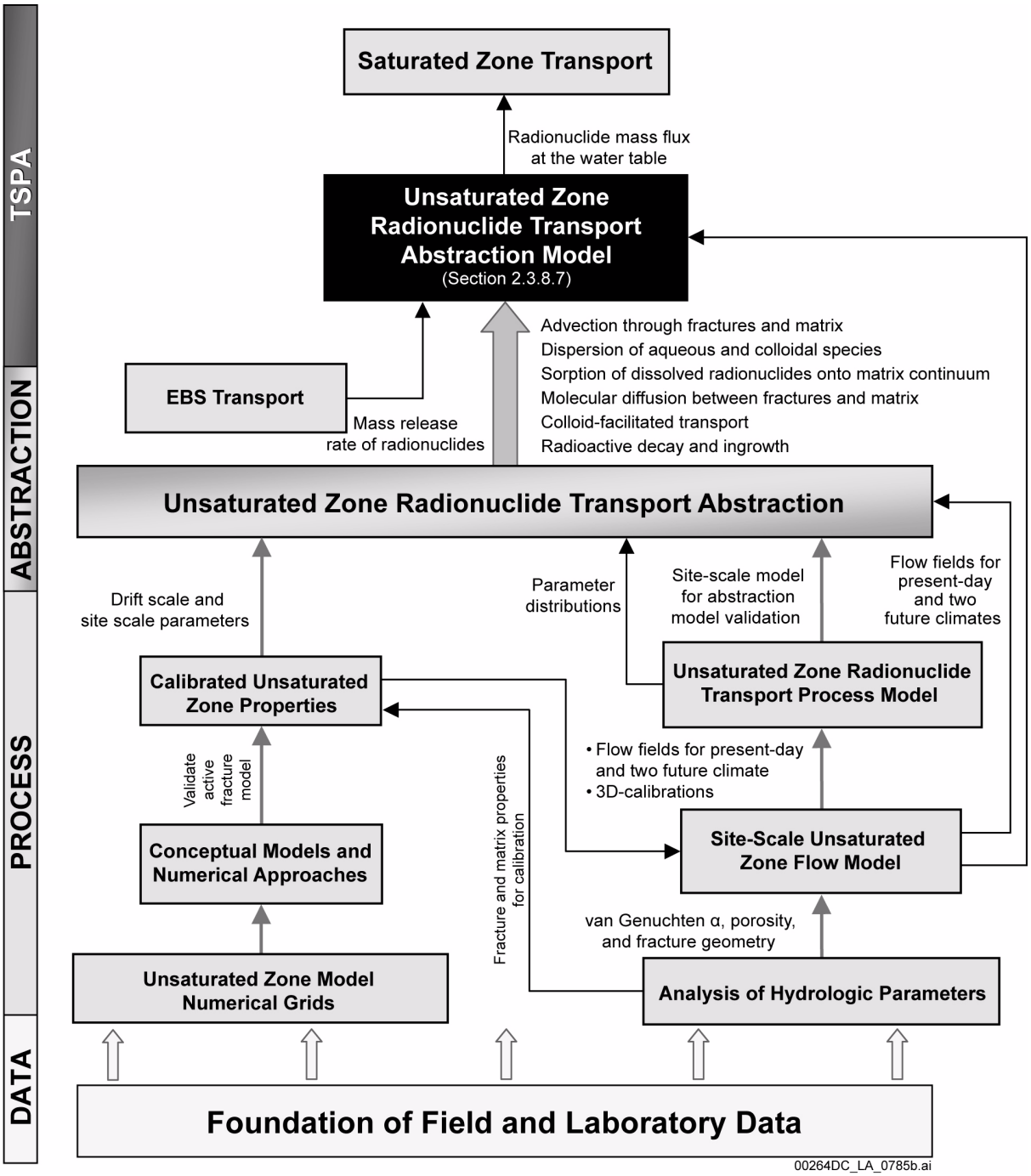

Figure 2.3.8-1. Information Flow Supporting Development of the Unsaturated Zone Radionuclide Transport Abstraction at the Data, Process, Abstraction, and TSPA Levels

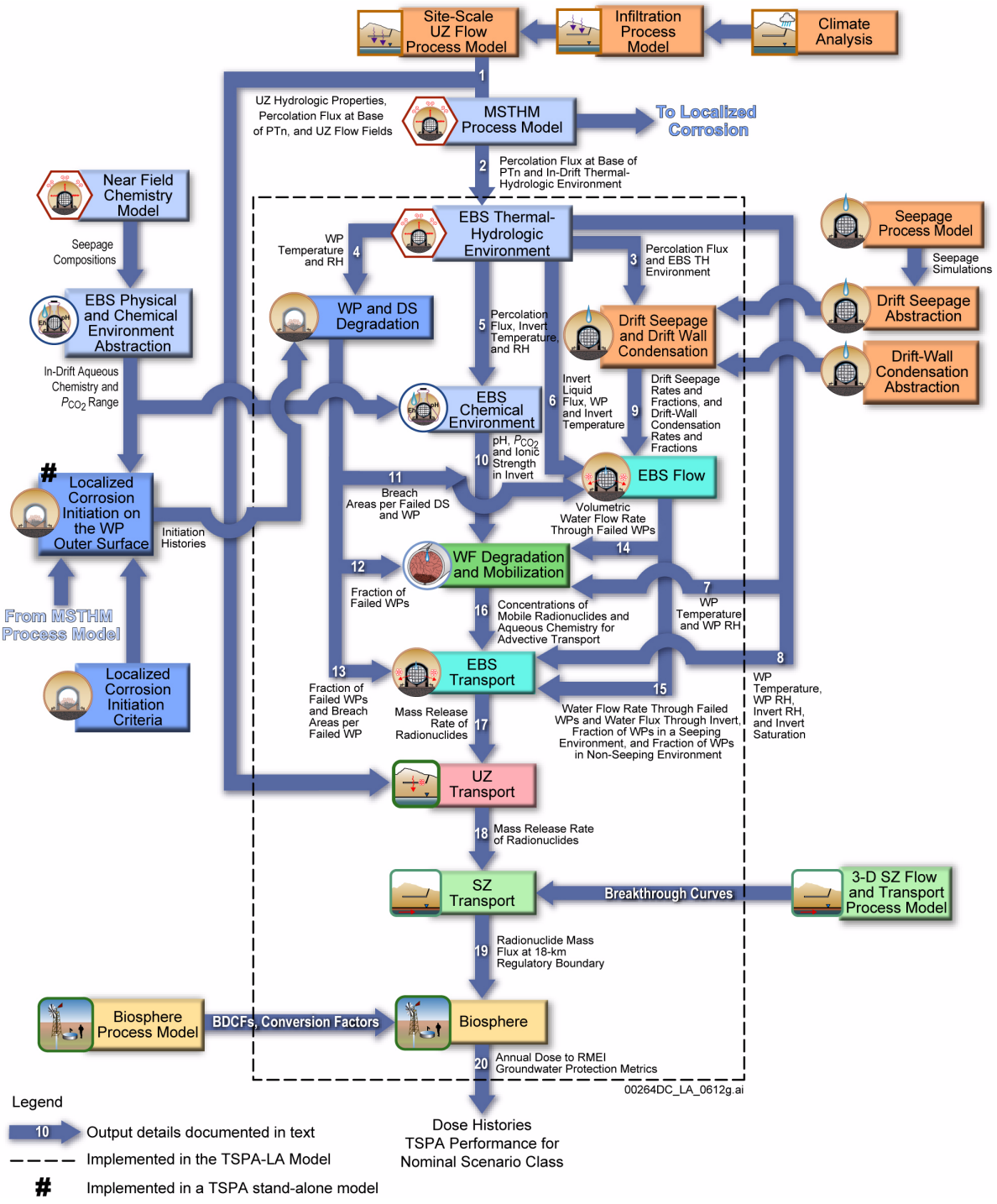

Figure 2.3.8-2. Information Transfer among the Principal Model Components of the TSPA Nominal Scenario Class Model

NOTE: The unsaturated zone transport model shown in the figure is also called the unsaturated zone radionuclide transport abstraction model. For details about outputs and information transfer shown on this figure, see Section 2.4.2.3.2.1.
DS = drip shield; EBS = Engineered Barrier System; LC = localized corrosion; PA = performance assessment; RH = relative humidity; SZ = saturated zone; TH = thermal-hydrologic; THC = thermal-hydrologic-chemical; UZ = unsaturated zone; WF = waste form; WP = waste package.

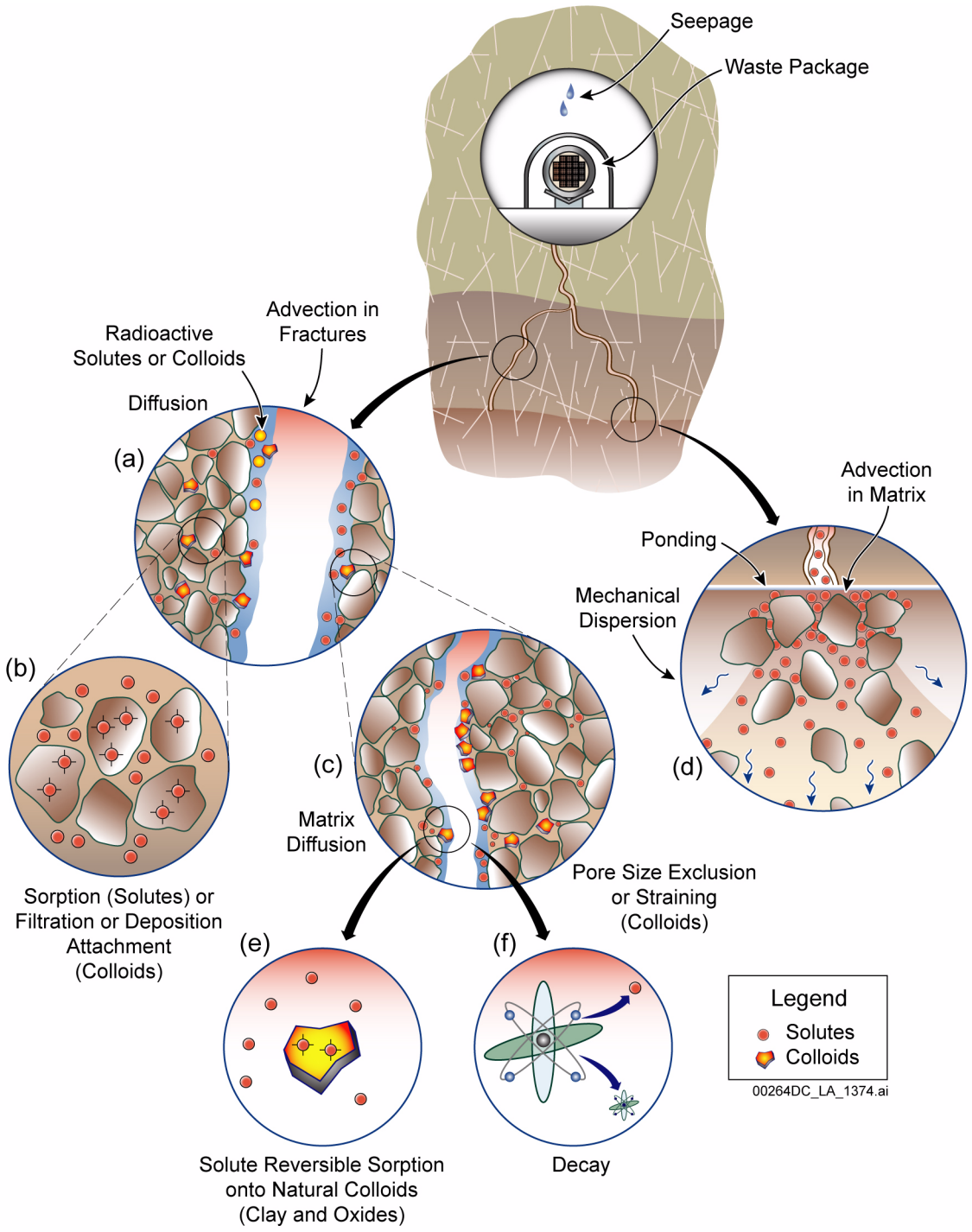

Figure 2.3.8-3. Processes Affecting Transport of Radionuclides

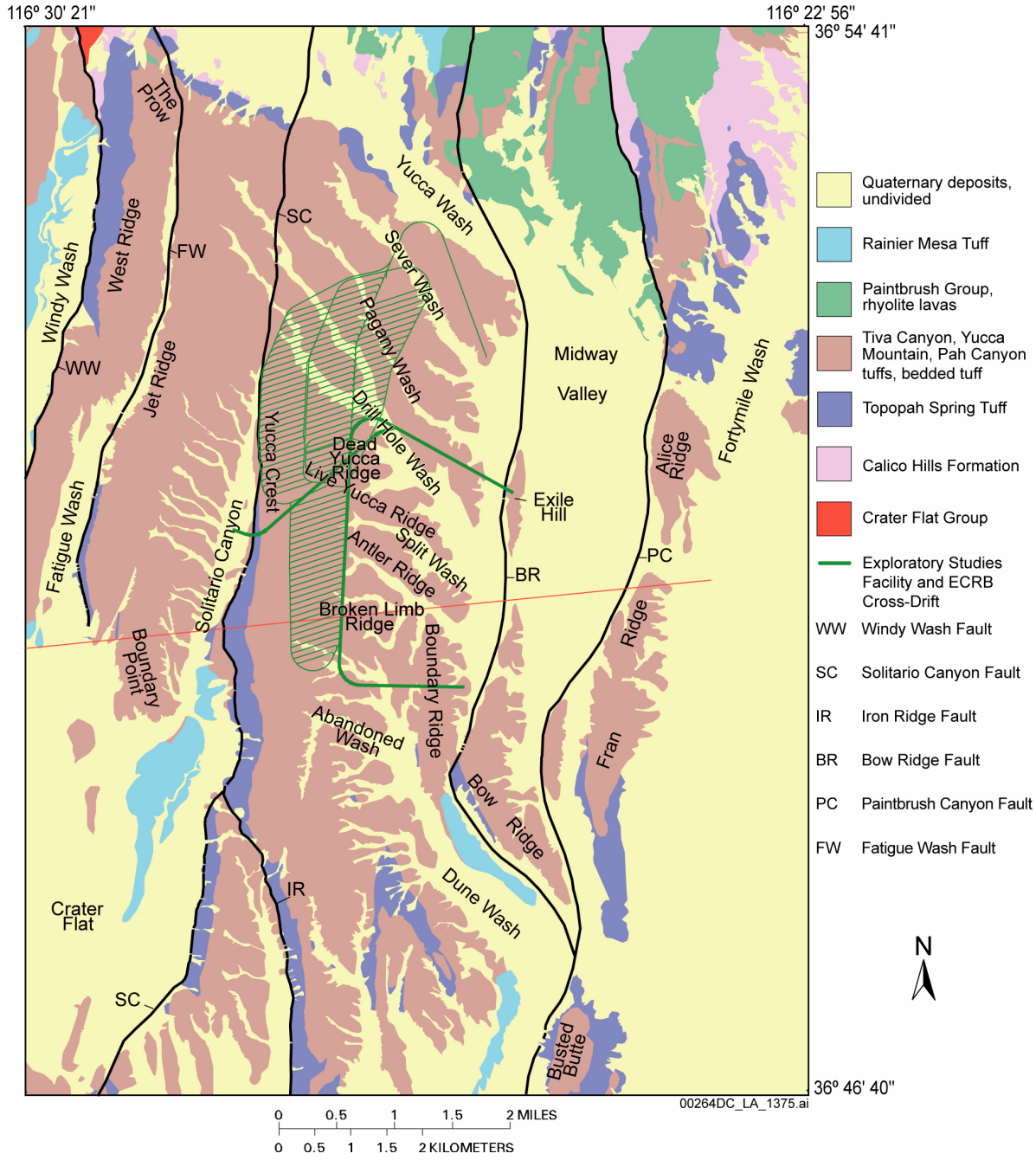

Figure 2.3.8-4. Simplified Geologic Map Showing Distribution of Major Lithostratigraphic Units in the Yucca Mountain Site Area and Vicinity

NOTE: Repository footprint is shown for illustration purposes only.

Source: Potter et al. 2002.

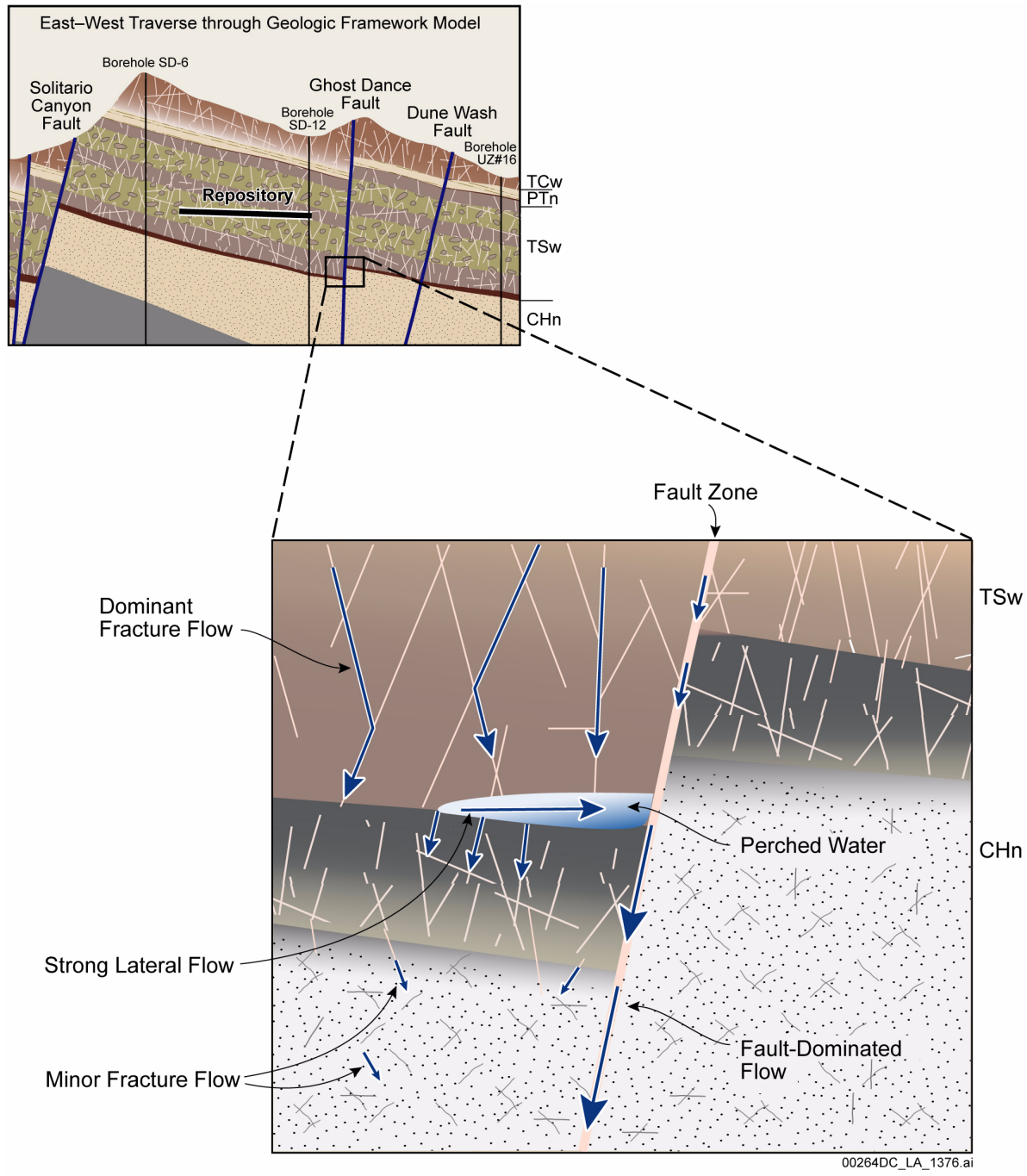

Figure 2.3.8-5. Flow Patterns within and near a Perched Water Body and the Associated Fault-Dominated Flow

NOTE: TCw, PTn, TSw, and CHn are major hydrogeologic units. Flow patterns within and near a perched water body are characterized by strong lateral flow.
CHn = Calico Hills nonwelded; PTn = Paintbrush nonwelded; TCw = Tiva Canyon welded; TSw = Topopah Spring welded.

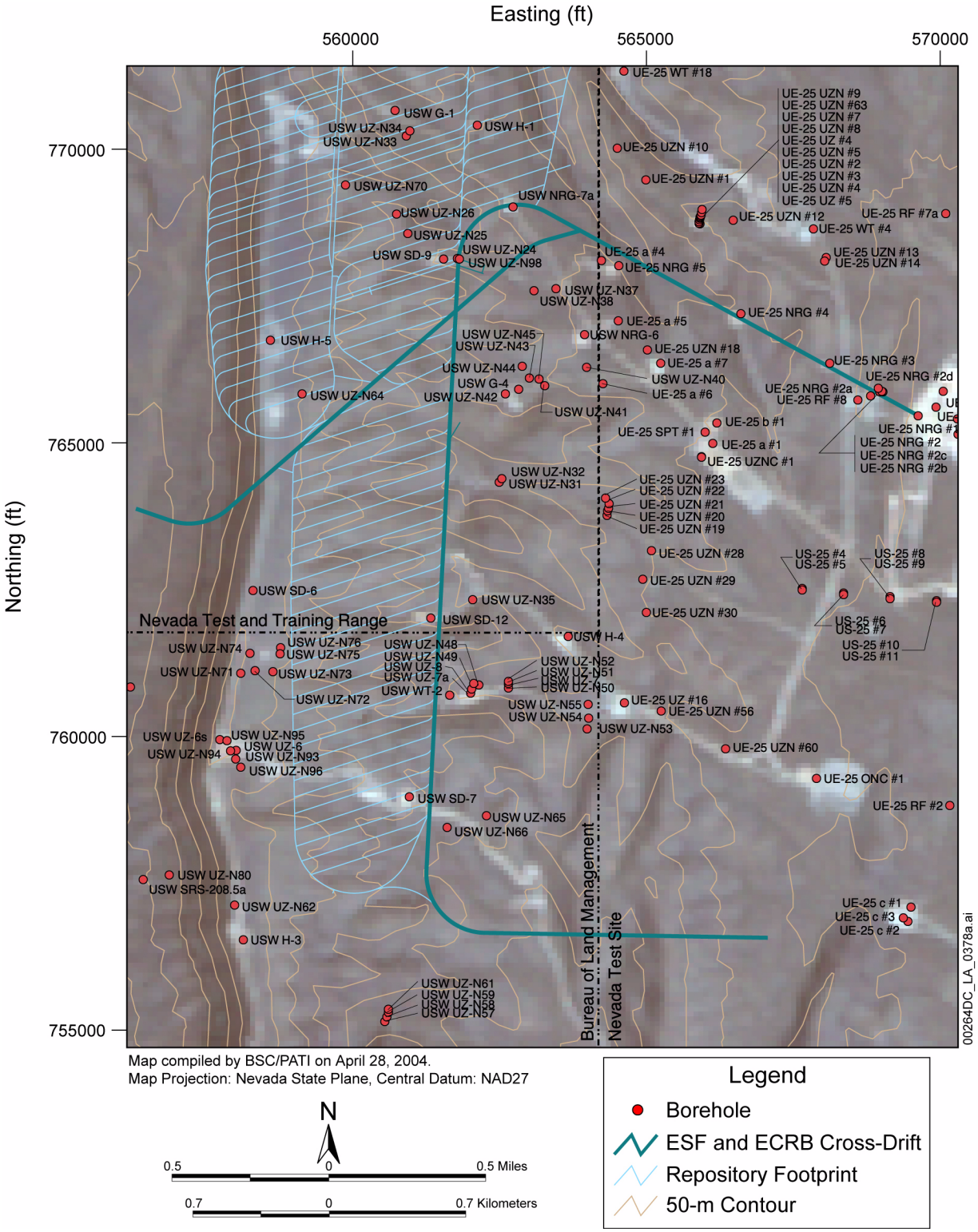

Figure 2.3.8-6. Map Showing Repository Area Boreholes, the Exploratory Studies Facility, and the Enhanced Characterization of the Repository Block Cross-Drift

NOTE: Repository footprint is shown for illustration purposes only.

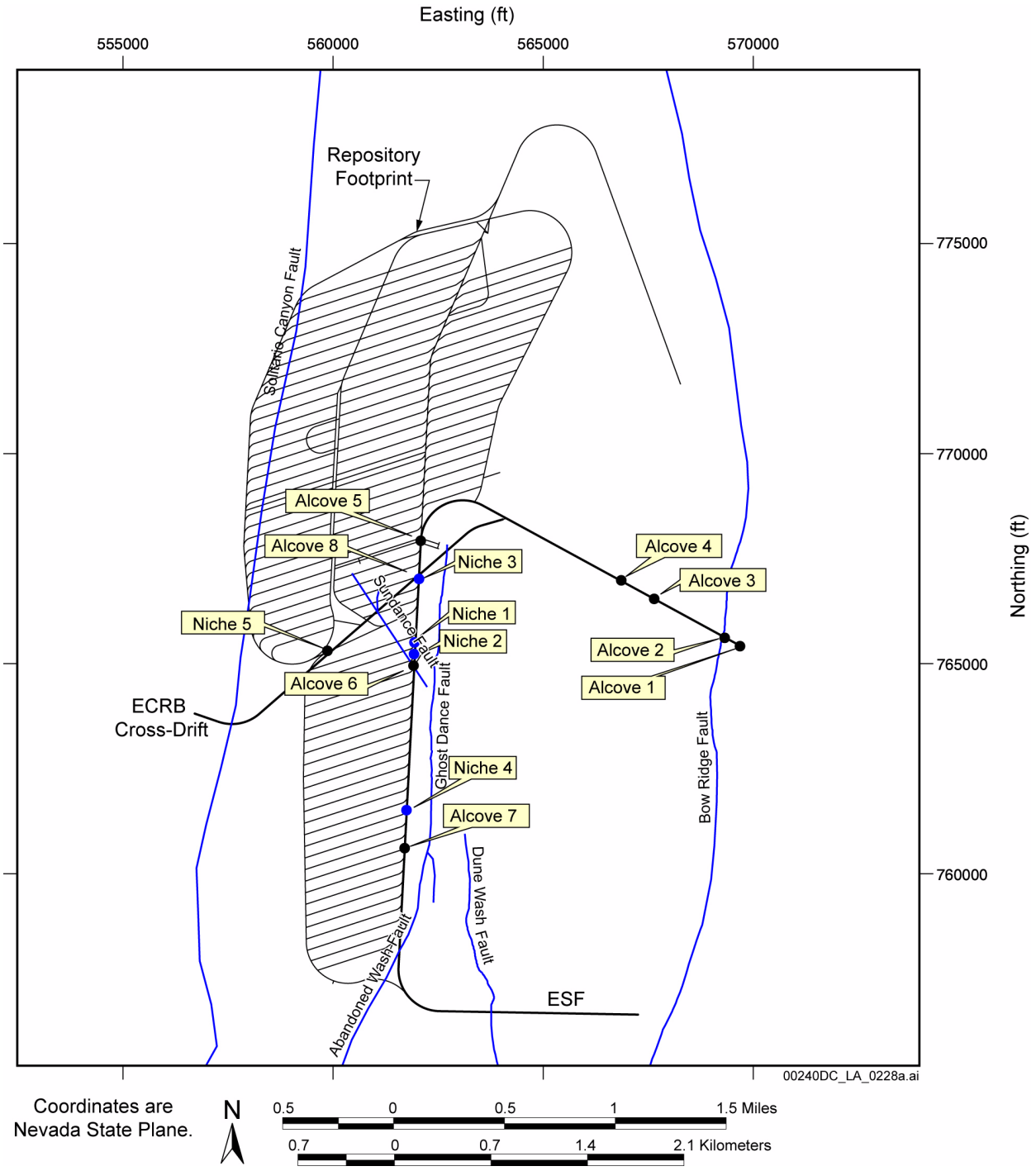

Figure 2.3.8-7. Map Showing Locations of Testing Alcoves and Niches in the Exploratory Studies Facility and the Enhanced Characterization of the Repository Block Cross-Drift

NOTE: Repository footprint is shown for illustration purposes only.

Source: BSC 2004d, Figures 1-3, 3-20, and 7-2; BSC 2004c, Figure 1-2.

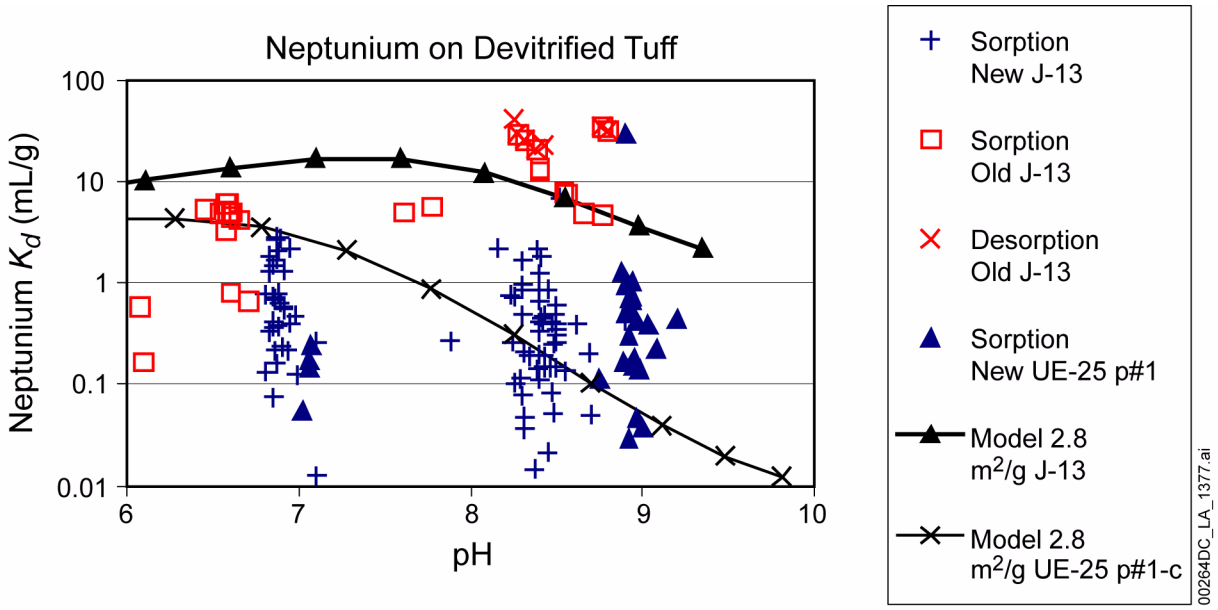

Figure 2.3.8-8. Neptunium Sorption Coefficient K_d on Devitrified Tuff in J-13 and Synthetic UE-25 p#1 Waters versus Solution pH in Sorption and Desorption Experiments

NOTE: PHREEQC model results for J-13 well water and synthetic UE-25 p#1 water are also plotted. "Old" data refers to data collected before 1990; "new" data were collected since 1990. In this plot, the distinction is that the "old" experiments were conducted over a longer duration, and thus may be exhibiting less kinetics effects than the "new" data. The value 2.8 m^2/g is the surface area selected as a representative average for the devitrified tuff of Yucca Mountain.

Source: SNL 2007b, Figure A-20a.

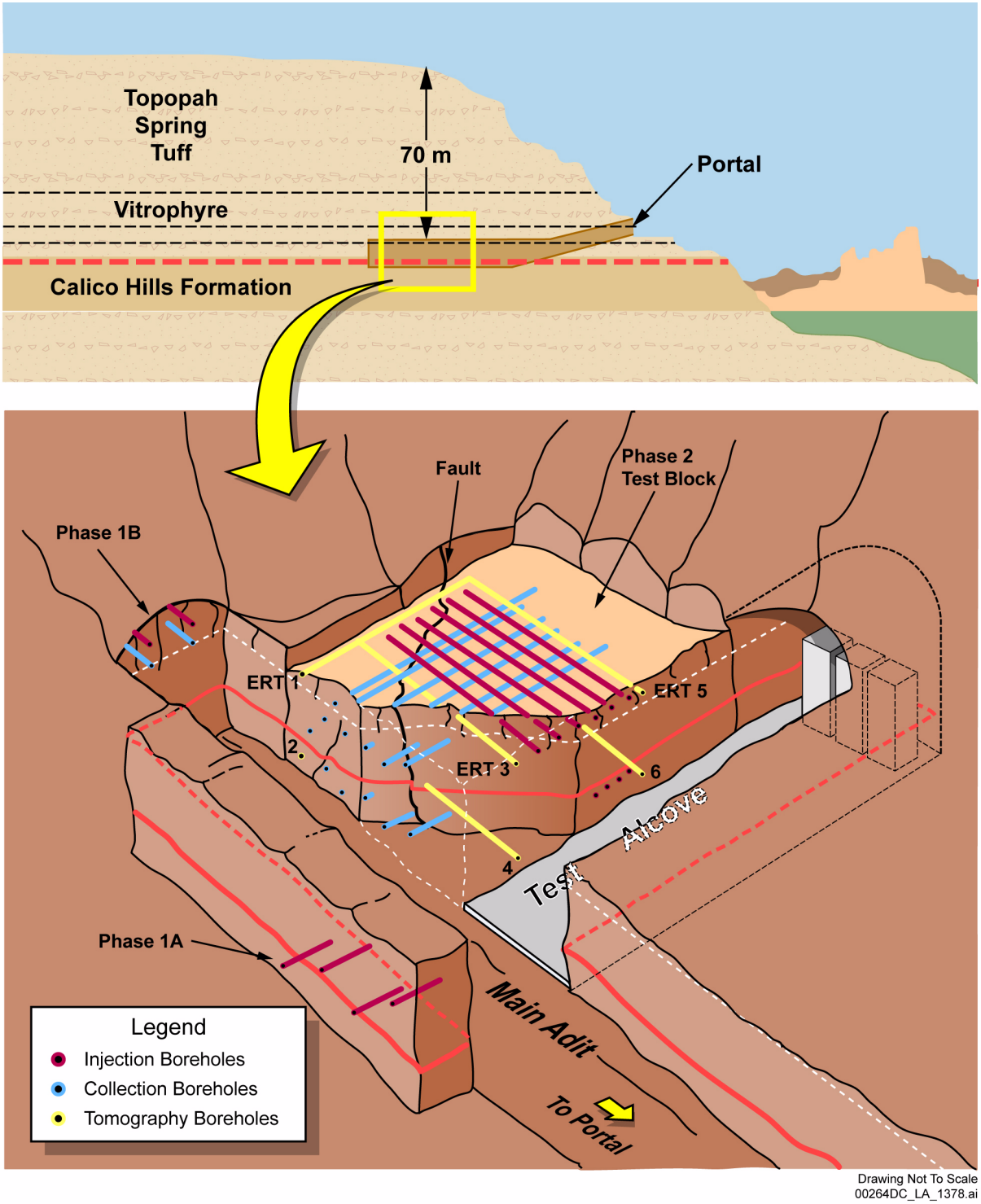

Figure 2.3.8-9. Schematic Layout of Busted Butte Unsaturated Zone Transport Test

NOTE: The shows the relative locations of the test's phases and borehole locations. Orange solid and dotted line indicates contact between Tptpv1 and Tac units.
ERT = electrical resistivity tomography.

Source: BSC 2004c, Figure 6-168.

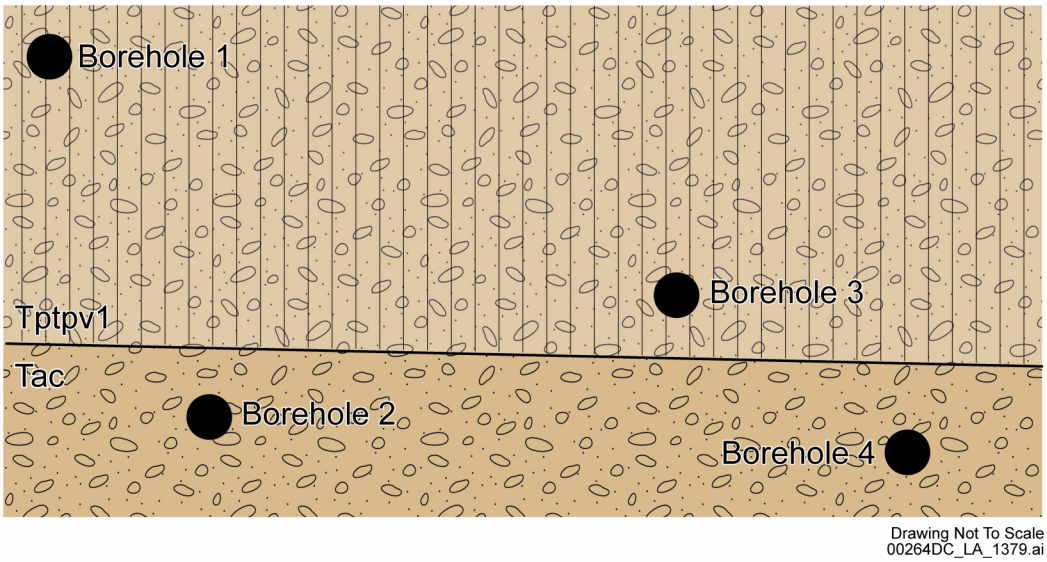

Figure 2.3.8-10. Geologic Unit Contact and Borehole Locations in Phase 1A of Busted Butte Unsaturated Zone Transport Test

Source: BSC 2004c, Figure 6-170.

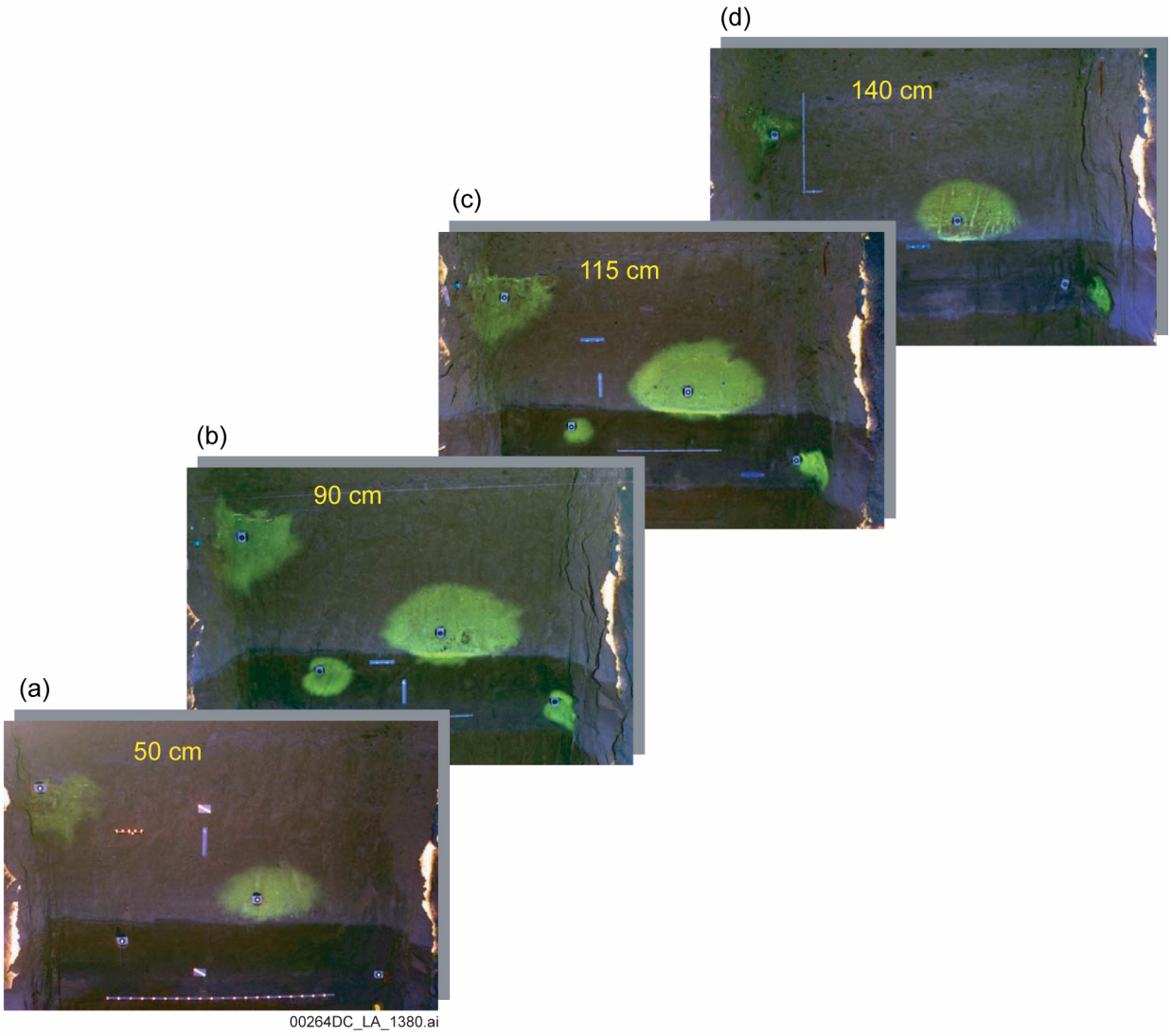

Figure 2.3.8-11. Fluorescein Plume at Each of Four Successively Deeper Mineback Faces at Borehole 3 in Phase 1A of Busted Butte Unsaturated Zone Transport Test

Source: BSC 2004c, Figure 6-172.

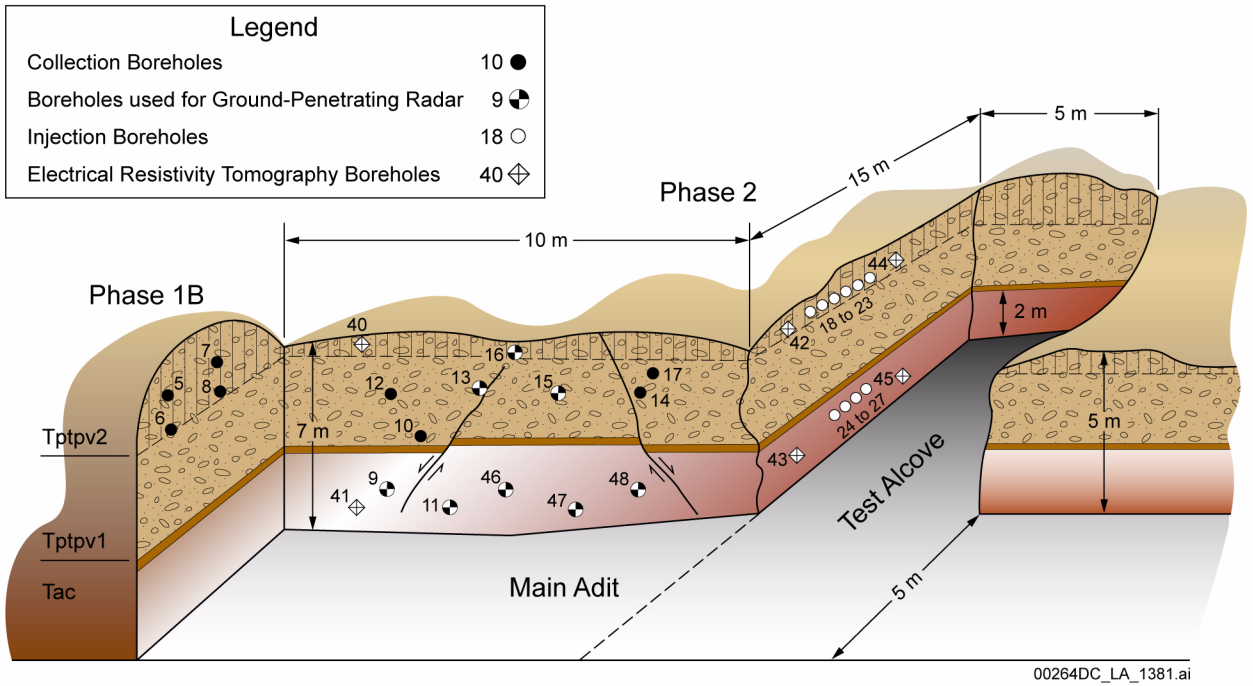

Figure 2.3.8-12. Schematic Layout of Geologic Unit Contacts and Borehole Locations in Phases 1B and 2 of Busted Butte Unsaturated Zone Transport Test

NOTE: Not all of the collection boreholes are shown on this figure.

Source: BSC 2004c, Figure 6-171.

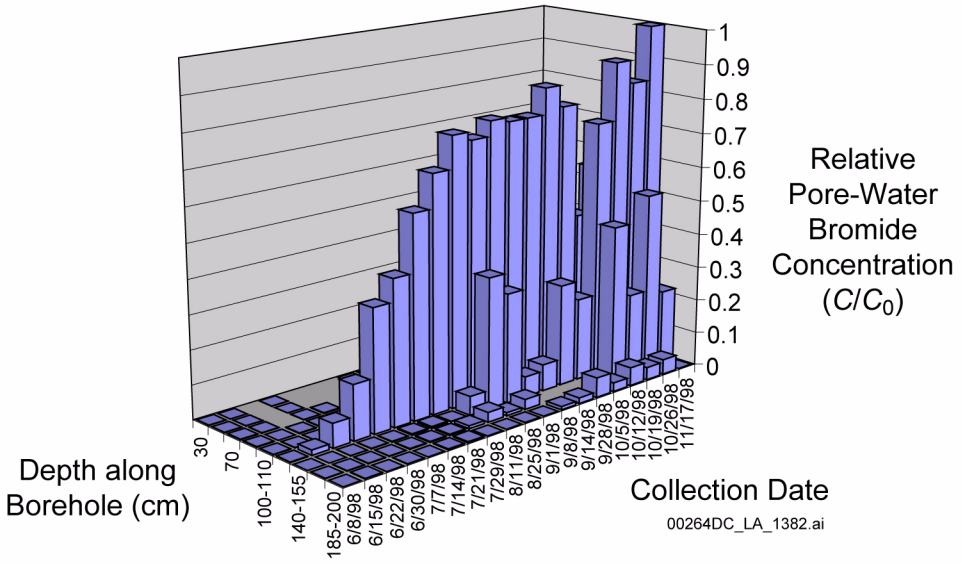

Figure 2.3.8-13. Bromide-Relative Concentrations in Borehole 6 in Phase 1B of Busted Butte Unsaturated Zone Transport Test

NOTE: C = pore-water bromide concentration; C_0 = injection concentration.

Source: BSC 2004c, Figure 6-175.

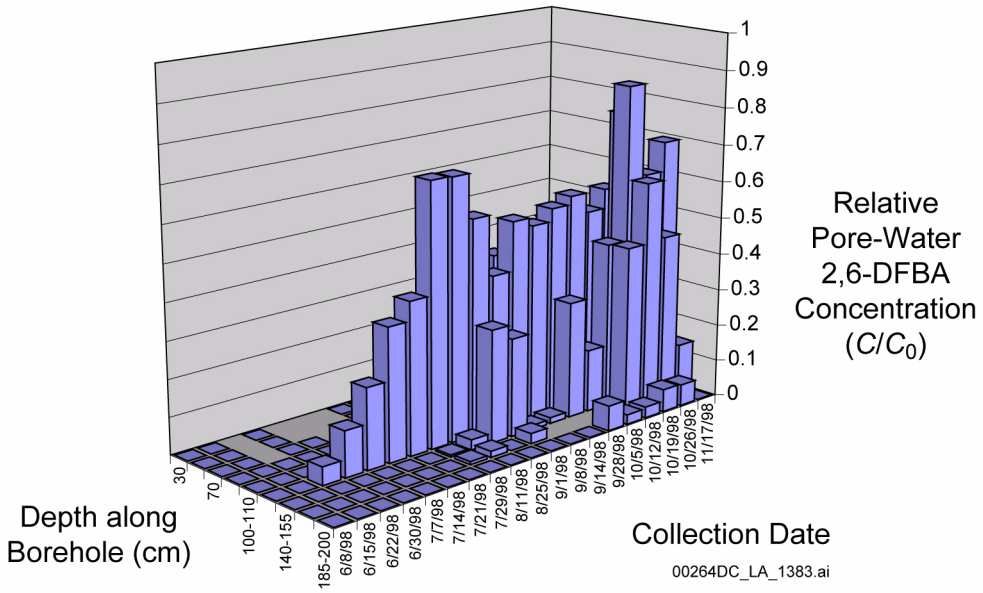

Figure 2.3.8-14. 2,6-Difluorobenzoic Acid–Relative Concentrations in Borehole 6 in Phase 1B of Busted Butte Unsaturated Zone Transport Test

NOTE: C = pore-water 2,6-DFBA concentration; C_0 = injection concentration; DFBA = difluorobenzoic acid.

Source: BSC 2004c, Figure 6-176.

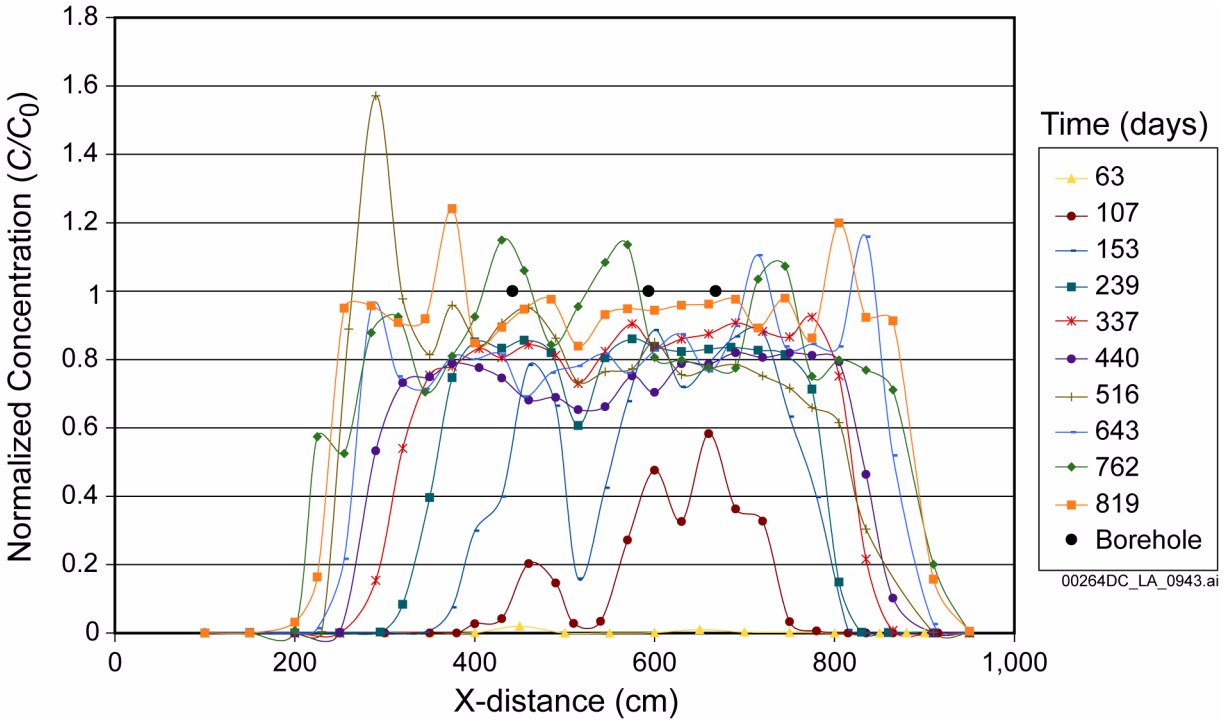

Figure 2.3.8-15. Spatial Distributions of Bromide-Relative Concentrations in Sampling Borehole 16 at Different Times during Phase 2C of Busted Butte Unsaturated Zone Transport Test

NOTE: C = pore water concentration; C_0 = injection concentration.

Source: Modified from SNL 2007b: includes data from DTN: LA0112WS831372.003.

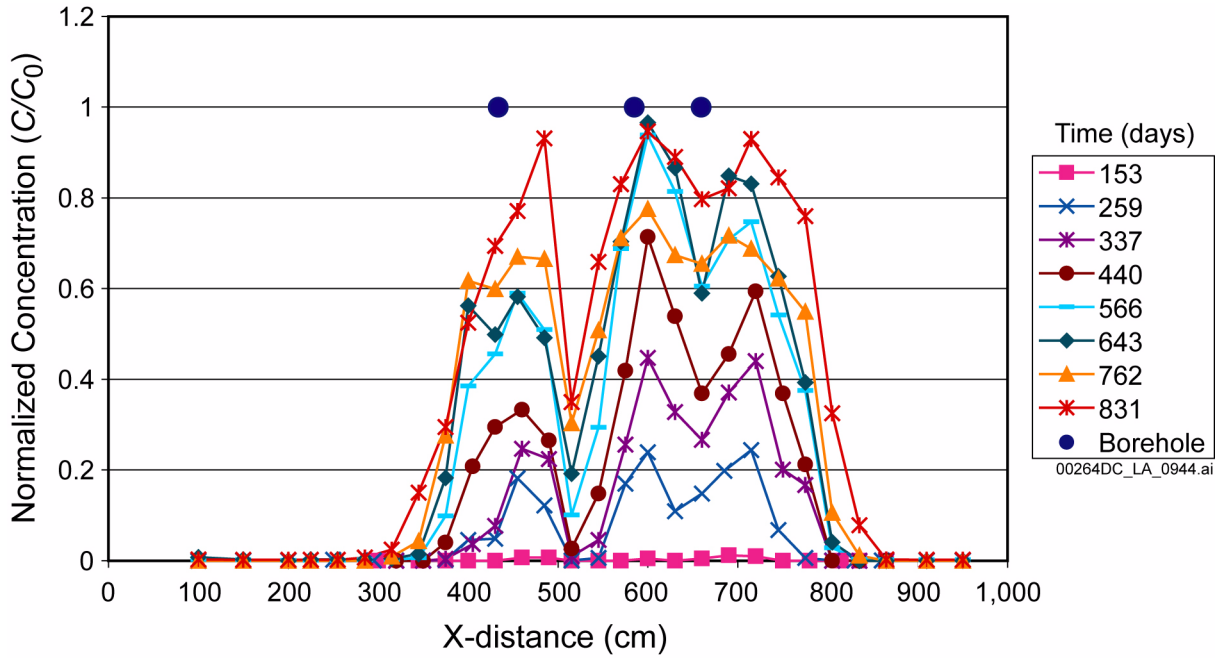

Figure 2.3.8-16. Spatial Distributions of Lithium-Relative Concentrations in Sampling Borehole 16 at Different Times during Phase 2C of Busted Butte Unsaturated Zone Transport Test

NOTE: C = pore water concentration; C_0 = injection concentration.Source:Modified from SNL 2007b: includes data from DTN: LA0201WS831372.007.

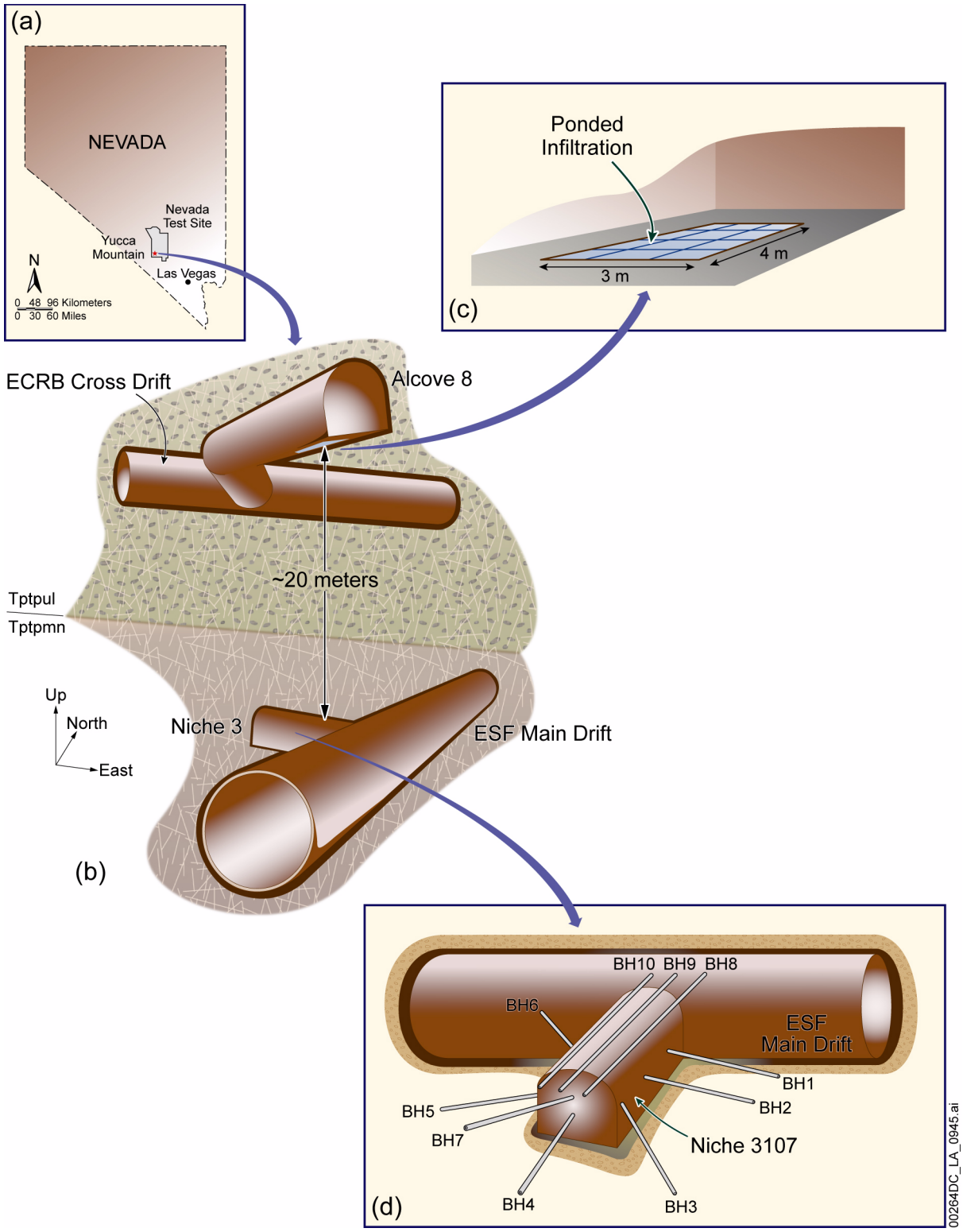

Figure 2.3.8-17. Test Bed for the Alcove 8–Niche 3 Tests

NOTE: The ECRB Cross-Drift crosses the ESF at a distance of about 20 m above the ESF (Inset (b)).

Source: BSC 2006a, Figure 6.1-1.

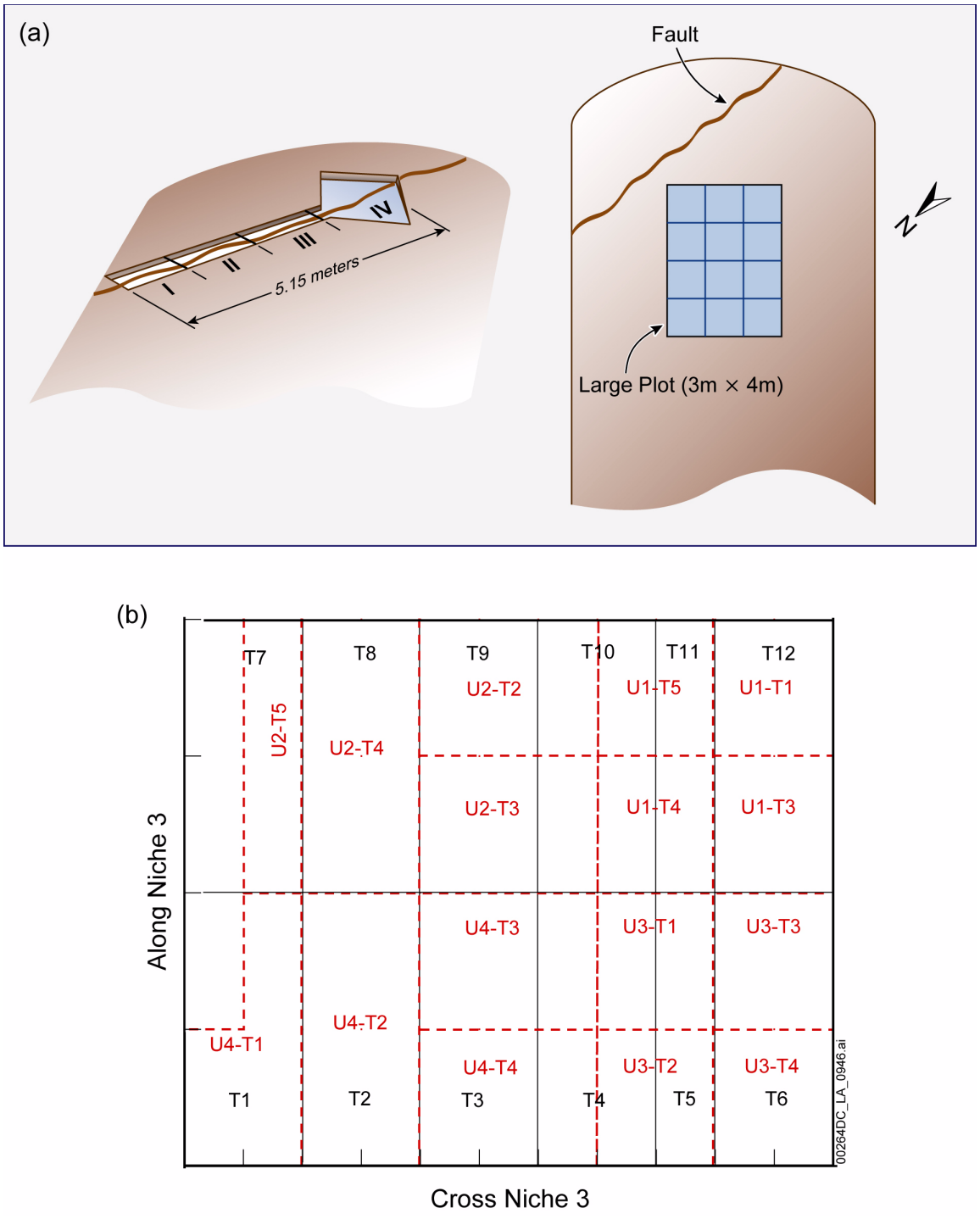

Figure 2.3.8-18. Schematic Illustration of the (a) Infiltration Zones along the Floor of Alcove 8 and (b) Seepage Water Collection in Niche 3

NOTE: The seepage collection areas are designated as U1-T1, U2-T2, etc. The "U" denotes the collection unit, and the "T" denotes a collection bottle. Only collection bottles where seepage was collected are shown. The ceiling of Niche 3 is divided into 12 columns for purposes of developing the numerical model; these columns are designated by T2, T2, etc.

Source: (a) BSC 2004c, Figure 6-150; (b) BSC 2006a, Figure 6.1-5.

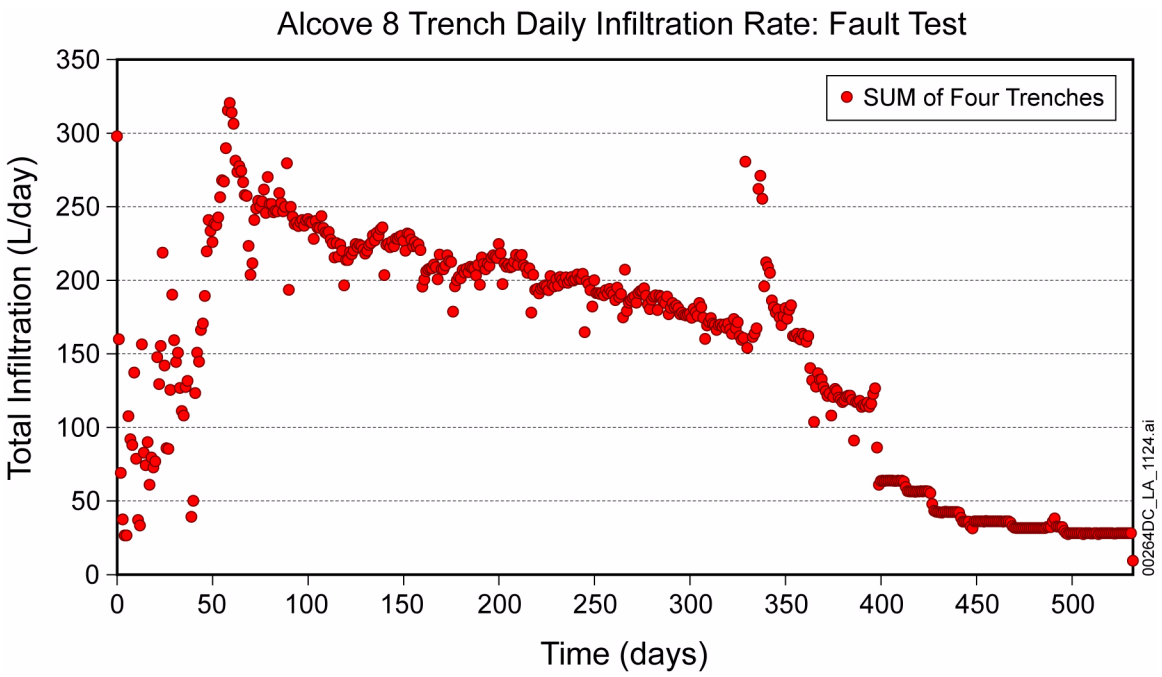

Figure 2.3.8-19. Total Percolation Rate During the Alcove 8–Niche 3 Fault Test, Obtained by Summing the Daily Average Percolation Rates into the Four Trenches

Source: Modified from BSC 2004c, Figure 6-152.

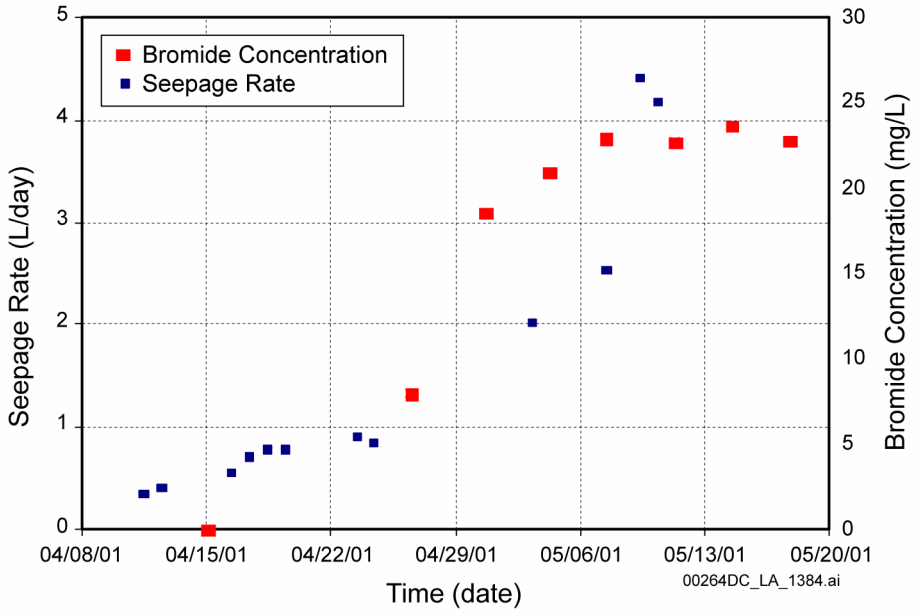

Figure 2.3.8-20. Bromide Concentration and Water Seepage Rates Plotted against Time into Niche 3, Measured for 45 Days after First Observations of Drips in Tray 6 in the Alcove 8–Niche 3 Test

NOTE: The figure illustrates the similar trends of seepage rate and bromide concentration with time.

Source: BSC 2004c, Figure 6-158.

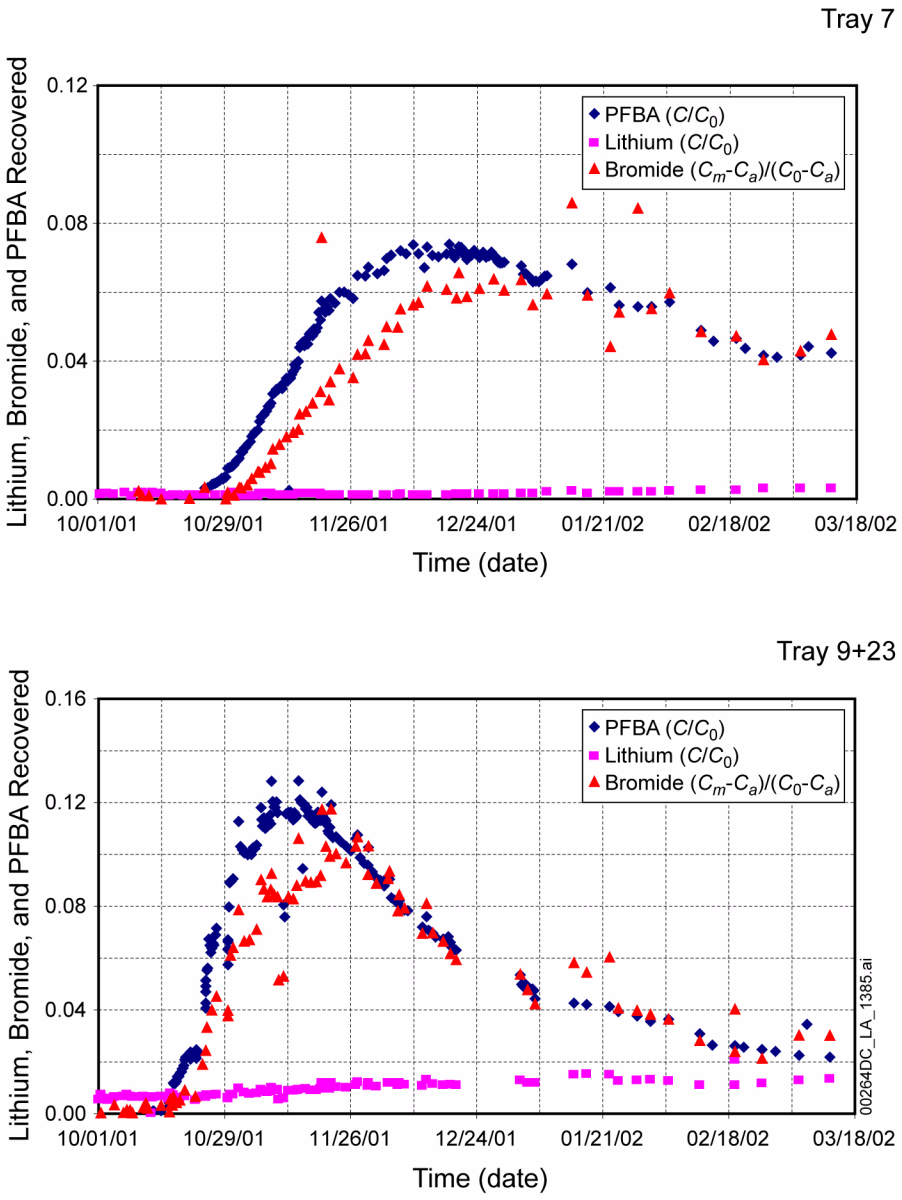

Figure 2.3.8-21. Relative Concentrations of Tracers Measured in Seepage in Niche 3 in the Alcove 8–Niche 3 Test

NOTE: C_m is the measured concentration, C_a is the background concentration in the leachate, and C_0 is the injection concentration.
PFBA = pentafluorobenzoic acid.

Source: BSC 2004c, Figure 6-159.

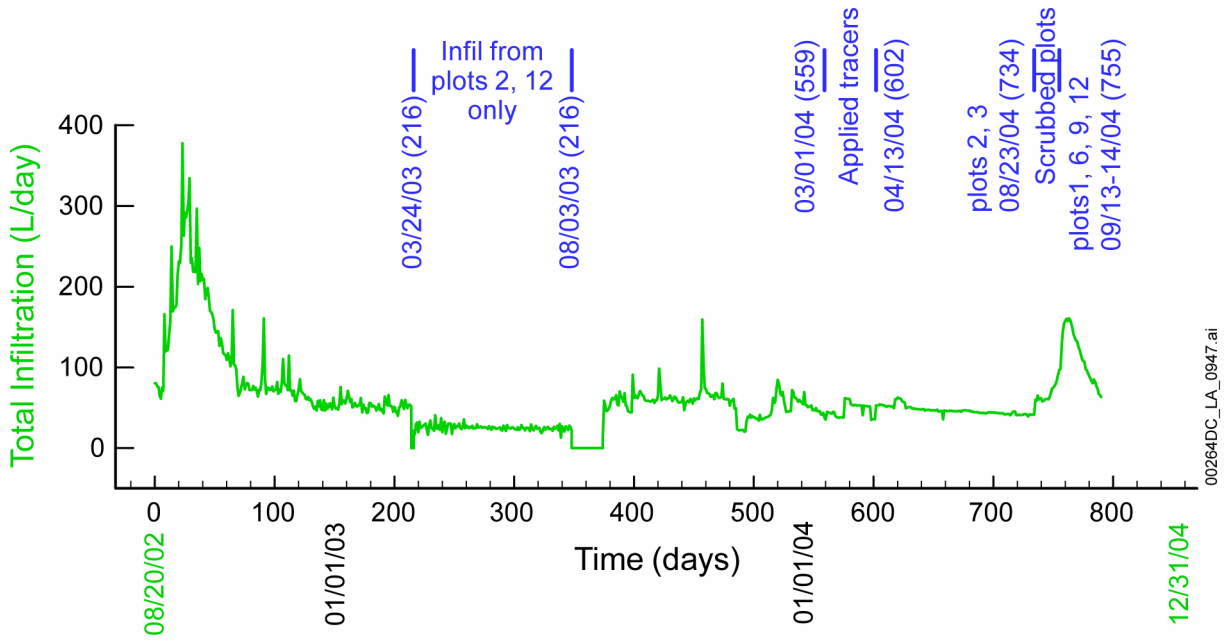

Figure 2.3.8-22. Total Flow Rate into the Alcove 8 Large Plot as a Function of Time

Source: BSC 2006a, Figure 6.1-4.

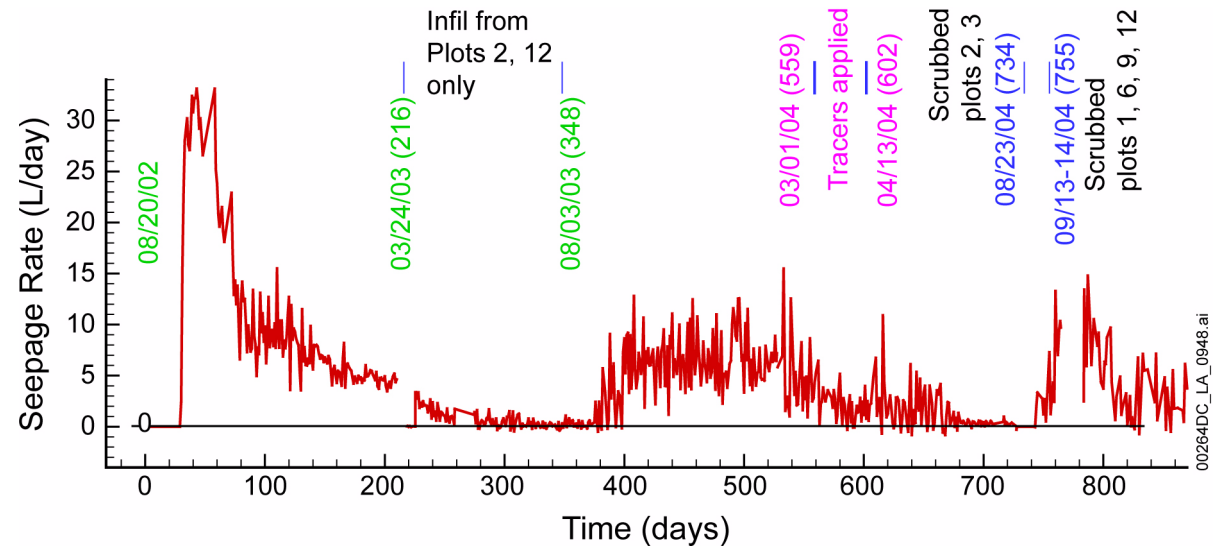

Figure 2.3.8-23. Total Seepage Rate into Niche 3 as a Function of Time for the Large Plot Test

Source: BSC 2006a, Figure 6.1-7.

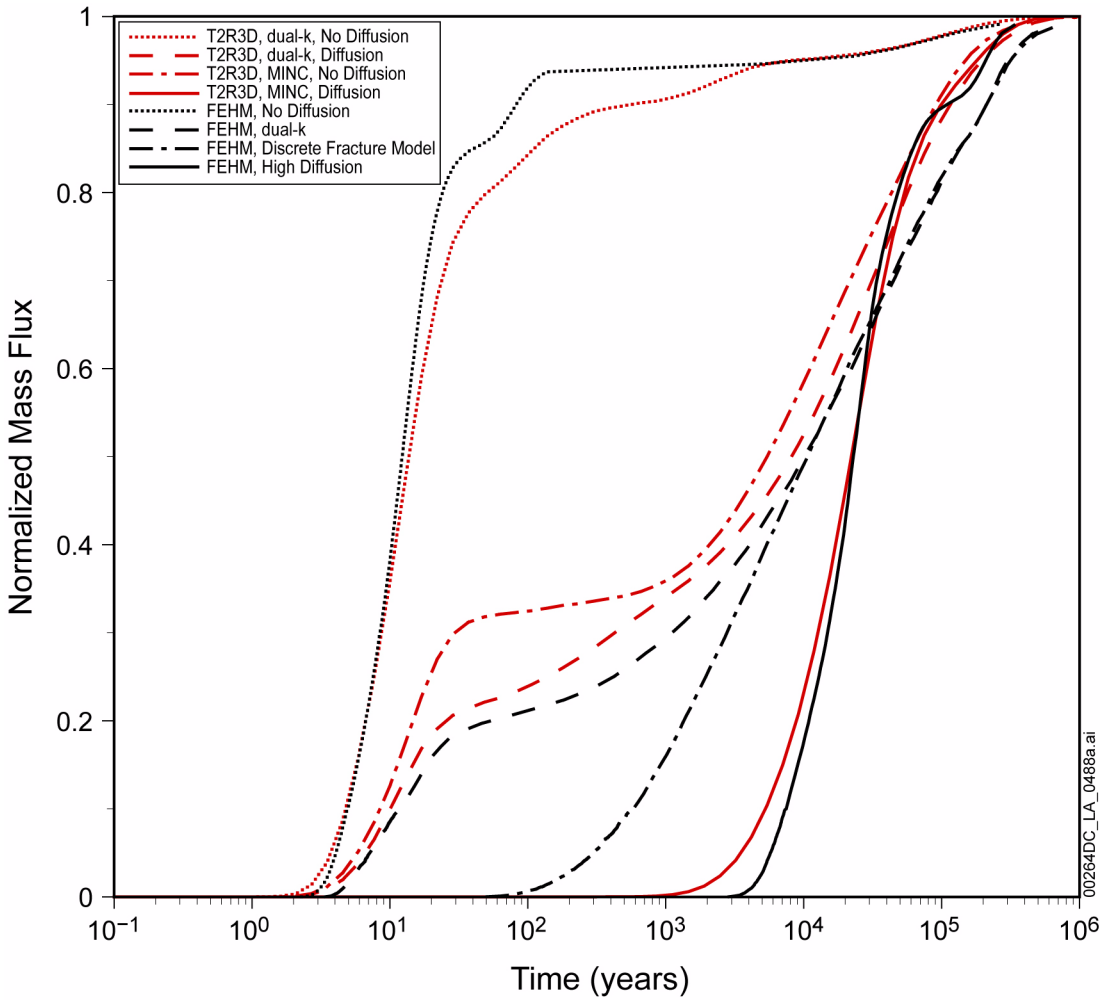

Figure 2.3.8-24. Comparison of Dual-k, MINC, and Particle Tracking Breakthrough Predictions for an Instantaneous Release of a Conservative Tracer at a Two-Dimensional Vertical Cross Section of the Unsaturated Zone

NOTE: T2R3D, EOS9nT, and FEHM are software used to compute solute transport in the unsaturated zone. Dual-k and MINC are alternative dual-continuum gridding schemes for fracture–matrix interaction. Dual-k uses a single grid cell, and MINC uses two or more grid cells to represent the matrix. T2R3D and EOS9nT use direct numerical solution methods for the conservation equations. FEHM uses a particle-tracking method. Dual-k and MINC calculations are shown with and without matrix diffusion FEHM particle tracking simulations are assuming the dual-k model and a discrete fracture model similar to MINC. Normalized mass fraction M_R is the ratio of the cumulative mass arrival at the water table to the initial pulse mass release. Transport parameters have representative values. Conservative tracer is treated as nonsorbing, nondecaying solute. Infiltration rate is derived from a previous version of the unsaturated zone flow and transport model in which the average across the repository footprint was 4.7 mm/yr. The bottom boundary was defined as the present-day water table.

Source: SNL 2008a, Figure 7-9 in Addendum 1.

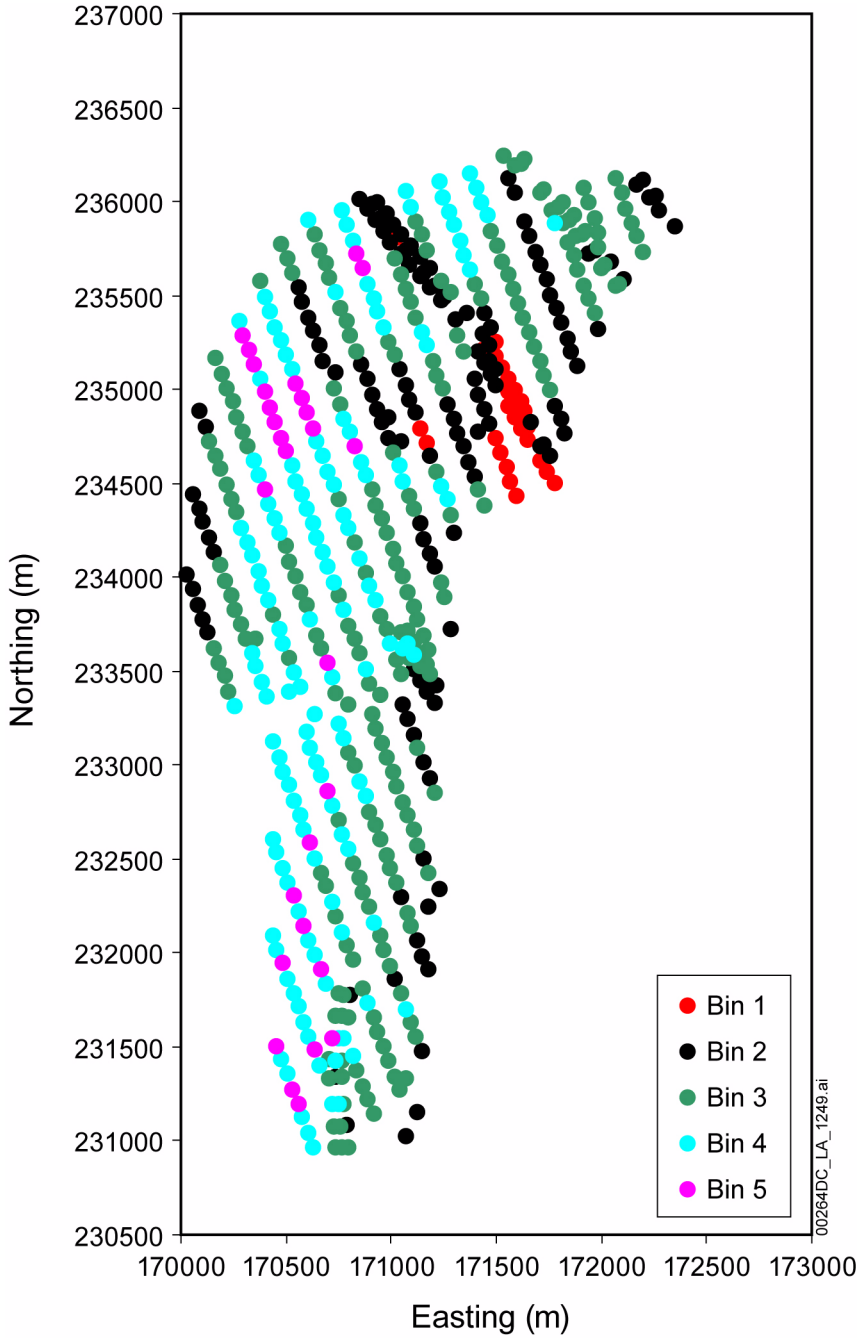

Figure 2.3.8-25. Repository Nodes Colored by Percolation Bin for the Flow Field Based on the Glacial-Transition, 10th percentile Infiltration Map

NOTE: Ranges of percolation flux values associated for each bin for this flow field are as follows (ranges in the cumulative distribution for each bin are given in parentheses): Bin 1 (0 to 0.05): 0.15 to 0.82 mm/yr; Bin 2 (0.05 to 0.30): 0.82 to 4.55 mm/yr; Bin 3 (0.30 to 0.70): 4.55 to 14.06 mm/yr, Bin 4 (0.70 to 0.95): 14.06 to 26.16 mm/yr, Bin 5 (0.95 to 1): 26.16 to 36.19 mm/yr

Source: SNL 2008a, Figure 6-14 in Addendum 1.

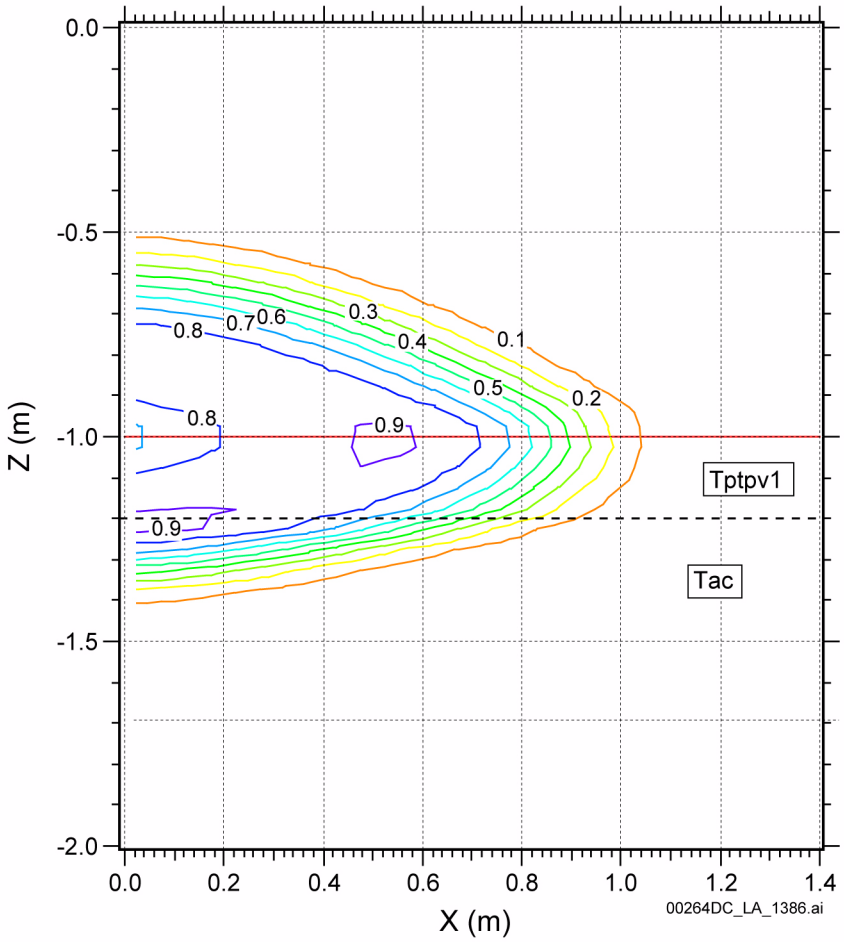

Figure 2.3.8-26. Numerical Calculation of the Distribution of Fluorescein Relative Concentrations Using Calibrated Parameters in Phase 1A of the Busted Butte Unsaturated Zone Transport Test

NOTE: The dashed horizontal line at –1.2 (z axis) represents the approximate contact between the Tptpv1 and Tac units.

Source: SNL 2007b, Figure 7-8.

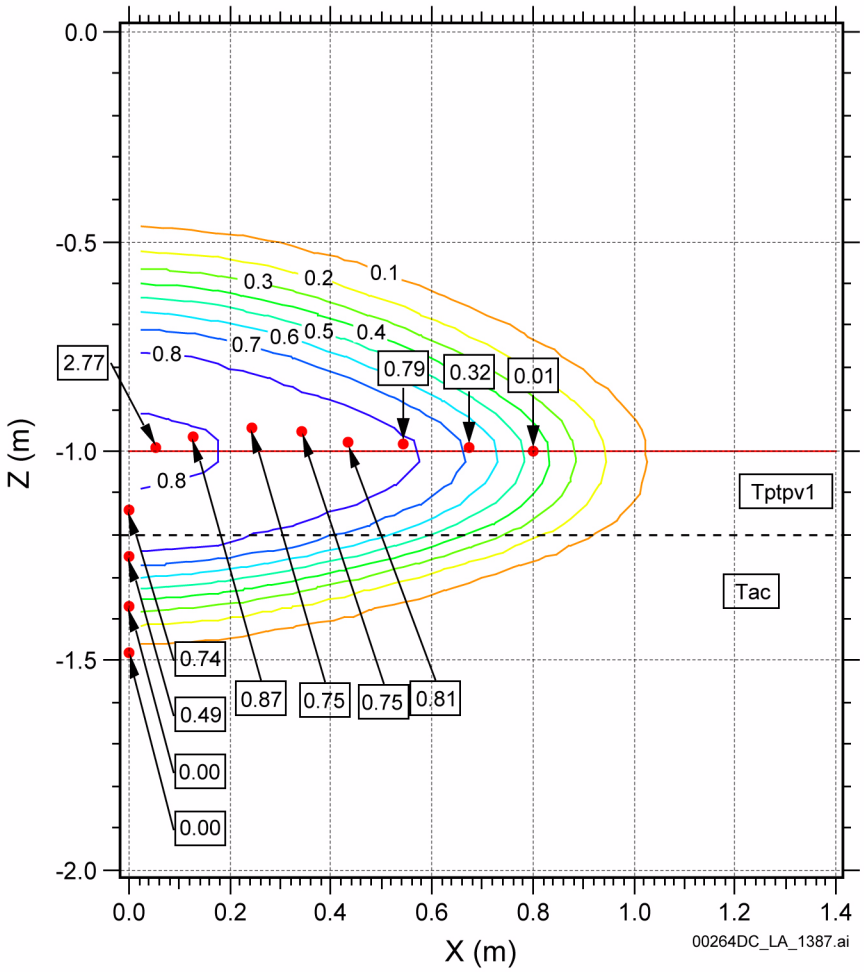

Figure 2.3.8-27. Field Measurements and Numerical Prediction of the Distribution of Bromide-Relative Concentrations in Phase 1A of the Busted Butte Unsaturated Zone Transport Test

NOTE: The solid circles indicate the location of bromide relative concentration measurements, which appear in the corresponding boxes. The dashed horizontal line at –1.2 (z axis) represents the approximate contact between the Tptpv1 and Tac units.

Source: SNL 2007b, Figure 7-9.

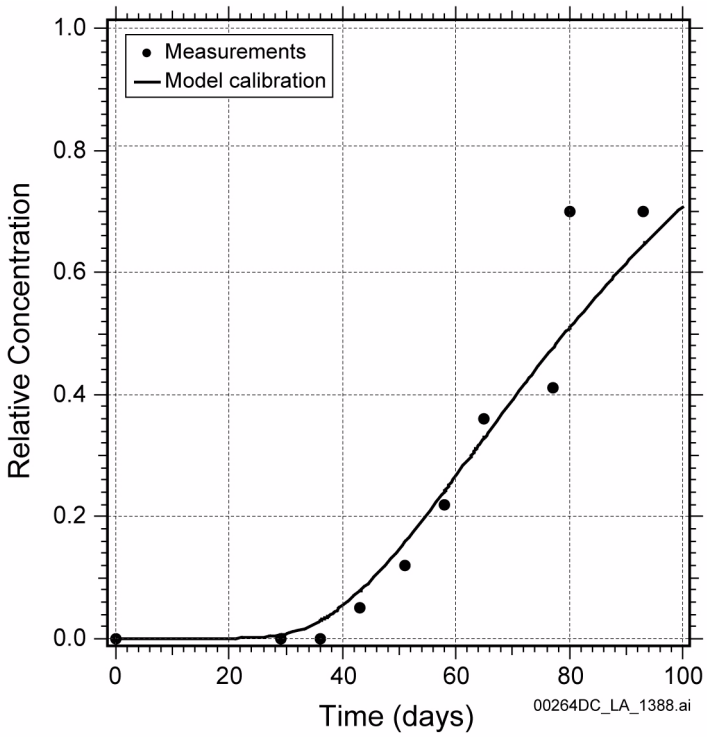

Figure 2.3.8-28. Observed and Numerically Predicted (Calibrated) Breakthrough Curves of 2,6-Difluorobenzoic Acid in Phase 1B of the Busted Butte Unsaturated Zone Transport Test

NOTE: Relative concentration is the observed concentration relative to injection concentration.

Source: SNL 2007b, Figure 7-10.

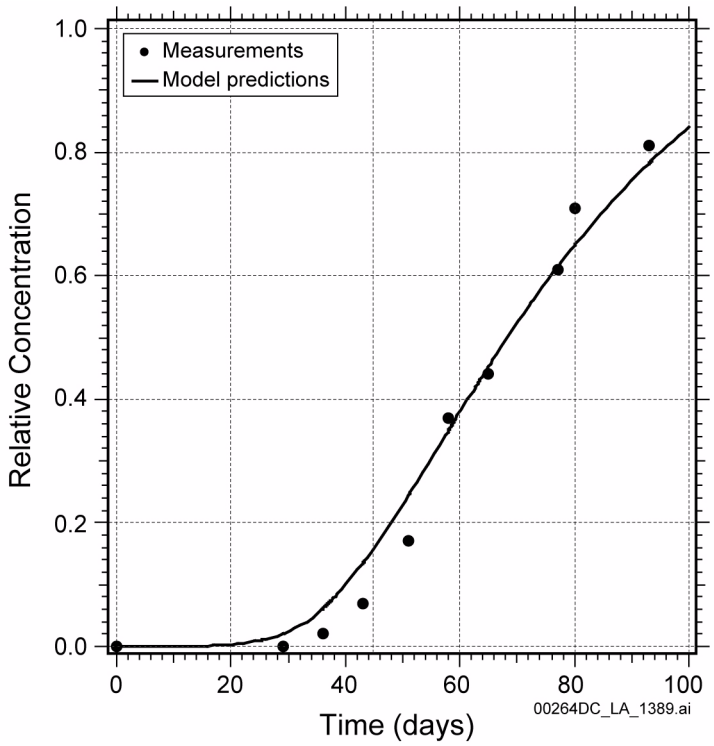

Figure 2.3.8-29. Observed and Numerically Predicted (at Verification) Breakthrough Curves of Bromide in Phase 1B of the Busted Butte Unsaturated Zone Transport Test

NOTE: Relative concentration is the observed concentration relative to injection concentration.

Source: SNL 2007b, Figure 7-11.

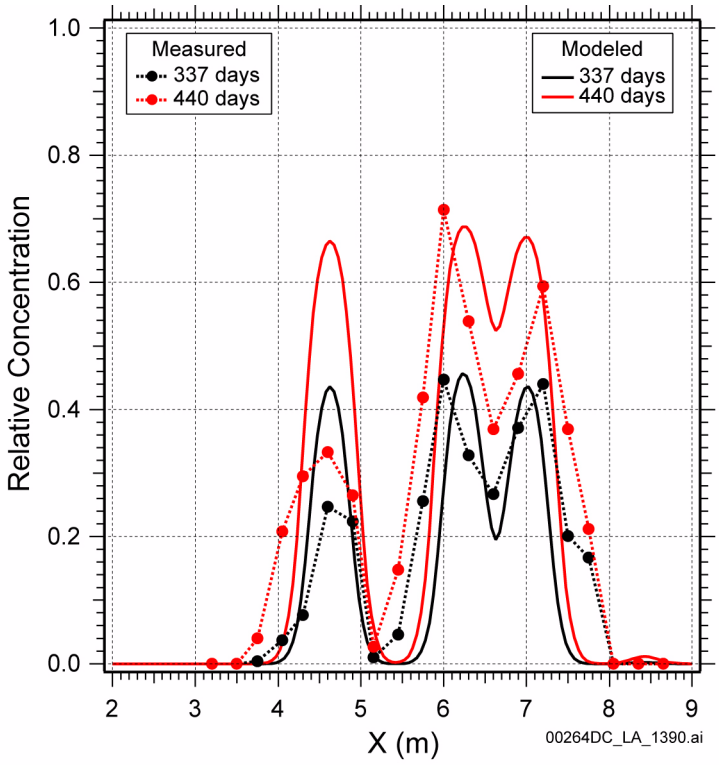

Figure 2.3.8-30. Observed and Calculated Relative Lithium Concentrations as a Function of Distance from Face of Collection Borehole 16 in Phase 2C of the Busted Butte Unsaturated Zone Transport Test

NOTE: Relative concentration is the observed concentration relative to injection concentration. X is the distance along collection borehole 16 from its face. Concentration peaks correlate to locations of three horizontal injection boreholes overlying and perpendicular to the horizontal collection borehole 16. Measured data points were connected to better illustrate the pattern of change.

Source: SNL 2007b, Figure 7-12.

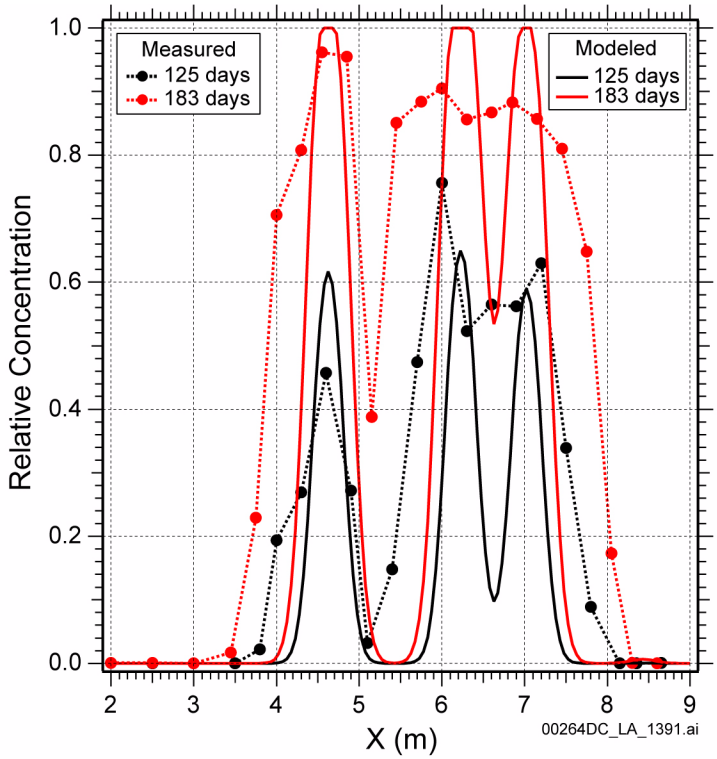

Figure 2.3.8-31. Observed and Predicted Relative Bromide Concentrations as a Function of Distance from Face of Collection Borehole 16 in Phase 2C of the Busted Butte Unsaturated Zone Transport Test

NOTE: Relative concentration is the observed concentration relative to injection concentration. X is the distance along collection borehole 16 from its face. Concentration peaks correlate to locations of three horizontal injection boreholes overlying and perpendicular to the horizontal collection borehole 16. Measured data points were connected to better illustrate the pattern of change.

Source: SNL 2007b, Figure 7-13.

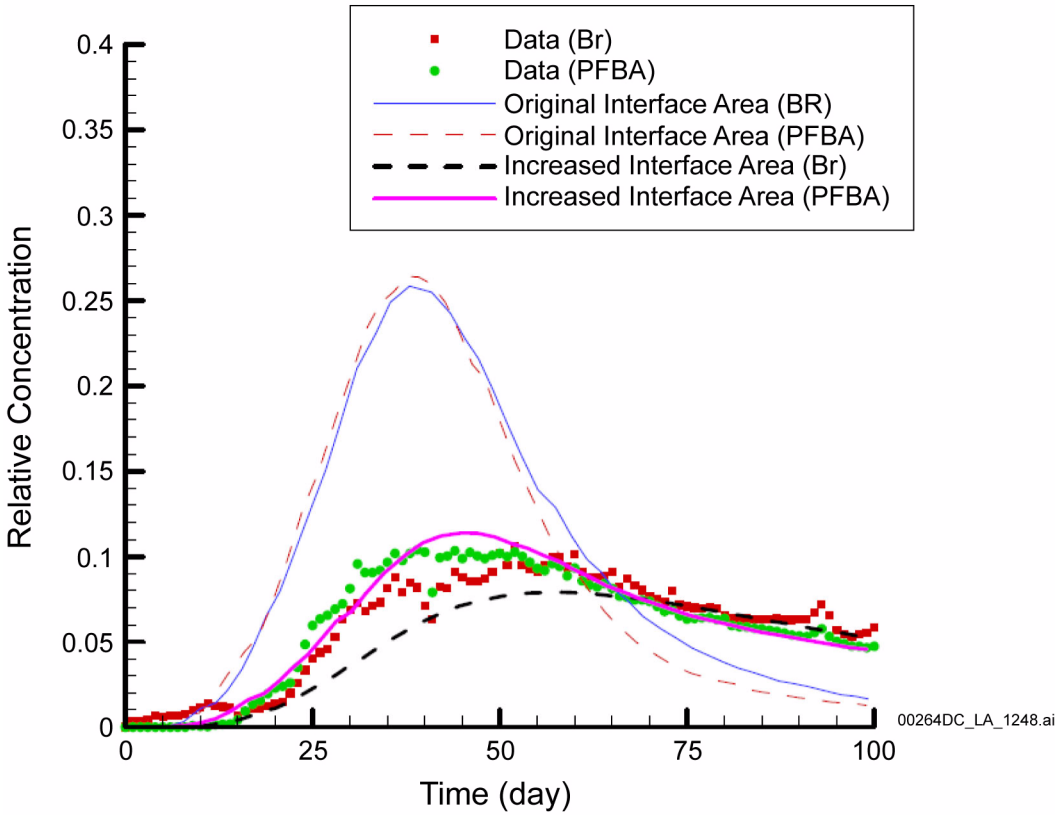

Figure 2.3.8-32. Comparisons between Calculated Breakthrough Curves at the Niche for Two Different Fault–Matrix Interface Areas and the Observed Data in the Alcove 8–Niche 3 Test

NOTE: Relative concentration is the observed concentration relative to injection concentration. The increase in interface area identified in this is not used in the transport model used in TSPA.
PFBA = pentafluorobenzoic acid.

Source: SNL 2007b, Figure 7-22.

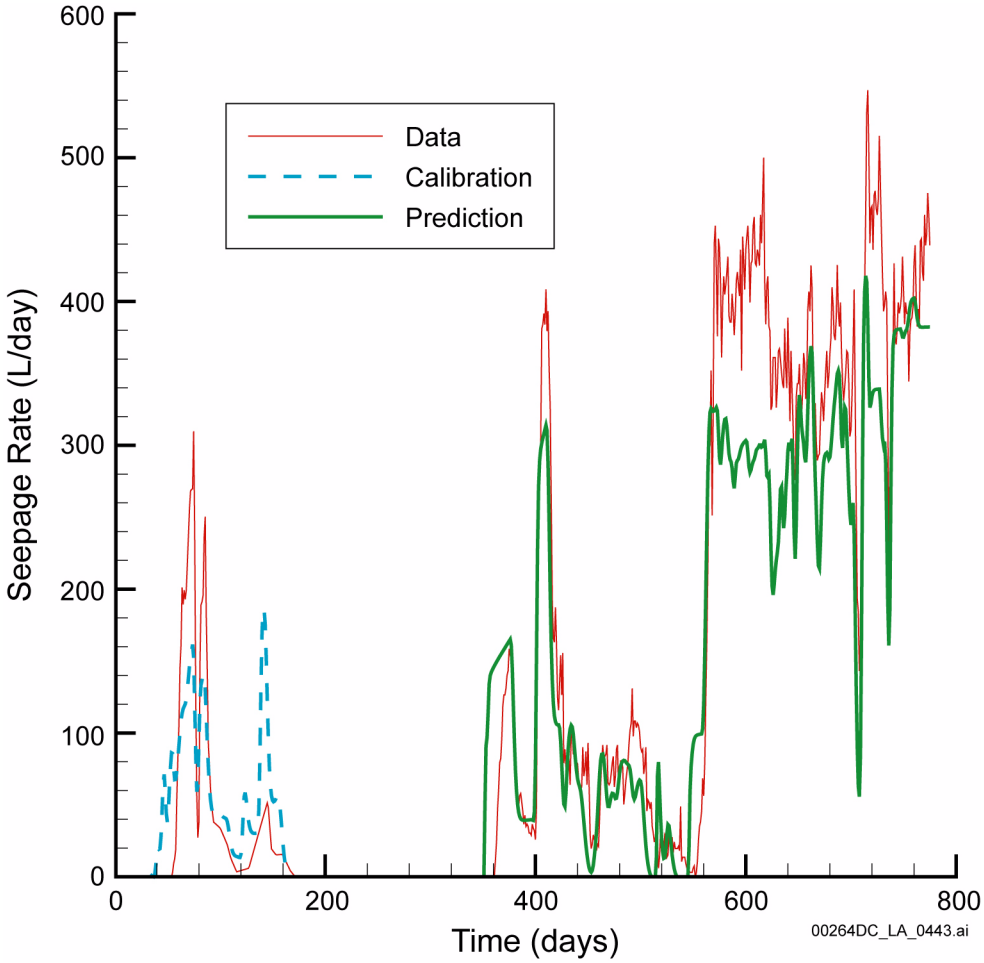

Figure 2.3.8-33. Comparison of Model Calibration using the Seepage Rate Data from Phase I (Alcove 1, early time data) and Model Prediction Compared to Phase II (Alcove 1, late time data)

Source: Liu, Haukwa et al. 2003, Figure 3.

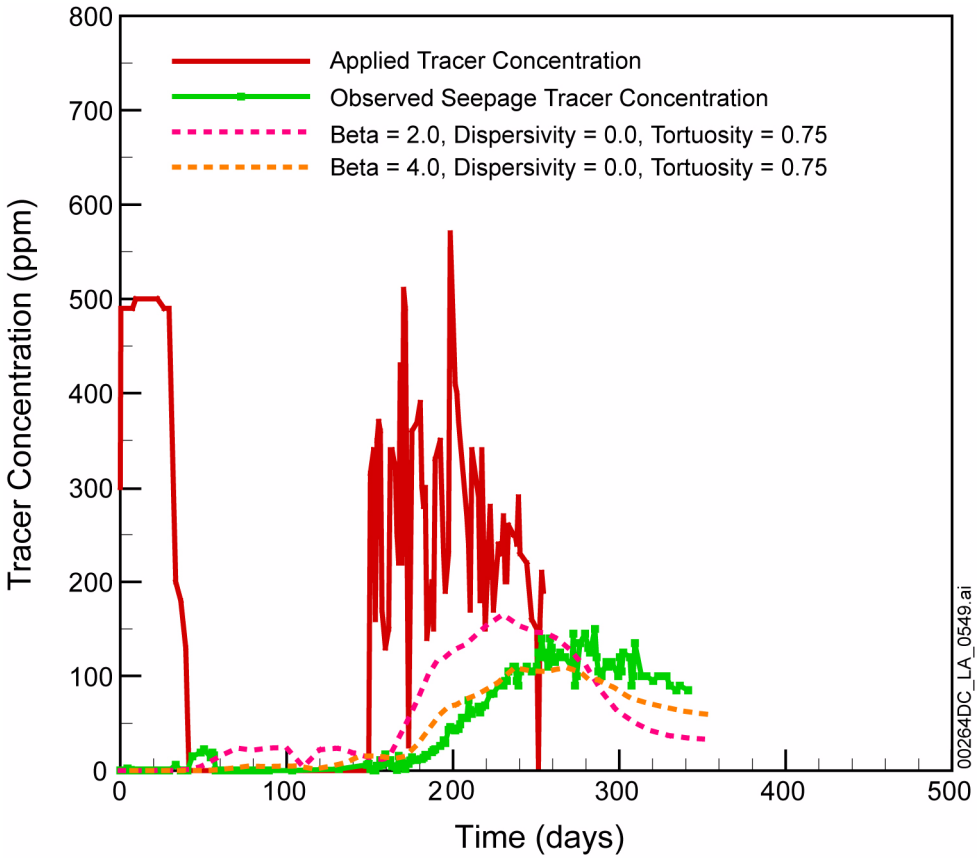

Figure 2.3.8-34. Comparison Between the Observed Tracer Concentrations and Modeling Results with Adjusted Fracture–Matrix Interface Area in the Alcove 1 Test

NOTE: Beta is an adjustment factor for fracture–matrix interface area. Dispersivity is in units of meters. Tortuosity is dimensionless.

Source: Liu, Haukwa et al. 2003, Figure 7.

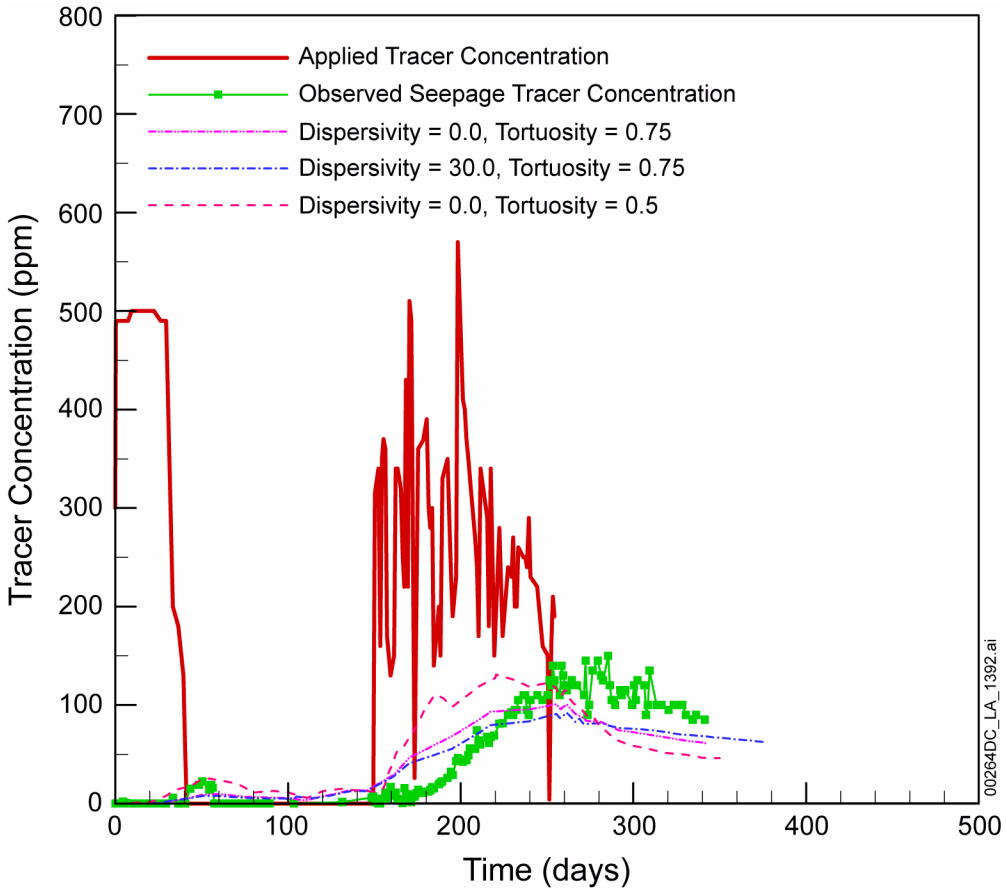

Figure 2.3.8-35. Comparison Between Model Predictions of Bromide Tracer Transport and Observations in the Alcove 1 Test

NOTE: Time at 0 days corresponds to the initial introduction of the tracer to the applied water. Dispersivity is in units of meters. Tortuosity is dimensionless.

Source: Liu, Haukwa et al. 2003, Figure 5.

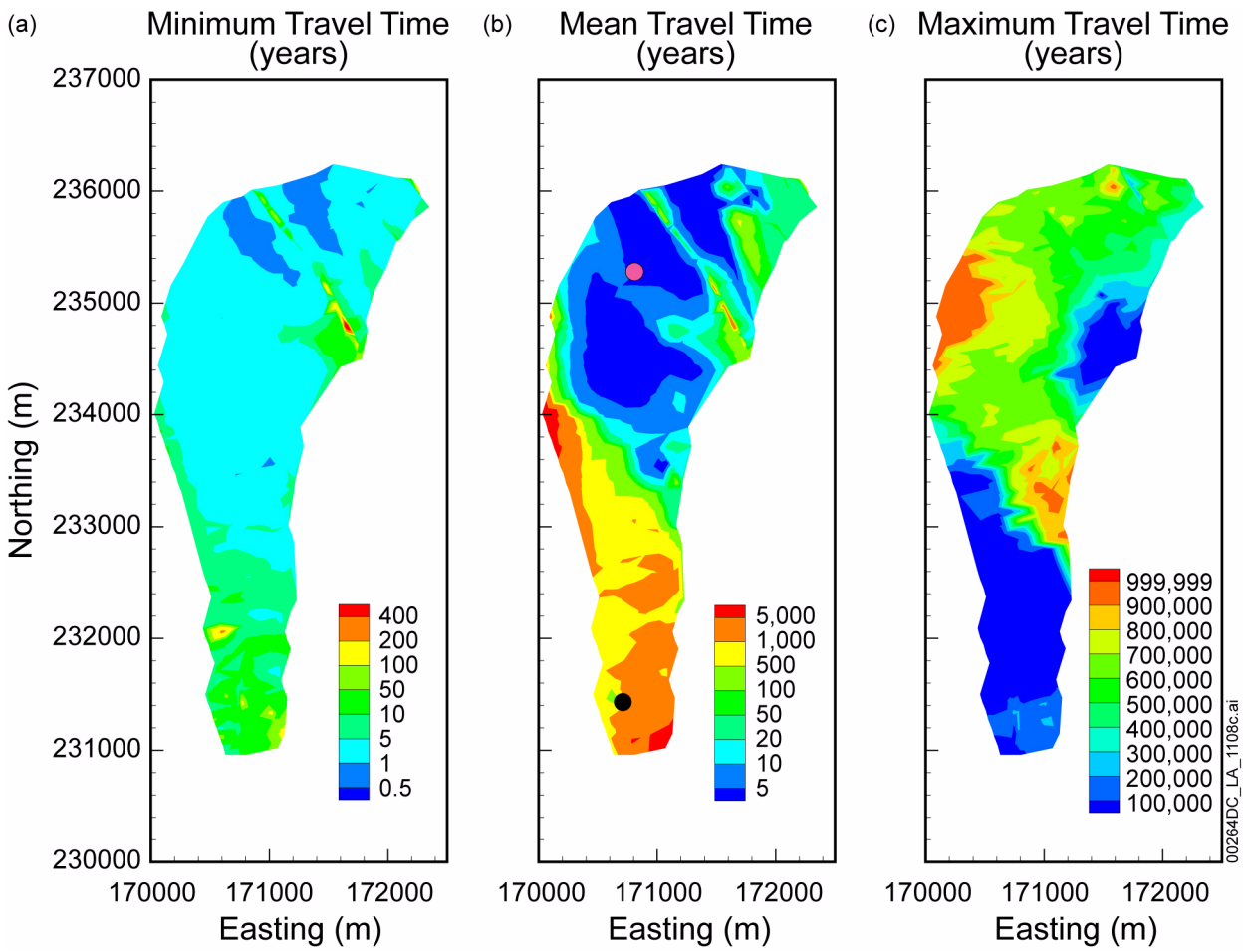

Figure 2.3.8-36. Contour Maps of (a) the Minimum Travel Time, (b) the Mean Travel Time, and (c) the Maximum Travel Time for Particles Released at All Repository Nodes Using the Glacial-Transition, 10th Percentile Infiltration Map, and Conservative Species without Decay or Matrix Diffusion

NOTE: The outline of the contoured data corresponds to the repository footprint shown in Figure 2.3.8-4. The pink (Northern) and black (Southern) points in (b) are the individual release locations used in this study. The travel time, also referred to as the transport time, represents the time from the release from the repository to the arrival at the water table.

Source: SNL 2008a, Figure 6.6.2-1[b].

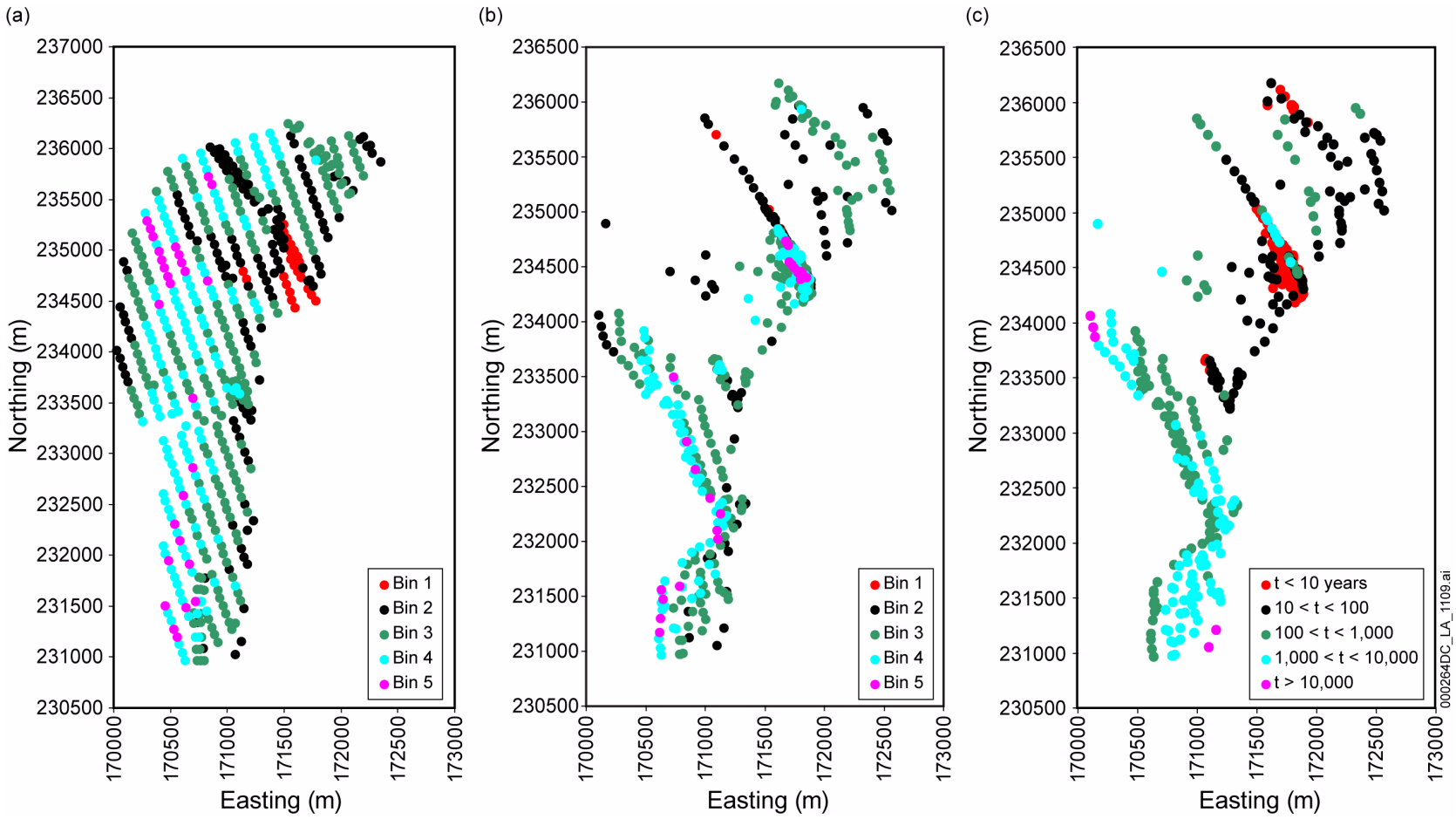

Figure 2.3.8-37. Comparison of Particle Release Locations (left) and Exit Locations in Terms of Percolation Bin Assignment (middle) or Mean Travel Time (right) for Flow Fields Developed Using the Glacial-Transition, 10th Percentile Infiltration Map

NOTE: For this flow field, upper percolation rates for each bin are Bin 1 = 0.82, Bin 2 = 4.55, Bin 3 = 14.06, Bin 4 = 26.16, and Bin 5 = 36.19 mm/yr. The figure on the right shows the exit locations from the unsaturated zone at the water table plotted with mean travel time of a conservative species without decay or matrix diffusion.

Source: SNL 2008a184748, Figure 6.6.2-3 in Addendum 1.

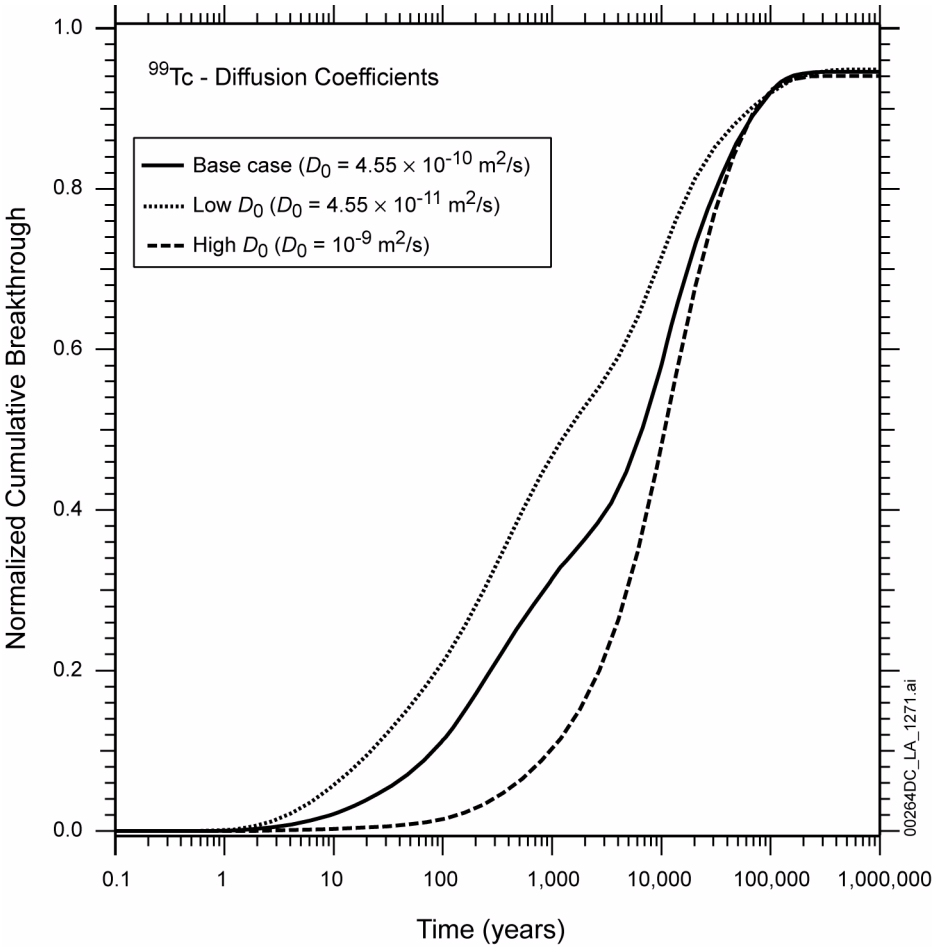

Figure 2.3.8-38. Effect of Varying Diffusion Coefficients (D_0) on the Cumulative Breakthrough of the ^{99}Tc Normalized Mass Fraction

NOTE: These results are for comparison purposes only. Simulation is based on an older version of the unsaturated zone flow model. Base case is as defined in the site-scale unsaturated zone radionuclide transport process model for the mean present-day infiltration case developed in the previous version of the infiltration model (BSC 2004h, Section 6.11.1). In this model, the average infiltration rate across the repository footprint was 4.7 mm/yr, the bottom boundary was defined as the present-day water table, and releases occurred across the entire repository footprint. Normalized mass fraction is the ratio of the cumulative mass arrival at the water table to the initial mass release. Release of ^{99}Tc is instantaneous. Transport parameters have representative values.

Source: SNL 2007b, Figure 6-35.

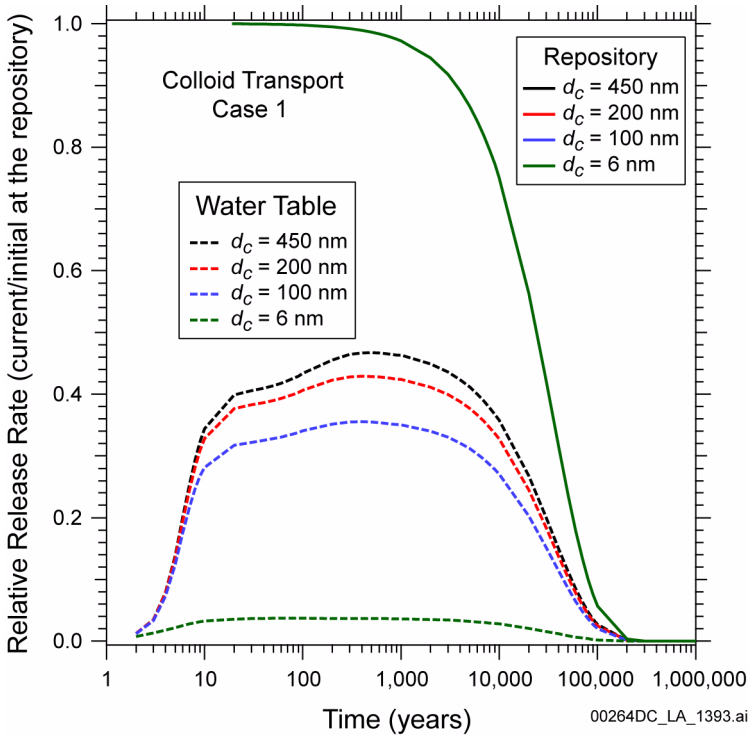

Figure 2.3.8-39. Normalized Release at the Water Table of the Colloid Mass Flux for Several Colloid Sizes for the Case of No Declogging Following Attachment

NOTE: These results are for comparison purposes only. Simulation is based on an older version of the unsaturated zone flow model. The solid green line plots the colloid mass flux at the repository divided by the initial colloid mass flux at the repository for four selected colloid diameters. Dashed lines plot the colloid mass flux at the water table divided by the initial colloid mass flux at the repository for selected colloid diameters. Release of ^{239}Pu is represented as continuous. Transport parameters have representative values. Simulation is based on a flow field developed using the mean present-day infiltration case developed in a previous version of the infiltration model (BSC 2004h, Section 6.11.1). In this model, the average infiltration rate across the repository footprint was 4.7 mm/yr, the bottom boundary was defined as the present-day water table, and releases occurred across the entire repository footprint.
d_c = colloid diameter.

Source: SNL 2007b, Figure 6-59(a).

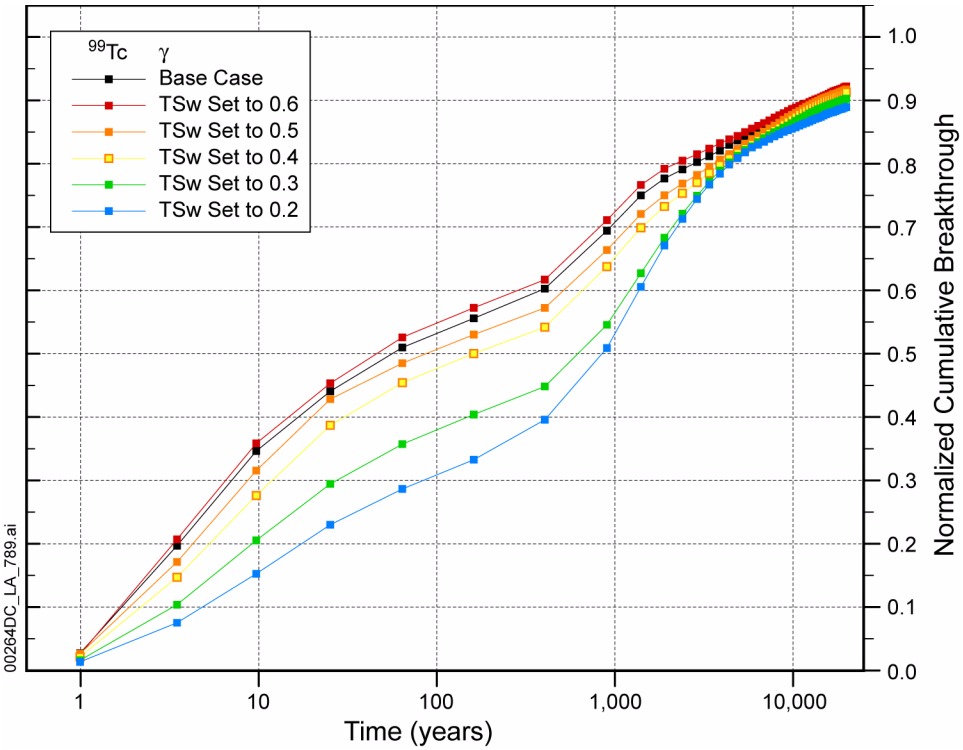

Figure 2.3.8-40. Unsaturated Zone Radionuclide Transport Abstraction Model Results for Normalized Mass Flux at the Water Table for ^{99}Tc, for Different Values of the Active Fracture Model γ Parameter

NOTE: These results are for comparison purposes only. Simulation is based on an older version of the unsaturated zone flow model. Actual radionuclide mass flux reaching the water table will depend on release rates and locations and are simulated in the TSPA model. Simulation is based on a flow field developed using the mean glacial-transition infiltration case developed in a previous version of the infiltration model (BSC 2004h, Section 6.11.3). In this model, the average infiltration rate across the repository footprint was 19.8 mm/yr, and releases occurred across the entire repository footprint. The bottom boundary was defined as the elevated water table at a minimum of 850 meters above sea level.

Source: SNL 2008a, Figure 6-33.

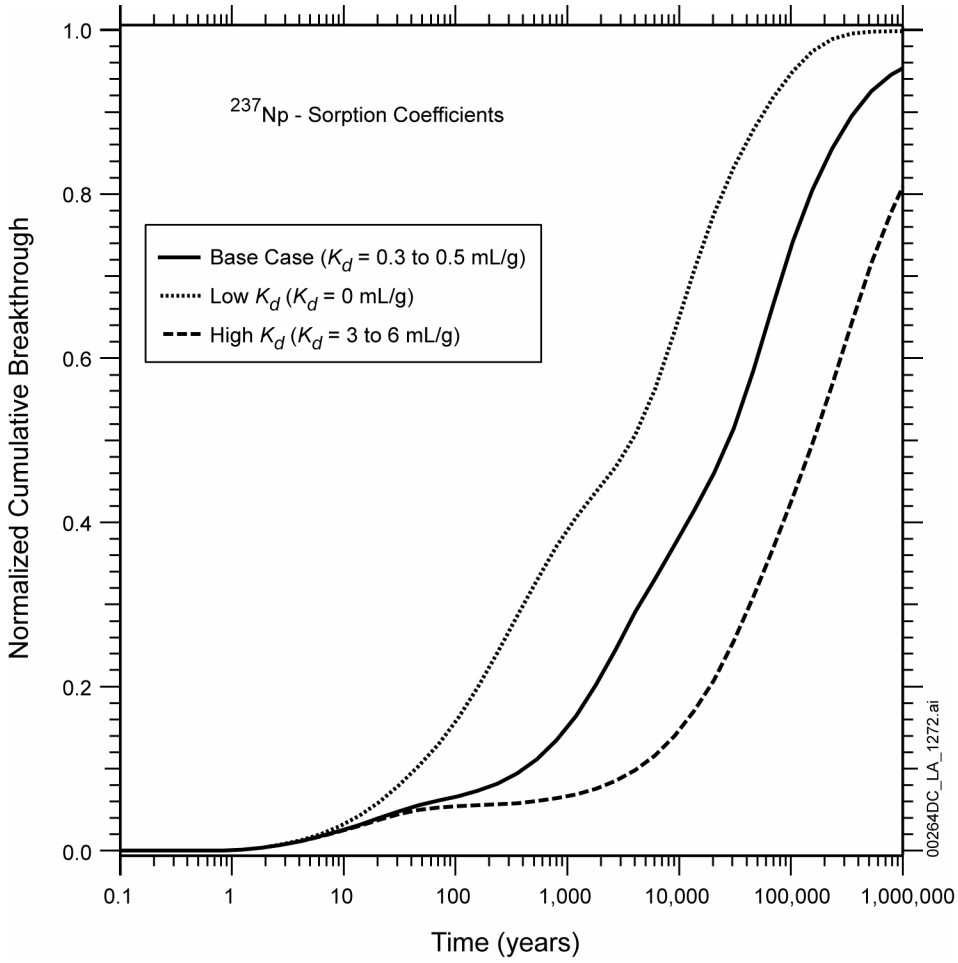

Figure 2.3.8-41. Effect of Varying Sorption Coefficients (K_d) on the Cumulative Breakthrough of the ^{237}Np Normalized Mass Fraction

NOTE: These results are for comparison purposes only. Simulation is based on an older version of the unsaturated zone flow model. The range in K_d values indicates differences in the various hydrogeologic units. Base case is as defined in the site-scale unsaturated zone radionuclide transport process model for the mean present-day infiltration case developed in the previous version of the infiltration model (BSC 2004h, Section 6.11.1). In this model, the average infiltration rate across the repository footprint was 4.7 mm/yr, the bottom boundary was defined as the present-day water table, and releases occurred across the entire repository footprint. Normalized mass fraction is the ratio of the cumulative mass arrival at the water table to the initial mass release. Release of ^{237}Np is instantaneous.

Source: SNL 2007b, Figure 6-41.

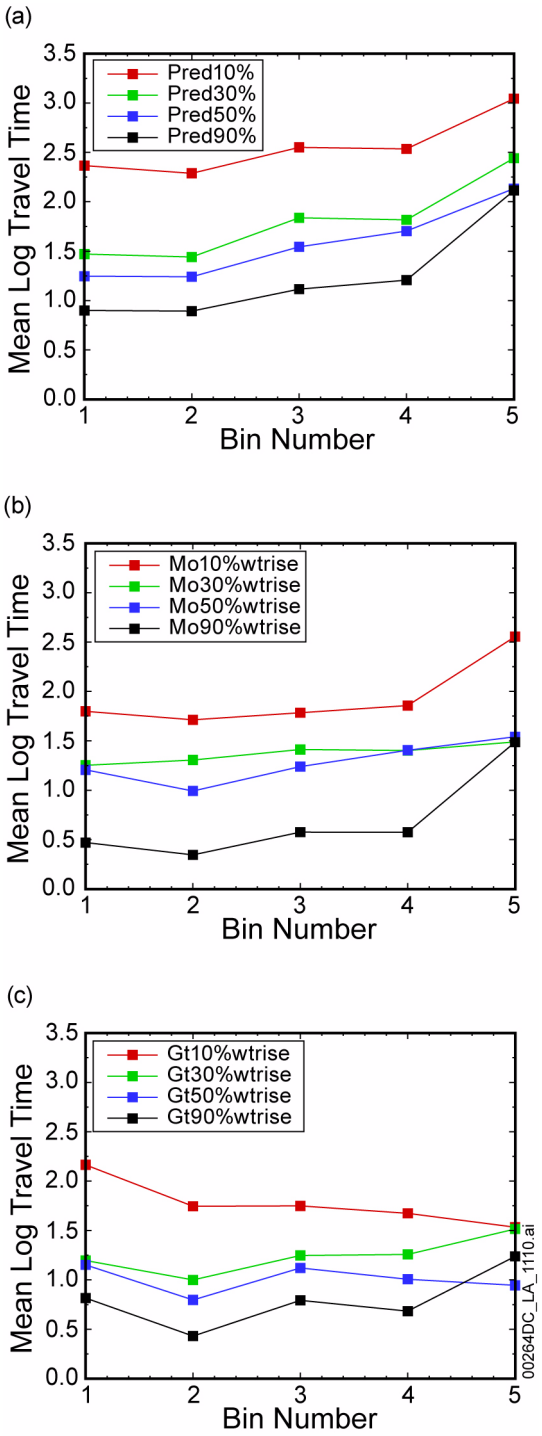

Figure 2.3.8-42. Comparison of the Bin-Averaged Log Travel Time for Particles Released at All Repository Nodes for Three Climate Conditions (a) Present-Day, (b) Monsoon, and (c) Glacial-Transition and Four Infiltration Maps, and Conservative Species without Decay or Matrix Diffusion

Source: SNL 2008a, Figure 6.6.2-4 in Addendum 1.

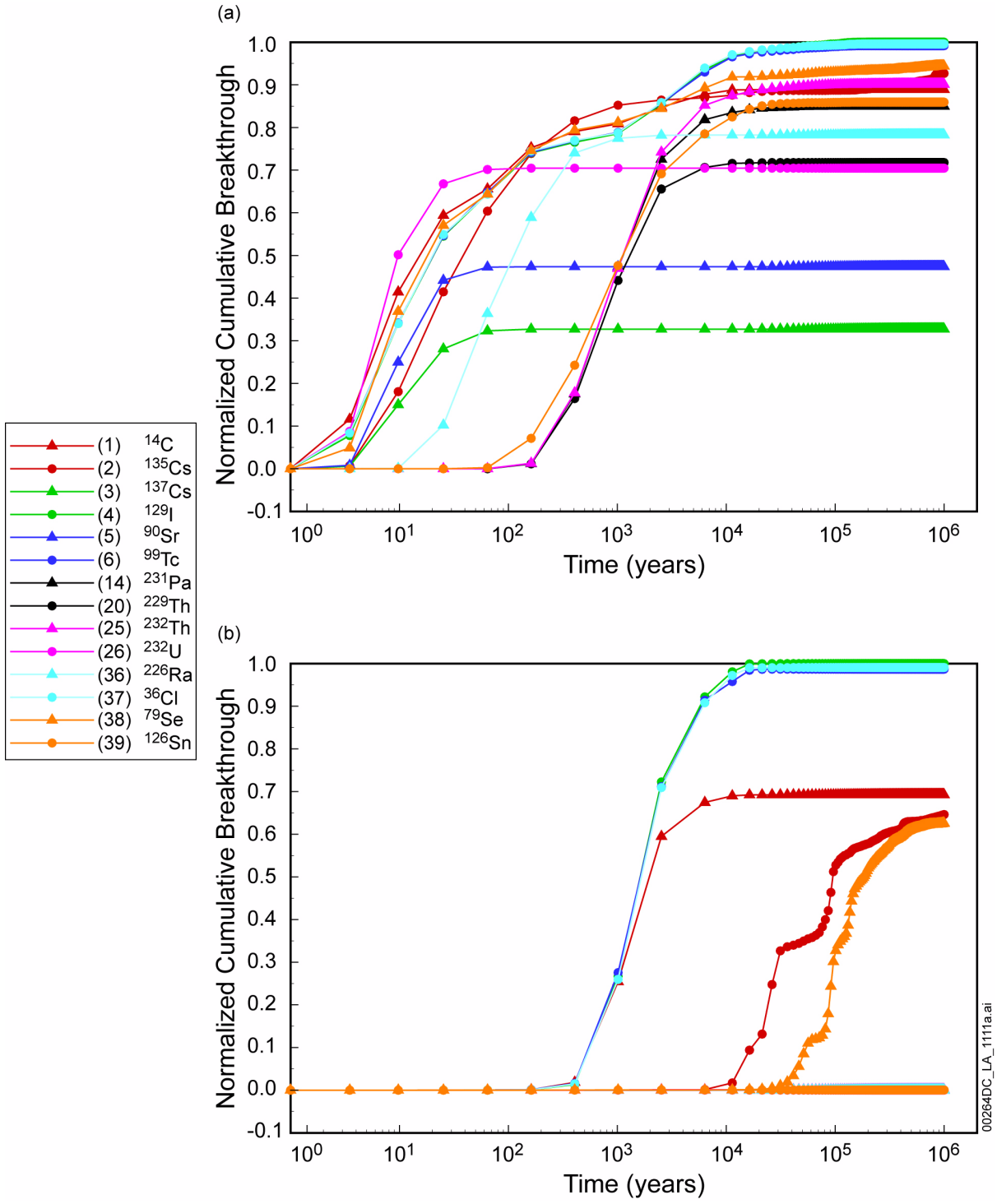

Figure 2.3.8-43. Normalized Cumulative Breakthrough Curves of 14 Radionuclides with Simple Decay the Flow Field Developed Using the Glacial Transition 10th Percentile Infiltration Map and Representative Parameter Values

NOTE: (a) Northern release location, (b) Southern release location. Curves at 0 for all times represent minute or no breakthrough at the water table during the simulation period.

Source: SNL 2008a, Figure 6.6.2-5[b].

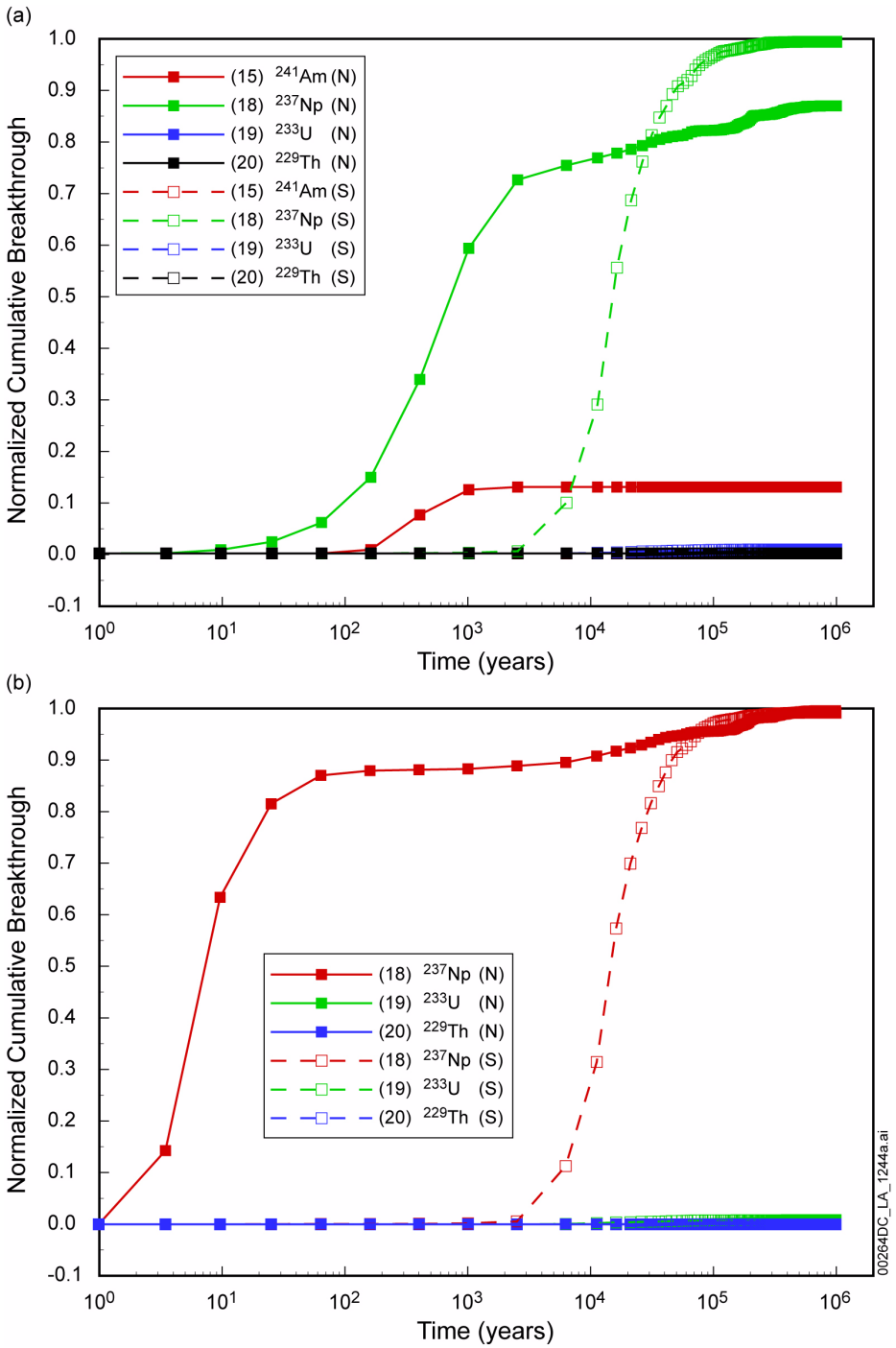

Figure 2.3.8-44. Normalized Cumulative Breakthrough Curves of Neptunium Series, for the Flow Field Developed Using the Glacial-Transition, 10th Percentile Infiltration Map and Representative Parameter Values

NOTE: (a) Decay Chain $^{241}Am \rightarrow ^{237}Np \rightarrow ^{233}U \rightarrow ^{229}Th$, with releases as ^{241}Am, (b) $^{237}Np \rightarrow ^{233}U \rightarrow ^{229}Th$, with releases as ^{237}Np. Curves at 0 for all times represent minute or no breakthrough at the water table during the simulation period.
N = northern release location; S = southern release location.

Source: SNL 2008a, Figures D.2-3[b] and D.2-4[b].

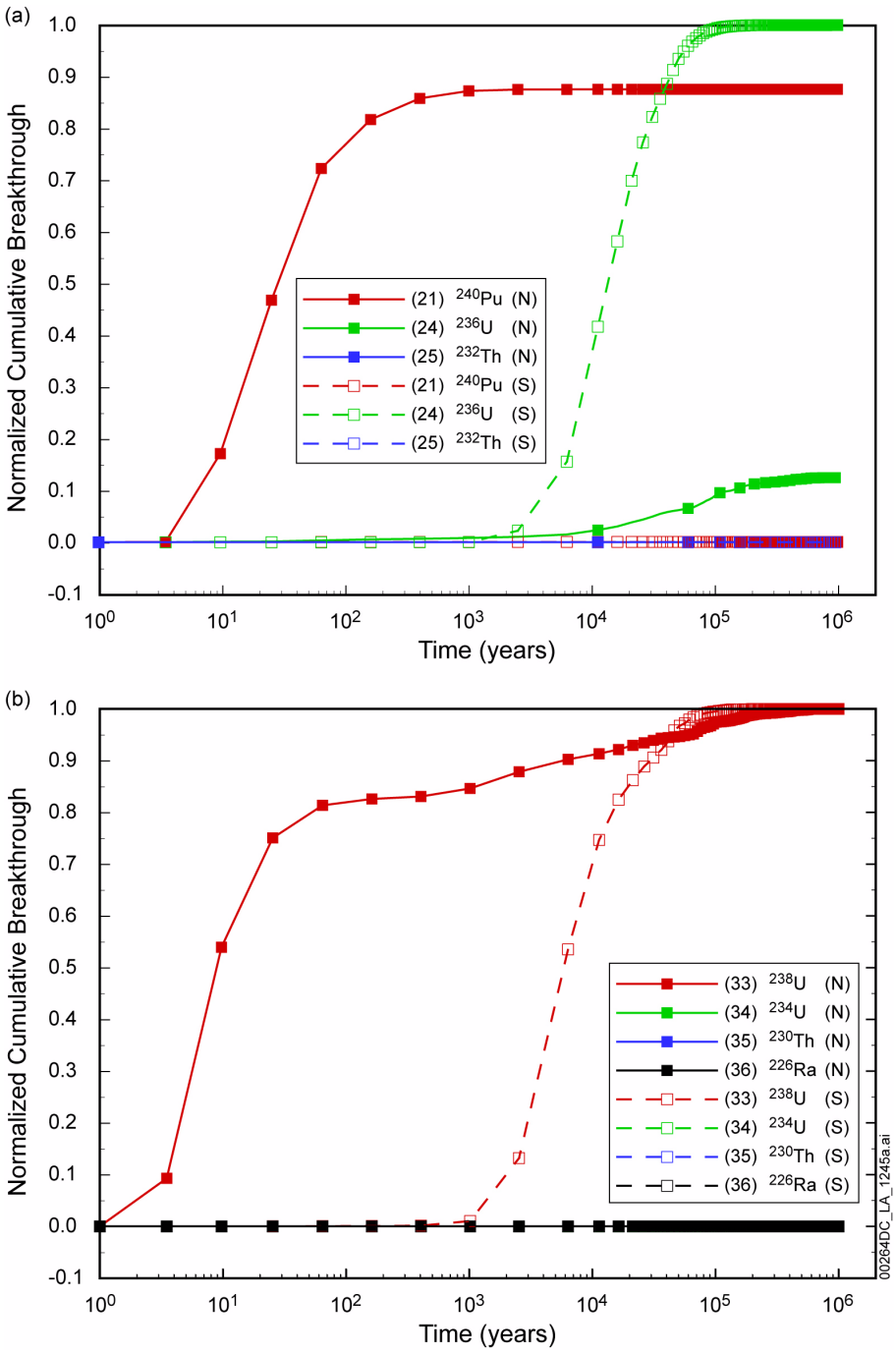

Figure 2.3.8-45. Normalized Cumulative Breakthrough Curves of Thorium Series (Top) and a Portion of the Uranium Series (Bottom), for the Flow Field Developed Using the Glacial-Transition, 10th Percentile Infiltration Map and Representative Parameter Values

NOTE: (a) Decay Chain $^{240}Pu \rightarrow ^{236}U \rightarrow ^{232}Th$, with releases as ^{240}Pu, (b) $^{238}U \rightarrow ^{234}U \rightarrow ^{230}Th \rightarrow ^{226}Ra$, with releases as ^{238}U. Curves at 0 for all times represent minute or no breakthrough at the water table during the simulation period.
N = northern release location; S = southern release location.

Source: SNL 2008a, Figures D.2-6[b] and D.2-8[b].

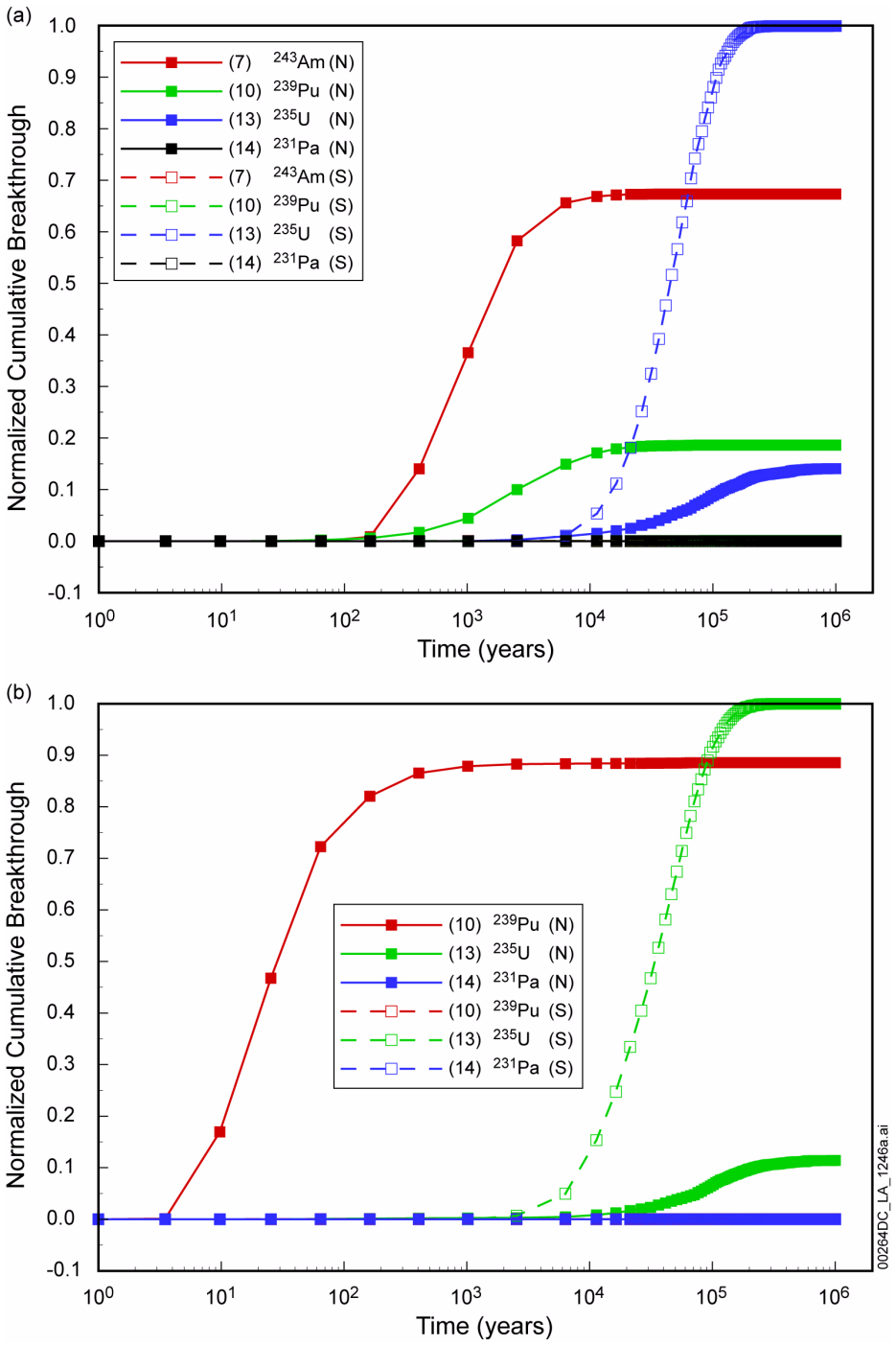

Figure 2.3.8-46. Normalized Cumulative Breakthrough Curves of Actinium Series, for the Flow Field Developed Using the Glacial-Transition, 10th Percentile Infiltration Map and Representative Parameter Values

NOTE: (a) Decay Chain $^{243}Am \rightarrow ^{239}Pu \rightarrow ^{235}U \rightarrow ^{231}Pa$, with releases as ^{243}Am, (b) $^{239}Pu \rightarrow ^{235}U \rightarrow ^{231}Pa$, with releases as ^{239}Pu. Curves at 0 for all times represent minute or no breakthrough at the water table during the simulation period.
N = northern release location; S = southern release location.

Source: SNL 2008a, Figures D.2-1[b] and D.2-2[b].

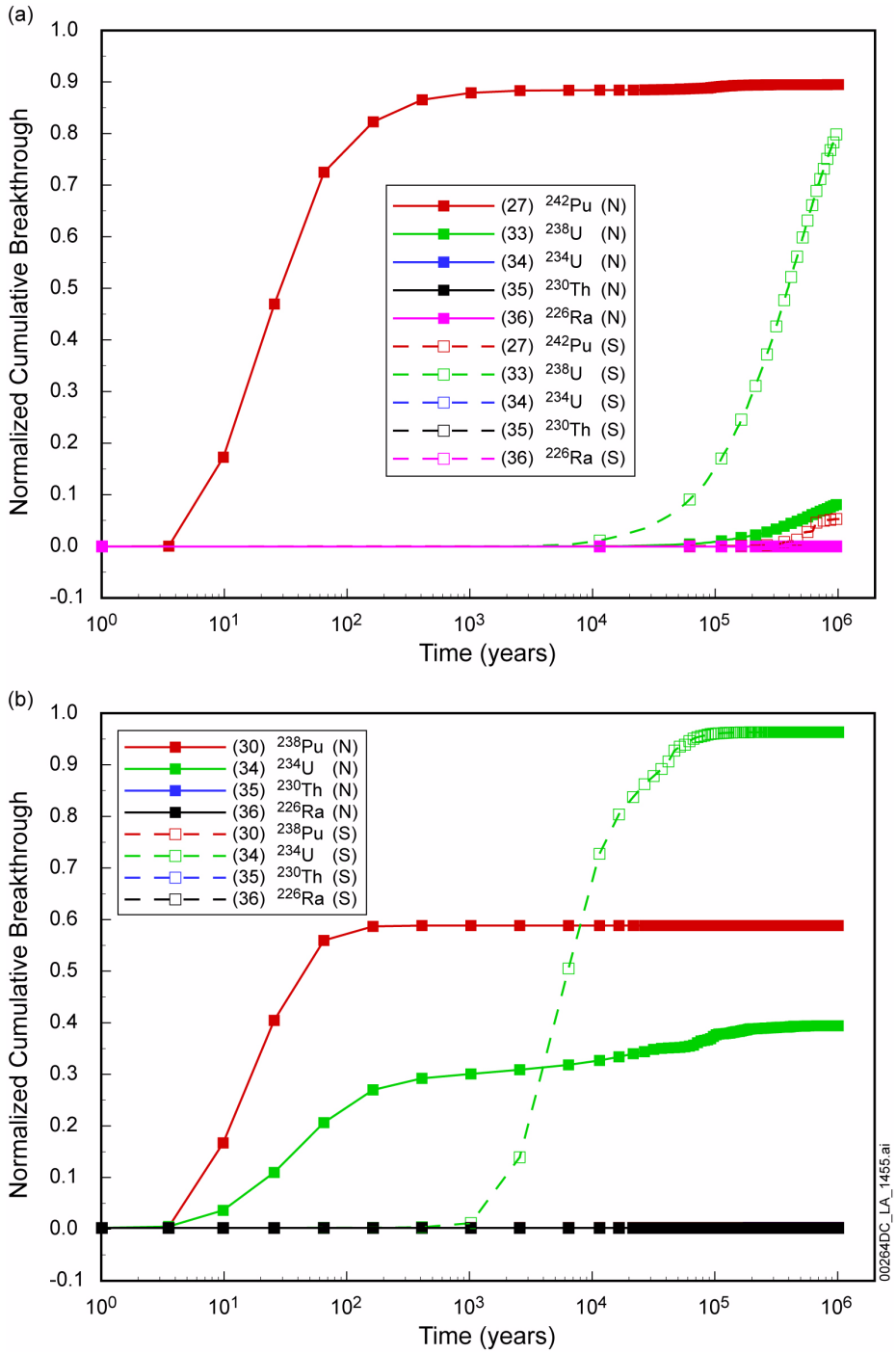

Figure 2.3.8-47. Normalized Cumulative Breakthrough Curves of Uranium Series, for the Flow Field Developed Using the Glacial-Transition, 10th Percentile Infiltration Map and Representative Parameter Values

NOTE: (a) Decay Chain $^{242}Pu \rightarrow ^{238}U \rightarrow ^{234}U \rightarrow ^{230}Th \rightarrow ^{226}Ra$, with releases as ^{242}Pu, (b) $^{238}Pu \rightarrow ^{234}U \rightarrow ^{230}Th \rightarrow ^{226}Ra$, with releases as ^{238}Pu. Curves at 0 for all times represent minute or no breakthrough at the water table during the simulation period.
N = northern release location; S = southern release location.

Source: SNL 2008a, Figures D.2-5[b] and D.2-7[b].

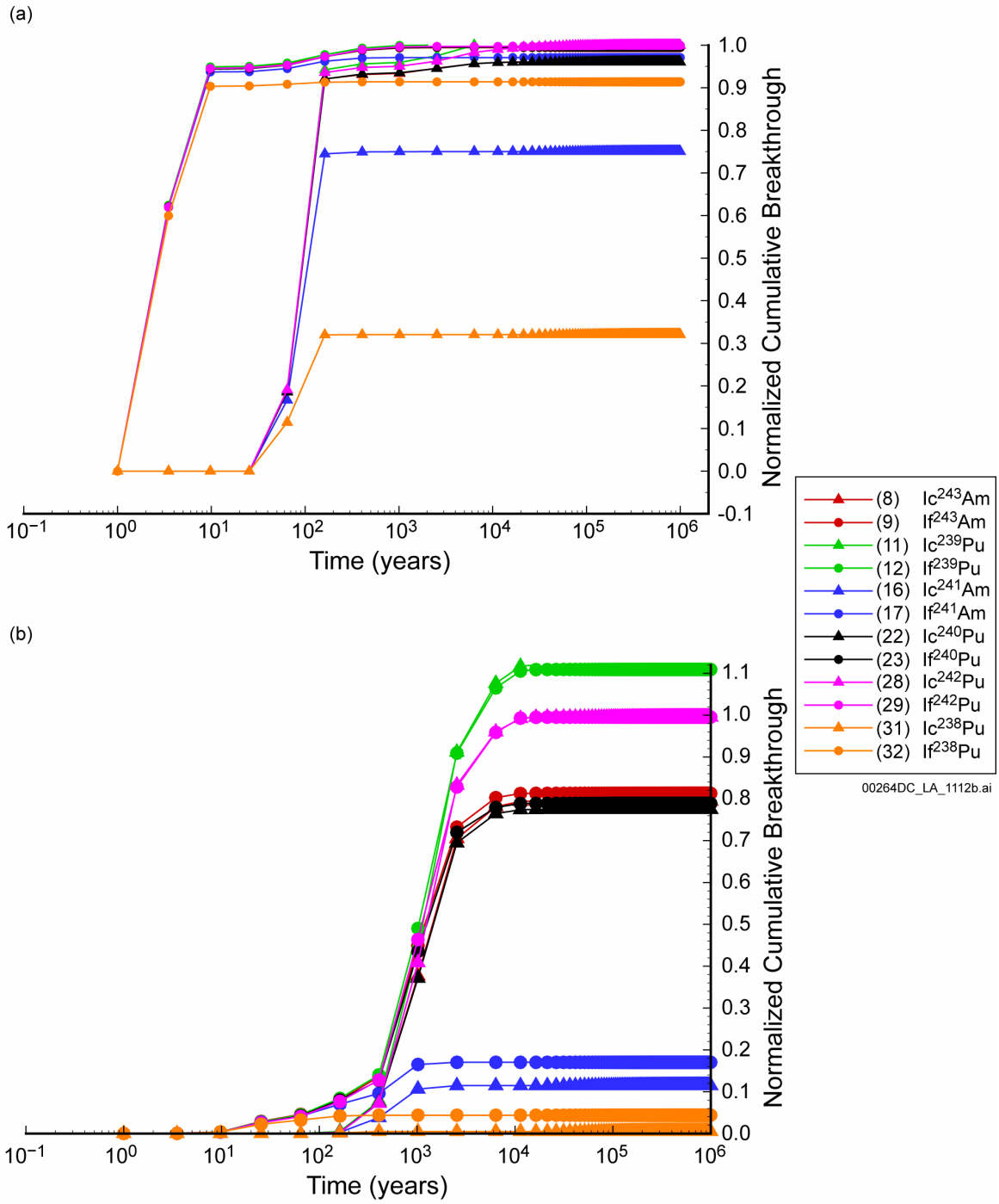

Figure 2.3.8-48. Normalized Cumulative Breakthrough Curves of Six Irreversible Fast Colloids and SIx Irreversible Slow Colloids for the Flow Field Developed Using the Glacial Transition 10th Percentile Infiltration Map and Representative Parameter Values

NOTE: (a) Northern Release Location, (b) Southern Release Location.
The If colloid represents 0.168% of the released inventory of colloid-facilitated radionuclide for each species.
Curves at 0 for all times represent minute or no breakthrough at the water table during the simulation period.
Ic = irreversible colloid; If = irreversible fast colloid.

Source: SNL 2008a, Figure 6.6.2-6[b].

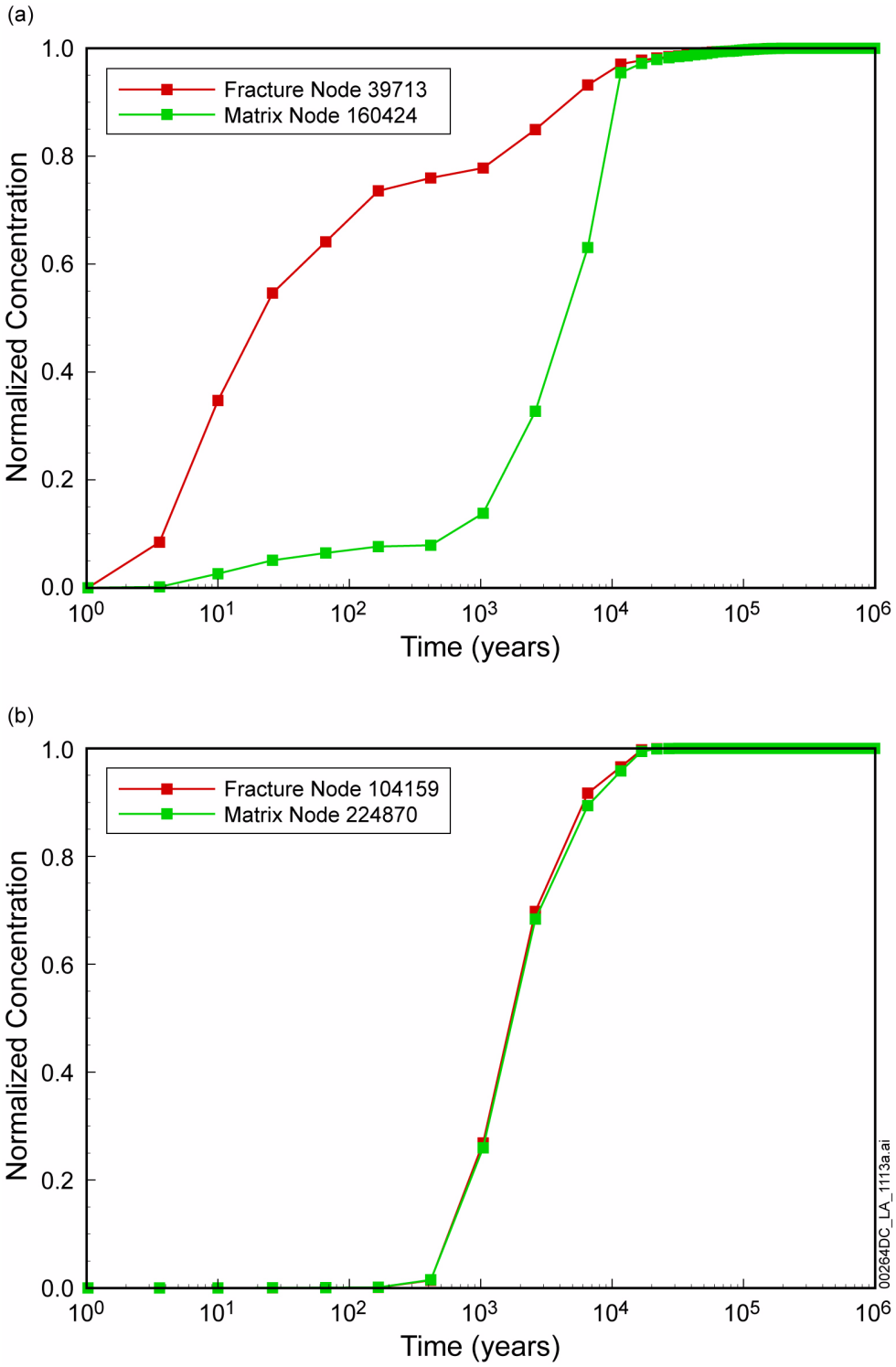

Figure 2.3.8-49. Comparison of Normalized Cumulative Breakthrough Curves of ^{99}Tc for Particles Released at Fracture Node or Matrix Node for the Flow Field Developed Using the Glacial Transition, 10th Percentile Infiltration Map, Representative Parameter Values

NOTE: (a) Northern release location, (b) Southern release location.

Source: SNL 2008a, Figure 6.6.2-8[b].

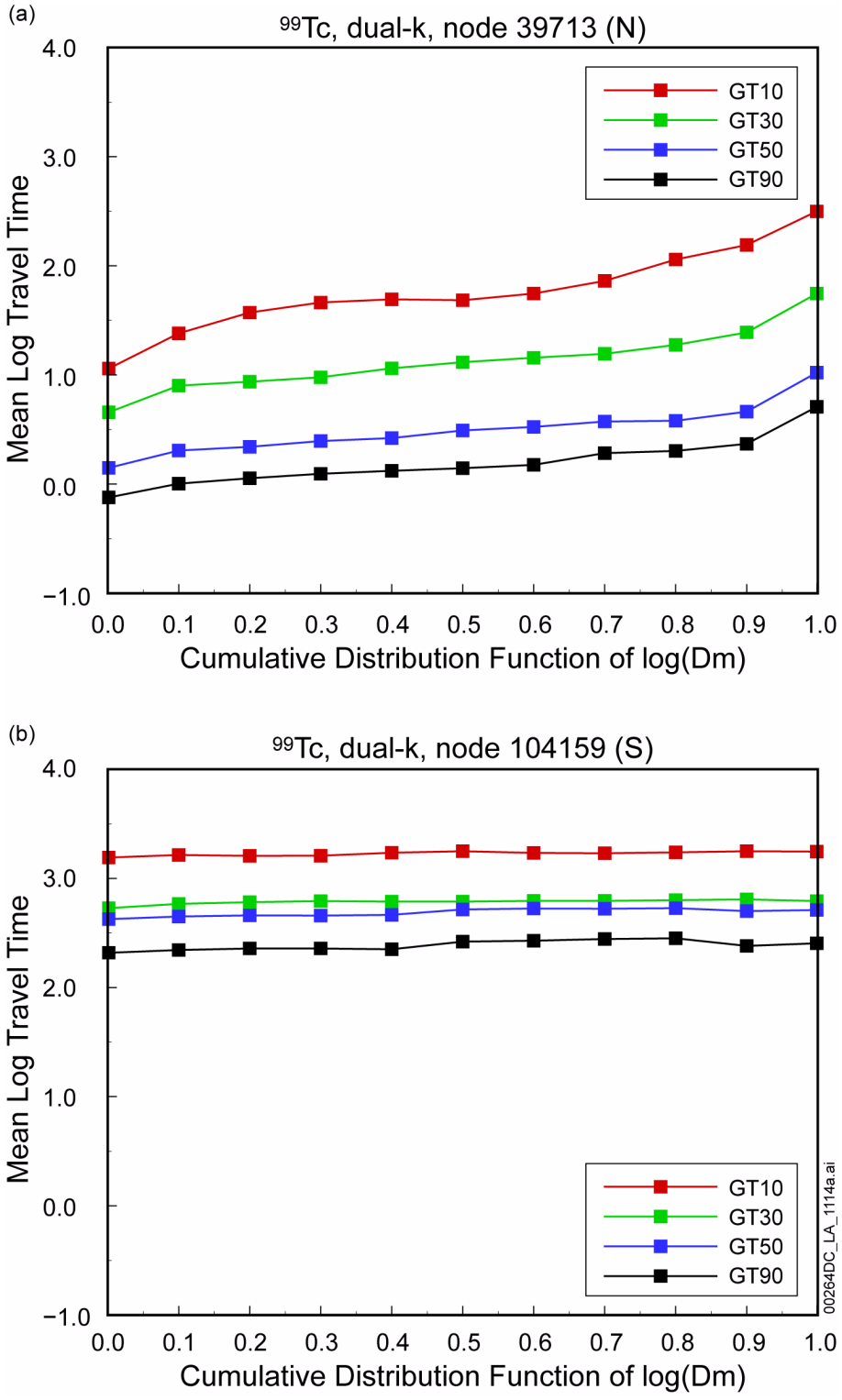

Figure 2.3.8-50. Comparison of Mean Travel Time of ^{99}Tc as a Function of Matrix Diffusion Coefficient under Glacial Transition Climate Conditions for the dual-k Model

NOTE: (a) Northern release location, (b) Southern release location.

Source: SNL 2008a, Figure 6.8.2-1[b].

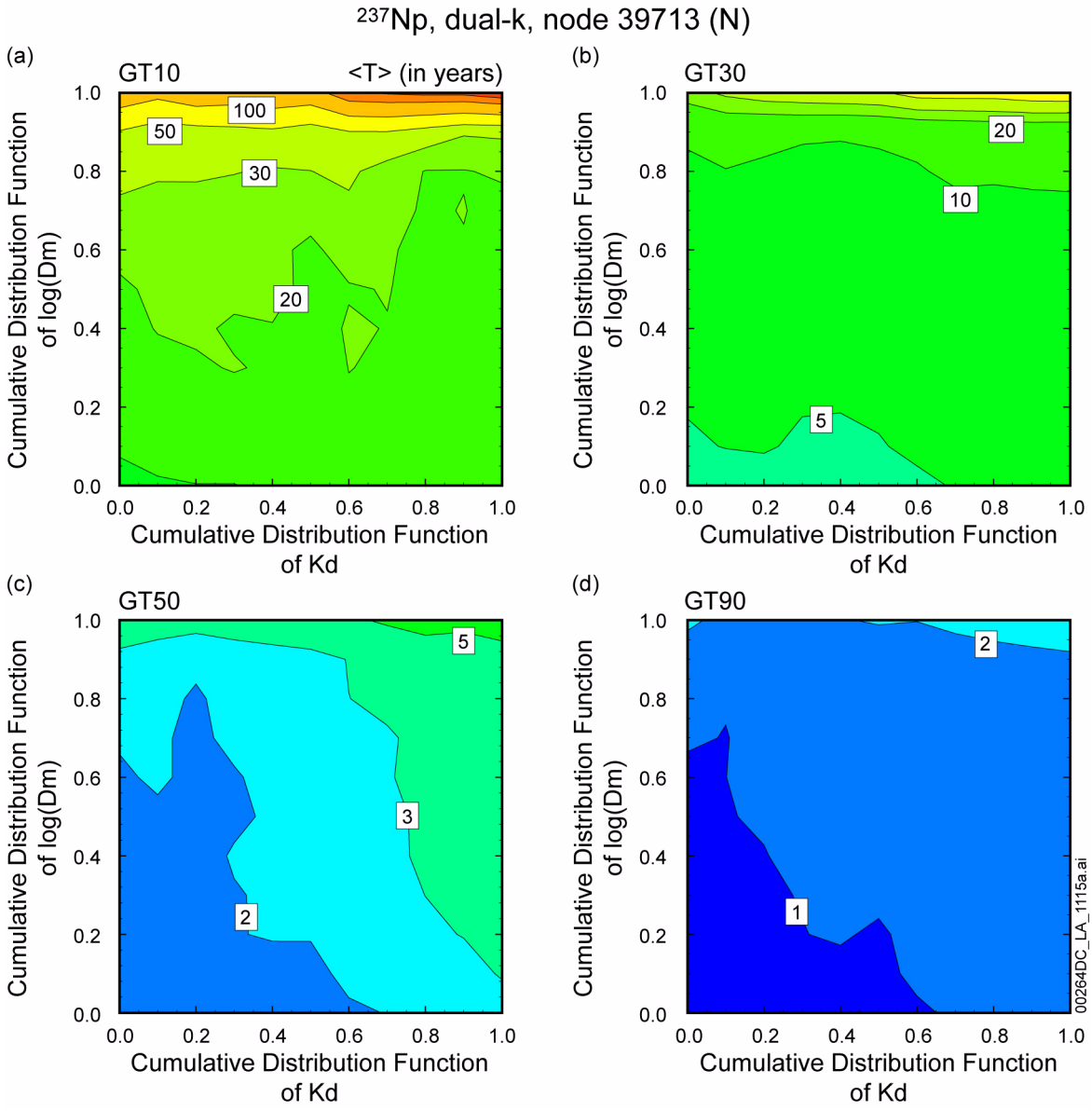

Figure 2.3.8-51. Mean Travel Time of ^{237}Np as a Function of Matrix Diffusion Coefficient and Sorption Coefficient for the Glacial Transition Climate Condition, dual-k Model, and Northern Release Location

Source: SNL 2008a, Figure 6.8.2-3[b].

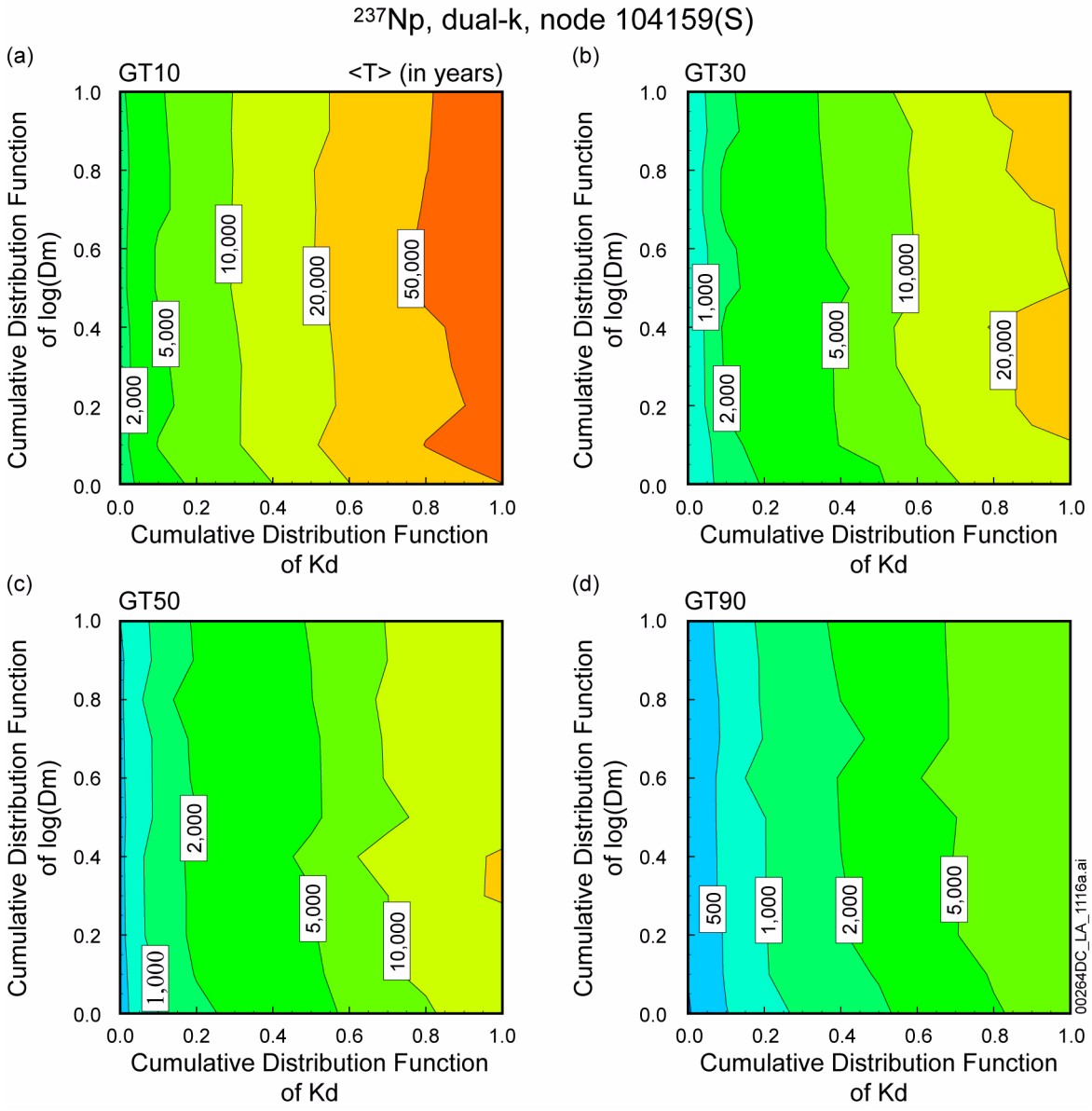

Figure 2.3.8-52. Mean Travel Time of ^{237}Np as a Function of Matrix Diffusion Coefficient and Sorption Coefficient for the Glacial Transition Climate Condition, dual-k Model, and Southern Release Location

Source: SNL 2008a, Figure 6.8.2-4[b].

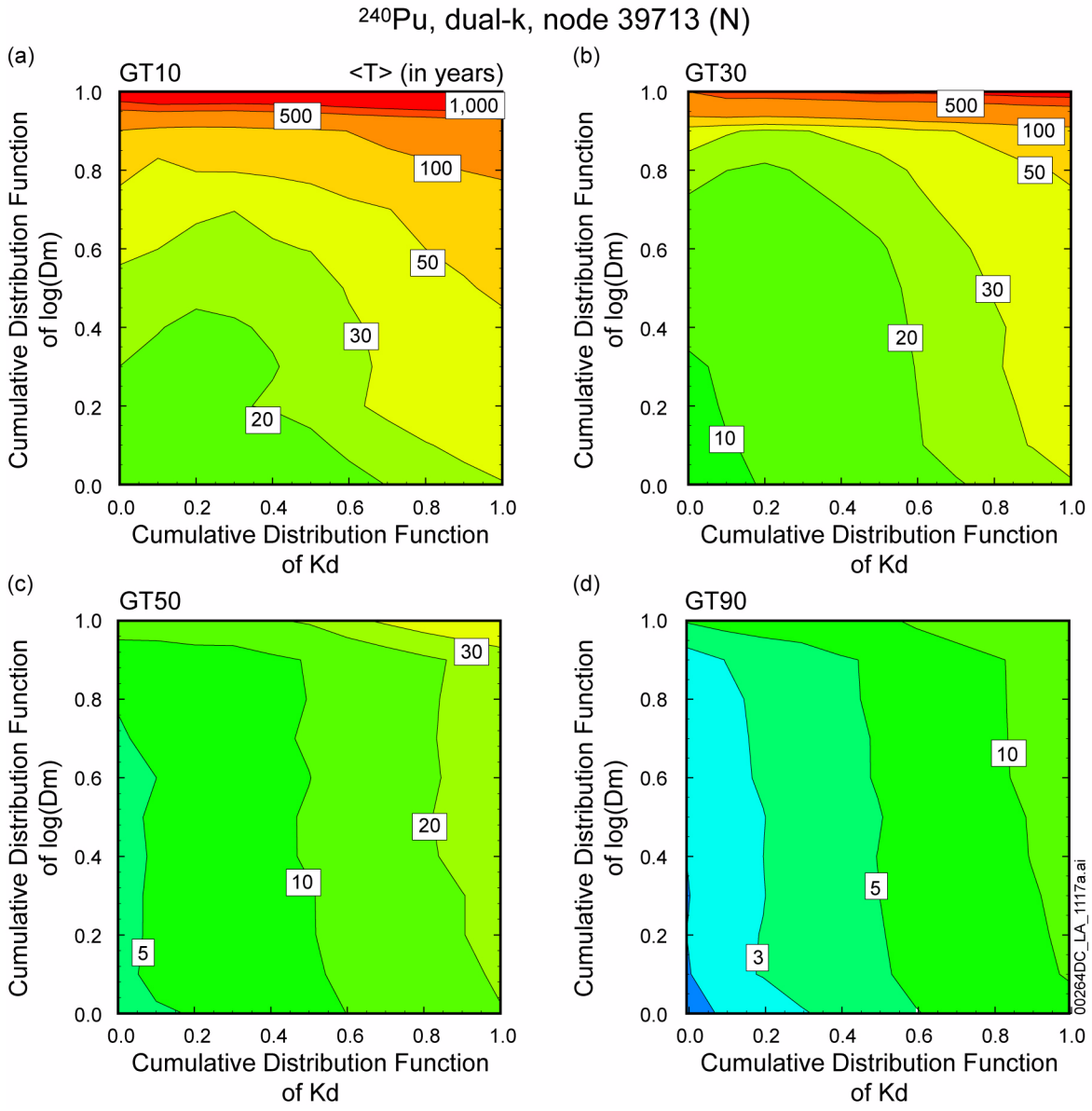

Figure 2.3.8-53. Mean Travel Time of ^{240}Pu as a Function of Matrix Diffusion Coefficient and Sorption Coefficient for the Glacial-Transition Climate Condition, dual-k Model, and Northern Release Location

Source: SNL 2008a, Figure 6.8.2-7[b].

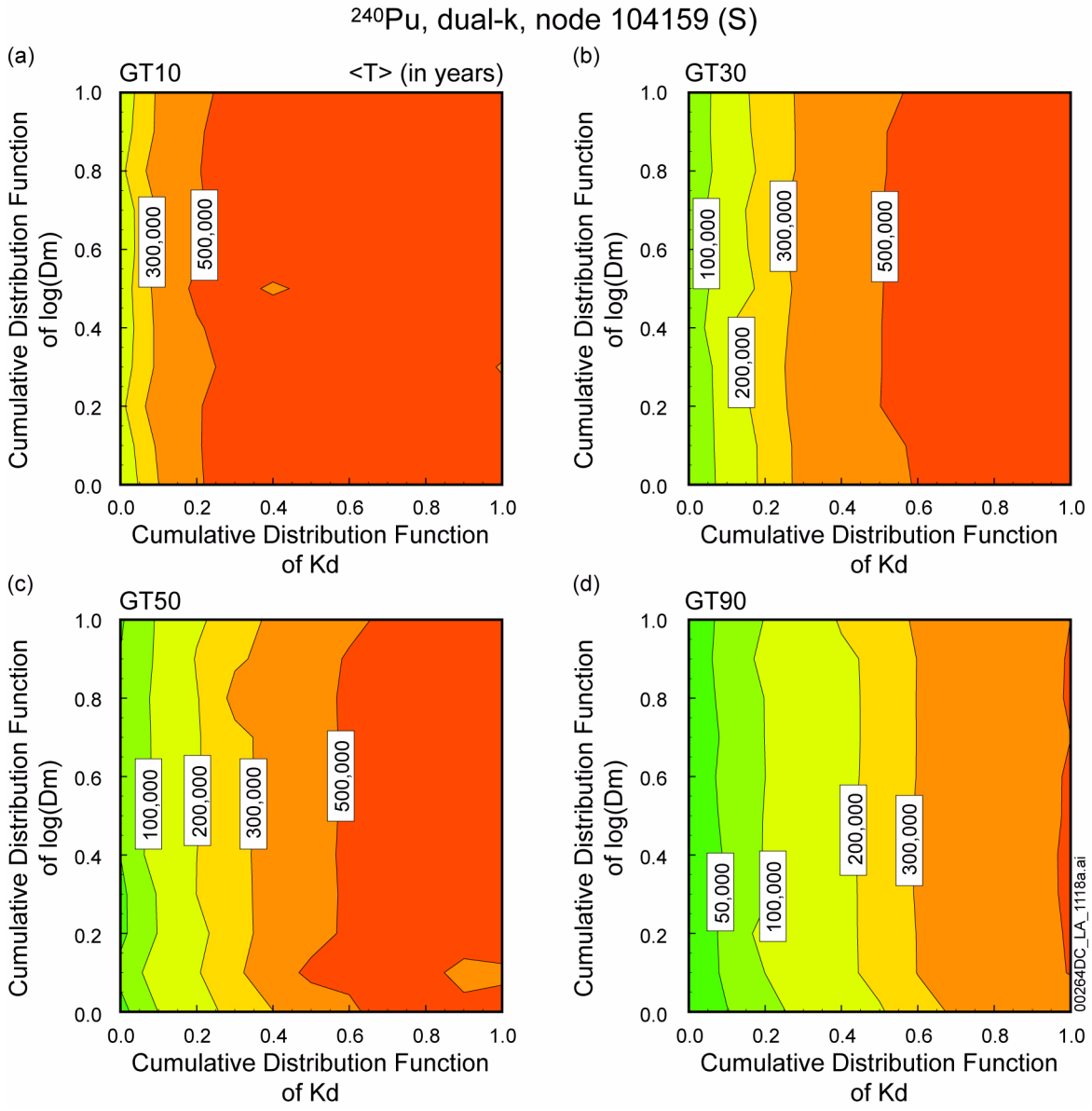

Figure 2.3.8-54. Mean Travel Time of ^{240}Pu as a Function of Matrix Diffusion Coefficient and Sorption Coefficient for the Glacial Transition Climate Condition, dual-k Model, and Southern Release Location

Source: SNL 2008a, Figure 6.8.2-8[b].

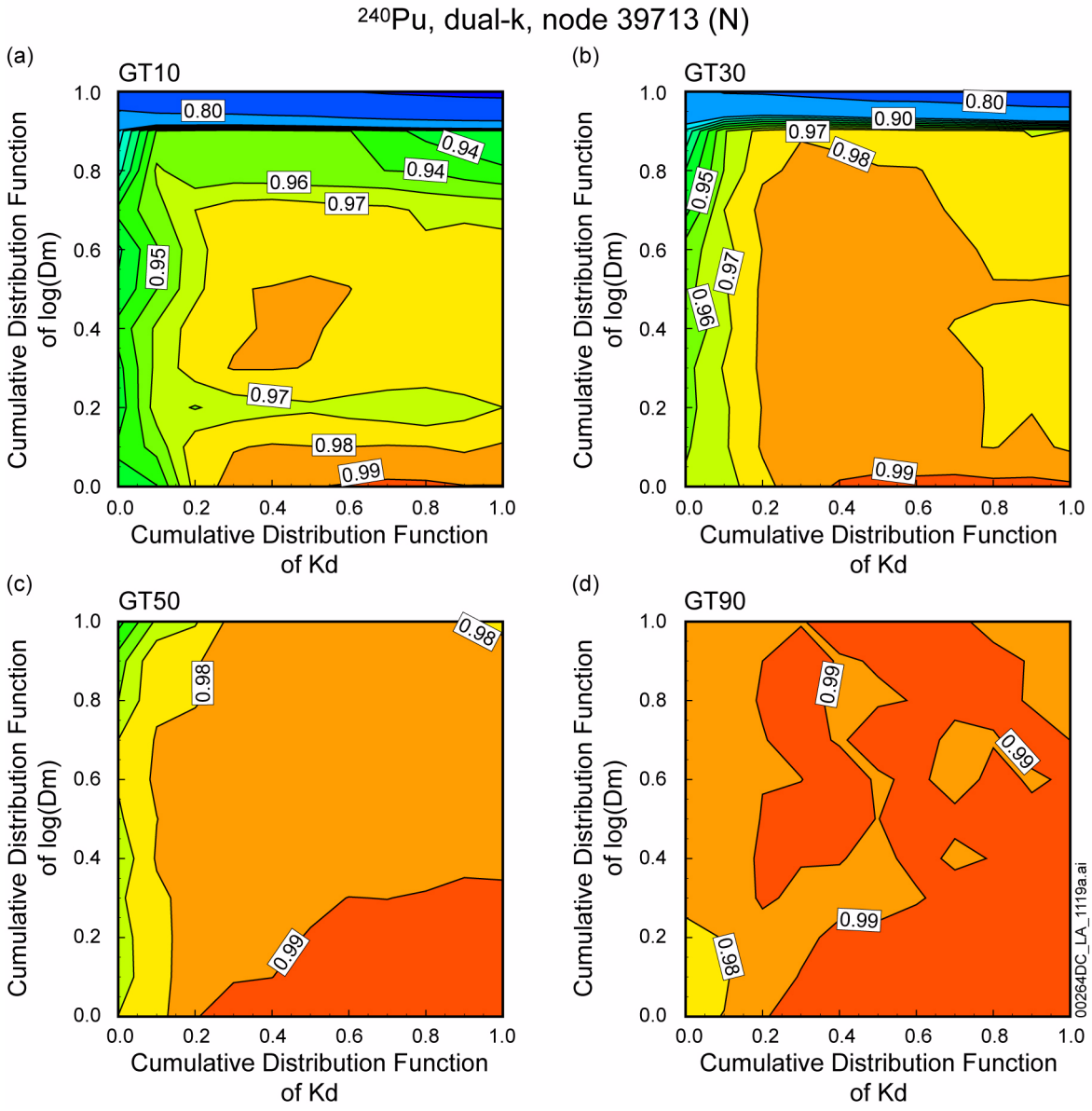

Figure 2.3.8-55. Normalized ^{240}Pu Concentration (Decay Fraction, Computed from Travel Time Distributions) as a Function of Matrix Diffusion Coefficient and Sorption Coefficient for the Glacial-Transition Climate Conditions, dual-k Model, Northern Release Location

Source: SNL 2008a, Figure 6.8.2-19[b].

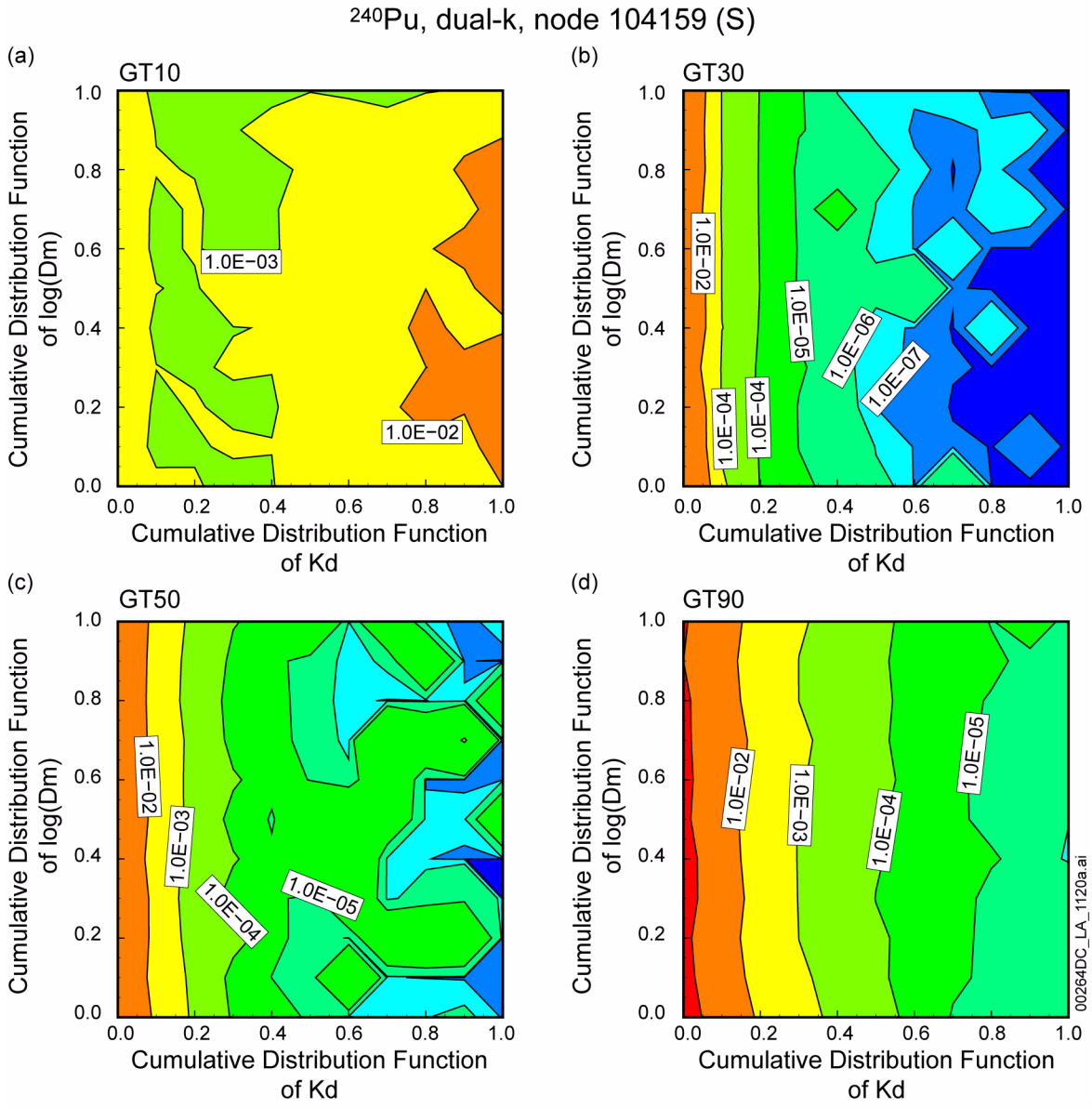

Figure 2.3.8-56. Normalized ^{240}Pu Concentration (Decay Fraction, Computed from Travel Time Distributions) as a Function of Matrix Diffusion Coefficient and Sorption Coefficient for the Glacial Transition Climate Condition, dual-k Model, Southern Release Location

Source: SNL 2008a, Figure 6.8.2-20[b].

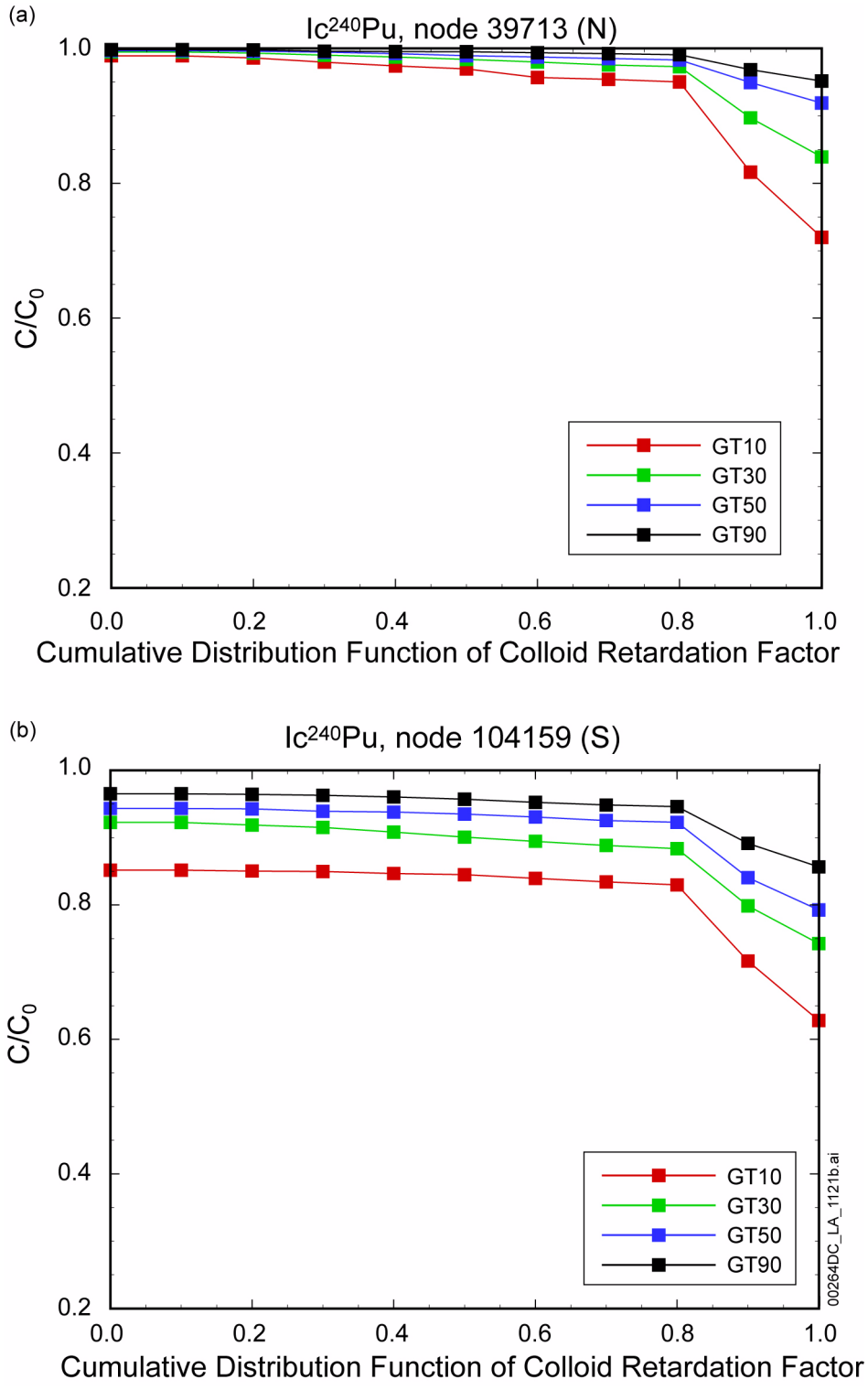

Figure 2.3.8-57. Normalized Concentration of $Ic^{240}Pu$ (Decay Fraction, Computed from Travel Time Distributions) as a Function of Colloid Retardation Factor for the Glacial Transition Climate Condition

Source: SNL 2008a, Figure 6.8.2-24[b].

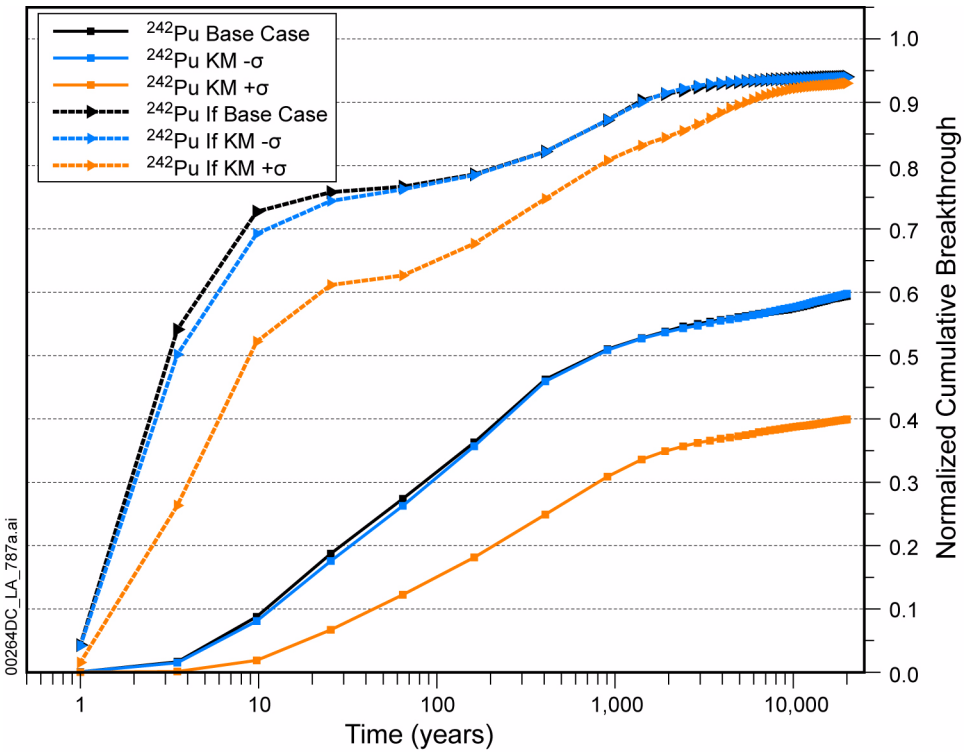

Figure 2.3.8-58. Unsaturated Zone Radionuclide Transport Abstraction Model Results for Normalized Mass Flux at the Water Table for Different Species of ^{242}Pu, for ±1σ from the Base Case of the Values for Permeabilities of the Matrix Continuum

NOTE: These results are for comparison purposes only. Simulation is based on an older version of the unsaturated zone flow model. Actual radionuclide mass flux reaching the water table will depend on release rates and locations and are simulated in the TSPA model. Simulation is based on a flow field developed using the mean glacial-transition infiltration case developed in a previous version of the infiltration model (BSC 2004h, Section 6.11.3). In this model, the average infiltration rate across the repository footprint was 19.8 mm/yr, and releases occurred across the entire repository footprint. The bottom boundary was defined as the elevated water table at a minimum of 850 meters above sea level.
If = colloid with irreversibly attached radionuclide; KM = matrix permeability; σ = one standard deviation in the matrix permeability uncertainty.

Source: SNL 2008a, Figure 6-32.

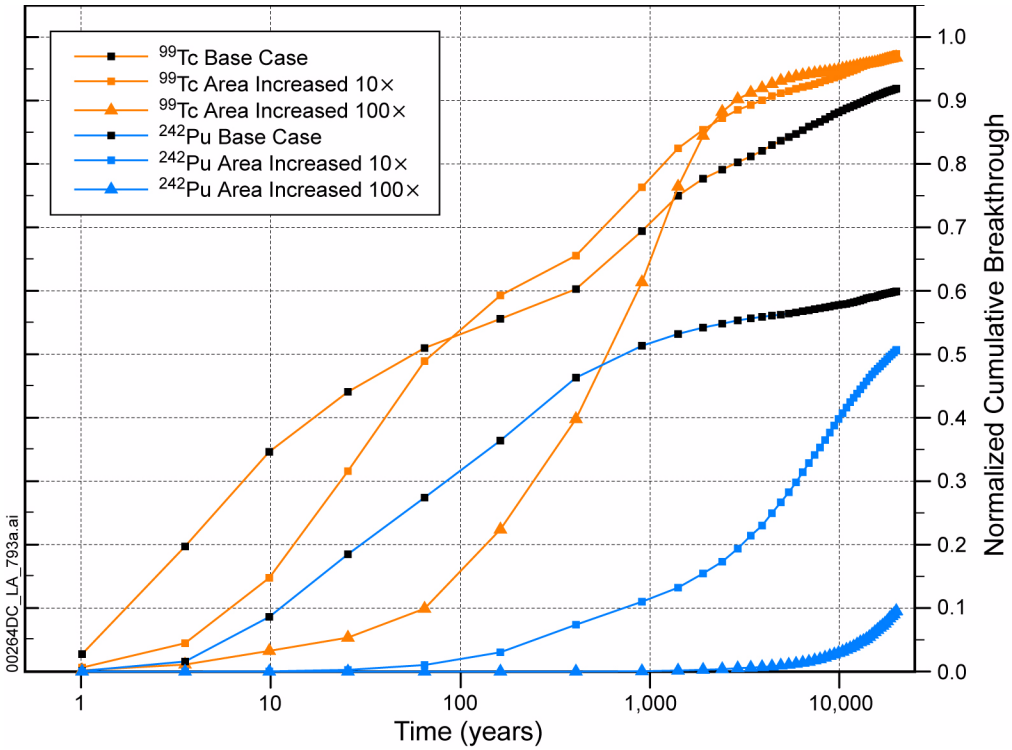

Figure 2.3.8-59. Unsaturated Zone Radionuclide Transport Abstraction Model Results for Normalized Mass Flux at the Water Table for ^{99}Tc and ^{242}Pu for 10- and 100-fold Increases in the Effective Surface Area for Diffusion

NOTE: These results are for comparison purposes only. Simulation is based on an older version of the unsaturated zone flow model. Actual radionuclide mass flux reaching the water table will depend on release rates and locations and are simulated in the TSPA model. Simulation is based on a flow field developed using the mean glacial-transition infiltration case developed in a previous version of the infiltration model (BSC 2004h, Section 6.11.3). In this model, the average infiltration rate across the repository footprint was 19.8 mm/yr, and releases occurred across the entire repository footprint. The bottom boundary was defined as the elevated water table at a minimum of 850 meters above sea level.

Source: SNL 2008a, Figure 6-37.

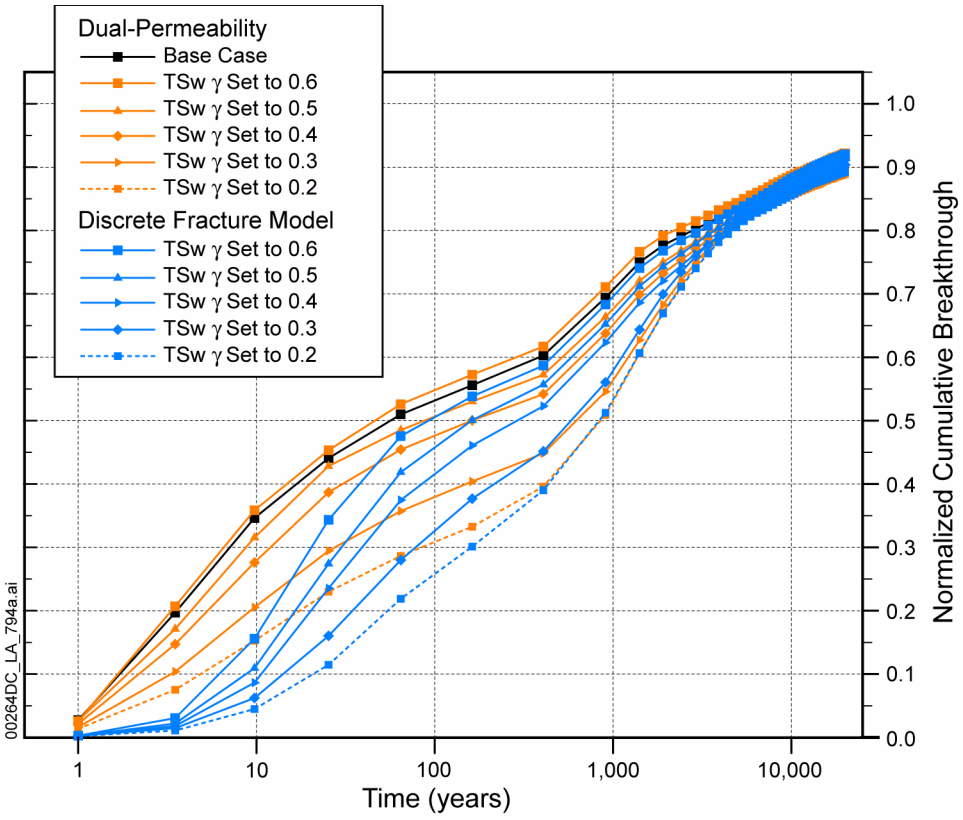

Figure 2.3.8-60. Unsaturated Zone Radionuclide Transport Abstraction Model Results for Normalized Mass Flux at the Water Table for ^{99}Tc for Different Values of the Active Fracture Model γ Parameter and Different Fracture–Matrix Diffusion Conceptual Models (Dual-Permeability Versus Discrete Fracture Model)

NOTE: These results are for comparison purposes only. Simulation is based on an older version of the unsaturated zone flow model. Actual radionuclide mass flux reaching the water table will depend on release rates and locations and are simulated in the TSPA model. Simulation is based on a flow field developed using the mean glacial-transition infiltration case developed in a previous version of the infiltration model (BSC 2004h, Section 6.11.3). In this model, the average infiltration rate across the repository footprint was 19.8 mm/yr, and releases occurred across the entire repository footprint. The bottom boundary was defined as the elevated water table at a minimum of 850 meters above sea level.

Source: SNL 2008a, Figure 6-38.

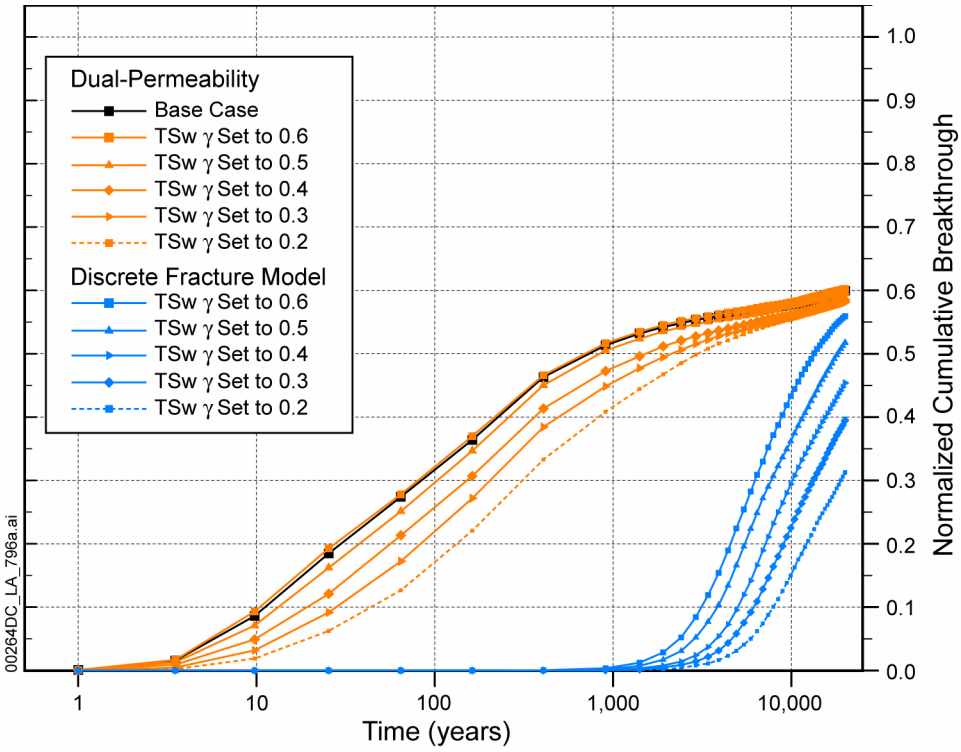

Figure 2.3.8-61. Unsaturated Zone Radionuclide Transport Abstraction Model Results for Normalized Mass Flux at the Water Table for ^{242}Pu for Different Values of the Active Fracture Model γ Parameter and Different Fracture–Matrix Diffusion Conceptual Model (Dual-Permeability Versus Discrete Fracture Model)

NOTE: These results are for comparison purposes only. Simulation is based on an older version of the unsaturated zone flow model. Actual radionuclide mass flux reaching the water table will depend on release rates and locations and are simulated in the TSPA model. Simulation is based on a flow field developed using the mean glacial-transition infiltration case developed in a previous version of the infiltration model (BSC 2004h, Section 6.11.3). In this model, the average infiltration rate across the repository footprint was 19.8 mm/yr, and releases occurred across the entire repository footprint. The bottom boundary was defined as the elevated water table at a minimum of 850 meters above sea level.

Source: SNL 2008a, Figure 6-40.

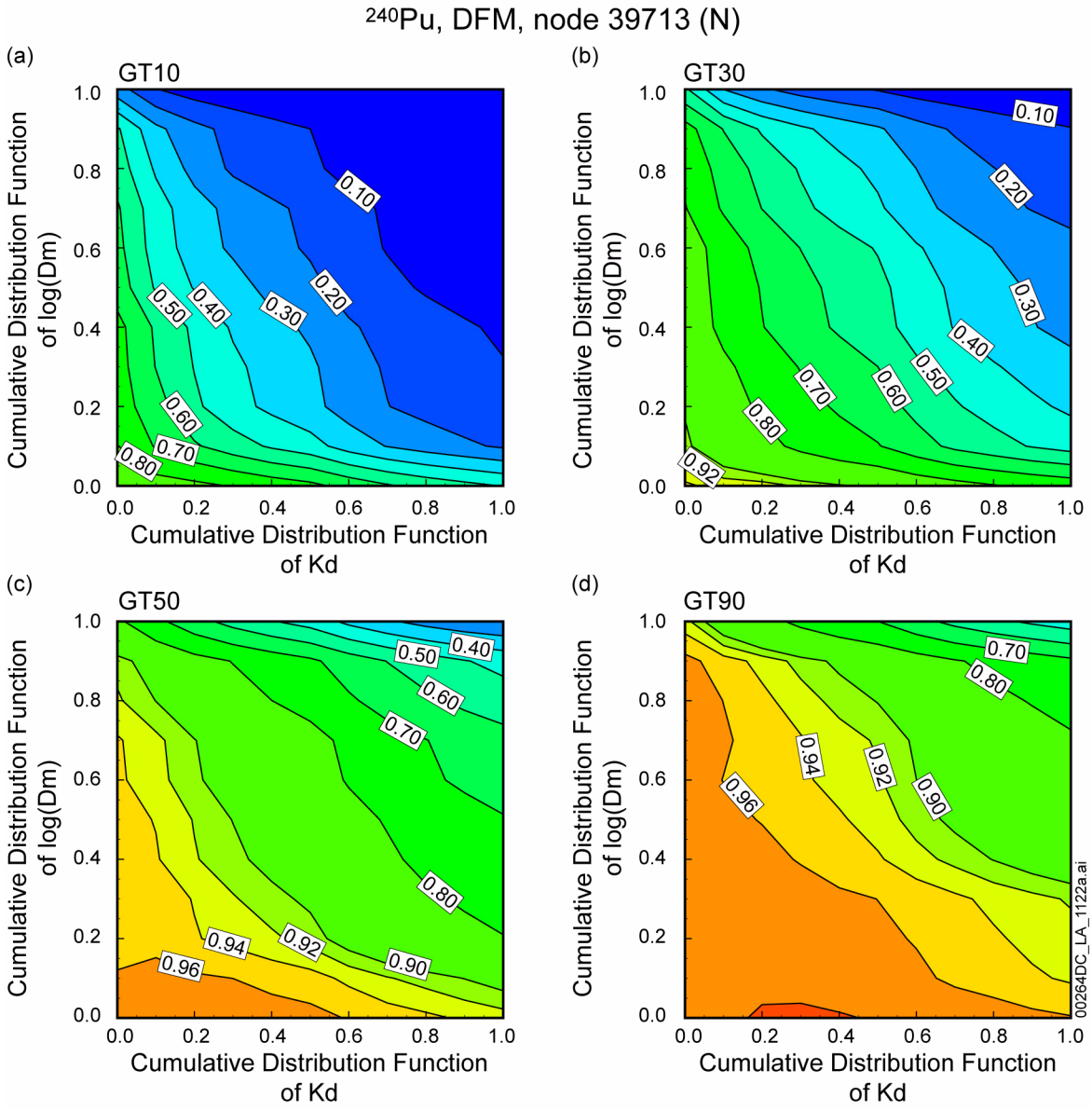

Figure 2.3.8-62. Normalized ^{240}Pu Concentration (Decay Fraction, Computed from Travel Time Distributions) as a Function of Matrix Diffusion Coefficient and Sorption Coefficient for the Glacial-Transition Climate Condition, Discrete Fracture Model, Northern Release Location

Source: SNL 2008a, Figure 6.8.2-21[b].

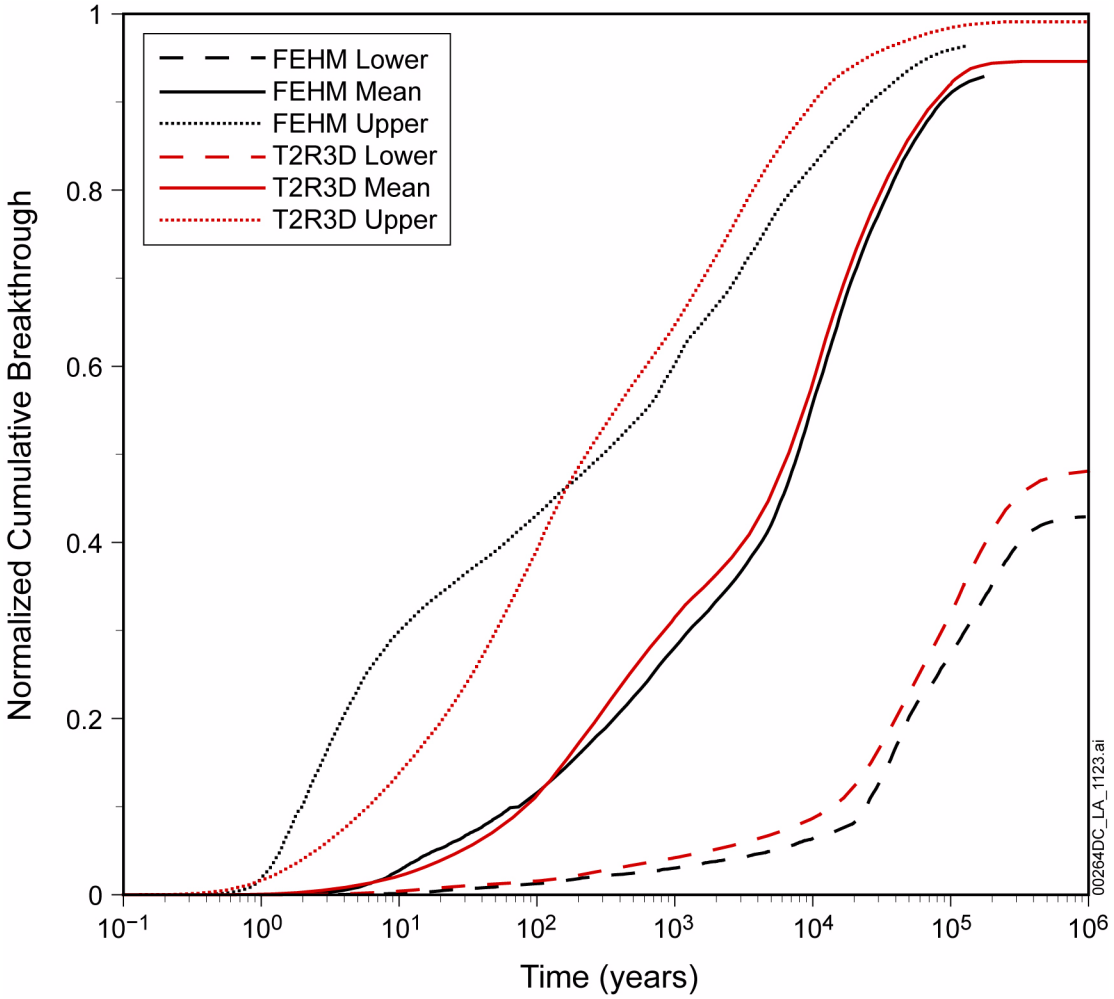

Figure 2.3.8-63. These results are for comparison purposes only. Comparison of ^{99}Tc Breakthrough Curves for the Unsaturated Zone Transport Process Model (T2R3D) and the Unsaturated Zone Radionuclide Transport Abstraction Model (FEHM) Simulations for Three Infiltration Rate Scenarios

NOTE: These results are for comparison purposes only. Simulations are based on an older version of the unsaturated zone flow model. Normalized breakthrough is the cumulative ^{99}Tc mass arrival at the water table divided by the initial ^{99}Tc mass released at the repository. Simulations are based on flow fields developed using the three present-day infiltration cases developed in a previous version of the infiltration model (BSC 2004h, Section 6.11.1). In this model, the average infiltration rates across the repository footprint were 0.4 mm/yr for the curves labelled “Lower,” 4.7 mm/yr for the curves labelled “mean,” and 11.6 mm/yr for the curves labelled “Upper.” The bottom boundary was defined as the present-day water table, and releases occurred across the entire repository footprint.

Source: SNL 2008a Figure 7-10 in Addendum 1.

INTENTIONALLY LEFT BLANK